University of Alberta

Nonstationary and Nonlinear Approaches for the Analysis and Prediction of Hydroclimatic Variables in Eastern and Southern Africa

by

Davison Mwale ©

A thesis submitted to the Faculty of Graduate Studies and Research in partial
fulfillment of the degree of Doctor of Philosophy

in

Water Resources Engineering

Department of Civil and Environmental Engineering

Edmonton, Alberta
Spring, 2005.

Library and
Archives Canada

Published Heritage
Branch

395 Wellington Street
Ottawa ON K1A 0N4
Canada

Bibliothèque et
Archives Canada

Direction du
Patrimoine de l'édition

395, rue Wellington
Ottawa ON K1A 0N4
Canada

0-494-08279-8

Your file Votre référence
ISBN
Our file Notre reference
ISBN

NOTICE:
The author has granted a non-exclusive license allowing Library and Archives Canada to reproduce, publish, archive, preserve, conserve, communicate to the public by telecommunication or on the Internet, loan, distribute and sell theses worldwide, for commercial or non-commercial purposes, in microform, paper, electronic and/or any other formats.

The author retains copyright ownership and moral rights in this thesis. Neither the thesis nor substantial extracts from it may be printed or otherwise reproduced without the author's permission.

AVIS:
L'auteur a accordé une licence non exclusive permettant à la Bibliothèque et Archives Canada de reproduire, publier, archiver, sauvegarder, conserver, transmettre au public par télécommunication ou par l'Internet, prêter, distribuer et vendre des thèses partout dans le monde, à des fins commerciales ou autres, sur support microforme, papier, électronique et/ou autres formats.

L'auteur conserve la propriété du droit d'auteur et des droits moraux qui protège cette thèse. Ni la thèse ni des extraits substantiels de celle-ci ne doivent être imprimés ou autrement reproduits sans son autorisation.

In compliance with the Canadian Privacy Act some supporting forms may have been removed from this thesis.

While these forms may be included in the document page count, their removal does not represent any loss of content from the thesis.

Conformément à la loi canadienne sur la protection de la vie privée, quelques formulaires secondaires ont été enlevés de cette thèse.

Bien que ces formulaires aient inclus dans la pagination, il n'y aura aucun contenu manquant.

Canada

ABSTRACT

Motivated by the lack of knowledge on the nonstationarity of hydroclimatic processes and the nonlinearity of the interation among hydroclimatic variables in Eastern Africa (EA), Central Southern Africa (CSA), Southern Africa (SA), and the Indian and Atlantic Oceans, this thesis has developed the methods of Wavelet and Hilbert empirical orthogonal functions (WEOF and HEOF) and the Wavelet and Hilbert independent component (WICA and HICA) analyses to identify the spatial, temporal and frequency variability regimes of the regional climate.

The nonlinear genetic algorithm neural network algorithm (ANN-GA) model is developed to predict the variability of hydroclimatic variables through teleconnection. The ANN-GA–disaggregation-soil moisture accounting (ANN-GA-DIS-SMA) model is developed to predict weekly streamflow from seasonal oceanic variability. The combination of ANN-GA and a statistical disaggregation model is developed to predict weekly streamflow directly from predicted seasonal rainfall.

The WEOF and HEOF have helped to extract information on nonstationary spatial, temporal and frequency patterns of the sea surface temperature (SST) of the Indian and Atlantic Oceans and the rainfall of EA, CSA and SA. This new information facilitates the accurate prediction of seasonal rainfall for the East and Southern Africa region and long term planning of agriculture and water resource management. For an 11-year validation period (1987-1997), ANN-GA accounted for 49-81% of the variance of observed EA September-November and SA summer rainfalls and 67-81% of the observed EA March-May rainfall. Using the 1984-1995 validation period for CSA rainfall, ANN-GA captured 64-81% of the rainfall

variance. The ANN-GA-DIS-SMA has shown considerable skill in predicting weekly streamflow from weekly rainfall disaggregated from seasonal rainfall predicted from the seasonal SST data, and can explain 81-96% of the observed weekly streamflow variance. The ANN-GA-DIS model has shown relatively weaker skill with only 61-84% of variance explained.

The analysis of scale-based energy helped determine the effects of the El Niño southern oscillation (ENSO) on the rainfall of EA, CSA and SA. Knowledge of this effect will be useful to the countries of the region in preparing themselves for the impending droughts threat and mitigating the ENSO impact.

ACKNOWLEDGEMENTS

I am grateful to the International Canadian Commonwealth Scholarship program that helped me undertake PhD studies at the University of Alberta. During my four-year PhD program, many people have helped me. My supervisor, Dr. Thian Yew Gan provided academic guidance, encouragement, and financial support. Dr. Samuel Shen introduced me to much of the material in the thesis and offered his time to discuss the development and applications of the WEOF. He also supported my conference presentations and my visit to the NASA Goddard Space Flight Center (GSFC) in Maryland, USA. Dr. Ingrid Daubechies, known for Daubechies wavelets, enthusiastically guided me through the multivariate wavelet analysis and paved the way for the WEOF concept. Dr. William Hsieh of the University of British Columbia helped with the development of the ANN-GA prediction model. Dr. Norden Huang of NASA GSFC, inventor of the Hilbert-Huang Transform (HHT) provided much insight on the analysis of nonstationary and nonlinear signals. TingTing Shu assisted me with the HHT computations. The Committee Members, Drs Nallamuthu Rajaratnam, Andrew Bush, Tong Yu, Samuel Shen, Thian Gan provided valuable suggestions.

My heartfelt thanks go to my parents, Wilson and Tryness Mwale and my Fiancée, Zanete Coates, soon to be Mrs. Zanete Coates Mwale. This thesis is dedicated to them.

TABLE OF CONTENTS

Chapter 1: Introduction

1.1 Problem Identification........1
    1.1.1 Non-stationarity and Identification of Robust Climate Predictors.......3
    1.1.2 Non-Linearity and Inadequacy of Prediction Models........5
1.2 Research Objectives........8
1.3 Research Contributions........9
1.4 Dissertation Organization........10

Chapter 2: Data and Analyses Techniques

2.1 Data Sources........11
    2.1.1 Rainfall Data........11
    2.1.2 Sea Surface Temperature Data........11
2.2 Analyses Methods........13
    2.2.1 Introduction........13
    2.2.2 Wavelet Analysis........14
    2.2.3 Empirical Mode Decomposition and the Hilbert Spectral Analysis......17
    2.2.4 Wavelet Empirical Orthogonal Function Analysis (WEOF)........21
    2.2.5 Wavelet Independent Component Analysis (WICA)........24

Chapter 3: Space-Time-Frequency Analysis of Rainfall and Sea Surface Temperatures

3.1. Introduction........27
3.2.Climatology of Eastern, Central-South and Southern Africa........29
    3.2.1 Central-South and Southern Africa........29
    3.2.2 Eastern Africa........32
3.3. Dominant Modes of SST and Rainfall Variability........33
    3.3.1 Dominant Periods........33

3.3.2 Variability of East Africa September-November (SON) Rainfall............41
    3.3.2.1 Spatial Regimes...41
    3.3.2.2 Temporal Regimes..49
    3.3.2.3 Frequency Regimes...50
3.3.3 Variability of East Africa March-May (MAM) Rainfall......................56
    3.3.3.1 Spatial Regimes...56
    3.3.3.2 Temporal Regimes..61
    3.3.3.3 Frequency regimes...63
3.3.4 Variability of Central Southern African (CSA) Summer Rainfall...........68
    3.3.4.1 Spatial Regimes...68
    3.3.4.2 Temporal Regimes..69
    3.3.4.3 Frequency Regimes...69
3.3.5 Variability of Southern African Summer Rainfall............................72
    3.3.5.1 Spatial Regimes...72
    3.3.5.2 Temporal Regimes..77
    3.3.5.3 Frequency Regimes 79
3.3.6 Variability of the Atlantic Ocean Sea Surface Temperature 82
    3.3.6.1 Spatial Regimes...82
    3.3.6.2 Temporal Regimes..83
    3.3.6.3 Frequency Regimes 87
3.3.7 Variability of Indian Ocean Sea Surface Temperatures......................89
    3.3.7.1 Spatial Regimes 89
    3.3.7.2 Temporal Regimes..90
    3.3.7.2 Frequency Regimes...94
3.4 ENSO Impacts on Rainfall Variability via Space-Time analysis of Scale Energy.....96
    3.4.1 Introduction...96
    3.4.2 East Africa SON Rainfall 97
    3.4.3 East Africa MAM rainfall 98
    3.4.4 Central South and Southern Africa Summer Rainfall.........................100
3.5 Summary of Findings...100

Chapter 4: Associations Between Rainfall WPCs and the SST SAWP

4.1 Introduction 104
4.2 Association Between SON rainfall WPCs and Atlantic and Indian Ocean SSTs SAWP 106
4.3 Association Between MAM rainfall WPCs and Atlantic and Indian Ocean SSTs SAWP 110
4.4 Association Between Central Southern Africa WPCs and Atlantic and Indian Ocean SSTs SAWP 114
4.5 Association Between Southern Africa Summer Rainfall and Atlantic and Indian Ocean SSTs SAWP 116
4.6 Summary of Findings 119

Chapter 5: Development and Application of the ANN-GA Model for Seasonal Climate Prediction

5.1 Introduction 121
5.2 Origins of Genetic Algorithms 124
    5.2.1 Biological Roots of Genetic Algorithms 125
    5.2.2 The Genetic Algorithm in Function Optimization 126
        5.2.2.1 Representation of Solutions in the Genetic Algorithm.......... 127
        5.2.2.2 Creation and Evaluation of Solutions in the Genetic Algorithm 128
        5.2.2.3 Selection of Solutions in the Genetic Algorithm 129
        5.2.2.4 Crossover Procedures in the Genetic Algorithm 131
        5.2.2.5 Mutation Operators in the Genetic Algorithm 134
        5.2.2.6 Convergence of the Genetic Algorithm 135
5.3 Overview of Artificial Neural Networks 135
    5.3.1 The Neuron 136
    5.3.2 The Neural Network 137
        5.3.2.2 Training of Neural Networks 138
5.4 The Integrated Genetic Algorithm Neural Network Model (ANN-GA) 139
    5.4.1 Generalization in Neural Network Training 143
        5.4.1.1 Bootstrap Split-Sampling Training 145

5.5 Application of the ANN-GA model 146
5.5.1 Introduction 146
5.5.2 Evaluation of the Prediction Skill 146
5.5.3 Predictor Data Selection 148
5.5.4 Prediction of the SON Rainfall of East Africa 150
5.5.5 Prediction of the MAM Rainfall of East Africa 152
5.5.6 Prediction of the Central Southern Africa summer Rainfall 152
5.5.7 Prediction of the Southern SUMMER Africa Rainfall 154
5.6 Recent developments in Genetic Algorithms 156
5.6.1 Competent Genetic Algorithms 156

Chapter 6: Prediction of Weekly Streamflow From Seasonal Oceanic Variability

6.1 Introduction 158
6.2 Valencia and Schaake Model 164
6.3 The Sacramento Soil Moisture Accounting (SAC-SMA) Model 170
6.3.1 Evapotranspiration in SAC-SMA 174
6.4 Hydrologic Modeling of the Kafue and Lunga River Catchments 177
6.4.1 Introduction 177
6.4.2 Land Surface Characteristics 178
6.3.3 Climate of the Basin 183
6.4.4 Application of ANN-GA-DIS-SMA and ANN-GA-DIS 184
6.4.4.1 Travel Time 185
6.4.4.2 Water Balance and Dynamics of Rainfall-Runoff 186
6.4.4.3 Disaggregation of Seasonal to Weekly Rainfall 188
6.4.4.4 Model Parameters 201
6.4.5 Direct Disaggregation of Seasonal Rainfall to Weekly Streamflow 203
6.5 Summary of Findings 208

Chapter 7 Conclusions and Suggested Future Work

7.1 Summary and Conclusions 210

7.2 Suggested Future Work 214

    7.2.1 The End-point Problem 214

    7.2.2 Experimentation with Wavelet or Hilbert Spectral Images 215

    7.2.3 Application of WEOF, HEOF, WICA and HICA to Global Scales and other Atmospheric Variables 215

    7.2.4 Improvements in the ANN-GA prediction Model 216

References 217

APPENDIX 234

LIST OF TABLES

Chapter 3

Table 3.1. Explained variances of scale-based WPCs computed for the SON rainfall of East Africa using the 1950-1997 period…………………… …..52

Table 3.2. Explained variances of scale-based WPCs computed for the MAM rainfall SAWP of East Africa using the 1950-1997 period…………………52

Table 3.3. Explained variances of scale-based WPCs computed for the summer rainfall SAWP of southern Africa using the 1950-1997 SAWP…………..52

Chapter 6

Table 6.1. Summary statistics of SAC-SMA's predicted versus observed streamflow under the observed rainfall of the Kafue River basin ……………………..……195

Table 6.2. Summary statistics of ANN-GA-DIS-SMA's predicted versus observed streamflow for the Kafue River basin ……………………..……………….195

Table 6.3. Summary statistics of SAC-SMA's predicted versus observed streamflow using the observed rainfall in the Lunga River basin ………………………..200

Table 6.4. Summary statistics of SAC-SMA's predicted versus observed streamflow under the observed rainfall of the Kafue River basin ………………………..200

Table 6.5. Optimal parameters for the Kafue and Lunga River basins…………………203

Table 6.6. Summary statistics between observed and simulated weekly Kafue River streamflow, where the latter was directly disaggregated from the difference between seasonally predicted rainfall and evapotranspiration …..206

Table 6.7. Summary statistics between observed and simulated weekly Lunga River streamflow, where the latter was directly disaggregated from the difference between seasonally predicted rainfall and evapotranspiration …..206

LIST OF FIGURES

Chapter 2

Figure 2.1. Map showing data and study locations...12
Figure 2.2. The Morlet Wavelet...16
Figure 2.3. An example of the EMD-HHT decomposition showing, (a) 1900-97 rainfall time series of the East Africa September-November (SON) rainfall obtained from Lake Victoria region, and (b) the IMFs extracted from the same SON rainfall data for the 1900-97 period.........................20

Chapter 3

Figure 3.1 Typical 850-hPa winds showing the prevailing atmospheric circulation and moisture transport in terms of wind speed (m/s) and direction throughout the year, (a) OND, (b) JFM, (c) AMJ and (d) JAS......30
Figure 3.2 Examples of local and global wavelet spectra and corresponding Hilbert spectra constructed for, (a & b) Indian Ocean SST, (c & d) East Africa SON rainfall (e & f) Southern Africa summer, (g & h) East Africa MAM rainfall and (i & j) Atlantic Ocean SST. The dotted line in the wavelet spectra is the cone of influence, COI. In the global wavelet spectrum, the dotted curve represents the 95% confidence level, and peaks above the curve are considered statistically significant at the 95% level 34
Figure 3.3 Spatial displays at 0.1 intervals of the correlation between (a) WPC1 and SAWP (b) WPC2 and SAWP (c) WPC3 and SAWP of the SON rainfall. Percentage values above the figures represent proportions of total variance explained by each WPC. Dotted areas represent positive correlation, while hatched areas represent negative correlation. The areas without shading represent areas with zero correlation. The corresponding time domain WPCs are shown in (d) WPC1 (e) WPC2 and (f) WPC3 43

Figure 3.4 Spatial displays of the correlation between Hilbert energy principal components and the scale averaged Hilbert power, (a) HPC1 and SAHP

(b) HPC2 and SAHP (c) HPC3 and SAHP of the SON rainfall. Percentage values above the figures represent proportions of total variance explained by each HPC. Dotted areas represent positive correlation, while hatched areas represent negative correlation. The areas without shading represent areas with zero correlation. The corresponding time domain WPCs are shown in (d) HPC1 (e) HPC2 and (f) HPC3..47

Figure 3.5 The contours plotted at 0.1 intervals showing the spatial patterns of the variance of the SON rainfall SAWP explained by power at (a) the 2-year and (b) the 8-year period. The corresponding time domain WPCs of the 2 and 8- year cycles are shown in (c) and (d) respectively. The percentage values in (c) and (d) represents the variance of the total individual scale power explained by the leading WPC at that scale. More variance of SAWP is explained by the higher frequencies throughout East Africa. As one goes to lower scales, less variance of the SAWP is explained for the SON rainfall...........................53

Figure 3.6 The Hilbert spectrum showing variation of energy between 1900 and 1997 for periods between 2 and 8 years for the SON rainfall time series (a) southern Tanzania (b) Central Tanzania (c) southern half of Lake Victoria and (d) Northern half of Lake Victoria. All power is in mm^2......................55

Figure 3.7 Spatial displays at 0.1 intervals of the correlation between (a) WPC1 and SAWP, and (b) WPC2 and SAWP of the MAM rainfall. Percentage values above the figures represent proportions of total variance explained by each WPC. Dotted areas represent positive correlation, while hatched areas represent negative correlation. The areas without shading represent areas with zero correlation. The corresponding time domain WPCs are shown in (d) WPC1 (e) WPC2...57

Figure 3.8 The spatial patterns plotted at 0.1 intervals showing the correlation between (a) HPC1 and SAHP, and (b) HPC2 and SAHP of the MAM rainfall. Percentage values above the figures represent proportions of total variance explained by each HPC. Dotted areas represent positive correlation, while hatched areas represent negative correlation. The areas without shading represent areas with zero correlation. The corresponding time domain HPCs are shown for, (c) HPC1 and for (d) HPC2 58

Figure 3.9. Spatial variability patterns of the MAM rainfall WPC and WICs computed for the 1950-1997 period: (a) WPC1 (b) WPC2, (c) WIC1 and (d) WIC2. The independent component values associated with the 21 patterns are shown in the scree plot, (e) ....

Figure 3.10 The contours plotted at 0.1 intervals for the MAM rainfall showing the WPC spatial patterns of the power at (a) the 2-year, (b) the 2.4-year (c) the 2.8-year period, (d) the 3.5-year, (e) 5.6 and (f) 6.7-years and the corresponding temporal variabilities in at (f) the 2-year, (g) the 2.4-year (h) the 2.8-year period, (i) the 3.5-year, (j) 5.6 and (k) 6.7-years...............65

Figure 3.11 The Hilbert spectra showing variations of energy between 2 and 8-year cycles for the 1900-1997, MAM rainfall time series of, (a) eastern Tanzania (b) Central Tanzania (c) southern half of Lake Victoria (d) Northern Lake Victoria, (e) Northern Uganda, and (f) Northern Kenya. All power is in mm^2...67

Figure 3.12 Spatial displays of the correlation between WPCs and the SAWP (a) WPC1 and (b) WPC2 of the summer rainfall of Central South Africa. Percentage values above the figures represent proportions of total variance explained by each WPC. Dotted areas represent positive correlation, while hatched areas represent negative correlation. The areas without shading represent areas with zero correlation 70

Figure 3.13 The contours plotted at 0.1 intervals showing the spatial patterns of the variance of the CSA summer rainfall SAWP explained by power at (a) the 2-year and (b) the 2.4-year, (c) 3.4-year and (d) 5.6 years and their corresponding time-domain WPCs in (e) and (f) 71

Figure 3.14 The spatial patterns of the WPCs for the 1900-1997-summer rainfall, (a) WPC1 (b) WPC2 and (c) WPC3 and the corresponding temporal variabilities in (d), (e), (f) 74

Figure 3.15 Spatial displays of the correlation between the (a) WPC1 and (b) WPC2 of the summer rainfall of southern Africa and the SAWP of individual grids. Dotted areas indicate positive correlations, while hatched areas indicate negative correlations. The blank locations indicate areas of zero correlation. Percentage values above the figures represent proportions of total variance explained by each WPC. The corresponding time domain

WPCs are shown in (c) and (d)..76

Figure 3.16 The spatial distribution pattern of power for the leading modes at (a) the 2-year and (b) 5.6-year periods for southern Africa................................80

Figure 3.17 The contours plotted at 0.1 intervals showing the spatial patterns of the variance of the southern Africa summer rainfall SAWP explained by power at (a) the 2-year and (b) the 5.6-year period and the corresponding time domain WPCs in (c) and (d) respectively. The percentage values in (c) and (d) represents the variance of each scale power explained by the leading WPC..81

Figure 3.18 Contour plots of the spatial correlation patterns between, (a) WPC1, and (b) WPC2, of annual Atlantic Ocean SST and SAWP of individual grids at 0.1contour intervals. The numbers shown above represent the percentage (%) of the total variance explained by each WPC. The dark areas correspond to correlations significant at the 95% confidence level. The temporal variations of the two WPCs of Atlantic Ocean SST are shown in (c) and (d)..84

Figure 3.19 Contour plots of the spatial correlation patterns between WPC1 of seasonal Atlantic Ocean SST and SAWP of individual grids at 0.1 contour intervals for the, (a) October-December (OND), (b) January-March (JFM), (c) April-June (AMJ), and (d) July-September (JAS) seasons. The corresponding temporal variabilities are shown in (e), (f), (g) and (h). The numbers shown above represent the percentage (%) of the total variance explained by each WPC1. The seasonal migration of spatial variability patterns of SST can be seen from (a) to (d)................85

Figure 3.20 The spatial and temporal patterns of energy at the 2 and 5.6 year periods of the Atlantic Ocean: (a) 2-year period, (b) 5.6-year periods and (c) the temporal models...88

Figure 3.21 Contour plots of the spatial correlation patterns between, (a) WPC1, and (b) WPC2, of annual Indian Ocean SST and SAWP of individual grids at 0.1 contour intervals. The numbers shown above represent the percentage (%) of the total variance explained by each WPC. The temporal variations of the two WPCs of the Indian Ocean SST are shown in (c) and (d), respectively...91

Figure 3.22 Contour plots of the spatial correlation patterns between WPC1 of seasonal Indian Ocean SST and SAWP of individual grids at 0.1 contour intervals for the, (a) October-December (OND), (b) January-March (JFM), (c) April-June (AMJ), and (d) July-September (JAS) seasons. The numbers shown above represent the percentage (%) of the total variance explained by each WPC1. Correlations between 0 and 0.2 are not included in the spatial patterns 92

Figure 3.23 The spatial and temporal patterns of energy at the 2 and 5.6-year periods of the Indian Ocean, (a) 2-year period, (b) 5.6-year period, and (c) the temporal models..95

Chapter 4.

Figure 4.1 The spatial display of the correlation pattern plotted at 0.2 contour intervals between WPCs of the SON rainfall of EA and individual 5°×5° SST SAWP time series of the Indian and Atlantic Oceans, for both annual ((a) and (c)), and AMJ ((b) and (d)) SST data. The darker shadings in (b) and (d) indicate ocean regions where the predictor SST data was collected as input data..108

Figure 4.2 Associations between MAM rainfall and SST of the Atlantic Ocean for the periods (a) April-June (AMJ), (b) July-September (JAS), and (c) October-December (OND) from the Atlantic Ocean...112

Figure 4.3 Associations between MAM rainfall and SST of the Atlantic Ocean for the periods (a) April-June (AMJ), (b) July-September (JAS), and (c) October-December (OND)...113

Figure 4.4 Plots showing the spatial correlation patterns between WPC1 of CSA rainfall and individual 5°×5° AMJ SST SAWP time series of the (a) Atlantic, and (b) Indian oceans. The areas inside the dotted line correspond to ocean zones with correlations greater than 0.5. Data from these delineated zones were later used to predict the CSA rainfall......................115

Figure 4.5 Associations between southern Africa summer rainfall and SST SAWP (a) rainfall WPC1 and Indian ocean SST SAWP (b) rainfall WPC1 and

Atlantic Ocean SST SAWP (c) rainfall WPC2 and Atlantic ocean SST. It is clear that the main mode of variability of summer rainfall is associated with the Brazil ocean current, Sierra Leon basin and the Guinea ocean current SST, while rainfall along the coastal areas is associated with the variations of the Benguela ocean current SST 117

Chapter 5

Figure 5.1 An example of crossover 133
Figure 5.2 An example of mutation using binary notation 133
Figure 5.3a The neuron 137
Figure 5.3b Configuration of the neural network 138
Figure 5.4 The ANN-GA model. 143
Figure 5.5 Contour plots at 0.05 or 0.1 intervals (to avoid crowding) showing (a) correlation coefficient, (b) RMSE, and (c) HK scores between predicted and observed SON standardized rainfall of East Africa using the ANN-GA model, driven by SST predictor fields from the Indian and Atlantic Oceans 151
Figure 5.6 Contour plots at 0.1 intervals showing (a) the correlation coefficient, (b) RMSE, and (c) HK scores between predicted and observed MAM standardized rainfall of East Africa using the ANN-GA model, driven by SST predictor fields from the Indian and Atlantic Oceans 153
Figure 5.7 Contour plots at 0.1 intervals showing the correlation coefficient, RMSE, and HK scores between predicted and observed standardized summer rainfall of Central Southern Africa using the ANN-GA model driven by the SST predictor fields from the Indian and Atlantic Oceans, (a) Correlation, (b) RMSE and (c) HK 154
Figure 5.8 Contour plots at 0.1 intervals showing the (a) correlation coefficient, (b) RMSE, and (c) HK scores between predicted and observed standardized summer rainfall of greater southern Africa using the ANN-GA model driven by SST predictor fields from the Indian and Atlantic oceans shown in shaded dark areas of Figs. 4.5(a) and (b) 155

Chapter 6

Figure 6.1 The flowchart of the ANN-GA-DIS-SMA approach 166

Figure 6.2 The flowchart of the ANN-GA-DIS approach 167

Figure 6.3 Flow diagram of the Sacramento Model as implemented in this thesis.......171

Figure 6.4 An illustration of the complementary relationship between potential and actual evapotranspiration. 175

Figure 6.5 The location of the Kafue and Lunga river basins, and the stream gauging (SG) and rainfall stations 180

Figure 6.6. The spatial distributions of basin soils and vegetation 181

Figure 6.7 Topographic features of the Kafue basin. 182

Figure 6.8. The water balance of the (a) Kafue, and (b) Lunga River catchments 186

Figure 6.9 The data used in the study, (a) Kafue basin rainfall, (b) Kafue basin runoff, (c) Lunga river basin rainfall and (d) Lunga river rainfall 189

Figure 6.10 Plots of: (a) the predicted and observed seasonal rainfall of the Kafue basin, (b) the observed and statistically predicted weekly rainfall of the Kafue basin, (c) the predicted and observed seasonal rainfall of the Lunga river basin, and (d) the observed and statistically predicted weekly rainfall for the Lunga River basin 191

Figure 6.11 Plots showing observed and predicted weekly streamflow (m3/s) from the SAC-SMA model using (a) Observed rainfall and, (b) from the ANN-GA-DIS-SMA model using statistically predicted rainfall 194

Figure 6.12 Scatter plots of observed versus predicted Kafue river weekly streamflow (m3/s) based on observed input rainfall, (a),(c) (e), (g) and (i); and that based on statistically predicted rainfall, (b), (c), (e), (g) and (h) for the period 1984 to 1988 196

Figure 6.13 Plots showing observed and predicted weekly streamflow (m3/s) by SAC-SMA forced by (a) Observed rainfall and, (b) statistically predicted rainfall 199

Figure 6.14 Scatter plots between the Lunga River's observed and predicted weekly streamflow of SAC-SMA forced by observed data (a),(c),(e), and that of ANN- GA-DIS-SMA forced by statistically generated rainfall data (b), (d), and (f) 201

Figure 6.15 Plots showing observed and predicted weekly streamflow (m3/s) from the direct disaggregation of statistically predicted net rainfall for (a), Kafue River basin and (b) Lunga River basin 205

Figure 6.16 Scatter plots between the observed and predicted weekly streamflow of the Kafue river, (a),(b),(c) (d), and that of Lunga River, (e), (f) (g) 207

LIST OF ABBREVIATIONS

AMJ	April-May-June
ANN	Artificial Neural Network
ANN-GA	Genetic Algorithm Neural Network
ANN-GA-DIS	Genetic Algorithm Neural Network Disaggregation
ANN-GA-DIS-SMA	Genetic Algorithm Artificial Neural Network Disaggregation Soil Moisture Accounting
ARMA	Autoregressive Moving Average
CCA	Canonical Correlation Analysis
COI	Cone of Influence
CRAE	Complementary Relationship Areal Evaporation
CSA	Central Southern Africa
EA	East Africa
ENSO	El Niño Southern Oscillation
ET	Evapotranspiration
ET_a	Actual Evapotranspiration
ET_p	Potential Evapotranspiration
EMD	Empirical Mode Decomposition
EMD-HHT	Empirical Mode Decomposition -Hilbert-Huang transformation
EOF	Empirical Orthogonal Function

GCM	General circulation Model
GRV	Great Rift Valley
HPC	Hilbert Principal Component
HEOF	Hilbert Empirical Orthogonal Functions
HICA	Hilbert Independent Component Analysis
HK	Hansen Kuipers
IE	Instantaneous Energy Density
ITCZ	Inter-tropical Convergence Zone
IMF	Intrinsic Mode Function
JAS	July-August-September
JFM	January-February-March
LZFPM	Lower zone primary free water capacity
LZFSM	Lower zone free water capacity
LZTWM	Lower zone tension water
LZSK	Lower zone secondary withdrawal rate
LZPK	Lower zone primary withdrawal rate
MAM	March-May rainfall of East Africa
PCA	Principal Component Analysis
PEADJ	ET-demand adjustment factor
REXP	Exponent for the percolation Equation
RMSE	Root Mean Square Error
SA	Southern Africa
SADC	Southern Africa Development Community

SAWP	Scale Averaged Wavelet Power
SON	September-November rainfall of East Africa
SST	Sea Surface Temperature
UKMO	United Kingdom Meteorological Office
UZFWM	Upper zone free water capacity
UZTWM	Upper zone tension water
UZK	Upper zone withdrawal rate
WEOF	Wavelet Empirical Orthogonal Function
WIC	Wavelet Independent Component
WICA	Wavelet Independent Component Analysis
WPCA	Wavelet Principal Component Analysis
ZPERC	Maximum percolation rate

LIST OF SYMBOLS

Δ	Slope of the saturation vapor pressure/temperature curve at air Temperature.
δ_j	Factor for scale averaging.
δ_t	Sampling period.
ε	Surface emissivity.
γ	Kurtosis.
γ_p	Psychometric constant (66.8 Pa/°C).
ζ	Dimensionless stability factor.
σ	Stephan Boltzmann constant (5.87×10^{-8} Wm^{-2} °K^{-4}).
Ψ	Mother wavelet.
e_{km}	Eigen vectors.
e_a	Saturation vapor pressure.
$f(u)$	Wind function.
ω	Instantaneous frequency.
p	Atmospheric pressure (mbar).
p_o	Atmospheric pressure at sea level (mbar).
S	Original signals.
T	Air temperature
u	Principal components.
X, x	Observations.
ρ	Density of air

CHAPTER 1

INTRODUCTION

1.1 Problem Identification

Existing records of the twentieth century hydroclimatic variables, such as rainfall and streamflow, over Eastern, Central South and Southern Africa show that the region's climate exhibited significant variations at interannual (2-6 years) and interdecadal (11-22 years) time scales. For example, droughts dominated the late 1920s, late 1940s, late 1960s, and 1980 in most areas of Southern Africa (Mason and Tyson, 2001), while in the 1990s, dry conditions lasted for almost the entire decade. Between 1947 and 1997, streamflow from major rivers in most parts of Southern Africa declined considerably (Fanta et al., 2001). Southern Africa experienced wet periods, such as in the 1950s and 1970s (Dlamini, 1995). Conversely, East Africa experienced the worst droughts of the century between 1965 and 1997 (Ntale, 2001), in addition to two other droughts in 1900 and 1949. East Africa also experienced serious floods, such as in 1961 and 1997 (Philippon et al., 2002).

In Southern Africa, these events were simply taken as a normal part of climate variability and regarded to recur in regular fashion, often between 18 and 20 years, (Tyson, 1971; Currie, 1993). Studies by Abbot and Dyer (1976) and Alexander (1995) found these oscillations in tree ring, streamflow and temperature data and were attributed to the 18-year cycle in the lunar solar tide and the 11 and 22–year cycles in the sunspot variability. These oscillations were utilized in long-range seasonal forecasting models from the early 1970's (e.g., Dyer and Tyson, 1977) until the late 1990's (e.g., Alexander, 1995).

Following the failure to predict the 1991/1992 droughts and below normal rainfall for much of the 1990-2000 decade, which was expected to be wet, considerable concern began to emerge that our prediction skill of summer rainfall variability of Southern Africa had actually been declining consistently since the 1980's (Mason, 1997). Conversely, despite numerous studies and progress in understanding the East Africa climate, prediction of the September-November (SON) and March-May (MAM) rainfall has not been satisfactory (Ntale et al., 2003).

The decreased prediction skill was not confined to Eastern and Southern Africa only, but was also detected elsewhere. For example, for over 100 years, the Indian Meteorological Department utilized models that exploited empirical relationships between Monsoon and worldwide climate predictors with good skill up to the 1970's (Hastenrath 1995; Webster et al., 2002). However, after the 1980's, performance of the statistical models drastically reduced. Equally, between 1984 and 1988, there were remarkable seasonal forecasts of the North Atlantic hurricane activity, but in 1989 and the following years, prediction failed (Hastenrath, 1995).

The El Niño Southern Oscillation (ENSO) has been another popular climate phenomenon used to forecast climate variability in many parts of the world. Rainfall variability of several regions of Africa has been found to respond to ENSO events. In particular, Nicholson and Kim (1997) confirmed the relationship between ENSO and rainfall variability in some parts of Eastern and Southern Africa. During the occurrence of an El Niño episode, droughts were generally predicted in Eastern and Southern Africa. However, despite this ostensibly deterministic variability, a number of surprises were encountered during the 1990-2000 decade. As noted by Zebiak

(2003), ENSO variabilities in the 1990's and early 2000's became much more unpredictable and considerable ambiguity was found in the forecast guidance from various forecast centers even though they utilized the same dataset.

This led Mason (1997) and us (Mwale et al., 2004; Mwale and Gan 2004) to believe that the disappointing performance of seasonal forecasts in Eastern and Southern Africa since the 1980's is not an isolated case, but a reflection of the general decrease in the prediction skill observed elsewhere. The uncertainties and ambiguities in the character of El Niño and the decreased prediction skill observed especially within the tropics raised important questions for research. There is a general consensus that decreased skill in predictability of the climate and some limitations in effectively analyzing the climate variability can be attributed to four main problems, below:

(1) The non-stationarity of the ocean-atmosphere system (Allan et al., 1995; Landman et al 2001),
(2) The non-linearity of the ocean-atmosphere interaction (Barnston et al., 1994),
(3) The inadequacy of prediction models (Webster et al., 2002),
(4) Failure to identify robust climate predictors (Singh et al., 1995).

1.1.1 Nonstationarity and Identification of Robust Climate Predictors

In the past, the global-energy-frequency distributions of climate data were normally decomposed and analyzed using Fourier basis functions (i.e., e^{ikx}). These functions assume that climate processes are linear and stationary. This means that climate time series have one or more oscillations, which span the entire time series.

These periods are assumed to have constant amplitudes. With this simplicity, Fourier analysis has been applied to all kinds of data. In some areas of science and engineering (e.g., electrical engineering), where time series signals are expected to occur at fixed amplitude and phase, Fourier decomposition has worked well. However, many natural phenomena such as climate processes demonstrate strong non-stationary and non-linear characteristics (Landman and Mason, 1999; Landman et al., 2001), and so the use of Fourier analysis and the adoption of the stationary and linear assumptions may give misleading results (Huang et al., 1998). For example, periodicities of between 2 and 7 years have been identified in Eastern and Southern African rainfall and the SSTs of the surrounding Atlantic and Indian Oceans (Mason, 1995). However, even if we may be aware of the general spectral characteristics of the rainfall and SST data, we still do not have information on the spatial distribution and temporal resolution of such frequencies. Therefore, it is not surprising that following the 18 to 20-year oscillations in the rainfall of Southern Africa, wet conditions were expected in the 1990-2000 period. However, the year 1991/92 was particularly dry and was followed by an entire decade of less than average rainfall. The abrupt and irregular changes observed in the 1990-2000 decade from what appeared to be a regular 18-20-year cycle is a good example of the nonstationarity of the rainfall process.

Because of the non-stationary characteristics exhibited by climate processes, the investigation of rainfall and SST variability should employ methodologies that make proper use of non-stationary approaches, so that in addition to the spatial and temporal regimes of the rainfall and SST processes, the frequency regimes contained in the rainfall and SST processes may also be resolved in space and time. This will automatically assist in the identification of robust climate predictors.

In addition, most of the analyses for Southern Africa rainfall have one major shortcoming: the lack of a regional approach to the analysis of rainfall. Hence the regional-scale variability of rainfall is ignored (e.g. Jury 1996; Nicholson et al., 2001; Reason and Mulenga, 1999; Mason, 1995; Jury and Engert, 1999). The region-wide approach to rainfall analysis is important in the light of extreme nonstationary climate variability observed on region-scales in recent years (BBC, 2002a, b and c), issues related to climate change especially for developing countries where many systems and polices are not well adjusted even to today's climate variability (IPPC, 1998), and the formation of regional groupings, such as the Southern Africa Development Community (SADC), which has shifted the region towards more integrated or holistic approaches to issues affecting the region.

1.1.2 Nonlinearity and Inadequacy of Prediction Models

The general consensus is that nonlinear interactions among climate elements in the spatial and temporal domains are responsible for the unpredictability of weather and climate. Thus, besides the understanding of the nonstationarity of rainfall and SST, we should also develop accurate nonlinear models to teleconnect relationships between climate processes and enhance our ability of climate prediction. The traditional approach for teleconnecting the climate elements in Eastern and Southern Africa has been based on linear statistical prediction models, dynamical models or hybrids of statistical and dynamical models. For example, Mutai et al., (1998) and

Jury and Engert (1999) have used linear regressions to teleconnect the SON rainfall of Eastern Africa and the summer rainfall of Namibia using global SST and other atmospheric variables. The canonical correlation analysis (CCA) and its improvements such as the Nelder-Mead CCA (CCA-NMS) of Ntale et al., (2003) have been used to teleconnect the SON and MAM rainfalls of Eastern Africa. Landman et al., (2001) used the Center for Ocean and Land –Atmospheric general circulation model (COLA-GCM) and the COLA 30 to predict rainfall in South Africa.

Theoretically, GCMs should out perform linear statistical models in short-term forecasts, since they are physically based. However, for Southern Africa, forecasts with a GCM were only accurate prior to 1990. The accuracy of GCMs depends largely on the prescribed boundary conditions and a number of other factors, such as land processes. For example, as shown by Landman et al., (2001), after 1990, the predictability of global SST fields (used as boundary conditions for the GCM) weakened considerably, which caused unavoidable errors in the GCM output, leading to poor forecast skill of the rainfall. Further, because of coarse resolution, climate processes at smaller spatial scales that cannot be adequately accounted for by GCMs are parameterized, adding more uncertainty to the GCM output.

Despite the aforementioned weaknesses, we cannot totally discount the value of GCM forecasts. As the skill in producing large amounts of up-to-date initial and boundary conditions improves, GCMs will also improve in rainfall forecasts. In the meantime, however, teleconnection of SST and rainfall variability has to proceed with other models. Since the relationship between rainfall and SST variability is nonlinear, a nonlinear statistical teleconnection model is apparently needed. Therefore, this thesis proposes the development and application of such a model.

In addition to addressing the above four concerns, which are universal in nature, there are other concerns that are very specific to Eastern and Southern Africa. Numerous rivers and lakes in Eastern and Southern Africa form or cross international boundaries. This problem has called for an integrated approach to managing water resources. The political frameworks, such as formal agreements to share water resources have been made for most of these lakes and rivers, e.g., through the Southern Africa Development Community protocol on shared water resources for countries within Southern Africa. However, since national interests often override regional objectives, extreme variabilities in streamflow, such as significant reductions following sudden or extended periods of below normal rainfall or droughts could exceed the management capacity of these agreements, giving way to water related conflicts.

Hence, while accurate prediction of rainfall is very vital, a step further is to establish proper relationships between precipitation and hydrological processes. The capability to provide adequate information on the relationship between precipitation and streamflow, for the coming year(s) or decades, both for local water resource planning needs and for cross-border negotiations, is essential. There is a general consensus among local and international communities that as population grows, water demand increases while resources become scarcer, water will become a limiting factor for economic and social development across the world, and particularly in developing and relatively arid countries such as those of Eastern and

Southern Africa. Therefore, this thesis advocated for and developed models to transform predicted seasonal precipitation from seasonal sea surface temperature variability to streamflow at weekly time steps, which we believe are adequate for regional and country specific planning purposes.

1.2 Research Objectives

Following the above problems, the objectives of this research are as follows:

(1) To identify and analyze the dominant regimes of spatial, temporal and frequency variability of Eastern and Southern Africa rainfall and the SST fields of the Indian and South Atlantic Oceans.

(2) Explore associations between rainfall fields in Eastern and Southern Africa and the SST fields in the Indian and South Atlantic Oceans.

(3) Develop a non-linear statistical seasonal climate prediction model for teleconnecting the associations between SST fields of the oceans and rainfall of Eastern, Central South and Southern Africa.

(4) Develop statistical models to predict weekly streamflow from predicted seasonal precipitation by

4(a) Statistically disaggregating predicted seasonal rainfall to finer time scale rainfall, which will used to drive a hydrologic, rainfall-runoff model, and

4(b) Statistically disaggregating predicted seasonal rainfall directly into streamflow.

1.3 Research Contributions

The contributions of this research to climate and hydrology include the followings:

(1) Adoption and demonstration of the wavelet empirical orthogonal function analysis (WEOF), the wavelet independent component analysis (WICA) and the empirical mode decomposition (EMD)-Hilbert transformation EOF (HEOF) and HICA methodologies for multivariate nonstationary data analysis. The combination of these methods is a new direction in climate research and has helped to gain new understanding in the nonstationary variability of climate processes on regional and local scales.

(2) Development and demonstration of the non-linear statistical model for climate and hydrologic prediction based on artificial neural networks (ANNs) trained by genetic algorithms (GAs). The combined model is known as the ANN-GA and, this combination of models (ANNs and GAs) appears to be new to climate research, and has contributed to an improved prediction of hydroclimatic variables.

(3) Development and demonstration of the ANN-GA-DIS-SMA model by integrating ANN-GA, a disaggregation model, and an existing soil moisture accounting model, the Sacramento model (SAC-SMA) for predicting weekly streamflow from disaggregated seasonal precipitation. This system has accurately predicted weekly streamflow from seasonal oceanic variability;

(4) Development and demonstration of the integrated ANN-GA-DIS model for predicting weekly streamflow for the coming year for a single site by integrating ANN-GA, and a statistical disaggregation, and evaporation

models. The ANN-GA-DIS-SMA out-performed ANN-GA-DIS. This is not a surprise because SMA is designed for modeling basin-scale rainfall-runoff transformation, and specifically calibrated for the study site's hydrologic characteristics. ANN-GA-DIS serves as a comparison and provides us some ideas about the statistical relationships that exist between climate elements at various levels of time scale.

1.4 Dissertation Organization

The dissertation is organized in seven chapters. Chapter 2 presents methods used for the analyses of climate data. Chapter 3 presents the analysis of spatial, temporal and frequency regimes of rainfall and SSTs. Chapter 4r establishes the associations between rainfall and SSTs at seasonal time scales. Chapter 5 presents the development and application of the genetic algorithm neural network (ANN-GA) model. Chapter 6 presents the development and application of the ANN-GA-DIS-SMA and ANN-GA-DIS models. Conclusions and suggestions for future work are presented in Chapter 7.

CHAPTER 2

DATA AND ANALYSES TECHNIQUES

2.1 Data Sources

2.1.1 Rainfall Data

The monthly rainfall data (1900-1997) from 79 grid locations at a resolution of 2.5°×3.75° latitude and longitude were extracted for Eastern Africa from 2°N-12°S, 30°E-43°E, and Southern Africa (10°S-35°S, 15°E-43°E) (Figure 2.1). Monthly rainfall data (1950-1994) at 31 grid points were also extracted for Central Southern Africa (10°S-20°S, 12°E-42°E). All the rainfall data were part of a monthly precipitation dataset for global land areas from 1900 to 1998, provided by the UK meteorological office (UKMO). This data set was constructed by Hulme (1994) from station data and interpolated onto a 2.5° x 3.73° grid. Thiessen polygon weights were used to average the gauge data within each gridbox. The data for areas in Central Southern Africa (most of the areas north of 18°S) is not reliable for periods before 1945. Hence the 1950-1994 data was used for this region, which consists of Zambia, Angola, Malawi, parts of northern Zimbabwe and northern Mozambique.

2.1.2 Sea Surface Temperature Data

The SST-anomaly grid data at 5° x 5° latitude and longitude resolution were extracted to cover the Indian Ocean (20°N-40°S, 40°E-105°E) and the Atlantic (15°N-30°S, 50°W-10°E) (Figure 2.1).

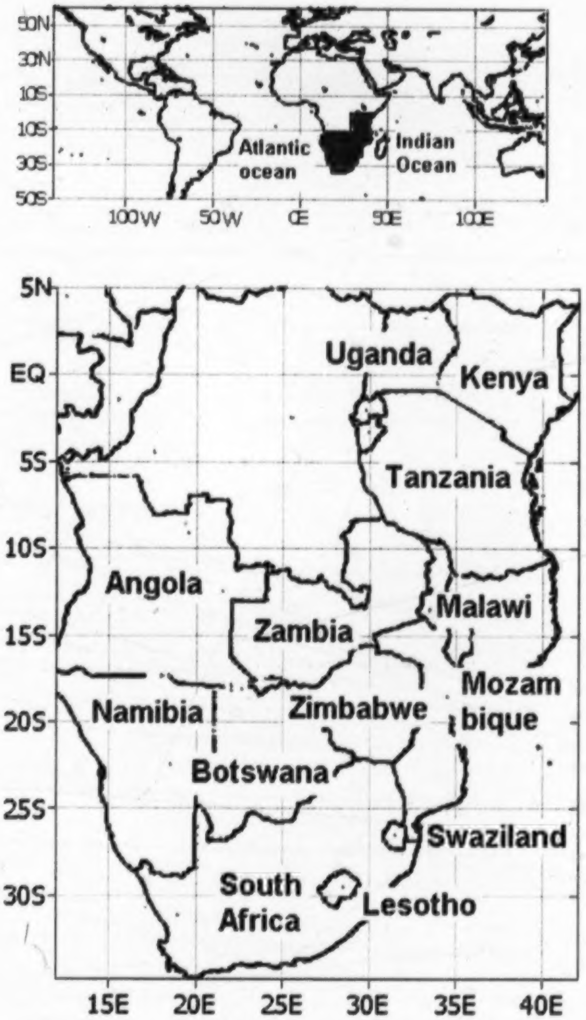
50N
30N
10S
10S
30S
50S
Atlantic ocean
Indian Ocean
100W
50W
0E
50E
100E
5N
EQ
5S
10S
15S
20S
25S
30S
Uganda
Kenya
Tanzania
Angola
Zambia
Malawi
Mozam bique
Namibia
Zimbabwe
Botswana
Swaziland
South Africa
Lesotho
15E
20E
25E
30E
35E
40E

Figure 2.1. Map showing data and study locations

The SST data sets were 48 years long (1950-1997) and were transformed into seasonal and annual data by computing seasonal averages (e.g., April-June) and annual averages, respectively. The SST dataset is part of UK Meteorological Office's historical global dataset of mean monthly global SST anomalies with respect to the 1961-1990 normals.

2.2 Analysis Methods

2.2.1 Introduction

The analysis of rainfall and SSTs was initially based on the wavelet analysis and the wavelet based empirical orthogonal functions (WEOF). The analysis was enhanced by the empirical mode decomposition (EMD) and the associated Hilbert transformation of Huang et al., (1998) and the independent component analysis (ICA) of Hyvärinen and Oja (2000). From the latter two methods, the EMD-Hilbert transformation based empirical orthogonal function analysis (HEOF), the EMD-Hilbert based independent component analysis (HICA) and the wavelet based independent component analysis (WICA) were developed for multivariate analysis of rainfall and SST fields.

The spatial and temporal patterns obtained from the WEOF, HEOF, WICA and HICA analyses are generally similar. Since the ICA has the disadvantage that it cannot identify the leading modes in order of importance, the WICA and HICA were rarely used in this thesis. Whenever WICA or HICA was used, it was only as an extension of the WEOF method, mainly to see if more details could be unearthed from the wavelet or Hilbert spectra.

2.2.2 Wavelet Analysis

Wavelet analysis is a suitable mathematical tool for analyzing time series that contain nonstationary power over many different frequencies. As the name implies, wavelets are formulated from small waves. Because they are small waves, they are of limited duration compared to the big waves, such as the sine or cosine waves, which have infinity duration. Wavelets are also called daughter wavelets, because they are formed by dilations and translations of a single prototype wavelet function $\psi(t)$, where t is real valued, called the basic or mother wavelet (Castleman, 1996). The mother wavelet is the basis function for wavelet based time series decomposition.

The mother wavelet is designed to oscillate as a wave and required to die out rapidly to zero as t tends to infinity in order to satisfy the requirements of it being a small wave or a wavelet. This requirement is popularly known as the "admissibility condition".

$$\int \Psi(t)dt = 0 \tag{2.1}$$

Hence the mother wavelet is typically localized in space as well as in frequency. A set of wavelets can be generated by translating and scaling the basic wavelet as follows:

$$\Psi_{a,b}(t) = \frac{1}{\sqrt{a}}\Psi\left(\frac{t-b}{a}\right) \tag{2.2a}$$

$$a = 2^{i\delta j} \tag{2.2b}$$

where the scale (width) of the wavelet and translated position along the t-axis (usually the x-axis in the x-y plane) are a and b respectively, i = 0,1,2,...and δj is a small number (e.g. 0.125) that allow wavelet widths to be scaled in small fractional powers of two. Thus, the fundamental property of the wavelets is the self-similarity at different scales. When a is increased, the wavelet width increases and a convolution of a time series with the wavelet isolates the low frequency part of the time series. Conversely, if a is decreased, the wavelet width decreases and the high frequency components of the time series can be isolated. This means that if the scale is continuously varied along the translation b, a picture can be constructed depicting how the frequency component of a time series varies with the time. Associated with the frequency are the numerical coefficients referred to as the energy of the wavelet at each of the scales. The size of these coefficients represents how well the wavelet at a particular scale matches with the time series. The parameters a and b in Eq (2.2) are real and a, always positive, may range over a continuous or a discrete set. The quantity $a^{-1/2}$ in Eq (2) is an energy normalization term, which ensures that the energy of the mother and daughter wavelets remain the same over all scales, making it possible to directly compare wavelet transforms of one time series with another (Torrence and Compo 1998).

The wavelet transform of a real time series signal X(t) with respect to the mother wavelet is a convolution integral given as

$$W(b,a) = \frac{1}{\sqrt{a}} \int_0^T X(t)\Psi^*\left(\frac{t-b}{a}\right)dt \tag{2.3}$$

where ψ^* is the complex conjugate of ψ. In this equation, $W(b,a)$ is a wavelet spectrum, a matrix of energy coefficients of the decomposed time series X(t). At each scale, the wavelet spectrum coefficients also depict the amplitude of the time series. In a rainfall or SST time series, power at each scale will therefore be a good measure of the magnitude of the rainfall or SST events.

In addition to energy or power at individual scales, power over a range of scales, the scale averaged wavelet power (SAWP), which represents the mean variance of wavelet coefficients over a range of scales, might also be used. The SAWP of the wavelet spectrum is computed as follows, (Torrence and Compo 1998):

$$W^2(b) = \frac{\delta_j \delta_t}{C_\delta} \sum_{j=j_1}^{j_2} \frac{\left|W(b,a_j)\right|^2}{a_j} \tag{2.4}$$

where C_δ is 0.776 for the Morlet wavelet (used in this thesis), δ_j is a factor for scale averaging, and δ_t is the sampling period. There are many different candidate functions to be used as mother wavelet and the Morlet wavelet is just one of those, albeit one of the most commonly used wavelets. Since the SAWP is a time series of average variance in a certain band, SAWP can be used to examine the modulation of one time series by another or modulation of one frequency by another within the same time series (Torrence and Compo, 1998). Having obtained the SAWP and individual scale power, wavelet energy based EOF analysis was then used to extract the joint modes of spatial and temporal variability of the SAWP and individual scale power. The wavelet power was computed using the Morlet wavelet (Figure 2.2) as follows,

$$\psi(t) = \pi^{\frac{1}{4}} e^{i6t} e^{-\frac{t^2}{2}} \tag{2.5}$$

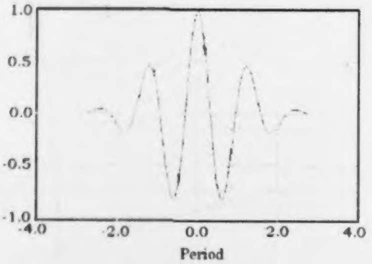

Figure 2.2 The Morlet Wavelet

2.2.3 Empirical Mode Decomposition and Hilbert Spectral Analysis

The empirical mode decomposition (EMD) and the Hilbert transformation (also known as the EMD-Hilbert-Huang transformation (EMD-HHT), named after Huang et al., (1998) is a two-step procedure for the analysis of non-stationary and nonlinear data. Unlike the wavelet analysis, which is directly applied to the data, the HHT first decomposes the data and isolates the intrinsic oscillations of the time series, the so-called intrinsic modes functions (IMFs). The IMFs form the basis functions of the data. The Hilbert transformation is then applied to these IMFs, to isolate the magnitudes and the instantaneous frequencies associated with each IMF. The coefficients of all the IMFs are then plotted at each of the localized frequencies associated with each IMF into what is called the Hilbert spectrum. The Hilbert spectrum provides a sharper representation of the energy-frequency-time distribution, compared to the wavelet analysis because the basis is defined by the data itself.

The formulation of the HHT is given below following Huang et al., (1998). For a time series, *x(t)*, we have its Hilbert Transform, *y(t)* as

$$y(t)=\frac{1}{\pi}P\int_{-\infty}^{\infty}\frac{x(t')}{t-t'}dt' \qquad (2.6)$$

where P indicates the Cauchy principal value. With this definition, *x(t)* and *y(t)* can be used to define an analytic signal *z(t)*, as

$$z(t)=x(t)+iy(t)=a(t)e^{i\theta(t)} \qquad (2.7)$$

in which

$$a(t)=\sqrt{x^2(t)+y^2(t)},\ \theta(t)=\arctan\left(\frac{y(t)}{x(t)}\right) \qquad (2.8)$$

Eq (2.6) defines the Hilbert spectrum as the convolution of $x(t)$ with $1/t$, emphasizing the local properties of $x(t)$. The polar coordinates shown in Eq (2.8) further clarifies the local nature of this representation, which is the best local fit of an amplitude and phase varying trigonometric function to $x(t)$. The instantaneous frequency of $x(t)$ is defined as

$$\omega = \frac{d\theta(t)}{dt} \tag{2.9}$$

Huang et al., (1998) proposed a class of functions designated as IMF for the instantaneous frequency to make sense. An IMF is a function that satisfies two conditions:

(1) The number of extrema and the number of zero-crossings in the IMF must either equal or differ by 1 in the entire data set, and

(2) The mean value of the envelope defined by the local maxima and the envelope defined by the local minima at any point is zero.

Using these definitions, the IMFs are thus made up of individual oscillations allowing the traditional narrow band requirements to be met. To decompose a time series into IMFs, the following steps outlined in Huang et al., (1998) are followed:

(1) Identify the extrema of the data set $x(t)$, and form the envelops defined by the local maxima and minima respectively.

(2) Form the mean values $m_1(t)$ by averaging the upper and the lower envelops and make the differences between the data and the mean values to get the first component, $h_1(t)=x(t)-m_1(t)$.

(3) If the first component is not an IMF, let $h_1(t)$ be the new data set, go to step 1

(4) The first IMF is called $c_1(t)$. Let $r_1(t)= x(t)-c_1(t)$. Repeat steps 1 through 3 until all

the IMFs have been found.

Because the time series are made up of several natural oscillations, usually more than one IMF is found that describes each of the oscillations. The Hilbert transform is applied to each IMF and the resulting energy and frequency are plotted to give the Hilbert spectrum. An example of a time series and its corresponding IMFs is given in Figure 2.3

Notice that the Hilbert transform is a Fourier transform performed on an IMF at each time step. The data can be recovered through an inverse Fourier transform as follows, Huang et al., (1998):

$$x(t)=\sum_{j=1}^{n}a_j(t)e^{\left(i\int\omega_j(t)dt\right)} \tag{2.10}$$

The time varying characteristics of Eq (2.10) enables us to accommodate the non-stationary data and also represent amplitude and instantaneous frequency as functions of time. Equation 2.10 can be considered as a generalized Fourier transform.

From the Hilbert spectrum, one can extract energy at each frequency through computation of the instantaneous energy density (IE) defined by Huang et al., (1998) as

$$IE(t)=\int_{\omega}H^2(\omega,t)d\omega \tag{2.11}$$

The IE is computed over a range of frequencies and the averaged instantaneous energy can be used in place of SAWP computed from wavelet analysis.

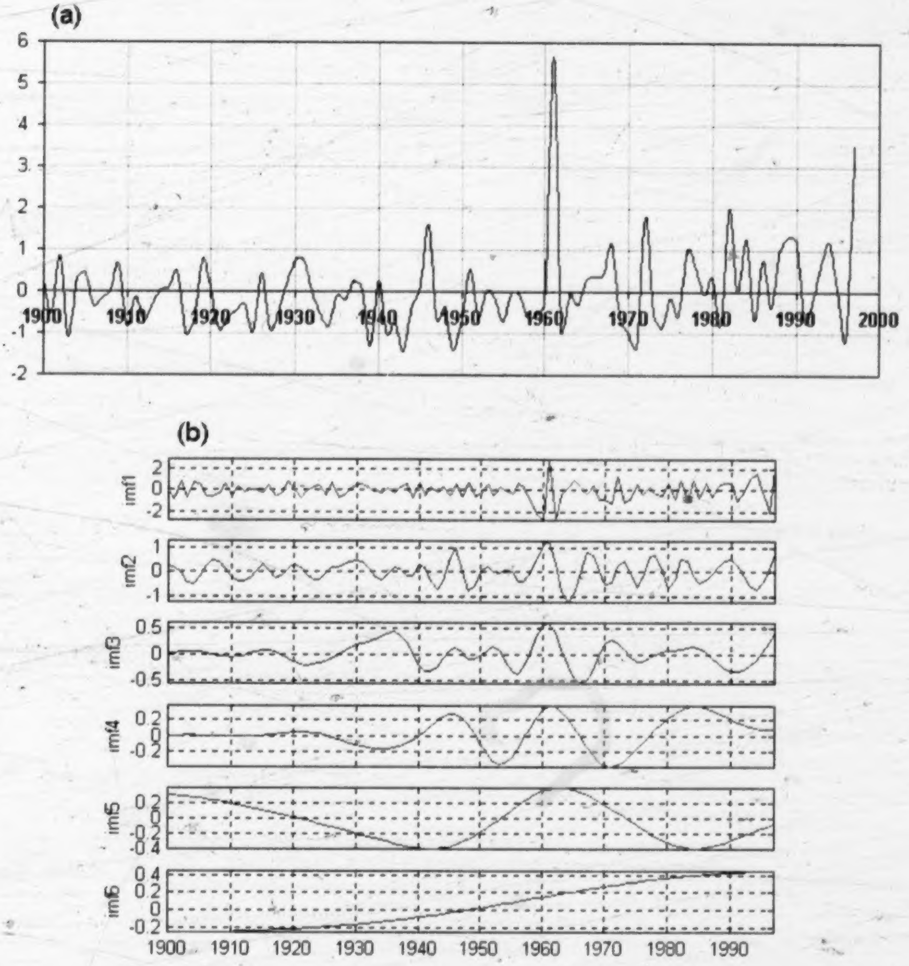

Figure 2.3 An example of the EMD-HHT decomposition showing, (a) 1900-97 rainfall time series of the East Africa September-November (SON) rainfall obtained from Lake Victoria region, and (b) the IMFs extracted from the same SON rainfall data for the 1900-97 period.

2.2.4 Wavelet Empirical Orthogonal Function Analysis (WEOF)

Empirical orthogonal function (EOF) analysis, also known as principal component analysis (PCA), is the most popular method capable of describing coherent spatial and temporal variability of large data sets (e.g., Mason, 1995; Venegas et al., 1997). Its general objectives are data compression (or dimension reduction) and interpretation. Data compression is achieved through the projection of the original variables through the eigenvectors of the variance-covariance matrix of the original data to form principal components (PCs). An analysis of the PCs often reveals relationships that are not usually suspected in the data and thereby allows interpretations that would otherwise not be possible by examining the original data.

The major assumption of the EOF method is that the data or observations at the different stations are related to one another (i.e., are linear combinations of the original signals) and hence by the central limit theorem, they should be Gaussian distributed. Usually as is the case for hydroclimatic variables, one or more original signals may be responsible for the variations in the observed data. For an "n x K" data matrix **X**, where n and K represent the length of time series and the number of data stations, respectively. The EOF analysis transforms the "n x K" data matrix **X** into another "n x K" matrix of these original signals (also called time domain principal components PCs), **U**, which account for all the variability of the matrix **X** and some noise due to measurement errors present in **X**. If indeed the hydroclimatic observations are a linear combination of a few original signals, the matrix **U** will have very few PCs, which account for the majority of the joint variation of the matrix **X**. Let us designate these original signals as u_m. Then u_m is computed as follows (Wilks, 1995)

$$u_m = e_m^T x' = \sum_{k=1}^{K} e_{km} x'_k , m = 1, \ldots\ldots\ldots\ldots\ldots\ldots, M, \ (where\, M << K) \qquad (2.13)$$

where, e_{km} are the eigen vectors, x'_k are the anomalies of **X**, and M represents the number of original signals (or PCs associated with the physics or variability of the data). The signals u_m are called temporal EOF patterns and can also be projected in space through temporal correlation with observed data.

To distinguish EOF of raw data from EOF performed on the wavelet-based energy, the latter is called wavelet empirical orthogonal function (WEOF) analysis or wavelet principal component analysis (WPCA) and their corresponding PCs are referred to as wavelet principal components (WPCs) (Mwale et al., 2004).

Physical interpretation of EOF patterns (or original signals) is dependent on the data being analyzed. The interpretation requires that signals be distinguished from the noise in the data. It should be emphasized that in this thesis, we consider noise to include not only measurement error but also any actual physical variability of the climate time series whose energy is statistically insignificant at the 95% level of a red noise process. This approach is different from the conventional one in that a large amount of noise is removed from the data before hand. Because the wavelet spectrum contains power that is not statistically significant everywhere, some noise is always present within the range of scales with power above the 95% level.

The WPCs obtained from SAWP are an average of wavelet scale power variance and are interpreted as frequency-compacted energy variability. When the period-time plane is examined, the convolution at every scale shows the variance (energy) of the time series at that scale. The energy is directly associated with the magnitudes of the event at that scale and time. The physical interpretation of these modes (in the temporal, spatial and frequency domains) is given in Chapter 3.

An important decision in EOF is to select an appropriate number of PCs that most strongly capture the joint variability of the original data, without discarding important information contained in the original data. For an "n x K" matrix **X**, there are K eigenvectors. However, atmospheric data contains substantial co-variances among the original variables and this implies that the first few eigenvectors will locate directions in which the joint variability of the data is largely accounted for (Wilks, 1995).

There are several techniques that have been devised to determine the optimal number of PCs from an EOF analysis. However, no universal consensus exists for a single clear criterion, as all criteria are subjective. Because WEOF is used for the first time the number of WPCs to be retained for analysis was not based on any of the available criterion, but visual inspection of the spatial and temporal modes of variability. In this thesis we concentrated on the regional analysis of climate variation, hence only modes describing these processes were retained and analyzed in detail. The number of WPCs retained from scale based WEOF was done in the same way, as wavelet analysis does not affect the underlying relationship between the variables at any scale (Bakshi, 1998).

Finally, analyses of WPCs are more of a means to an end than an end in themselves. In this thesis, interpretation of WPCs serves as an intermediate step.

The interpretation is further used to understand how climate processes are teleconnected over large areas (i.e., regional teleconnection). This information is further used to predict variability of one climate element from the other.

2.2.5 Wavelet Independent Component Analysis (WICA)

Independent component analysis (ICA) is a new field of research with a broad range of applications, such as telecommunications (Cardoso and Souloumiac, 1993), image processing (Ding and Zhang, 2003) and biomedical signal analysis (Jung et al., 1998). When applied to wavelet energy, ICA is referred to herein as wavelet ICA, or WICA. Like EOF, ICA is used to identify signals in observations. The difference between WICA and WEOF is that WICA uses higher order statistics, such as Kurtosis (shape parameter of the distribution) to decompose SAWP into modes of variability, while EOF uses the lower order statistics of the distribution (variance and co-variance). ICA has been used in recent years in place of EOF, or as an extension of EOF because although the WPCs are uncorrelated, sometimes they are not completely separated (i.e. independent) from one another, while the WICs are as independent as possible. When the extracted modes are not well separated, mode mixing is said to have occurred, making physical interpretation of mixed modes difficult such as the March-May rainfall of east Africa (Chapter 3).

The eigenvector modes computed by WICA cannot be classified by order. As a result, the method is also referred to as blind source separation (BSS) (Ding and Zhang, 2003). Hence WICA was used in this thesis as a compliment to WEOF.

Algebraically, ICs are linear combinations of observations and their computation is carried out as follows. Assuming we have a vector of n observed random variables, $\mathbf{x} = (x_1, x_2 \ldots x_n)^T$ and the vector is a linear mixture of n original signals, $\mathbf{s} = (s_1, s_2 \ldots s_n)^T$ then the linearly generated model is given by

$$x = As \tag{2.14}$$

where **A** is the n x n unknown mixing matrix. In this model, the matrix **A** and the random vector **s** are unknown and are estimated from the observed random variables, **x**. The first step is to estimate the matrix **A** and then compute its inverse, **W**. The independent components are then computed as

$$s = Wx \tag{2.15}$$

To estimate the matrix **A**, it is necessary to assume that the random variables in s are statistically independent and have non-Gaussian distributions. This assumption is valid because many of the original signals have distributions that are different from Gaussian, although their linear mixtures tend to have Gaussian distributions. Non-Gaussianity is quantified through fourth order moments, such as the Kurtosis (Hyvärinen and Oja, 2000). If $\mathbf{s} = \mathbf{w}^T\mathbf{x}$, is one of the independent components of **x**, the Kurtosis of **s**, γ, is computed as,

$$\gamma = \frac{\sum_{i=1}^{N} s^4}{N} - 3\left(\frac{\sum_{i=1}^{N} s^2}{N}\right)^2 \tag{2.16}$$

where N is the length of the observations. The random variable, **s**, being an anomaly is constrained to have unit variance. If **s** has a Gaussian distribution, its γ is zero. Distributions other than zero are super-Gaussian if their γ is positive and sub-Gaussian if γ is negative. Therefore an original signal, **s**, can be recovered from the observation, **x**, by finding a vector, **w**, that either maximizes (minimizes) the γ of **s**. Such a unit vector is usually unknown. Starting at an arbitrary unit vector **w**, an iterative procedure is used to improve **w** by maximizing (minimizing) γ, through gradient methods. The procedure is stopped if successive unit vectors **w** point in the same direction. Once the first vector has been found, the second vector is found by finding a vector constrained orthogonal to the first one. Subsequent vectors are also found similarly.

In this thesis, the FastICA algorithm of Hyvärinen and Oja (2000) was used to estimate **w**. In this algorithm, the update rule for **w** is given as follows:

$$w^{+} = E\{xg(w^{T}x)\} - E\{g'(w^{T}x)\}w \tag{2.17}$$

where $g(w^{T}x) = G(w^{T}x)'$. The choice of G that has proven useful is $G(u) = -\exp\left(\frac{-u^{2}}{2}\right)$. The new, improved matrix, **w**, is computed as

$$w = \frac{w^{+}}{\left\|w^{+}\right\|} \tag{2.18}$$

Convergence is reached when the old and new values of **w** point in the same direction. If convergence is not reached the process is repeated through Eq (2.17) and (2.18).

CHAPTER 3

SPACE-TIME-FREQUENCY ANALYSIS OF RAINFALL AND SEA SURFACE TEMPEARTURE

3.1. Introduction

Regimes of spatial, temporal and frequency variability of rainfall in Eastern, Central South and Southern Africa have been of interest to climatologists and meteorologists for many years (e.g., Tyson et al., 1975; Basalirwa, 1995; Mason, 1995) and have been used in long-range seasonal forecasting since the early 1970's (e.g., Dyer and Tyson, 1977; Currie, 1993; Ntale et al., 2004). Following the 1965-1997 droughts in Eastern Africa and the 1991/92 and 1994 droughts and an entire decade of less than average summer rainfall in Southern Africa (see BBC, 2002a, b, c), there has been a resurgence of extensive research to analyze and predict the nature of this variability, and how it is associated or teleconnected to the variability of predictable atmospheric and oceanic forcing (Mason 1995; Jury 1996; Reason and Mulenga 1999; Jury and Engert 1999; Richard et al., 2000; Philippon et al., 2002; Ntale et al., 2003; Mwale et al., 2004; Mwale and Gan, 2004). However, except for Mwale et al., (2004) and Mwale and Gan 2004, the majority of these studies normally applied Fourier-based approaches, thereby ignoring the non-stationary characteristics of climate processes. In addition, except for Eastern Africa, the majority of the studies in Southern Africa were carried out on small geographical areas, hence ignoring the regional-scale variability of rainfall.

The objectives of this chapter are to systematically identify the spatial, temporal and frequency regimes of rainfall variability of Eastern, Central South and Southern Africa and sea surface temperature (SST) of the Indian and Atlantic Oceans using a nonstationary approach. The wavelet empirical orthogonal function (WEOF) method (Chapter 2) is extensively used to identify the leading modes of rainfall and SST energy variability. Although the Hilbert-Huang transformation produces a comparatively sharper time-energy-frequency distribution than the wavelet transformation, the HEOF and WEOF lead to similar results of the spatial and temporal variability. Hence the HEOF approach is demonstrated using only the September-November (SON) and March-May (MAM) rainfall of Eastern Africa. When the decomposition of the leading modes of rainfall variability was not optimal or complete (i.e. mode mixing occurred), such as for the MAM rainfall SAWP, the WICA was used to separate the modes as much as possible.

Since data quality is poor for most parts of Central Africa (Angola, Democratic Republic of Congo, northern Mozambique and parts of northern Zambia) before 1950, the 1900-97 results are only presented for the SON and MAM rainfall and the summer rainfall of Southern Africa (south of 12°S). However, due to remarkable changes in the temporal variability of the leading modes of Southern Africa's rainfall, the analysis for the region is also presented using the 1950-97 period. The variability of SST in both the south Atlantic and Indian Oceans is analyzed using the 1950-1995 data.

Verification of the WEOF approach is made using SON rainfall data obtained from the SAFARI 2000 project (appendix A), gridded at 0.5° x 0.5°.

3.2. Climatology of Eastern, Central-South and Southern Africa

3.2.1 Central-South and Southern Africa

Except for the western cape of South Africa, which receives rainfall in the winter, rainfall in Central Southern Africa and most of Southern Africa (10°S-35°S, 10°E-43°E), (see Figure 2.1) occurs during southern hemisphere summer, which commences in October/November and ends in March/April.

During the first half of the southern hemisphere summer, October-December (OND), following the southward migration of the sun in August, intense heating takes place over Southern Africa, causing atmospheric pressure south of the equator (especially the interior) to fall. As a result of the formation of these low-pressure centers, the southeast trade winds over the South Atlantic Ocean are deflected and drawn into the Congo basin and onto the northern-most regions of the Southern Africa region (Figure 3.1(a)) (i.e. Central Southern Africa). Simultaneously, the southeast trade winds from the south Indian Ocean are also drawn into the region (see Figure 3.1(a)). In the northern sections of Southern Africa, showers and thunderstorms accompany the convergence of these two systems.

For the rest of Southern Africa, the system is made up of the tropical-temperate trough, which links the low pressure centers that form in the tropical easterlies over the landmass with a mid-latitude disturbance to the south of Africa, generally forming a band of clouds and associated convective storms oriented northwest-southeast (Reason and Mulenga, 1999). These systems are responsible for much of the summer rainfall over large regions of Southern Africa (Mason and Tyson, 2001).

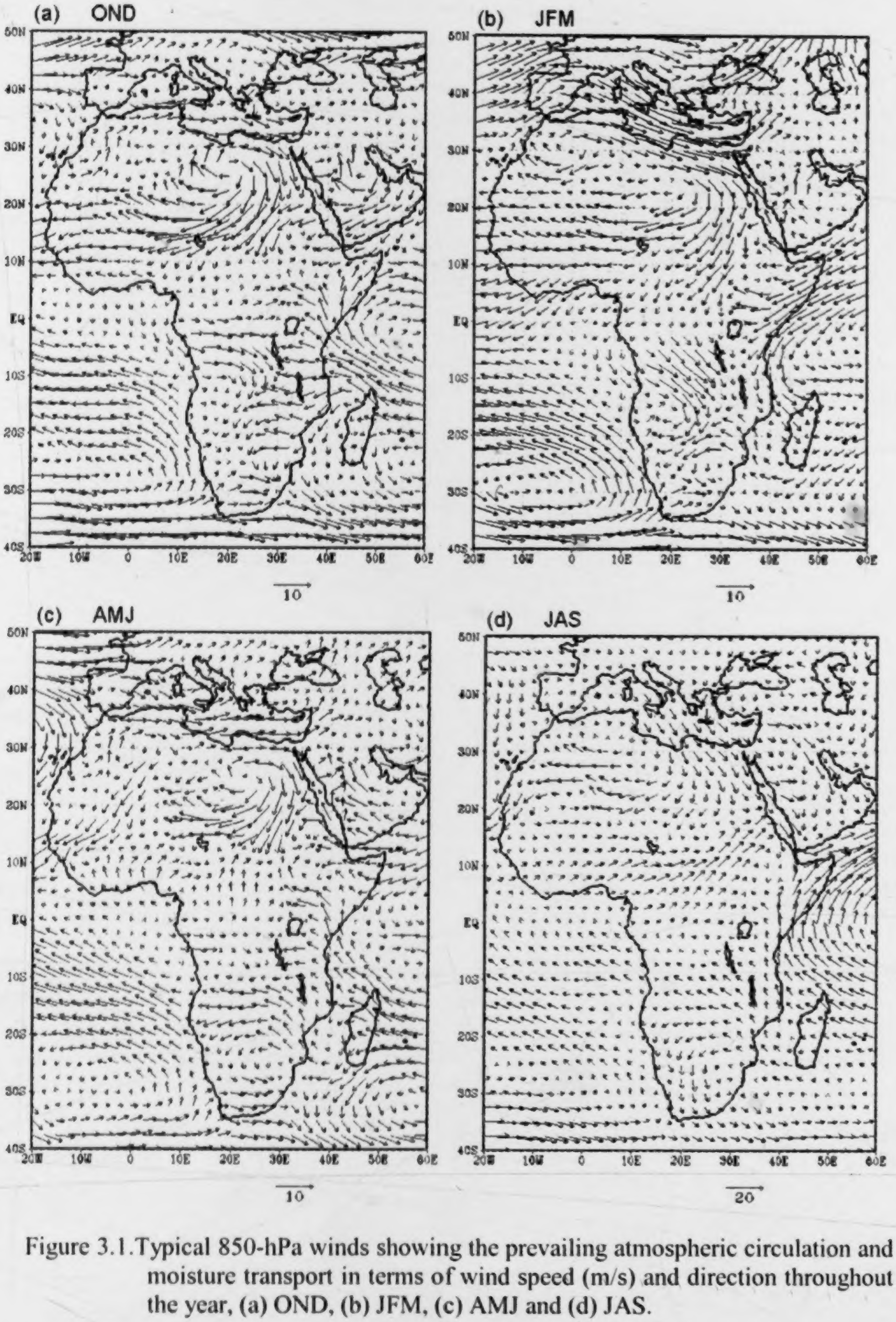
(a) OND
(b) JFM
(c) AMJ
(d) JAS
50N
40N
30N
20N
10N
EQ
10S
20S
30S
40S
20W
10W
0
10E
20E
30E
40E
50E
60E
10
10
10
20

Figure 3.1.Typical 850-hPa winds showing the prevailing atmospheric circulation and moisture transport in terms of wind speed (m/s) and direction throughout the year, (a) OND, (b) JFM, (c) AMJ and (d) JAS.

During periods of abundant rainfall the northwest-southeast orientation of the troughs are located as far north as the northern Namibia/Angola region (Harrison, 1984; Tyson, 1986). This orientation promotes easterly low-level flow from the southwestern Indian Ocean to advect moisture to Southern Africa. Stronger westerlies than normal to the north of the low-pressure troughs also advect moisture from the tropical South Atlantic Ocean. The convergence from these two sources is favorable for uplift and widespread rains (Reason and Mulenga, 1999). On the other hand, when the trough shifts and is located over the Mozambique Channel/Madagascar region, low level convergence flow and associated rains tend to lie over the Madagascar region (Reason and Mulenga, 1999). Since the winds flow offshore, Southern Africa tends to be dry. This occurs when the easterlies weaken, such as during El Niño events. During such times warming of the SST in the Nino3 region (90°W-150°W, 5°N-5°S) of equatorial pacific causes low pressure to develop in that region. The reversal in pressure gradient causes the easterlies to weaken and the troughs in the Southern Africa rainfall system to shift eastwards to the Mozambique Channel/Madagascar region.

During the second half of the rainfall season, moisture transport shifts from the southwest Indian Ocean to the northern Indian Ocean. Meanwhile, the Congo air mass continues to flow into the region (Figure 3.1 (b)). In March, the Congo air system withdraws northwards, as the sun starts its northward migration.

From April to September, Figures. 3.1(c) and (d)) shows that anticyclones are predominant over much of Southern Africa. These regions of higher pressure are seen at the 850 mb of the wind field. Since the winds in the high-pressure zone are always descending, dry, and flowing offshore, arid conditions persist during the April-September period, throughout much of Central South and Southern Africa. Hence April-September forms the dry season of the region.

3.2.2 Eastern Africa

Eastern Africa, consisting of Tanzania, Kenya and Uganda, located approximately 2°N-12°S and 30°E-43°E (see Figure 2.1), is known to experience two main rainfall seasons: SON, locally known as the 'short rains' and the MAM, locally known as the 'long rains' or 'Masika' in Swahili (Camberlin et al., 2002; Ntale et al., 2003). The SON rains are associated with the convergence into the Inter-tropical Convergence Zone (ITCZ) of the southeast monsoons controlled by the subtropical anticyclones over the Azores and the Arabian Peninsula, while the MAM coincide with the presence of the moist southeast monsoons from the Indian Ocean, which converge into the ITCZ (Ntale, 2001), also shown partly by Figures. 3.1 (a) and (c) which are plots for OND and AMJ seasons. These two rainfall seasons contribute 70% of the total annual rainfall in East Africa (Ntale, 2001).

The SON and MAM rainfalls are known to exhibit great spatial and temporal variability (Ogallo, 1989, Ntale et al., 2003). In the last four decades, however, the SON rainfall has experienced more temporal variability than the MAM rainfall (Philippon et al., 2002). The MAM rainfall is known to have a weak internal structure (Philippon et al., 2002).

Rainfall variability over East Africa has been attributed to synchronous anomalies of large scale variability such as the El Nino Southern Oscillation (ENSO), the east-west circulation over the Indian Ocean, SST variability in the Indian and Atlantic oceans, effects of large inland lakes such as Lake Victoria and the seasonal migration of the ITCZ (Nicholson and Kim, 1997, Hastenrath, 2000; Ntale et al., 2003; Goddard and Graham, 1999). Considering its equatorial position, East Africa does not receive much rainfall (Ntale, 2001). Humid conditions prevail in the highlands and near large water bodies, while dry areas include most of northern and northeastern Kenya, central Tanzania and northern Uganda (Ntale et al., 2003).

3.3. Dominant Modes of SST and Rainfall Variability

3.3.1 Dominant Periods

The local and global wavelet spectra and the corresponding Hilbert spectra were constructed using rainfall data for some locations in Eastern and Southern Africa and SST data of the Indian and South Atlantic Ocean SSTs (Figure 3.2). The region of the wavelet spectra enclosed by the dark line contains energy that is statistically significant at the 95% significance level of a red noise process. The 95% level of a red noise spectrum is modeled as the product of

$$P_k = \frac{1-\alpha}{1+\alpha^2 - 2\alpha\cos\left(\frac{2\pi k}{N}\right)} \tag{3.1}$$

and the 95th percentile value of the χ_2^2 distribution, where α is the lag-1 autocorrelation of the red noise process, $k = 0 \ldots N/2$ is the frequency index and N is the total length of the time series (Torrence and Compo, 1998). Eq (3.1) implies that the 95% level of the red noise process increases with decreasing frequency. Hence, lower frequencies require much higher power to reach the 95% confidence level (shown by same color-coding (i.e.

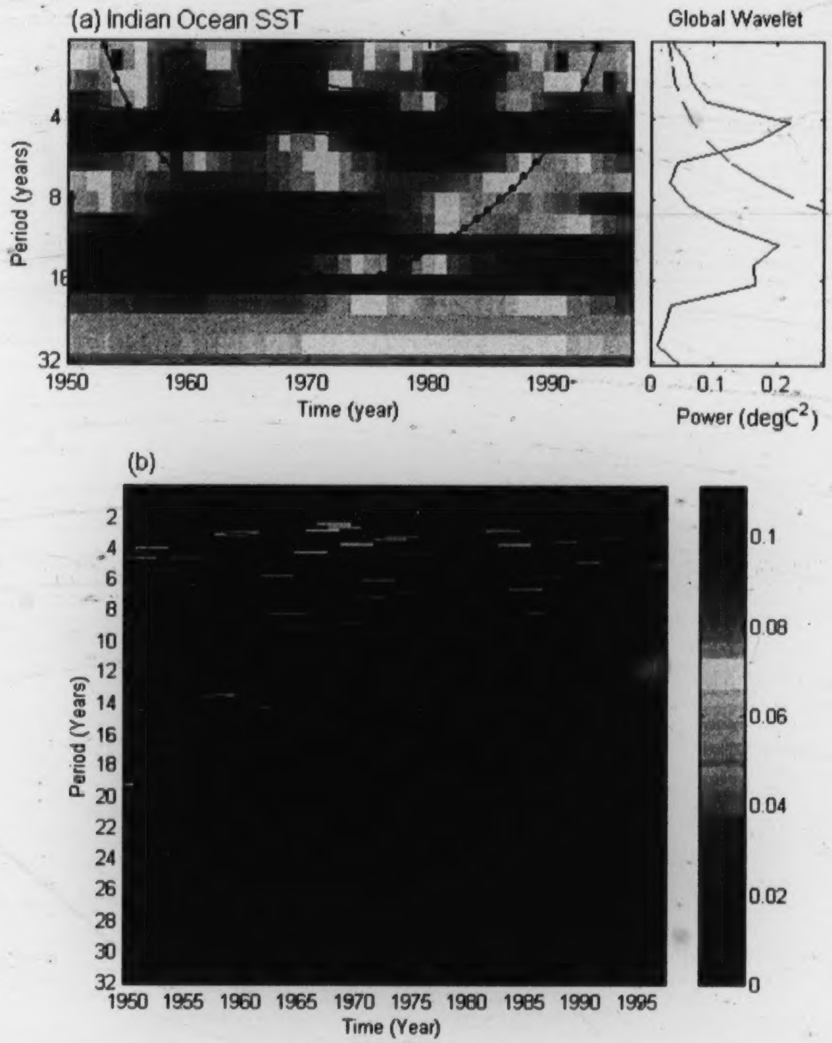

Figure 3.2 Examples of local and global wavelet spectra and corresponding Hilbert spectra constructed for, (a & b) Indian Ocean SST, (c & d) East Africa SON rainfall (e & f) Southern Africa summer, (g & h) East Africa MAM rainfall and (i & j) Atlantic Ocean SST. The dotted line in the wavelet spectra is the cone of influence, COI. In the global wavelet spectrum, the dotted curve represents the 95% confidence level, and peaks above the curve are considered statistically significant at the 95% level. Please note that wavelet and Hilbert plots are based on different colors to represent the energy levels.

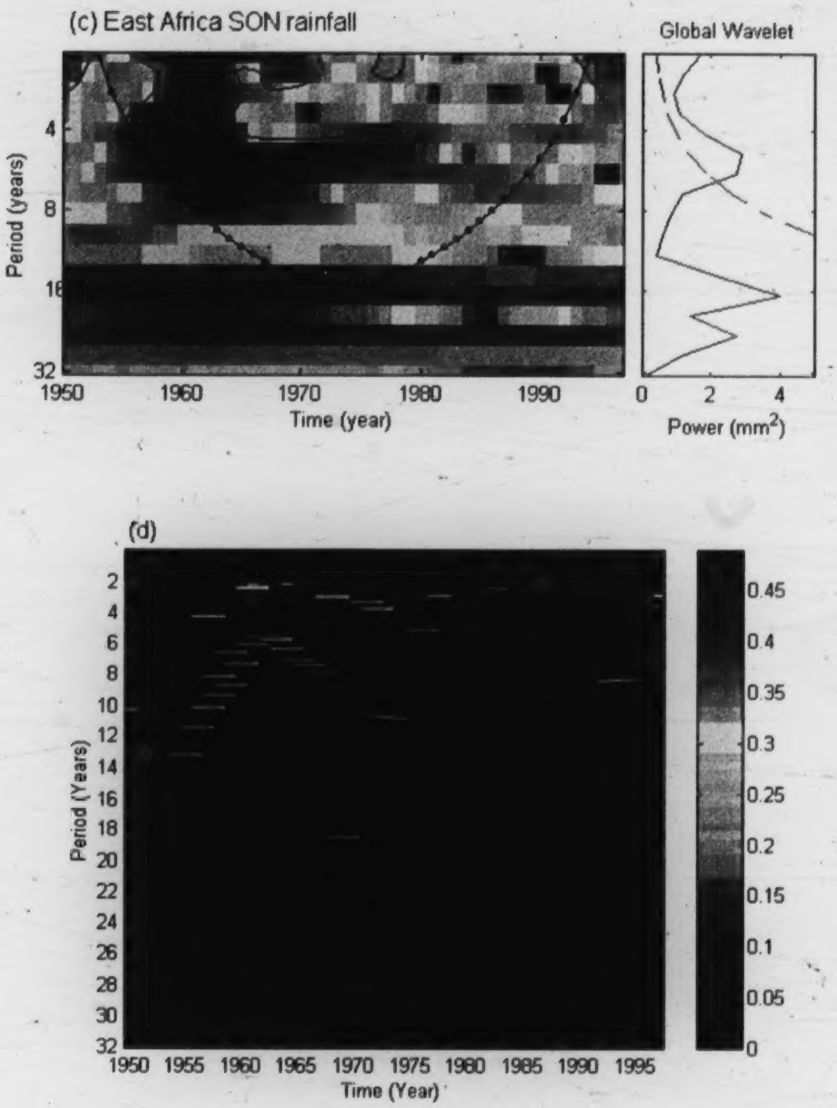

Figure 3.2 continued

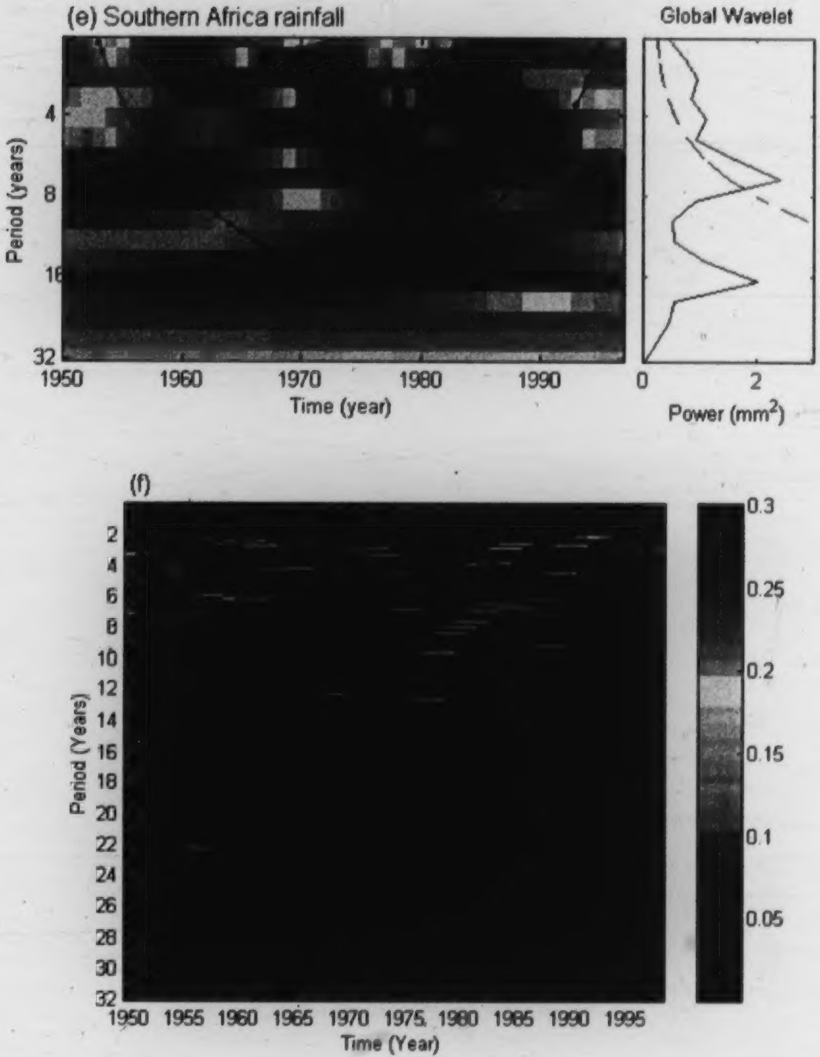

Figure 3.2 continued

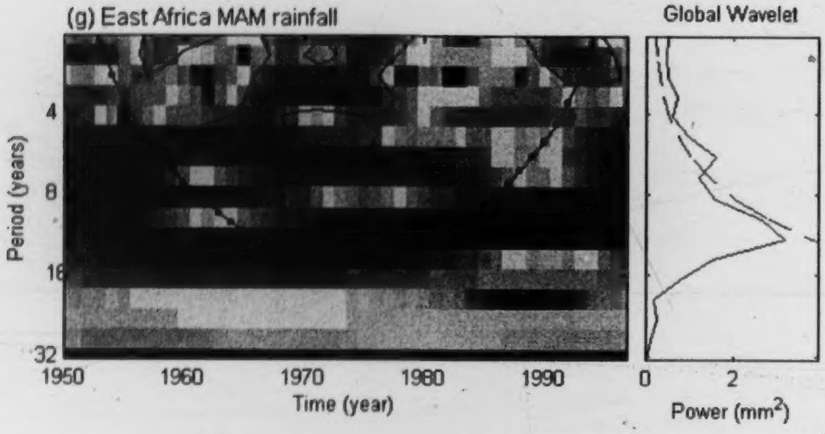

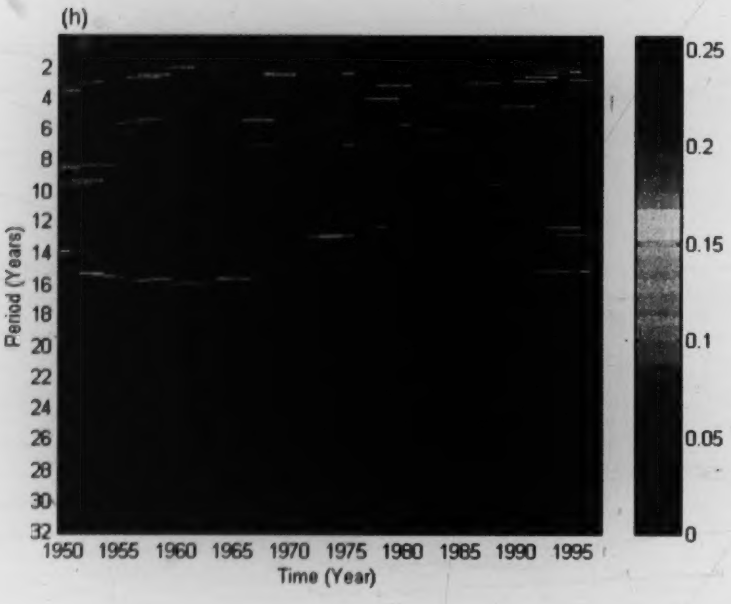

Figure 3.2 continued

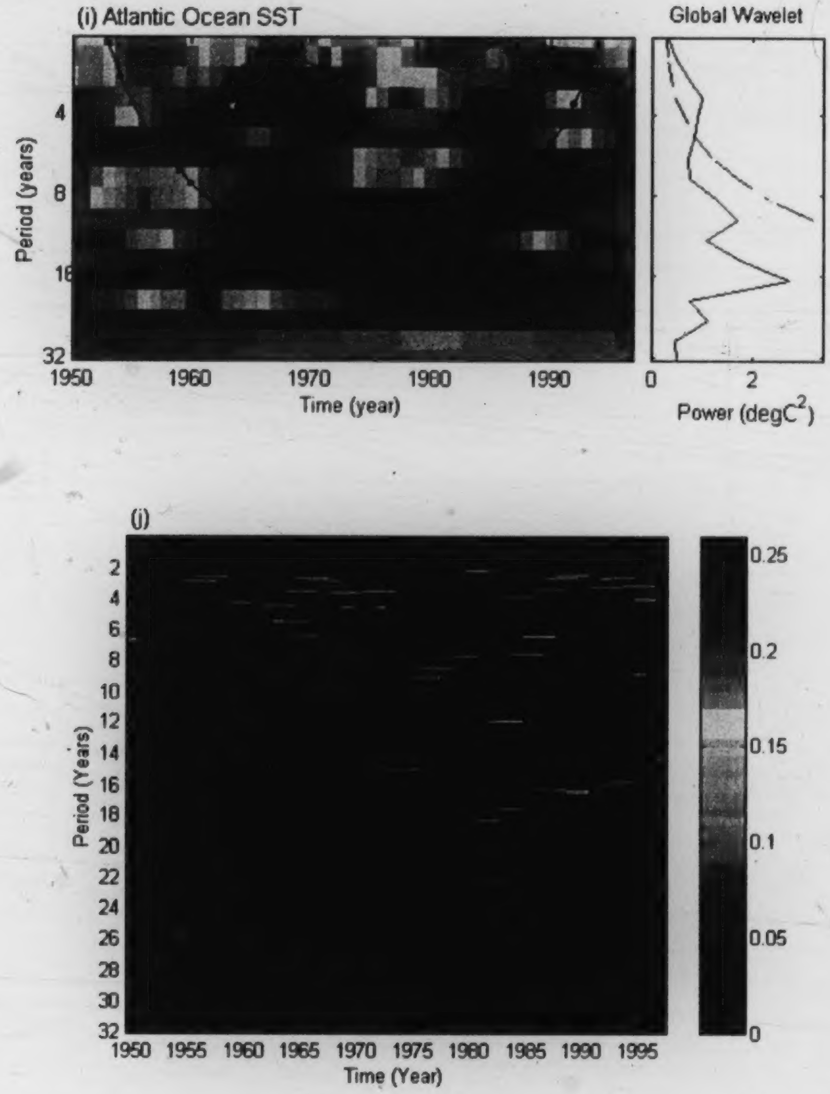

Figure 3.2 continued

brown) at lower frequencies as falling below the 95% confidence level in the wavelet spectra of Figure 3.2).

The line with dots through the wavelet spectra delineates the cone of influence (COI). Since the length of the data used is short, the ends of the time series were padded with zeros to bring the total length of the time series to the next-higher power of two, e.g., 512, 1024, etc. This facilitated the computation of wavelet energy at longer periods and also speeded up the computation of wavelet transformation. However, padding the ends of time series with zeros introduces discontinuities at the endpoints of the time series and as one goes towards larger scales, the amplitude near the edges decreases as more zeros enter the analysis. Therefore beyond the COI, the variation of power is suppressed.

Figure 3.2 shows that appreciable energy in the global wavelet spectra of both the rainfall and SST data exists between 2 and 8-year periods. The concentration of energy within these periods can be clearly seen from statistically significant peaks in the global spectra.

Figures 3.2(a) and (b) show the wavelet and Hilbert spectra of SST taken from the southwestern Indian Ocean, respectively. When these two figures are compared, it is seen that Figure 3.2(a) shows statistically significant power at the 2-year cycle in 1960, 1970 and 1985 and statistically significant power in the 6-8 year period throughout the 1950-1997 period. It also shows intense (but not significant) power within the 8-16 year periods during the 1950-1970 period and during the 1990-1997 period. Figure 3.2(b) shows that intense power exists at the 2-year cycle in 1960, 1970 and 1985. At the time of this work, we did not have an algorithm to measure the significance of power in the Hilbert spectrum. Figure 3.2 (b) also shows power exists within the 4-8 year periods throughout the 1950-1997 period. However, when the power within periods greater than 8 years is examined, it is seen that between 1950 and 1980, periodicity of the SST increased from 19 years to 6 years and between 1980 and 1997 the periods decreased from 6 years to 12 years.

Although the Hilbert and wavelet spectra are computed using spatially coarse data (i.e., averaged over 5° x 5° or 525 km x 525 km for SST and 3.75° x 2.5°, 394 km x 263 km for rainfall), Section 3.3.2 (e.g. Figure 3.3) and Section 3.3.7 (e.g., Figure 3.20) show that the frequency transitions between 1950 and 1997 are physically meaningful. Looking at Figure 3.2(a) we see that energy occurs extensively in the wavelet spectrum because of leakage problems (i.e., energy is computed even for periods that do not exist in the SST time series), while Figure 3.2(b) shows that hardly any energy leakage occurs in the Hilbert spectrum. Energy leakage is minimized in the Hilbert spectrum because actual data is used as the basis for decomposition (Chapter 2), while wavelet decomposition uses a mother wavelet that is dilated or compressed in fractional powers of two (i.e., $2^{i\delta j}$), where i = 0, 1, 2… and δj is the step size (e.g., 0.125). To include as many periods as possible in the wavelet spectrum, δj is made as small as practical. Choosing a small δj ensures that energy is computed at many periods that exist in the time series. However, this approach also makes it possible for energy to be computed for "ghost scales" (i.e., scales that do not exist in the time series). Energy associated with the ghost scales is sometimes statistically significant because these scales have almost the same periods as the scales that actually exist in the time series. Hence, Hilbert spectra have a much higher resolution of the frequency-time-energy distribution than wavelet spectra. Therefore, considering only the power spectra, the EMD and the associated Hilbert transformation methods are superior to the wavelet transformation.

3.3.2 Variability of East Africa September-November (SON) Rainfall

3.3.2.1 Spatial Regimes

WEOF analysis was applied to the SAWP of 21 grid points for the 1900-1997 period. Out of a possible 21 WPCs, only the first three leading modes of variability (also referred herein as "wavelet principal components", WPCs) were retained for further analysis. Together, these three WPCs explained a combined variance of 78%. WPC1 explained 53%, while WPC2 and WPC3 explained 14% and 11%, respectively. The remaining 18 WPCs explained less than 10% each, of the total SAWP variance. Each of these modes also covered small areas and were discarded.

Instead of having to contend with 21 separate SAWP vectors, WEOF allowed us to express the significant SON rainfall energy variability by using only three vectors. The use of WEOF also helped to compress large SAWP datasets during the analyses of SST (i.e., 154 grids for each of the Indian and Atlantic Ocean basins) and 58 grids for the southern Africa rainfall.

The WEOF analysis was based on the correlation matrix and the spatial distribution patterns of the WPCs are shown in form of the correlation coefficients between the time domain WPCs and each of the 21 gridded SAWP time series. The spatial patterns are shown in Figure 3.3. Although the correlation matrix as opposed to the covariance matrix is perceived as much more suitable for resolving spatial oscillations (Overland and Preisendorfer 1982), we did not notice any difference between the results obtained by either approach.

Spatially, WPC1 exhibits a monopole pattern extending over the entire East African region. Recalling that the square of correlation values represent the local variance explained (Houghton and Tourre, 1992), WPC1 accounts for 81% of the SAWP variance in the region of the largest loadings, namely at the center of Lake Victoria. In addition, 64% of the SAWP is accounted for in a large area encompassing much of Kenya and along the coastal regions. The explained variance suddenly decreases westwards from 34°E. Between 30°E and 34°E, an area that forms the Great Rift Valley (GRV), spatial correlations patterns show little local variance explained, generally varying between 4 and 36%. The fraction of local variance explained gradually decreases toward the south (Tanzania).

The 64-81% of local SAWP variance explained by WPC1 around Lake Victoria and eastern Kenya suggest that the lake and the northeastern Monsoons play a significant role in the variability of the SON rainfall. On the other hand, the low correlation values along the GRV suggest that either topography or a different climate forcing (e.g. the variations of the Congo air mass) regulates the SON rainfall variability.

WPC2 displays an out-of-phase relationship between the SAWP in Kenya and Uganda in the north and Tanzania in south. WPC2 is positively correlated to SAWP in Tanzania and negatively correlated to SAWP in both Uganda and Kenya. This mode explains between 1 and 25% of SAWP variance in Tanzania and 1 and 10% in Uganda and Kenya.

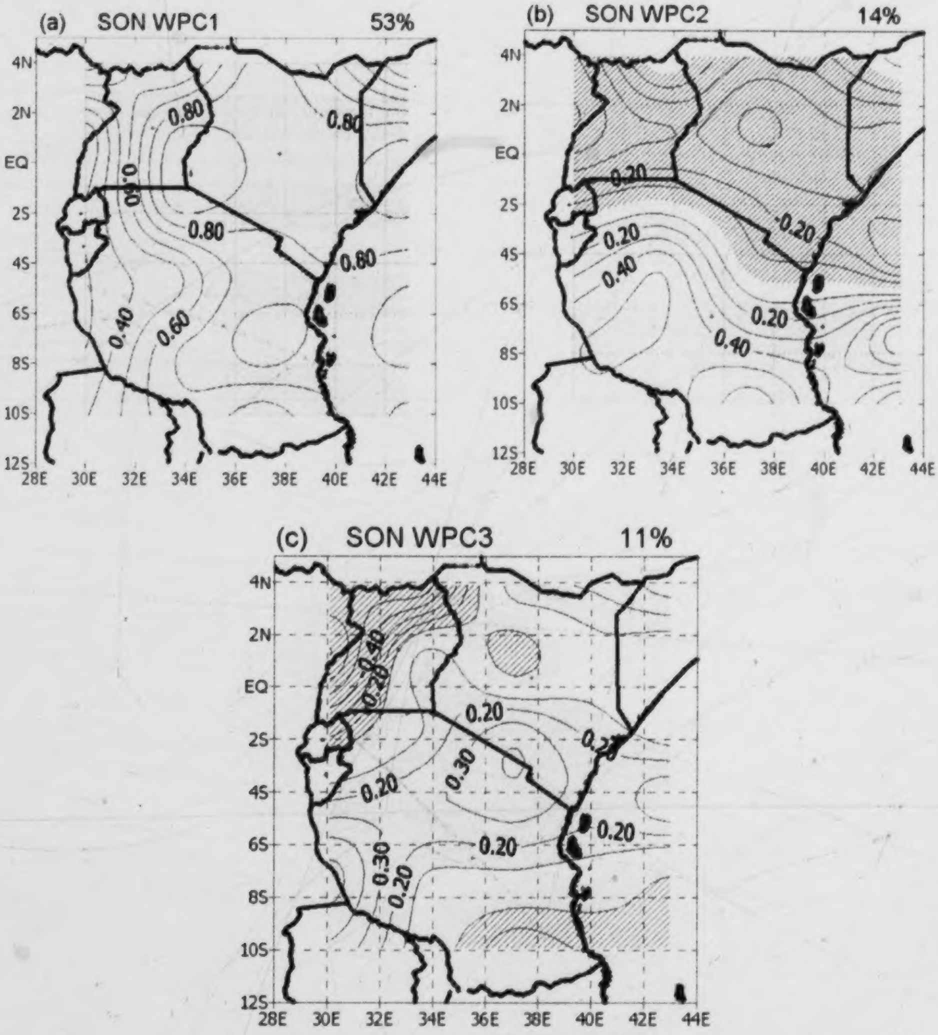
(a) SON WPC1 53%
(b) SON WPC2 14%
(c) SON WPC3 11%
0.80
0.60
0.40
0.20
0.30
-0.20
4N
2N
EQ
2S
4S
6S
8S
10S
12S
28E
30E
32E
34E
36E
38E
40E
42E
44E

Figure 3.3 Spatial displays at 0.1 intervals of the correlation between SAWP and (a) WPC1 (b) WPC2 (c) WPC3 of the SON rainfall. Percentage values above the figures represent proportions of total variance explained by each WPC. Dotted areas represent positive correlation, while hatched areas represent negative correlation. The areas without shading represent areas with zero correlation. The corresponding time domain WPCs are shown in (d) WPC1 (e) WPC2 and (f) WPC3.

(d) WPC1

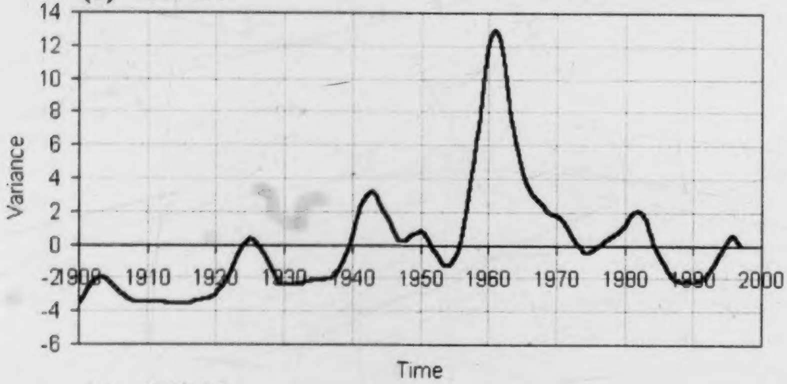

(e) WPC2

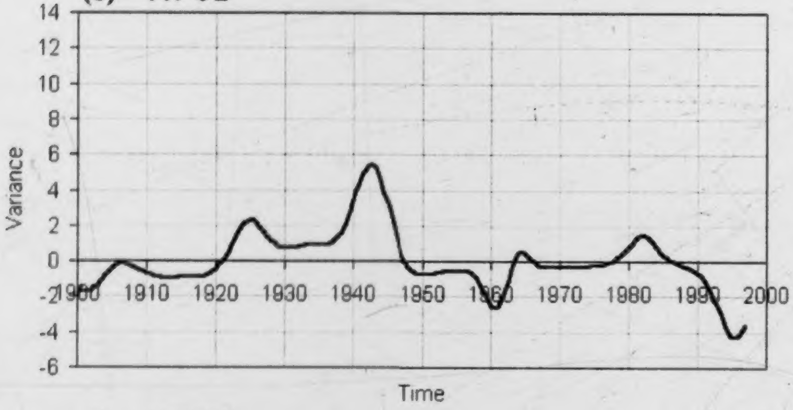

(f) WPC3

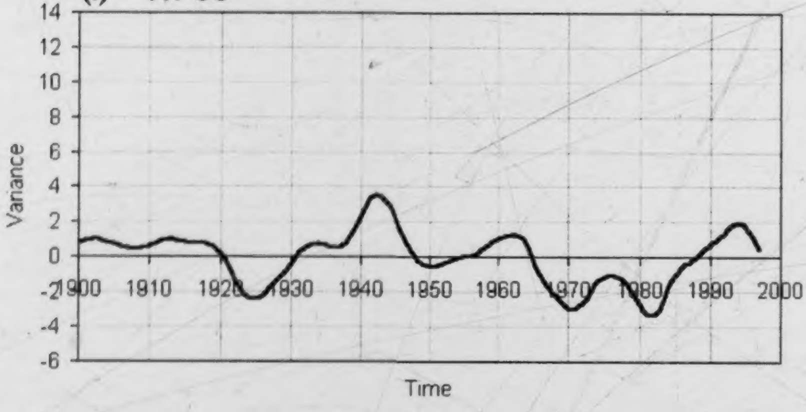

Figure 3.3 continued

The explained variance of SAWP by the WPC2 is much higher in Tanzania than in Uganda and Kenya because it explains the remainder of the variance not accounted for by WPC1 in these areas.

WPC3 describes variability of SAWP along the western border of East Africa (GRV of Uganda and Tanzania) and around mount Kilimanjaro (5895 meters amsl) not accounted for by both WPC1 and WPC2. The percentages of local SAWP variances explained (1 to 25%) are generally low depicting the damping effect of topography has on the SON rainfall variability. WPC3 is positively correlated to the area around Mount Kilimanjaro and southwestern Tanzania and negatively correlated to Uganda. This mode appears to describe the SAWP variations of areas associated with extreme altitude.

When WEOF was applied to the 1950-1997 East Africa SON rainfall SAWP, three leading WPCs explaining a combined variance of 90% were retained. Individually, the modes explained 63%, 17%, and 10% of the total SAWP variance. The spatial patterns of these modes were similar to the one computed for the 1900-1997 period and hence are not discussed further.

To check if further information could be uncovered from the SON rainfall variability, the SON rainfall patterns for the 1900-1997 period were analyzed using the scale power extracted from Hilbert-Huang spectra. Three leading Hilbert PCs (HPCs) that explained a combined variance of 55% were retained. Individually, these modes explained 35%, 12% and 8% of the total scale averaged instantaneous Hilbert spectral power. Although the spatial and temporal patterns of the modes from the WEOF and HEOF appear the same, the explained variance is much lower for the

HPCs than the WPCs. The apparent difference in the explained variance between WPCs and the HPCs is because of the higher lag-1 auto-correlation in SAWP (about 0.95) compared to the scale average power of Hilbert spectra (about 0.85). The tendency for comparatively lower values of the lag-1 auto-correlation in the HPCs is due to the fact that averaging is performed over energy associated with periods that actually exist in the time series. In the wavelet spectra, energy leakage results in smoothed SAWP and WPCs and therefore higher lag-1 auto-correlation between the two.

The spatial correlation patterns computed from the Hilbert spectral energy are shown in Figure 3.4. The core of the spatial pattern of the SON rainfall variability is also located at the middle of Lake Victoria, and is also strong in eastern Kenya, re-affirming that Lake Victoria and the Monsoon winds play a significant role in the variability of SON rainfall. Other than that, no new information on spatial variability was found in the SON rainfall variability using the Hilbert spectral energy.

Using the SON rainfall spatial patterns, East Africa may be delineated into two zones of rainfall variability, the GRV as one zone and the rest of the East Africa centered at Lake Victoria as another zone. This finding contrasts with those of Ntale (2001), Basalirwa (1995) and Ogallo (1989) who found between 6 and 26 zones of homogenous of rainfall variability in East Africa.

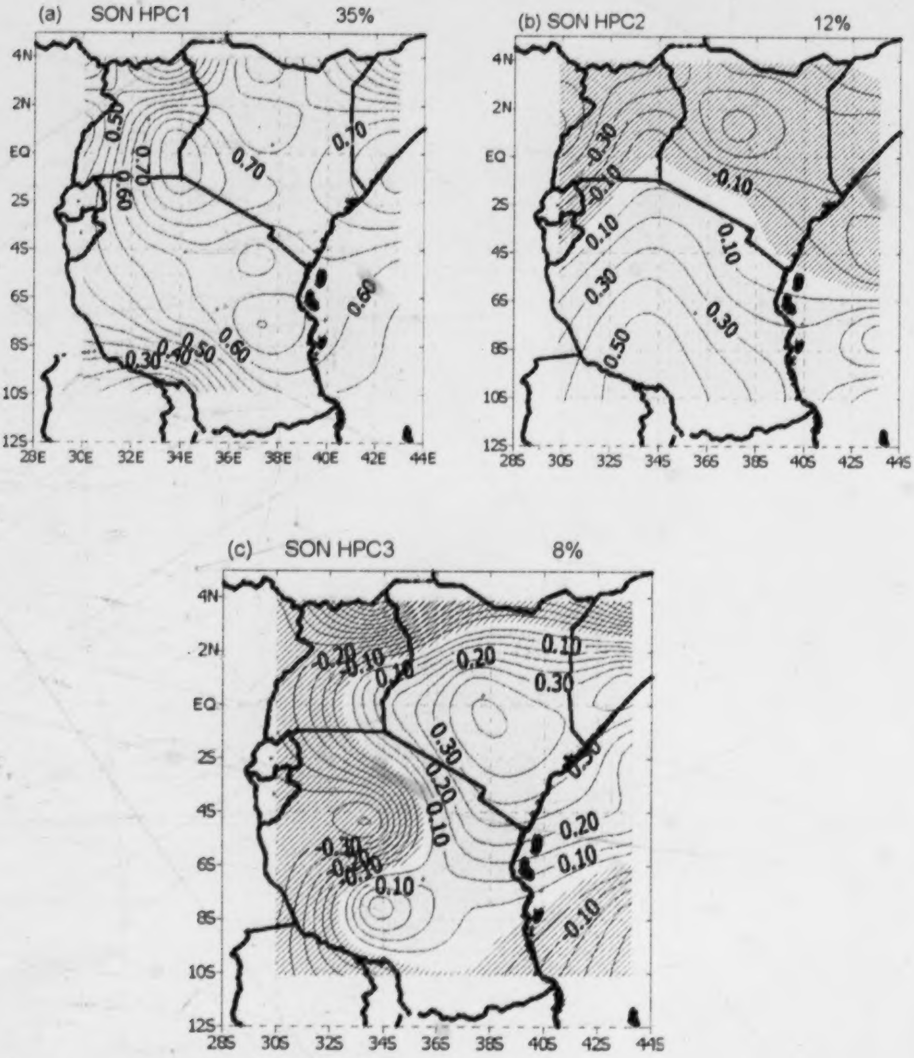
(a) SON HPC1 35%
(b) SON HPC2 12%
(c) SON HPC3 8%
4N
2N
EQ
2S
4S
6S
8S
10S
12S
28E 30E 32E 34E 36E 38E 40E 42E 44E
28S 30S 32S 34S 36S 38S 40S 42S 44S
0.50
0.70
0.60
0.30
0.40
0.10
-0.10
0.20
-0.20
-0.30

Figure 3.4 Spatial displays of the correlation between Hilbert energy principal components and the scale averaged Hilbert energy, (a) HPC1 and SAHP (b) HPC2 and SAHP (c) HPC3 and SAHP of the SON rainfall. Percentage values above the figures represent proportions of total variance explained by each HPC. Dotted areas represent positive correlation, while hatched areas represent negative correlation. The areas without shading represent areas with zero correlation. The corresponding time domain WPCs are shown in (d) HPC1 (e) HPC2 and (f) HPC3.

(d) HPC1

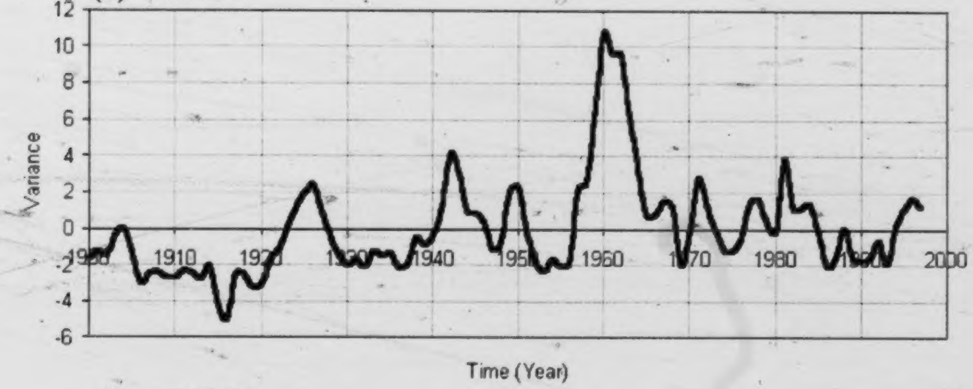

(e) HPC2

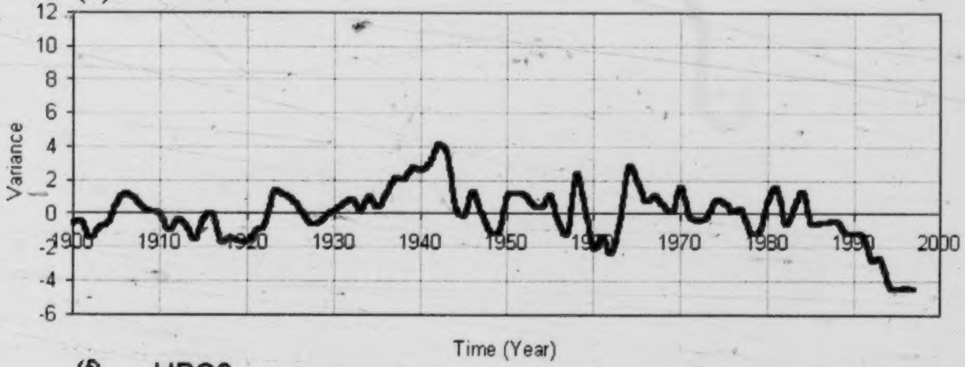

(f) HPC3

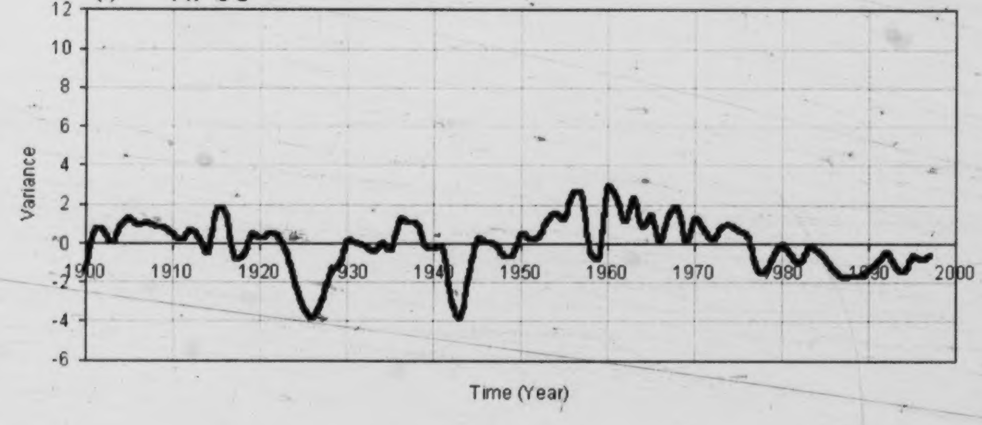

Figure 3.4 continued

3.3.2.2 Temporal Regimes

The temporal variability of the time domain WPCs is shown in Figures 3.3(d)-(f) and 3.4(d)-(f). The variance of WPC1 is seen to have increased gradually from 1900 to 1961 and decreased between 1962 and 1997. WPC1 is characterized by interdecadal fluctuations that appear fairly stationary with 18 to 20-year cycles. A closer examination, however, reveals that between 1900 and 1962, the 20-year period gradually increased towards 8 years and between 1962 and 1997 the periods gradually decreased towards 14 years. The change of periodicity in the SON rainfall of East Africa is a new finding that has implications for predictability of the SON rainfall at longer time scales.

Except at the ends of the WPC1 time series, the variation of power between 1900 and 1997 is consistent with the history of floods and droughts recorded during this period. The 1961-62 peak of WPC1 is associated with the rainfall event of 1961-62, which was unprecedented in intensity, duration and areal extent during the 20th century in East Africa. During the short period, between 300 and 500% of mean total rainfall fell causing the level of Lake Victoria to increase by 2.25 meters (Mistry and Conway, 2003). Slightly similar conditions occurred in 1997 when the Lake levels rose by 1.6 meters (Mistry and Conway, 2003), but that event is generally suppressed in WPC1 because of the end-point problem, inherent in wavelet analysis. Since WPC1 is also strongly correlated to Kenya, eastern Uganda and northern parts of Tanzania, floods were also experienced in these countries during the 1961-62 period.

On the other hand, of the fourteen droughts that occurred in East Africa between 1900 and 1997, twelve occurred between 1965 and 1996, with one each in 1949 and

1900. These droughts are also conspicuous in the time series of WPC1 as periods of decreasing power. Hence, for almost four decades (i.e., 1962-1997), East Africa generally experienced declining SON rainfall. The 1975-1982 increase in SON rainfall was largely small to offset the 1962-1974 decrease in the rainfall. Thus, the SAWP energy variability accurately represents the temporal variability of East African SON rainfall.

Compared to WPC1, the WPC2 time series is less variable between 1950 and 1997. WPC2 shows that between 1982 and 1997, northern and western Uganda (being negatively correlated) experienced an increase in SON rainfall, while Mt. Kilimanjaro in NE Tanzania and the SW Tanzania region experienced decreased rainfall during the same period. Because the SAWP of southwestern Tanzania and much of western and northern Uganda are out-of-phase, the reduction was probably greater for the former than the latter.

3.3.2.3 Frequency Regimes

To determine which periods of the SON rainfall account for most of the variability of the SAWP and hence the rainfall, in space and time, WEOF was applied to the time series of wavelet energy extracted for individual wavelet scales. The periods chosen were from the 2-8 year range found in Section 3.3.1. These periods match those found by other researchers, such as Potts (1971), Rodhe and Virji (1976), Ogallo (1979), Ropelewski and Halpert (1987) and Nicholson (1996), some of which are shown in Tables 3.1 to 3.3. The variation of the SAWP explained by each of the leading modes of the individual wavelet scales was also computed as a square of the correlation. Table 3.1 shows that most of the variance in the SON SAWP was explained by the periods around 2 years. The explained variance gradually decreased with increasing periods up to 3.5 years, but increased again with decreasing periods.

The spatial patterns, selected for some periods in the 2-8-year band are shown in Figure 3.5. At the center of Lake Victoria, between 64 and 81% of the variance of SAWP is accounted for by the 2-year period. This spatial pattern stretched eastwards to Kenya's east coast. The variance decreased gradually to the north and south and rapidly to the west. The dominance of the periods around 2 years in the spatial pattern of the SON rainfall throughout the 1900-1997 and 1950-1997 periods suggests that strong interannual variability is the chief characteristic of the SON rainfall. This was confirmed from the Hilbert spectrum of a SON rainfall time series of Figure 3.6. However, strong cycles in the longer periods (3-7 years) of the SON rainfall are also conspicuous especially for areas in western Uganda and eastern Kenya. As noted earlier, the SON rainfall variability in the GRV might be influenced from the west (i.e. Congo air mass from Atlantic Ocean), which has been shown to have El Niño like variations, with periods of between 3 and 7 years (Mason, 1995). On the other hand, rainfall in Eastern Kenya and coastal areas is influenced by the Monsoons from the Indian Ocean. Since ENSO has been shown to strongly interact with climate dynamics of the Indian Ocean, both in the monsoons seasons and in the northern Fall transition months (Camberlin et al., 2002), it is not surprising that SON rainfall in Kenyan and the coastal areas exhibits periods of between 3 and 7 years.

Table 3.1 Explained variances of scale-based WPCs computed for the 1950-1997, SON rainfall SAWP of East Africa.

No	Cycle(Period)	WPC1 % Variance	WPC2 % Variance	Total % Variance
1	2	63	19	82
2	2.4	63	19	82
3	3.5	39	18	57
4	4.8	30	20	50
5	5.6	51	21	72
6	8	58	20	78

Table 3.2 Explained variances of scale-based WPCs computed for the 1950-1997, MAM rainfall SAWP of East Africa.

No	Cycle(Period)	WPC1 % Variance	WPC2 % Variance	Total % Variance
1	2	31	24	55
2	2.4	25	21	46
3	3.5	26	19	45
4	4.8	32	22	54
5	5.6	31	24	55
6	8	32	23	55

Table 3.3 Explained variances of scale-based WPCs computed for the 1950-1997, summer rainfall SAWP of southern Africa.

No	Cycle(Period)	WPC1 % Variance	WPC2 % Variance	Total Variance
1	2	29	22	51
2	2.4	30	21	51
3	3.5	25	15	40
4	4.8	33	17	50
5	5.6	33	20	53
6	8	34	24	58

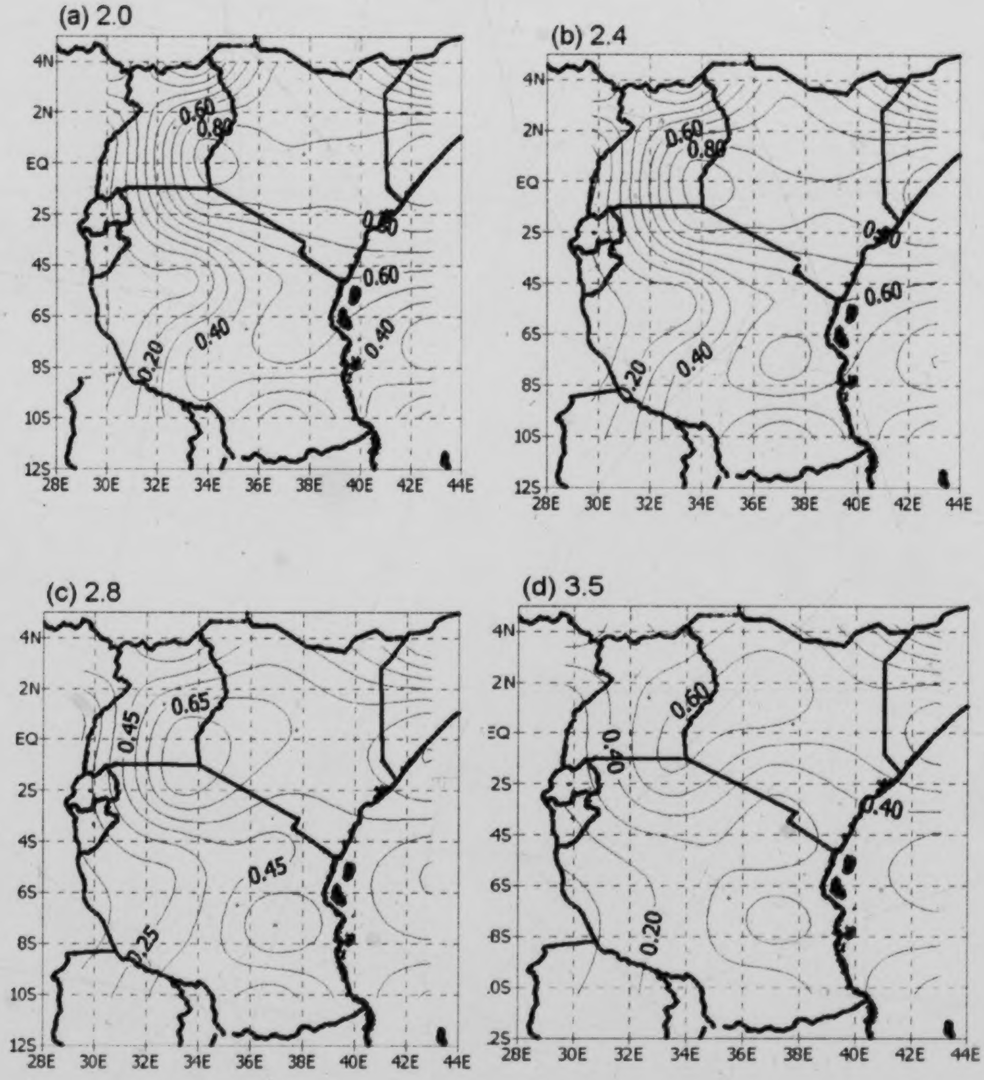
(a) 2.0
(b) 2.4
(c) 2.8
(d) 3.5
0.60
0.80
0.40
0.20
0.65
0.45
0.25
4N
2N
EQ
2S
4S
6S
8S
10S
12S
28E
30E
32E
34E
36E
38E
40E
42E
44E

Figure 3.5 Contours plotted at 0.1 intervals showing the spatial patterns of the variance of the SON rainfall SAWP explained by energy at (a) the 2-year, and (b) the 2.4-year period, (c) 2.8-year period, (d) 3.5-year period, (e) 6.7-year, and (f) 8-year period for the 1900-1997 period. The corresponding time domain WPCs of the 2 to 6.7-year cycles are shown in (g) to (l), respectively. The percentage values in (g) to (l) represents the variance of the total individual scale energy explained by the leading WPC at that scale. More variance of SAWP is explained by the higher frequencies throughout East Africa. As one goes to lower scales, less variance of the SAWP is explained for the SON rainfall.

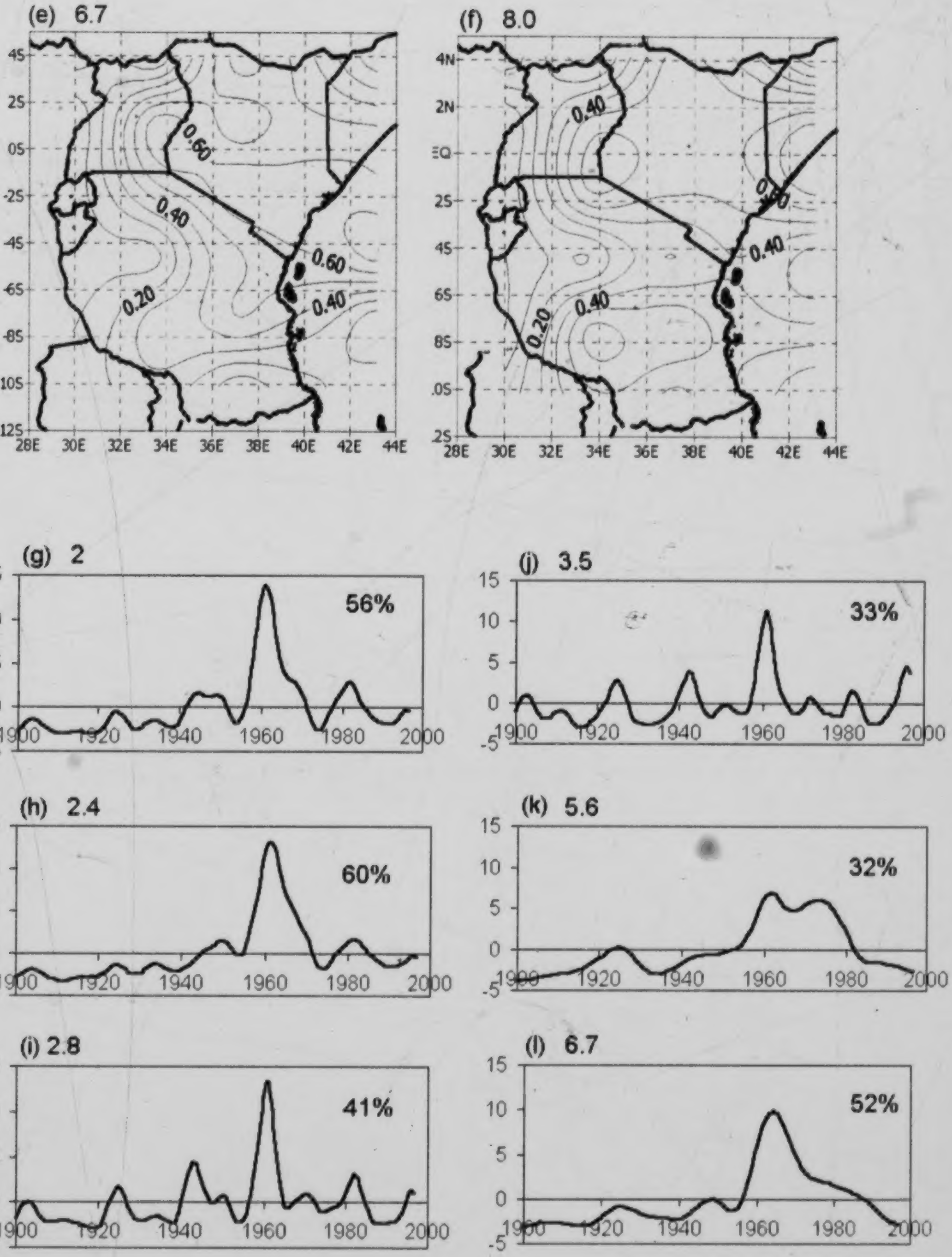

Figure 3.5 Continued

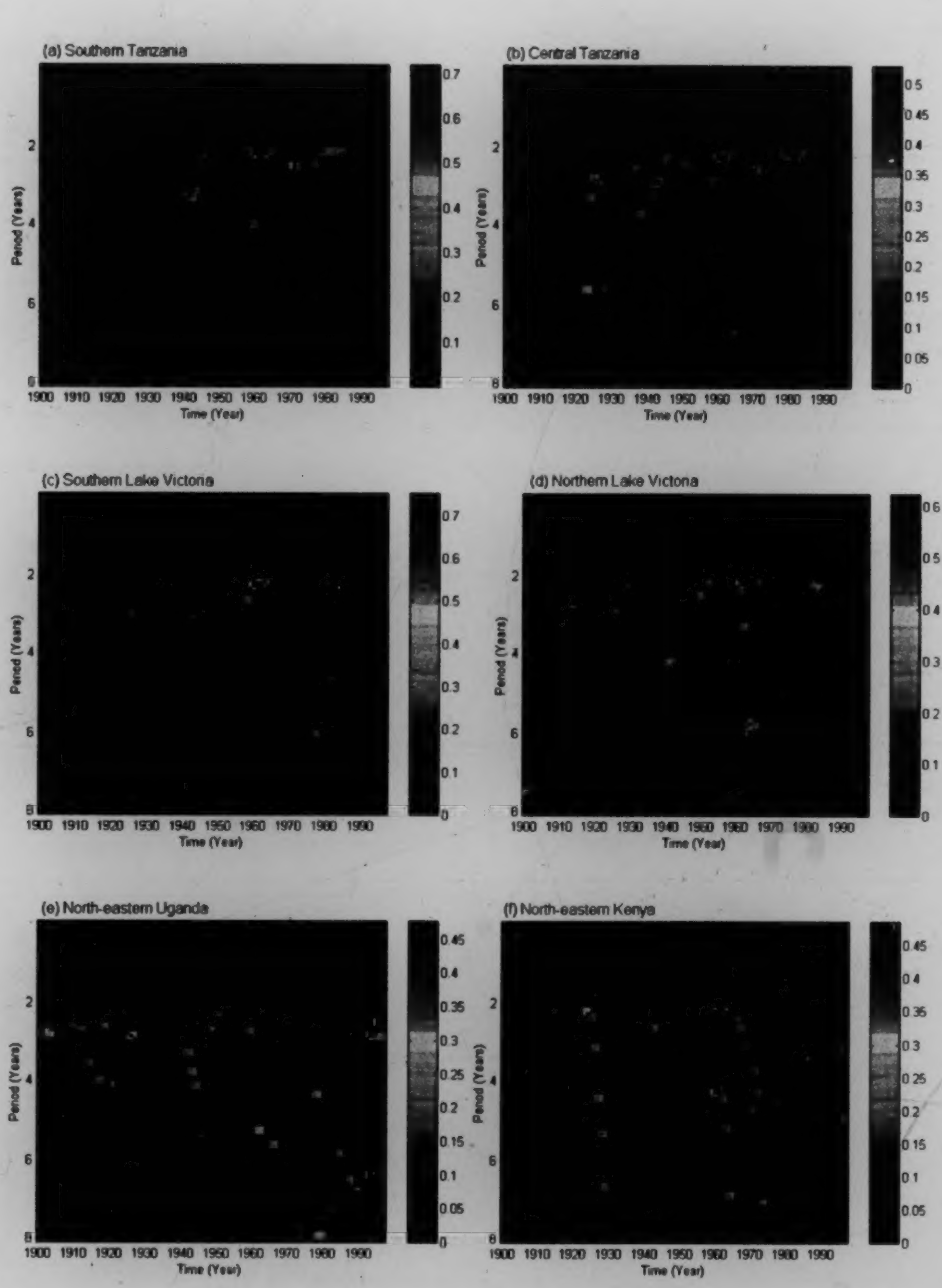

Figure 3.6 The Hilbert spectrum showing variation of energy between 1900 and 1997 for periods between 2 and 8 years for the SON rainfall time series of, (a) southern Tanzania (b) Central Tanzania (c) southern half of Lake Victoria and (d) Northern half of Lake Victoria. All power is in mm^2.

We suggest that the strong periods around 2-years in the SON rainfall SAWP variability might be associated with the quasi-biennial oscillation (QBO) with a period of about 2.2-2.3 years. The fact that much less variance in the center of Eastern Africa (i.e. Lake Victoria and the surrounding regions) is explained by energy at periods greater than 3 year shows that SON rainfall SAWP variability of this region is dominated by the inter-annual variabilities and is only weakly associated with El Niño or El Niño-like events.

3.3.3 Variability of East Africa March-May (MAM) Rainfall

3.3.3.1 Spatial Regimes

Application of the WEOF analysis technique to the MAM rainfall SAWP for the 1900-1997 and 1950-1997 periods both revealed two leading WPCs that accounted for a combined variance of 44% and 50% respectively. WPCs 1 and 2 obtained using the 1900-1997 SAWP explained 27% and 17%, respectively, while those for the 1950-1997 period accounted for 26% and 24% of the total SAWP energy variance.

The spatial patterns of the 1900-1997 WPCs are shown in Figure 3.7. Spatially, WPC1 is negatively correlated to the rainfall SAWP of most of East Africa and is weakly correlated to the SAWP of eastern Tanzania. The largest negative correlations are found at two locations, the northwestern and southwestern East Africa (49%).

The variance of SAWP explained by WPC1 at these centers is 64% in the northwest and 49% in the southwest. From these centers, the explained variance decreases eastwards until in eastern Tanzania, where very little of the SAWP variance is explained by this mode.

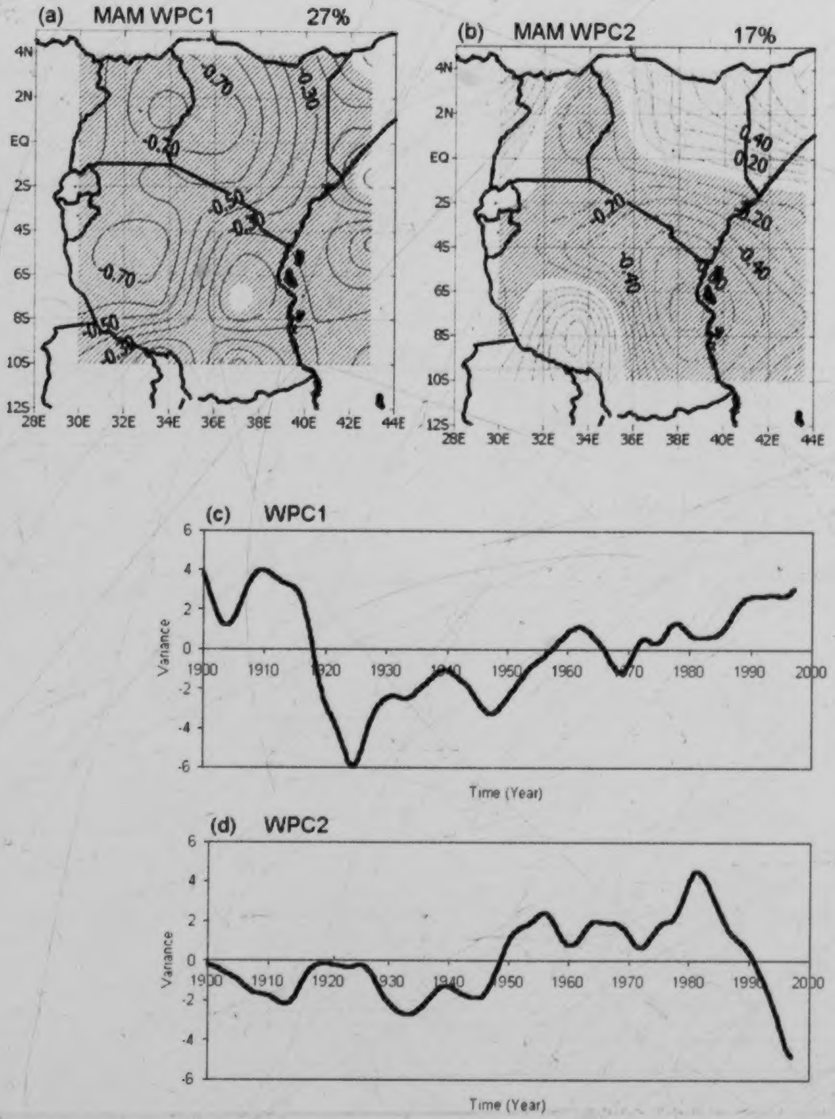

Figure 3.7 Spatial displays at 0.1 intervals of the correlation between (a) WPC1 and SAWP, and (b) WPC2 and SAWP of the MAM rainfall. Percentage values above the figures represent proportions of total variance explained by each WPC. Dotted areas represent positive correlation, while hatched areas represent negative correlation. The areas without shading represent areas with zero correlation. The corresponding time domain WPCs are shown in (d) WPC1, and (e) WPC2.

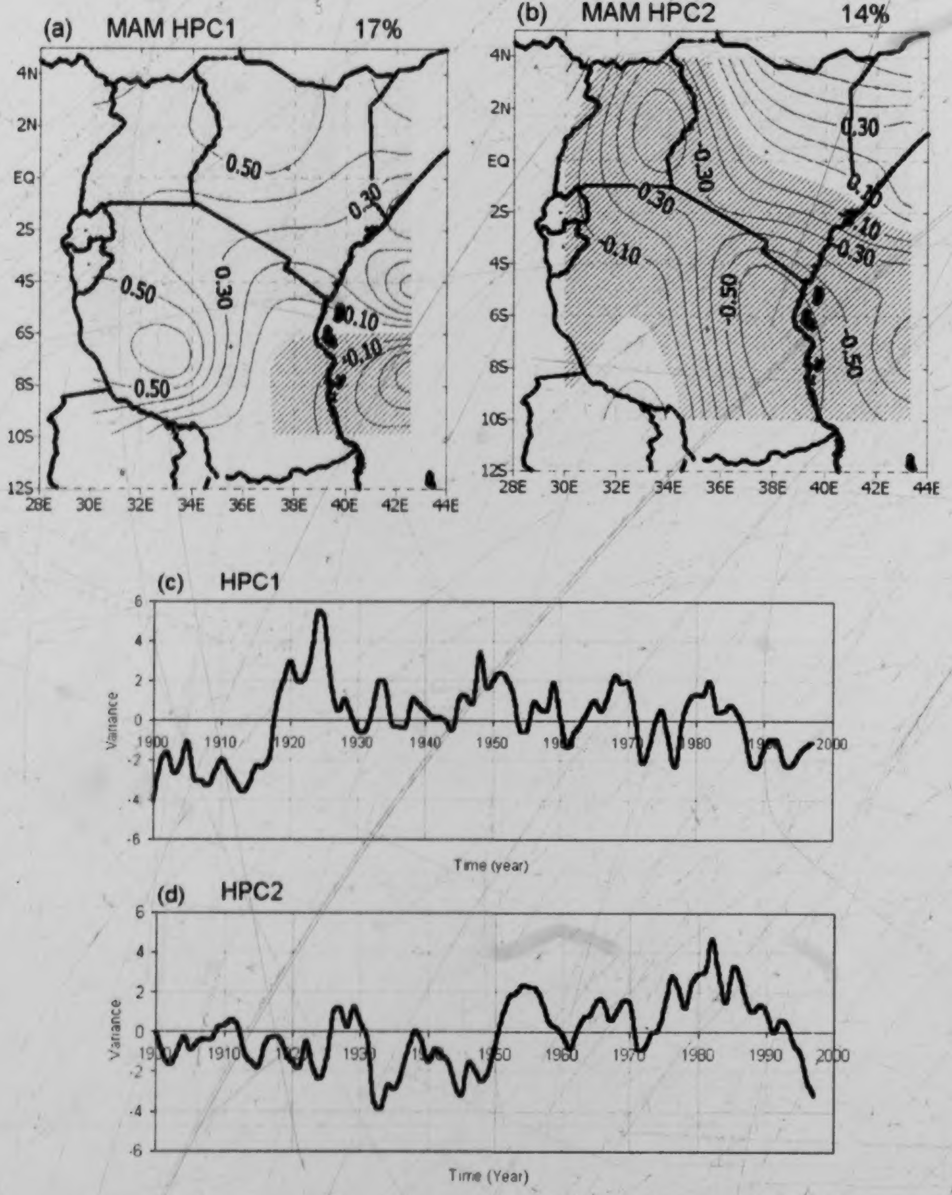

Figure 3.8 The spatial patterns plotted at 0.1 intervals showing the correlation between (a) HPC1 and SAHP, and (b) HPC2 and SAHP of the MAM rainfall. Percentage values above the figures represent proportions of total variance explained by each HPC. Dotted areas represent positive correlation, while hatched areas represent negative correlation. The areas without shading represent areas with zero correlation. The corresponding time domain HPCs are shown for, (c) HPC1, and for (d) HPC2.

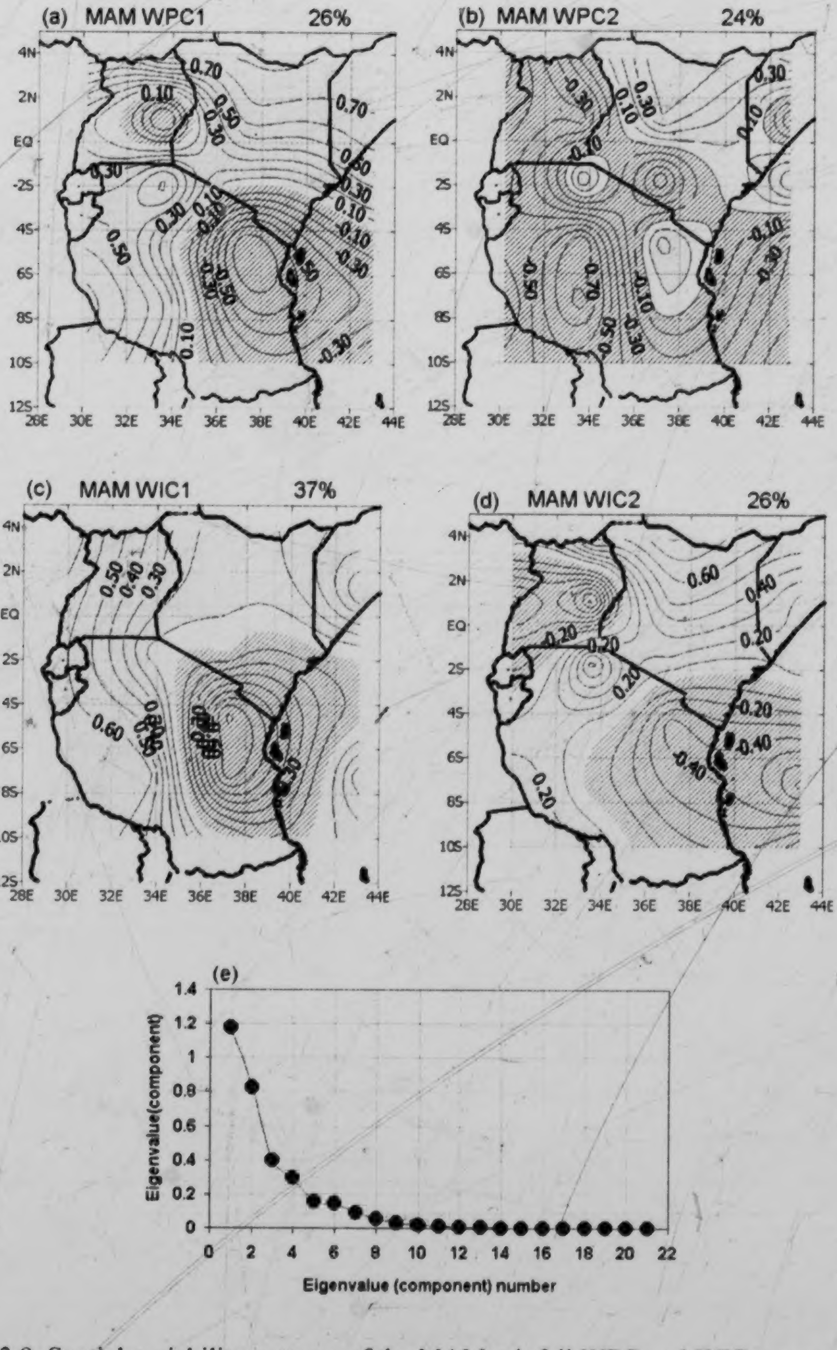
(a) MAM WPC1 26%
(b) MAM WPC2 24%
(c) MAM WIC1 37%
(d) MAM WIC2 26%
4N
2N
EQ
2S
4S
6S
8S
10S
12S
28E 30E 32E 34E 36E 38E 40E 42E 44E
0.70
0.50
0.30
0.10
-0.10
-0.30
-0.50
0.60
0.40
0.20
-0.20
-0.40
(e)
Eigenvalue(component)
Eigenvalue (component) number
0 0.2 0.4 0.6 0.8 1 1.2 1.4
0 2 4 6 8 10 12 14 16 18 20 22

Figure 3.9. Spatial variability patterns of the MAM rainfall WPC and WICs computed for the 1950-1997 period: (a) WPC1 (b) WPC2, (c) WIC1 and (d) WIC2. The independent component values associated with the 21 patterns are shown in the scree plot, (e).

The second mode, WPC2, is negatively correlated to the SAWP of eastern Tanzania, parts of southern Uganda and southern Kenya and is positively correlated to the SAWP of northern Kenya, southwestern Tanzania and western Uganda. Large negative correlations (up to 49% of SAWP variance) are predominant in eastern Tanzania and clearly explain the variance of SAWP not accounted for by WPC1.

As opposed to the spatial pattern of the SON rainfall WPC1, which explains more variance of SAWP in eastern parts of East Africa and at Lake Victoria, and then weakens westwards and southwards, the MAM WPC1 spatial pattern is strongest in the western parts of East Africa and weakens eastwards (see Figure 3.7). This pattern is found for both the 1900-1997 and 1950-1997 periods. This finding suggests that while Lake Victoria and the northeast monsoons play significant roles in the variation of the SON rainfall for most of East Africa, the Congo basin or the Atlantic Ocean SST variability are possible regulators of the MAM rainfall variability.

Application of the HEOF analysis produced spatial and temporal patterns as shown in Figure 3.8. Generally, the spatial and temporal patterns are similar to those of the WPCs. Since no new information is found using this method, the results are not discussed further.

With 26% and 24% of the SAWP variance explained by WPC1 and WPC2, it was suspected that the decomposition was not stable and the two modes were mixed. The 1950-1997 MAM SAWP was re-analyzed using WICA. Application of the WICA technique revealed two leading wavelet independent component (WIC) modes, explaining 63% of the total variance (i.e. 37 and 26% for each of the leading modes). Their spatial patterns together with the WICs are shown in Figure 3.9(c) and

3.9d. Generally, these figures show that eastern Tanzania and the rest of the region are out of phase. Figure 3.9(c) reiterates the existence of a strong MAM rainfall signal (36% of SAWP variance) from the western boundary of Eastern Africa, which decreases eastwards.

In Chapter 2, we noted that the optimization algorithm of ICA (FastICA algorithm) uses higher order statistical properties to look for the eigenvector spaces in data that are completely independent from one another. These eigenvectors (called independent component vectors) describe SAWP variations that are not only uncorrelated but independent from one another. The eigenvalues associated with the leading independent component vectors are shown in a scree plot (see Figure 3.9 (e)) and it is clear that they are well separated. The total sum of the 21 independent component values is 3.21. The two leading component (eigenvalues) are 1.18 and 0.83, accounting for 37% and 26% of the total SAWP variation, respectively. This explains the apparent increase in explained variance from 26 and 24% to 37 and 26%, respectively. Assuming the scree plot (Figure 3.9(e)) were used to choose the leading modes, only the first two eigenvector (components) (associated with eigenvalues to the left of the elbow), considered to be the signals in the MAM SAWP would be chosen, while the rest of the modes would be discarded as they are associated with "noise" in the SAWP. This agrees with results from visual inspection of the spatial modes.

3.3.3.2 Temporal Regimes

The temporal variabilities of the leading modes of the MAM rainfall SAWP are shown in Figures 3.7 and 3.8. Bearing in mind the negative correlation between

WPC1 and the SAWP, it is clear that the leading mode (WPC1 and HPC1) sharply increased in energy (variance) between 1900 and 1924. However, the energy in this WPC gradually decreased from 1925 to 1997. Areas strongly associated with this mode include most areas of East Africa, but not eastern Tanzania. The second mode also shows a general increase in energy between 1900 and 1980, followed by a sudden decrease of energy between 1980 and 1997.

The temporal variability shown by MAM rainfall is completely different from that of SON rainfall, showing that although these rainfall seasons are located in the same geographical zone, different climate forcings are responsible for their variability. Unlike the SON rainfall, which experienced a sudden decrease of energy between 1950 and 1997, with background variance modulated by periods decreasing from around 8 to 14 years, the MAM rainfall decreased gradually and was modulated by periods between 5 and 10 cycles. From the HPC1, it appears that a sudden increase of energy in the MAM rainfall occurred for about 25 years and is then followed by a gradual decrease of energy for about 72 years. From HPC2, the gradual increase in energy appears for about 82 years and is followed by a sudden decrease of energy for about 15 years. As seen in WPC2, the sudden decrease in energy between 1982 and 1997 and the continued decrease of energy in WPC1 resulted in the complete failure of the MAM rainfall in 1984. The 25/82-year increase in energy for Kenya, Uganda and western Tanzania/eastern Tanzania, followed by the 72/15-year decrease in energy is a new finding.

This finding basically shows that the MAM rainfall undergoes a gradual increase for 82 years in eastern Tanzania area, and is then followed by a sudden and sharp decrease for about 15 years. The exact timing of decrease is not known due to the short period of the data. For the rest of East Africa, rainfall suddenly increases for about 25 years and is followed by a gradual decrease of about 72 years. Due to the short data periods, the actual period over which energy decreases occur is also not known. These findings are important and could be integral components of long-term planning of water resources utilization and development.

3.3.3.3 Frequency regimes

The spatial patterns of some periods within the 2-8-year band are shown in Figures 3.10a. Figures 3.10a shows that the 2-year cycle is more variable in southwestern Tanzania and northern Kenya, where correlations between scale WPCs and scale energy ranged between 0.1 and 0.5, while in eastern Tanzania, the variations were generally low. The 3.5-year cycle appears strong in Uganda and western Kenya, while in Tanzania; variations of rainfall due to this cycle are almost non-existent. The largest variations of the MAM scale energy were associated with the 5.6-year cycle. Correlation of between 0.1 and 0.5 were found in Uganda, Kenya and southwestern Tanzania in a spatial pattern similar to that of WPC1.

The temporal patterns of the periods shown in Figures 3.10(a)-(f) are shown in Figures3.10 (g)-(l). From these figures, periods around 2 years appear to be modulated by a background period of about 45 years. Associated with this period, energy in the 2-2.4 year cycles increased between 1900 and 1930 and 1950 to 1975 and decreased between 1930 and 1950 and 1975 to 1997. The energy associated with longer periods within the 2-8 year band, i.e. 5.6 and the 6.7-years generally show increased energy between 1900 and 1935 and decreased energy between 1940 and 1997. From Figure 3.10(k) and (i), it appears that the 5.6 and 6.7-year periods are modulated by background periods that are longer than 60 years.

The interaction of energy within the 2-8-year periods provides a new insight in the variability and predictability of the MAM rainfall. For example, power at the 2 and 5.6-year cycles, show that when there is a synchronous decrease of energy between the two periods, droughts resulted, such as in 1984 and 2000, while when power at both periods or in the 2-year is increasing, normal or above normal rainfall occurs. This finding demonstrates that with longer datasets, the effect of events associated with the 5.6-year period (e.g. El Niño) may be predicted. More details are given in Section 3.4, where a scale-by-scale analysis of wavelet power is investigated against the evolution of ENSO events. The Hilbert spectra for the MAM rainfall, for the 1900-1997 period are shown in Figure 3.11 for some selected grid stations of Eastern Africa. High concentration of energy is observed between the 2 to 3-year and 5 to 7-year periods, reaffirming the dominance of the periods around 2 and those between 5.7 and 7 years in the SAWP. Very little energy is found between 3 and 4 years. This explains the little variance of the SAWP accounted for by power associated with these periods.

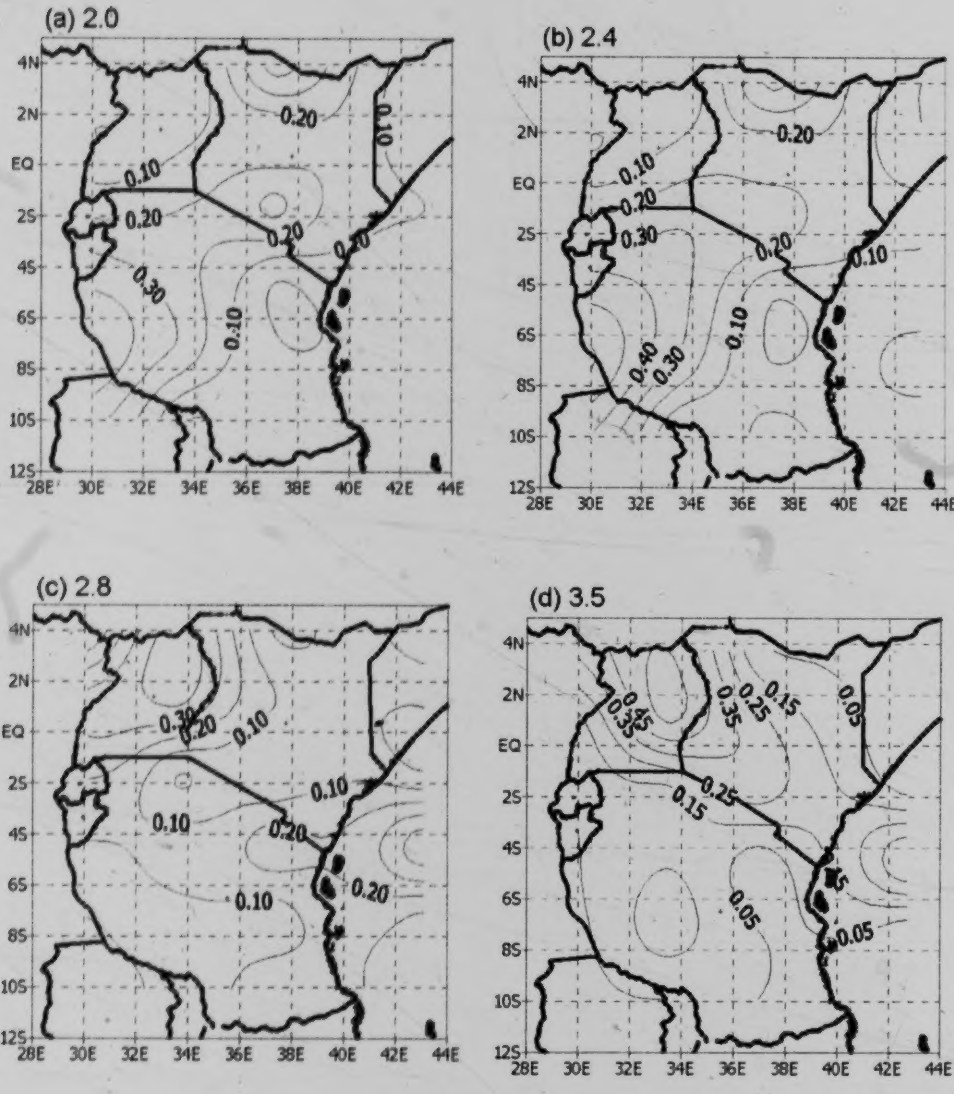
(a) 2.0
(b) 2.4
(c) 2.8
(d) 3.5
4N
2N
EQ
2S
4S
6S
8S
10S
12S
28E
30E
32E
34E
36E
38E
40E
42E
44E
0.10
0.20
0.30
0.40
0.05
0.15
0.25
0.35
0.45

Figure 3.10 The contours plotted at 0.1 intervals for the MAM rainfall showing the WPC spatial patterns of the energy at (a) the 2-year, (b) the 2.4-year (c) the 2.8-year period, (d) the 3.5-year, (e) 5.6 and (f) 6.7-years and the corresponding temporal variabilities in at (f) the 2-year, (g) the 2.4-year (h) the 2.8-year period, (i) the 3.5-year, (j) 5.6 and (k) 6.7-years.

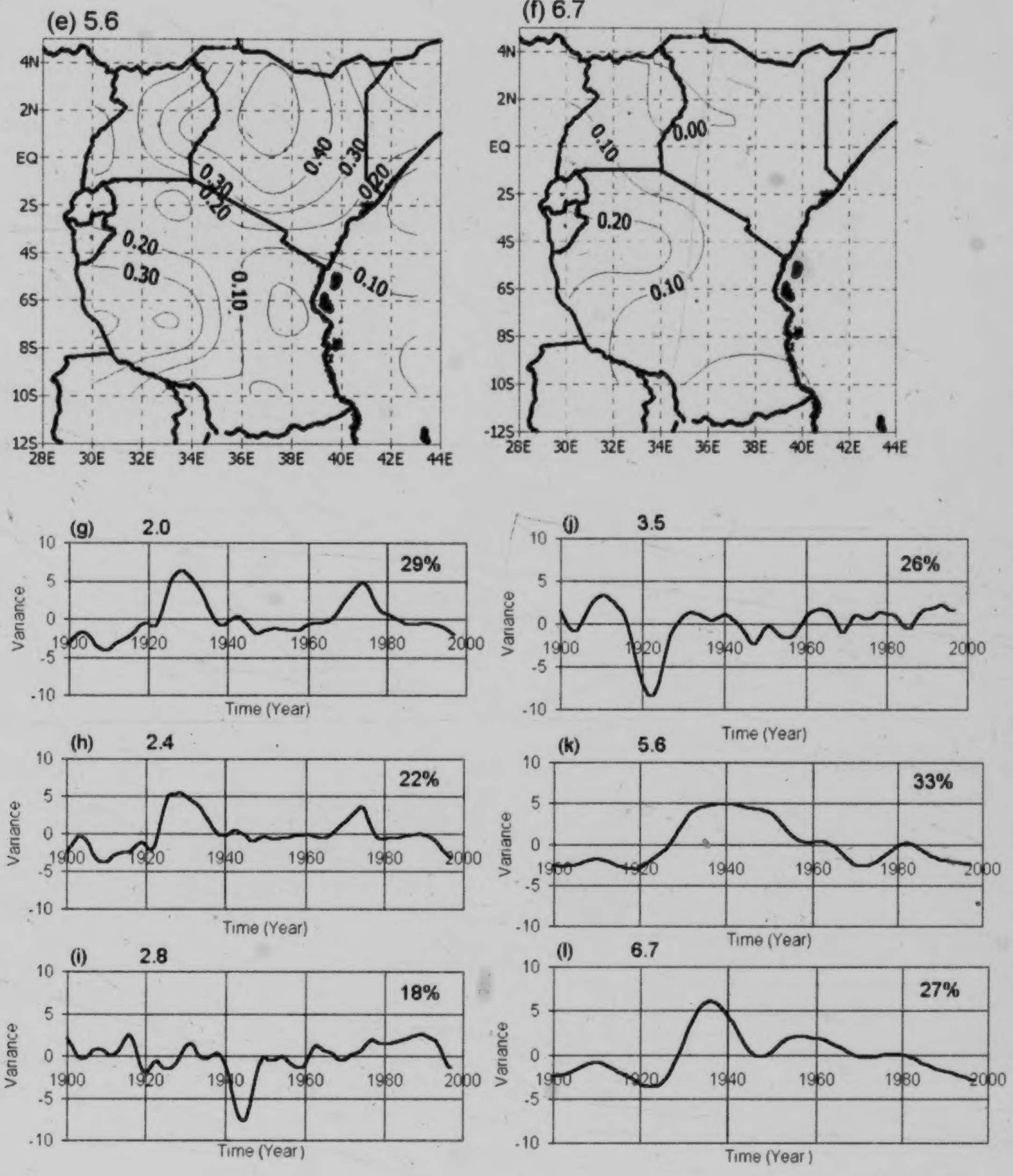

Figure 3.10 continued

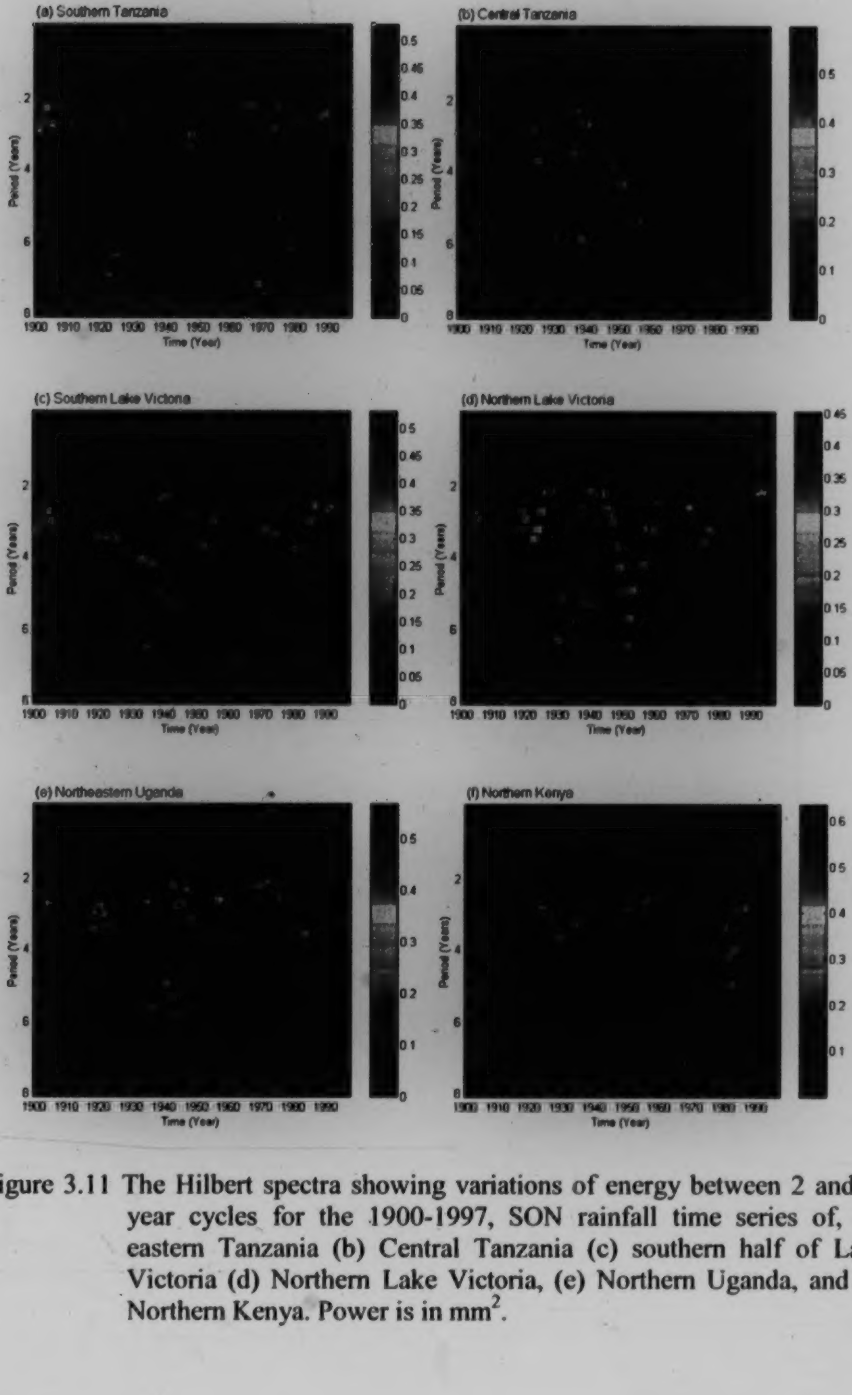

Figure 3.11 The Hilbert spectra showing variations of energy between 2 and 8-year cycles for the 1900-1997, SON rainfall time series of, (a) eastern Tanzania (b) Central Tanzania (c) southern half of Lake Victoria (d) Northern Lake Victoria, (e) Northern Uganda, and (f) Northern Kenya. Power is in mm^2.

3.3.4 Variability of Central Southern Africa (CSA) Summer Rainfall

3.3.4.1 Spatial Regimes

WEOF analysis was applied to the summer rainfall SAWP of 31 rainfall grid stations representing CSA. Two leading WPCs, which explained a combined variance of 52%, (i.e., 30% and 22% each, respectively) were retained for further analysis. Their spatial patterns are shown in Figure 3.12. The discarded WPCs mainly described SAWP variations of local features (e.g. the Zambezi River basin and the Lake Malawi basin). Since we were interested in the regional variation of SAWP and how it is related to oceanic climate predictors, the third and higher WPCs are not discussed.

WPC1 displays an out of phase relationship between the central CSA and the coastal regions along the east and west coasts. The correlation between WPC1 and SAWP in CSA is strongest in the north (36% of explained SAWP variance) and decreases southwards. Large negative correlations (64% of explained SAWP variance) between WPC1 and SAWP occur along the coastal regions of Angola. Large positive correlations are also evident over all of Zambia, Malawi, northern Zimbabwe and parts of Mozambique.

WPC2 displays an out of phase relationship that extends diagonally from the northwest to the southeast of CSA. WPC2 is positively correlated to large sections of northeastern CSA and parts of southwestern CSA and negatively correlated to SAWP of the rest of CSA. Maximum local variances explained by this mode are 64% in Zimbabwe and parts of central Mozambique and 25% in northeastern CSA.

3.3.4.2 Temporal Regimes

The temporal variability of the WPCs is shown in Figure 3.12(c) and (d). The variance of WPC1 increased between 1950 and 1970, but decreased significantly between 1971 and 1994. Since WPC1 is positively correlated to the central CSA rainfall SAWP (Zambia, Malawi, Zimbabwe and northern Mozambique), rainfall in these regions has been on the decline for over three decades (i.e. 1970-94). Since there is no snow all year round in this part of Africa, all rivers are dependent on the rainfall. Hence our results are consistent with Fanta et al., (2001), who found that streamflow generally declined between 1970 and 1997 in most rivers in eastern Angola, Zambia, and Zimbabwe. The time-domain WPCs therefore accurately represents the temporal variability of CSA rainfall.

3.3.4.3 Frequency Regimes

Figures 3.13 (a)-(d) shows the spatial patterns of the variance of CSA summer rainfall SAWP for periods of 2, 2.4, 3.4 and 5.6 years, respectively. These figures shows that the variation of power with periods around 2 years and at 5.6 years generally explain most of the variance over CSA. The 3.4-year period is dominant over the northern Namibia/southern Angola region. Figures 3.13(e) and (f) shows the corresponding time domain WPCs of the spatial patterns. Generally the periods around 2 years experienced an increase in energy between 1950 and early seventies and briefly between the mid eighties and early nineties, while the period at 5.6 years and 6.7 years experienced a general decrease of energy between 1960 and 1994 (Mwale et al., 2004).

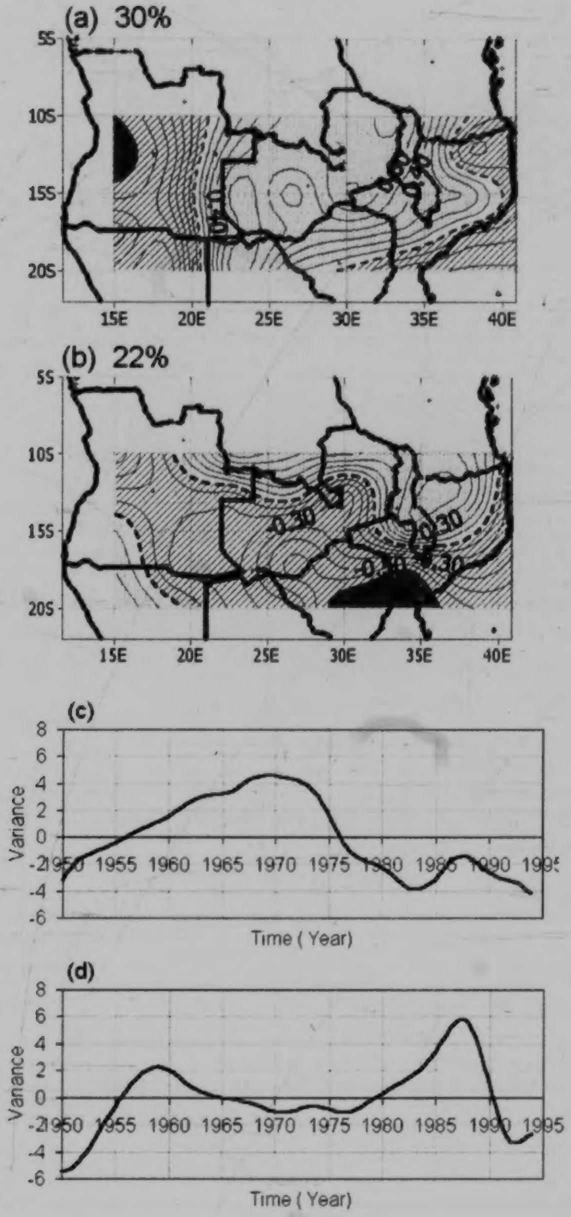

Figure 3.12 Spatial displays of the correlation between WPCs and the SAWP (a) WPC1 and (b) WPC2 of the summer rainfall of Central South Africa. Percentage values above the figures represent proportions of total variance explained by each WPC. Dotted areas represent positive correlation, while hatched areas represent negative correlation. The areas without shading represent areas with zero correlation.

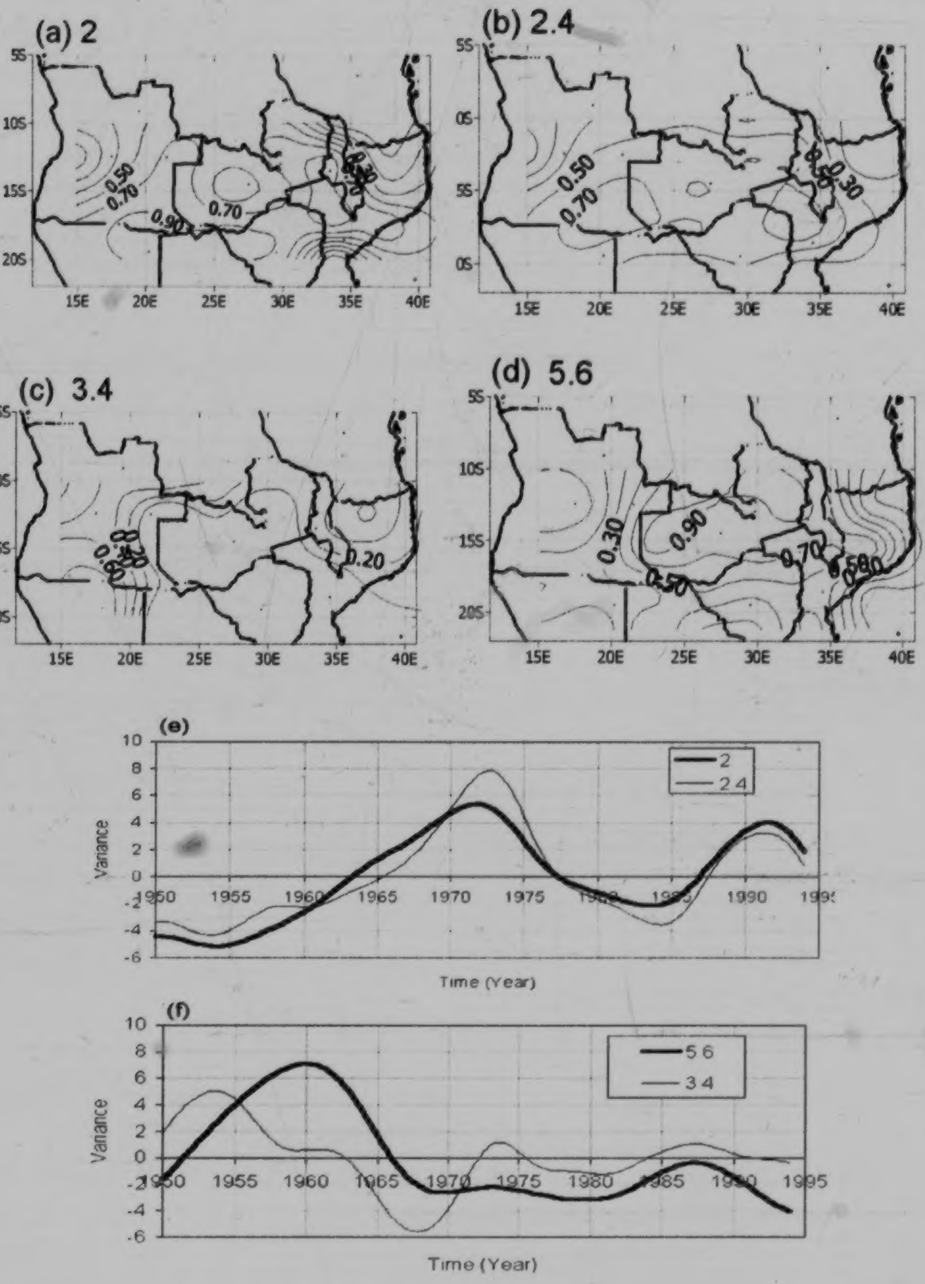

Figure 3.13 The contours plotted at 0.1 intervals showing the spatial patterns of the variance of the CSA summer rainfall SAWP explained by power at (a) the 2-year and (b) the 2.4-year, (c) 3.4-year and (d) 5.6 years and their corresponding time-domain WPCs in (e) and (f), respectively.

Correlations of 0.5 and 0.8 were found between WPC1 of CSA SAWP (Figure 3.12) and WPCs of the 2-2.4 and 5.6-6.7 year periods, respectively. This suggests that more variation in SAWP is explained by the 5.6-6.7 year periods (64%), followed by those between 2-2.4 years (25%). This shows that the 5.6-6.7 year periods provide the background variation to the 2-2.4 year periods in the rainfall of CSA

3.3.5 Variability of Southern African Summer Rainfall

3.3.5.1 Spatial Regimes

The WEOF technique was initially applied to the Southern Africa summer rainfall SAWP for the 1900-1997 period. Three leading WPCs that accounted for 44% of the total energy variance were retained for analysis. All the three modes showed a consistent spatial distribution, but with generally low locally explained variances. Individually the modes accounted for 17%, 15%, and 12% of the SAWP energy variance. Their spatial patterns are shown in Figure 3.14(a)-(c) and the temporal patterns are shown in Figs. 3.14(d)-(f). Since the WEOF decomposition appears sub-optimal (i.e., explained variances at 17%, 15%, and 12% are too close), and the temporal evolution of the modes appears to have changed between 1940 and 1997 for much of the region, (see Figs. 3.14(e) in conjunction with Fig 3.14(b)), the analysis was also done separately for the 1950-1997 period.

WPC1 shows positive correlation with SAWP in northern South Africa and to the northwest of the region (southern Angola/northern Namibia) and negative correlation over much of Southern Africa This mode accounts for only 16% in the region of largest loadings, namely, in the southern part of South Africa and elsewhere over Southern Africa, it accounts for about 1% of SAWP variance. Despite the consistent spatial distribution, the weak negative correlation between WPC1 and SAWP over much of region makes it difficult to define a concrete spatial variability of this WPC.

Except for the Cape region (32°S-35°S and 15°E-20°E), which also has winter rainfall, eastern coastal areas of South Africa and southern Malawi, Figure 3.14(b) shows that WPC2 is negatively correlated to the SAWP over the rest of the region. The strongest correlations occur in Zimbabwe, Mozambique, Botswana, Zambia and northern South Africa, where WPC2 explains between 9 and 36% of SAWP variance, with 36% of the variance explained in southern Zimbabwe.

WPC3 has a broad spatial distribution, indicated by an out of phase relationship formed by a region stretching diagonally from western half of Zambia through Zimbabwe to southern Mozambique and the coastal areas of Namibia, and South Africa. This WPC shows strong correlation with the SAWP of Zimbabwe and southern Mozambique, where 25% of the SAWP variance is explained by this WPC.

Using the 1950-1997 SAWP, two distinct leading WPCs accounting for 44% of the total energy variance were retained for analysis. The decomposition appeared stable and each of the two modes explained 27% and 17% of the total SAWP variation. Their spatial patterns are shown in Figure 3.15, and show a completely different spatial pattern from those found using the SAWP of the 1900-1997 period. The decomposition performed using the WICA method gave similar results and is not presented here.

The leading spatial mode, WPC1, shows that the variation of rainfall between countries in northern interior of Southern Africa is out of phase to the regions located south of 25ºS and areas in southern Malawi/northern Mozambique.

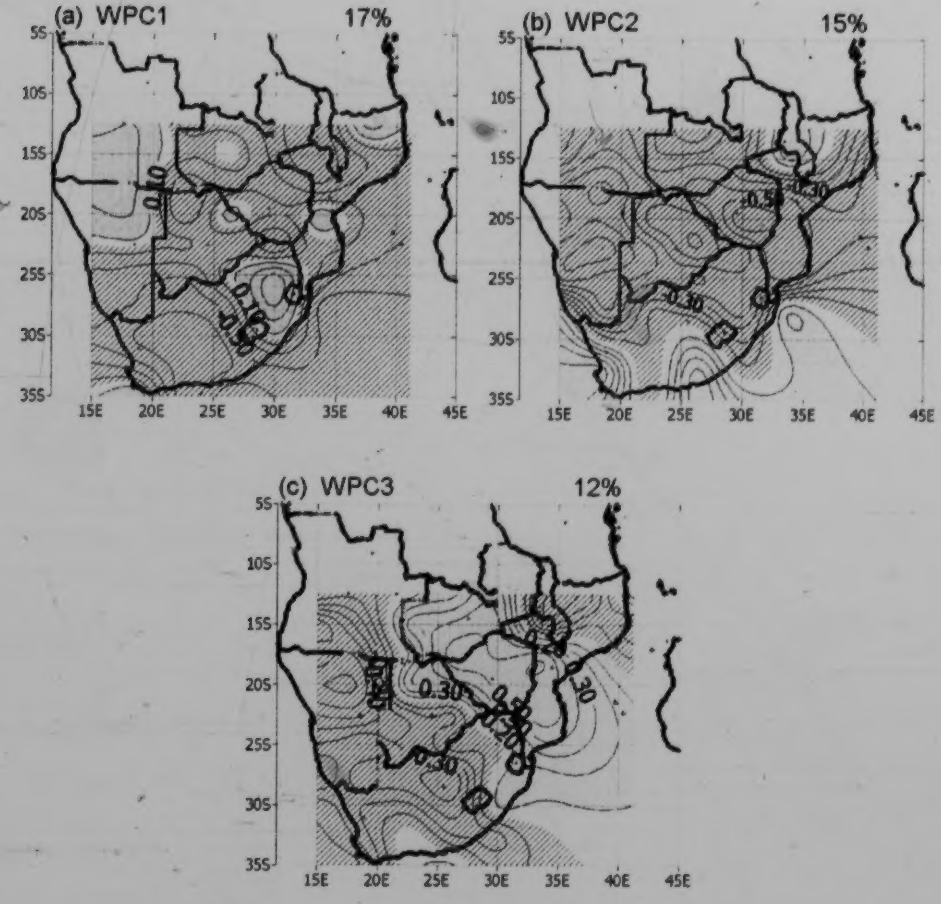
(a) WPC1
17%
0.10
0.10
0.30
(b) WPC2
15%
0.50
0.30
0.30
(c) WPC3
12%
0.30
0.30
0.20
0.30
0.30
5S
10S
15S
20S
25S
30S
35S
15E
20E
25E
30E
35E
40E
45E

Figure 3.14: The spatial patterns of the WPCs for the 1900-1997-summer rainfall, (a) WPC1 (b) WPC2 and (c) WPC3 and the corresponding temporal variabilities in (d), (e), and (f).

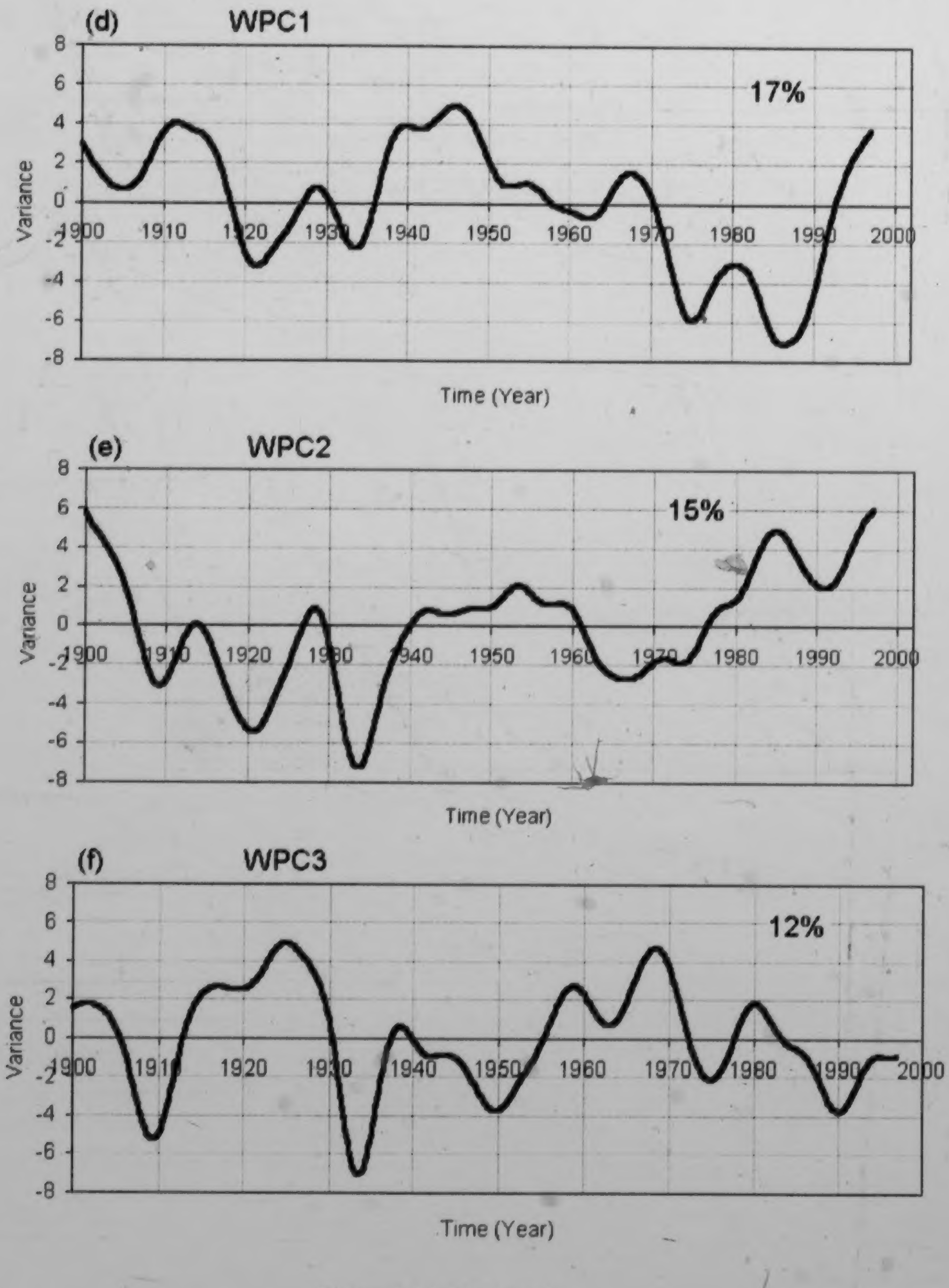

Figure 3.14 Continued.

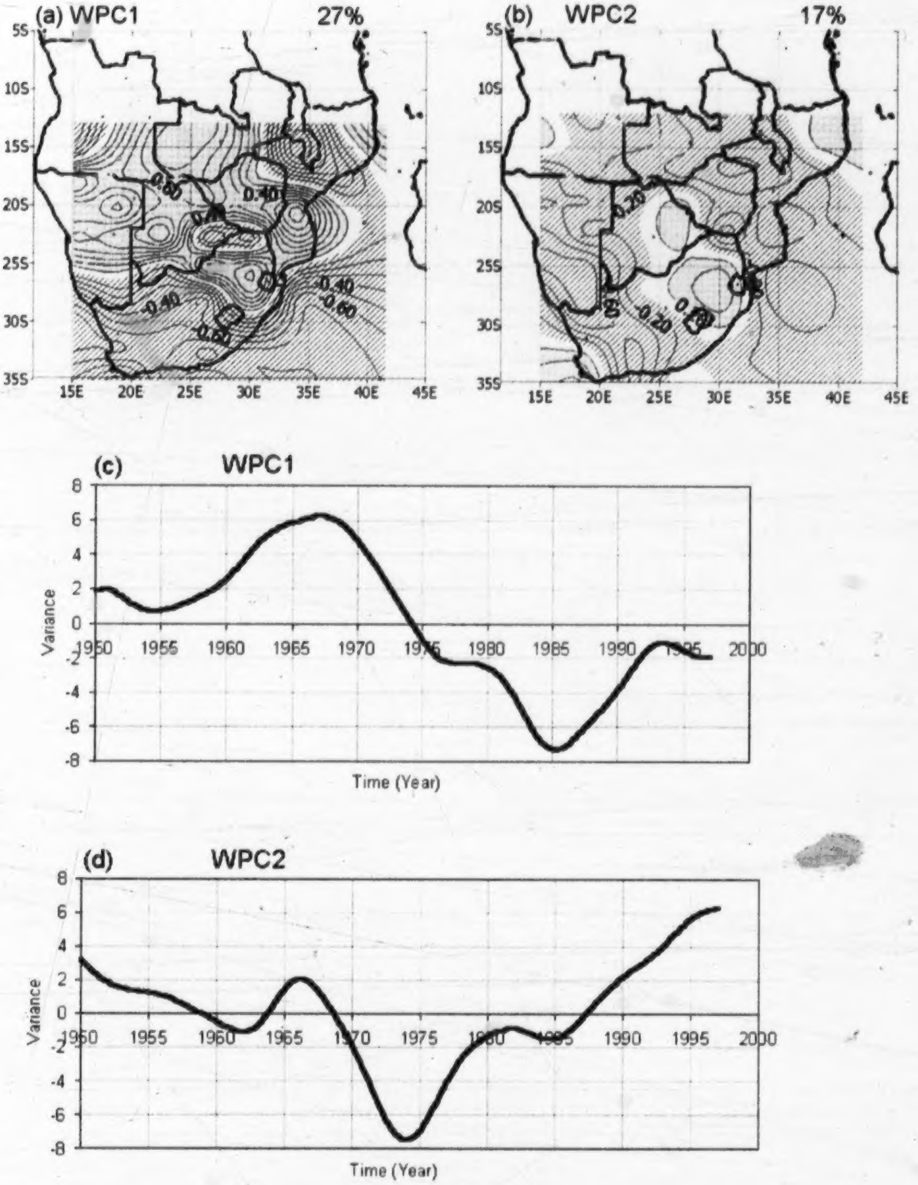

Figure 3.15 Spatial displays of the correlation between the (a) WPC1 and (b) WPC2 of the summer rainfall of southern Africa and the SAWP of individual grids. Dotted areas indicate positive correlations, while hatched areas indicate negative correlations. The blank locations indicate areas of zero correlation. Percentage values above the figures represent proportions of total variance explained by each WPC. The corresponding time domain WPCs are shown in (c) and (d).

The WPC is negatively correlated to areas south of 25°S and most areas along the east coast (southwest Indian Ocean) and Malawi but positively correlated to most of the areas north of 25°S. Strong correlations (up to 64% of explained SAWP variance) generally occur in the north, south and southeast of the region, but correlations with SAWP are weak in the interior. The 64% of explained SAWP variance in the northern part of the region is associated with variability of the Congo air mass (linked to Atlantic Ocean SST variability) and the variability of the northern Indian Ocean SST, while that in the south is associated with southern Indian Ocean SST variability or the Agulhas region (Chapter 4).

WPC2 explains part of the variation in SAWP not accounted for by WPC1. It is negatively correlated to Namibia, Angola, Zambia, Zimbabwe and Mozambique and positively correlated to northern South Africa and western Cape region, northeastern Mozambique, eastern Botswana and western Angola. This mode accounts for between 4 and 64% of the SAWP variance, with maximum loadings (64%) in southwest desert regions of Namibia.

3.3.5.2 Temporal Regimes

Figures 3.14(d)-(f) show the temporal variability of WPCs 1, 2 and 3 for the 1900-1997 period. WPC1 shows that the 1900-1997 SAWP variance was strongly regulated by quasi-20-year periods. In addition, the energy of WPC1 began to decrease after 1946 and continued until about 1985, after which the energy rose sharply until 1997. WPC2 was also regulated by quasi 20-year cycles between 1900 and 1940. After 1940, the quasi-20 year cycles vanished, changing the temporal variability of rainfall in much of Southern Africa. After 1940, WPC2 appeared with a variance of about 7-10 years and its energy generally decreased until about 1997. WPC3 displays a variation of SAWP that is largely interdecadal (about 10 to 15 years).

In South Africa, the five major drought periods occurred in 1925-33, 1944-53, 1963-1972, 1982-83 (Mason and Tyson, 2001) and 1991-1992. Since WPC1 is out of phase with the SAWP over most of the region, the drought periods appear as peaks in Figure 3.14(d). From the temporal variation of WPC2, the northern sections of Southern Africa experienced decreasing rainfall between 1934 and 1997. After 1970, Figure 3.14(e) shows that an accelerated decrease in the summer rainfall occurred in areas where the SAWP and WPC2 are positively correlated.

Fanta et al., (2001) found that some annual river flows of Southern Africa decreased between 1947 and the 1970's and others decreased further from the 1970's till about the mid-1980's, especially in Zambia, Angola, Mozambique and the High Veld (north regions) of South Africa. Although the spatial patterns of the 1900-1997 SAWP modes do not appear well organized, their temporal variations correctly represent the temporal evolution of rainfall events. Fanta et al., (2001) proposed that the most likely explanation of the reduction in streamflow was due to increased local abstractions for industrial or agricultural purposes. However, it is clear that rainfall reduction explains much of the variance in the decreasing streamflow.

Figure 3.15(c) and (d) shows the temporal variability of WPC1 and WPC2 for the 1950-1997 period. WPC1 shows an increase in power of the Southern African rainfall between 1950 and 1967 and between 1985 and 1993. The decrease in the energy of WPC1 was observed between 1968 and 1984 and after the early 1990's. WPC2 shows a general increase of energy between 1950 and 1974 and a steady decrease of energy between 1975 and 1997. Since WPC1 is positively correlated to northern areas of southern Africa, these areas experienced a relative increase of rainfall between 1950 and 1967, but a reduction in rainfall between 1968 and 1984 and after the early 1990's.

As shown in Figs. 3.15(b) and (d), WPC2 further emphasizes the localized nature of the variability of rainfall SAWP between 1950 and 1997 by suggesting that Namibia, Angola, Zambia, Zimbabwe and Mozambique all experienced an increase of rainfall between 1950 and 1973, which was followed by a consistent decrease between 1974 and 1997.

3.3.5.3 Frequency Regimes

The spatial distribution patterns of the leading modes of power extracted for the periods of 2, 5.6 and 6.7-years are shown in Figure 3.16. Inspection of Figure 3.16 and Table 3 shows that spatial variations of power at the 5.6 and 6.7-year cycles are highest, followed by those at the 2-year cycle. A comparison of Figure 3.16 and 3.15 shows that the power with a period of 5.6-year has similar spatial distribution patterns as the WPC1 of the SAWP, while the period around 2-year have spatial patterns similar to WPC2 of the SAWP. This relationship was also found between all periods between 5.6 and 8-year and the SAWP.

Figures 3.17(a) and (b) show the explained variance of SAWP by the energy at the 2 and 5.6-year periods. It is clear from these figures that the 5.6-year period explains more variance of SAWP than the power at the 2-year period. The finding shows that on a regional scale, the main mode of variation of rainfall within Southern Africa occurred following the 5.6 to 8-year periods, similar to the variability of summer and MAM rainfall of Central South and Eastern Africa, respectively. Besides the 5.6-year background power variations, the periods around 2-years were also active over the region, (i.e. areas where the WPC2 showed strong correlation with SAWP).

The temporal variations of power at 2 and 5.6-year periods are shown in Figs. 5.17(c) and (d). This figure shows that power variations peaked for the 2-year period in 1974 and declined between 1974 and 1997, while power at the 5.6-year period peaked around 1965 and declined till 1997. From these figures, it is clear that rainfall in areas north of 25°S generally declined after the mid 1960's, and the decline accelerated after 1974, while the reverse occurred for areas south of 25°S and southern Malawi.

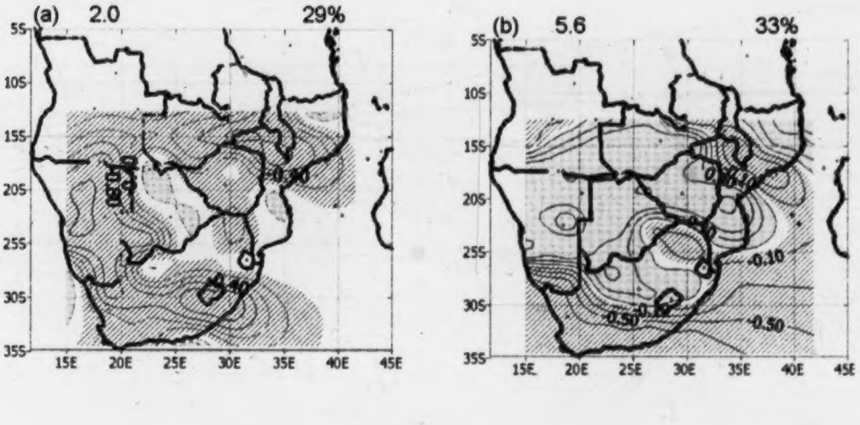

Figure 3.16 The spatial distribution pattern of power for the leading modes at (a) the 2-year and (b) 5.6-year periods for southern Africa.

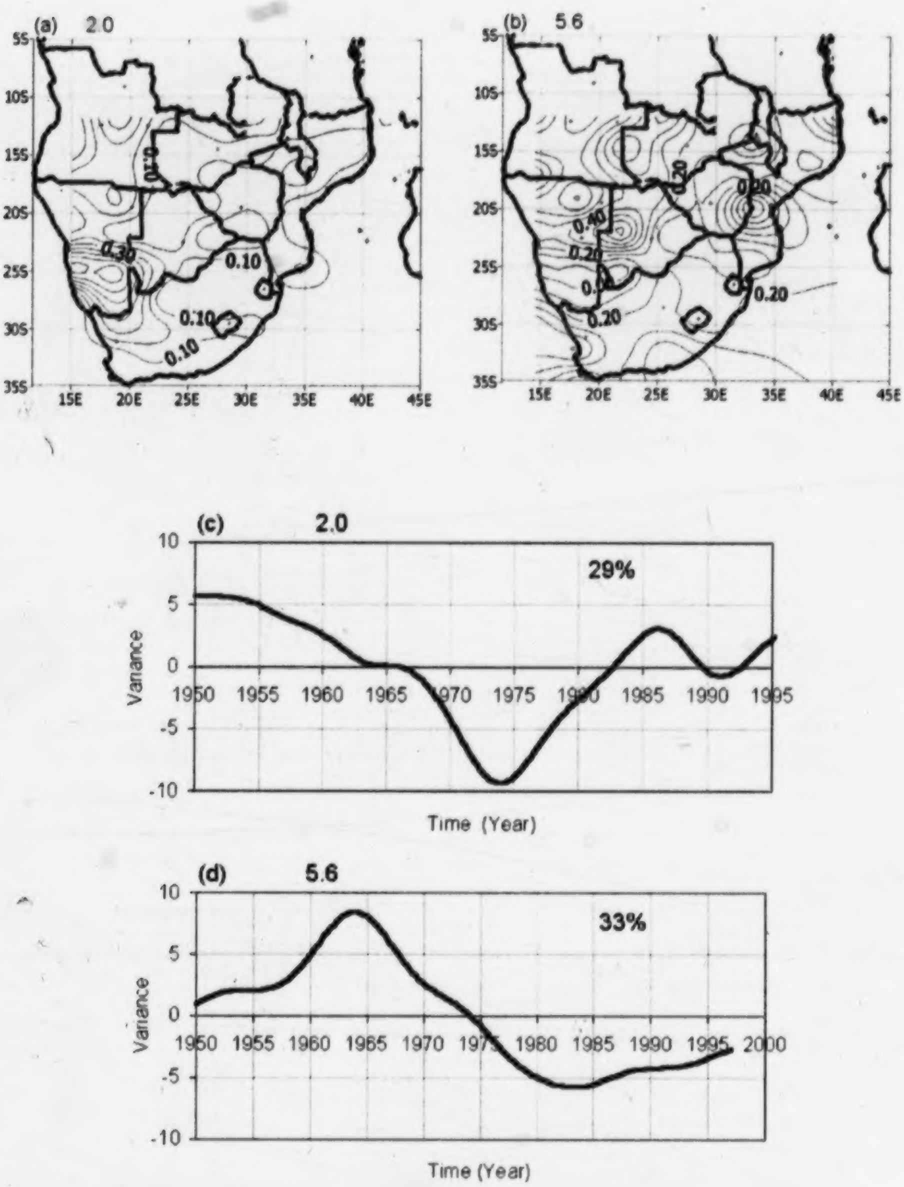

Figure 3.17 The contours plotted at 0.1 intervals showing the spatial patterns of the variance of the southern Africa summer rainfall SAWP explained by power at (a) the 2-year and (b) the 5.6-year period and the corresponding time domain WPCs in (c) and (d) respectively. The percentage values in (c) and (d) represents the variance of each scale power explained by the leading WPC.

3.3.6 Variability of the Atlantic Ocean Sea Surface Temperature

3.3.6.1 Spatial Regimes

At the annual time scale, the first two WPCs accounting for 28% and 22% of the total SAWP variance were retained for analysis, while at the seasonal time scale, only the leading WPC was retained for analysis. WPC1 explained 27% for JFM, 28% for AMJ, 27% for JAS, and 28% for OND. The spatial variability patterns of the annual WPCs are shown in Figure 3.18 and those of the seasonal WPCs are shown in Figure 3.19.

At the annual time scale, the largest WPC variations are associated with the warming and cooling of the Benguela Ocean SSTs, while the second largest variations are associated with the Brazil and the Guinea SST Ocean currents (WPC2). The annual WPC1 SST spatial variability patterns are similar to the patterns found by Venegas et al., (1997) and Houghton and Troure (1992) using observed monthly SST data.

At the seasonal time scale, the spatial variations patterns were discovered to be nonstationary throughout the year. In the OND season, the largest SAWP variations (with explained variance of up to 64%) are located along Africa's west coast. The Benguela Ocean Current SST and parts of Brazil Ocean SST form the dominant features of spatial variability for this season. During JFM season, the spatial variability patterns shifts westwards and intensify along the Equator and at about 20°S, 10°W. During this period, the Benguela Ocean Current SST appears as the only dominant feature of spatial variability. By the AMJ season, the variations cover the entire east coast of South America from 10°N to about 40°S, with maximum loadings of up to 64% along the northern Brazil coast. During this period, all the three ocean currents SST form the dominant spatial feature of variability. However, the variability of the Guinea Ocean current SST is out of phase with the rest of the Atlantic Ocean SST. In the JAS season, the spatial variability patterns begin to shift eastwards towards the Africa coastal areas, with the Benguela as the sole pattern of spatial variability.

The migration of the SAWP spatial variation patterns between South America and Africa is a new finding that has important implications for lagged and simultaneous relationships between SST in the South Atlantic Ocean and rainfall on the African and South American subcontinents.

3.3.6.2 Temporal Regimes

The WPCs for the annual and seasonal SAWP shows large variation between 1950 and 1980 followed by a relatively quiet period between 1980 and 1995, similar to the WPC1 of Central Southern Africa (see Figs. 3.4 and 3.6). SST power increased (temperatures increased) between 1950 and 1972 and was followed by a decrease (temperature decrease) between 1972 and 1980. WPC2 is less variable than WPC1 and shows increasing power from 1969 to1984 with a decrease that begun in 1985 until 1995.

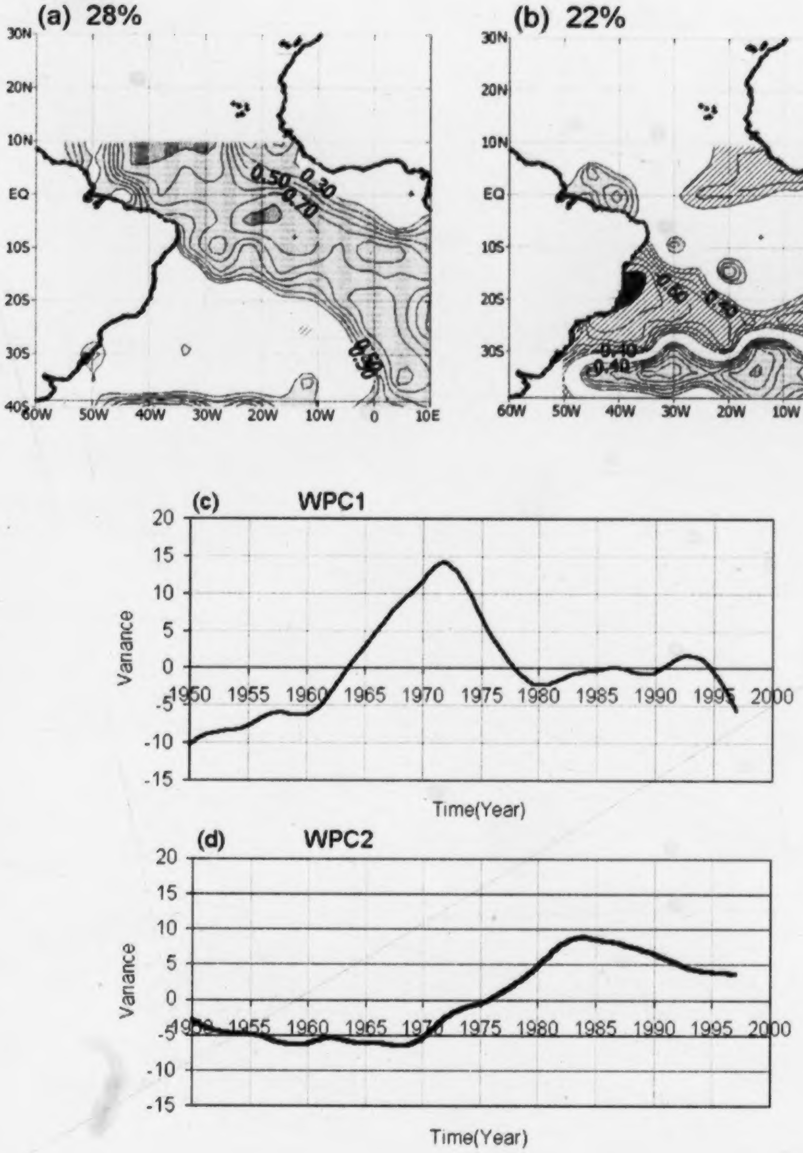

Figure 3.18 Contour plots of the spatial correlation patterns between, (a) WPC1, and (b) WPC2, of annual Atlantic Ocean SST and SAWP of individual grids at 0.1 contour intervals. The numbers shown above represent the percentage (%) of the total variance explained by each WPC. The dark areas correspond to correlations significant at the 95% confidence level. The temporal variations of the two WPCs of Atlantic Ocean SST are shown in (c) and (d).

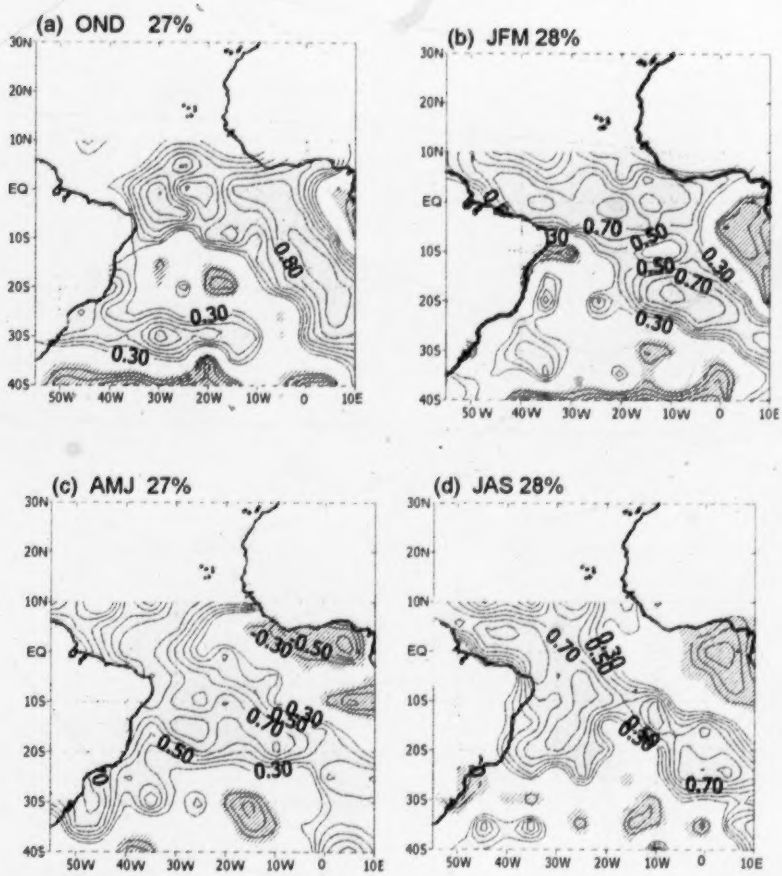
(a) OND 27%
(b) JFM 28%
(c) AMJ 27%
(d) JAS 28%
30N
20N
10N
EQ
10S
20S
30S
40S
50W
40W
30W
20W
10W
0
10E
0.80
0.30
0.70
0.50

Figure 3.19 Contour plots of the spatial correlation patterns between WPC1 of seasonal Atlantic Ocean SST and SAWP of individual grids at 0.1 contour intervals for the, (a) October-December (OND), (b) January-March (JFM), (c) April-June (AMJ), and (d) July-September (JAS) seasons. The seasonal migration of spatial variability patterns of SST can be seen from (a) to (d). The corresponding temporal variabilities are shown in (e), (f), (g) and (h). The numbers shown above represent the percentage (%) of the total variance explained by each WPC1.

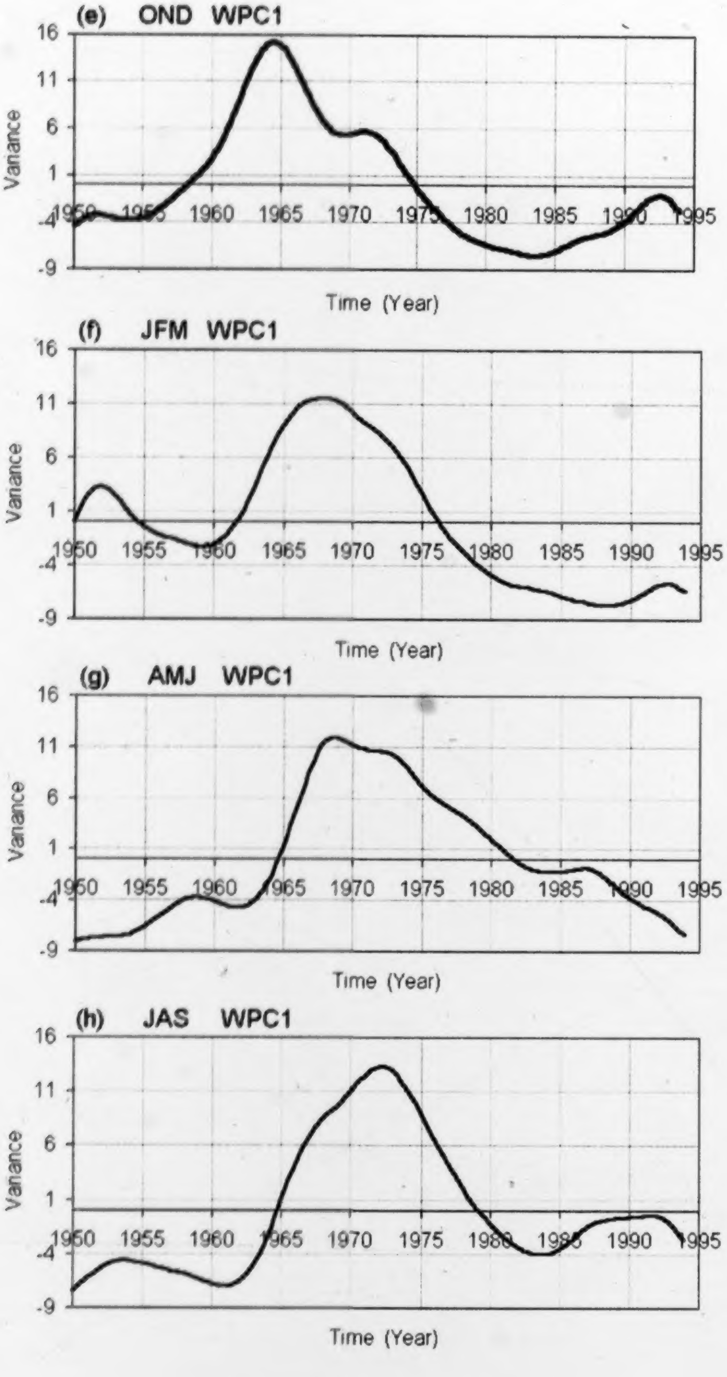

Figure 3.19 Continued

3.3.6.3 Frequency Regimes

The spatial patterns of WPC1 extracted for the periods of 2 and 5.6 (generally representing 2-2.4 and 5-6.7 year periods respectively) are shown in Figure 3.20. Inspection of this figure shows that spatial variation of power at both periods occurs almost everywhere in the Ocean. Generally power at the 5.6-year period shows much higher spatial variability than the power at the 2.0-year period.

The 2-year period explains more variation (64%) to an area covering the Atlantic Ocean, situated northeast of Brazil. Elsewhere, explained variance ranges from 4 to 36%. The Atlantic Ocean portion, located northeast of Brazil, is made up of Mason's (1995) PC1 (17%) and PC3 (11%), which were also found to have periods around 2-years, in addition to other periods (3.6, 9.6, 12.5, 14.4 and 21.9-years). In this region the warming and cooling of the Benguela Ocean SST extends far westwards along the Equator (Mason 1995).

The spatial pattern shown by the 5.6-year period encompasses the entire region of the Atlantic Ocean described by Mason's (1995) PC 1(17%), PC3 (11%), PC5 (7%) and PC6 (7%), which were found to have dominant periods of between 2 and 8 years. Local variance of up to 64% is explained over a wide area of the Atlantic Ocean by the leading mode of the 5.6-year period in a fashion similar to WPC1 of the SST SAWP (dotted area in Figure 3.20). The presence of variance associated with the 5.6-year period points to the occurrence of Atlantic Ocean events similar to El Niño and clearly shows that the periods around 5.6-year provide the background oscillation of all periods in the 2 to 8-year range.

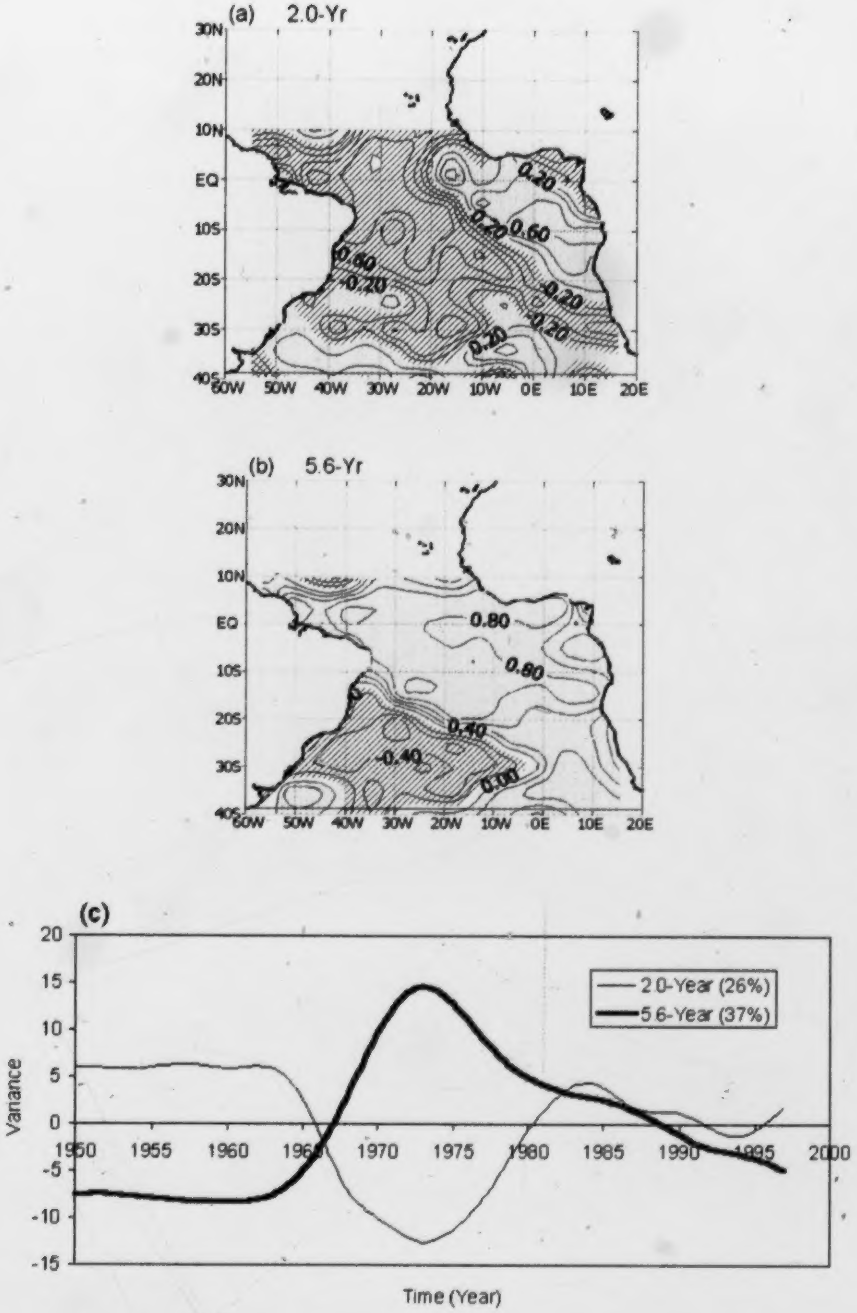

Figure 3.20. The spatial and temporal patterns of energy at the 2 and 5.6-year periods of the Atlantic Ocean: (a) 2-year period, (b) 5.6-year periods, and (c) the temporal models.

Warming events in the Benguela and Peru currents have been noted to occur concurrently, although the Benguela Ocean currents occur less frequently (Walker 1987). This clearly points to the occurrence of what has been termed as "El Niño-like" events in the Atlantic Ocean. The temporal variations of power at 2 and 5.6-year periods shown in Figs. 5.20 show that power variations peaked for both periods around 1974 and declined between 1974 and 1997.

3.3.7 Variability of Indian Ocean Sea Surface Temperatures

3.3.7.1 Spatial Regimes

WEOF analysis of the annual SAWP of the Indian Ocean SST revealed two leading WPCs, which explained 28% and 20% of the total SAWP variance, which were not much different from the leading modes of the South Atlantic Ocean SST. Their spatial variability patterns are shown in Figure 3.21. At the seasonal time scale, WPC1 explained 26% for the OND season, 35% for the JFM season, 23% for the AMJ season and 29% for the JAS season. The JFM season is clearly the most variable of all the four seasons and the AMJ season is the least variable. Unlike the Atlantic Ocean, the Indian Ocean seasonal spatial variability patterns appear stationary in space for the study period. As for the Atlantic Ocean SST, the WPC2 for each season was not spatially extensive and its spatial correlation patterns explained very little variance. Thus the WPC2 at the seasonal time scale is not discussed.

WPC1 mainly describes variation of SAWP of the northern Indian Ocean SST. It is positively correlated to SST SAWP of the northern Indian Ocean and negatively but weakly correlated to the southern Indian Ocean SST SAWP. Maximum variations of between 50%-64% are accounted for by this WPC in the central and western Indian Ocean SST. WPC2 describes the remainder of the variance in the south Indian Ocean SST SAWP not accounted for by WPC1. It is positively correlated to south Indian Ocean SST SAWP (extending from 40°E to 105°E) and negatively correlated but weakly to the northern Indian Ocean SST SAWP. This WPC appears as a part of Mason's (1995) PC2 (13%), which Mason attributed to warming and cooling of the Mozambique Channel current and Agulhas system.

At seasonal time scales, the northern Indian Ocean appeared as the main mode of spatial variability for OND, JFM and JAS seasons (see Figure 3.22). The southern Indian Ocean SST appears as a dominant spatial regime only during the AMJ season. This means that the largest contribution to WPC1 of Indian Ocean SST is from the three seasons (OND, JFM, and JAS). The AMJ season contributes more to the variation of WPC2.

3.3.7.2 Temporal Regimes

The WPCs for the annual SAWP (Figure 3.21(c)) shows that SST in the northern Indian Ocean increased from 1960 to 1990 and decreased after that, while that of the southern Indian Ocean increased from 1950 to 1968 and decreased between 1970 and 1997. The seasonal WPC time series are shown in Figs. 3.22 (e)-(h). The WPCs (Figs. 3.22(a) and (b)) show that SST peaked for OND and JFM season in about 1971/2 but similar changes were observed in the AMJ season in 1975 and for the JAS season in 1987.

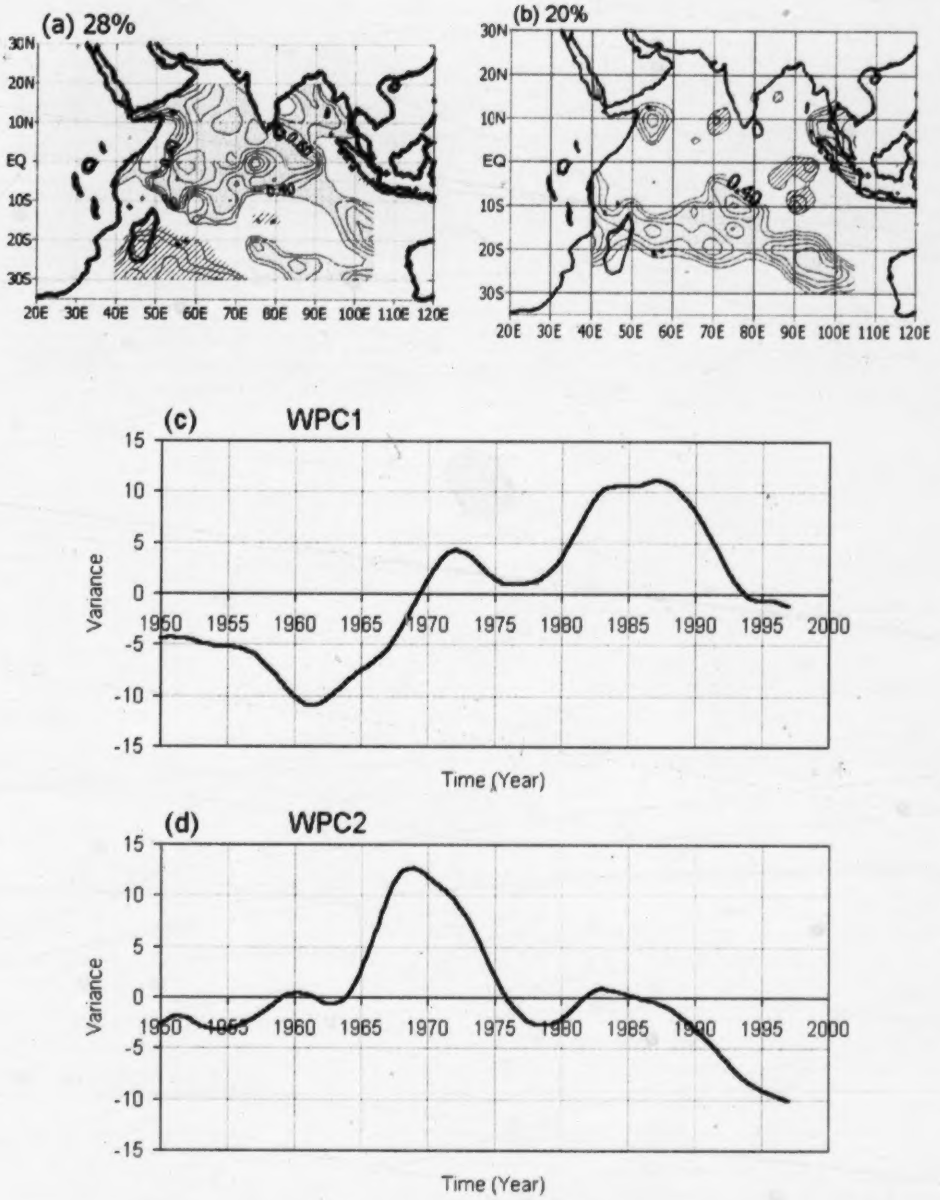

Figure 3.21 Contour plots of the spatial correlation patterns between, (a) WPC1, and (b) WPC2, of annual Indian Ocean SST and SAWP of individual grids at 0.1 contour intervals. The numbers shown above represent the percentage (%) of the total variance explained by each WPC. The temporal variations of the two WPCs of the Indian Ocean SST are shown in (c) and (d), respectively.

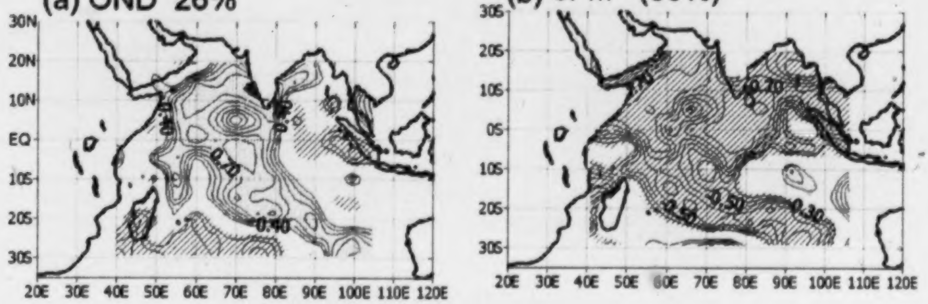
(a) OND 26%

(b) JFM (35%)

30N
20N
10N
EQ
10S
20S
30S
0.70
0.40
20E 30E 40E 50E 60E 70E 80E 90E 100E 110E 120E
30S
20S
10S
0S
10S
20S
30S
0.70
0.50
0.30
20E 30E 40E 50E 60E 70E 80E 90E 100E 110E 120E

(c) AMJ 23%

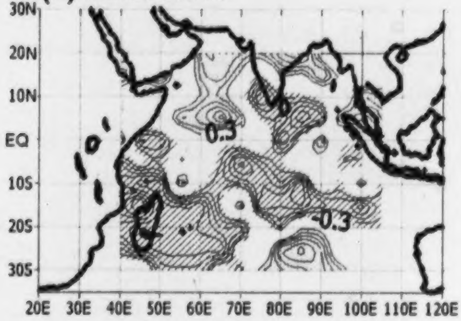
30N
20N
10N
EQ
10S
20S
30S
0.3
-0.3
20E 30E 40E 50E 60E 70E 80E 90E 100E 110E 120E

(d) JAS 29%

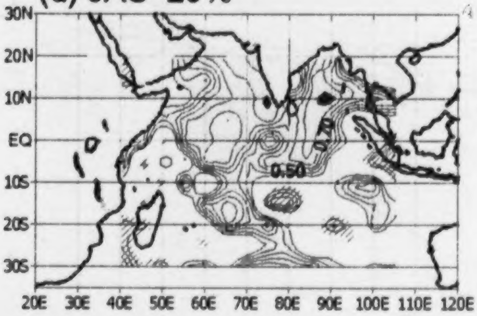
30N
20N
10N
EQ
10S
20S
30S
0.50
20E 30E 40E 50E 60E 70E 80E 90E 100E 110E 120E

Figure 3.22 Contour plots of the spatial correlation patterns between WPC1 of seasonal Indian Ocean SST and SAWP of individual grids at 0.1 contour intervals for the, (a) October-December (OND), (b) January-March (JFM), (c) April-June (AMJ), and (d) July-September (JAS) seasons. The numbers shown above represent the percentage (%) of the total variance explained by each WPC1. Correlations between 0 and 0.2 are not included in the spatial patterns.

(e) OND

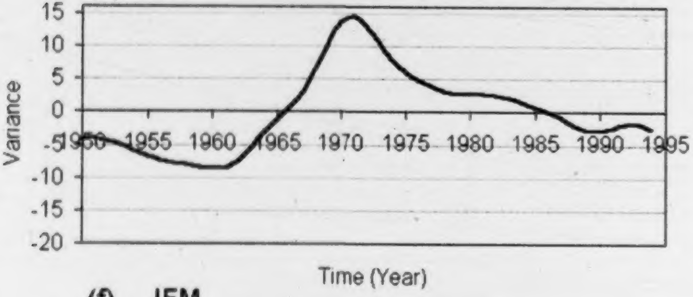

(f) JFM

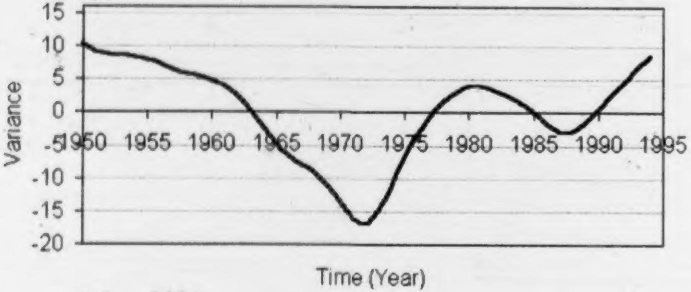

(g) AMJ

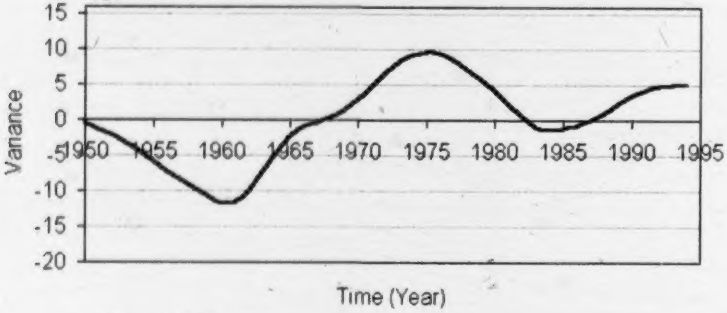

(h) JAS

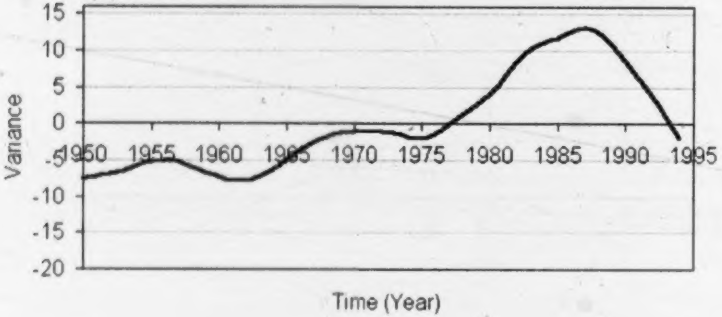

Figure 3.22 continued

3.3.7.3 Frequency Regimes

The spatial patterns corresponding to the periods of 2 and 5.6-years, which are also representative of the periods 2 to 2.4-years and 5 to 6.7-years, are shown in Figure 3.23. As was the case with the Atlantic Ocean, the variance of energy associated with the 5.6-year period is higher than that of the 2-year period. Although both periods cover the entire Indian Ocean, the spatial patterns associated with the 5.6-year period are much more coherent over wide areas of the ocean than the 2-year period.

The 2-year spatial pattern appears out of phase between the western (specifically northwest and southwest) portion of the Indian Ocean and the central portion of the Indian Ocean. Weak positive correlations are also observed to the east of the Indian Ocean. The variance of the 2-year is strongest in the northwest and southwest corners of the Indian Ocean, with up to 36% of the local variance accounted for by the leading mode. This region was also seen to have strong 850 hPa winds associated with the Monsoon (see Figure 3.1). This region is also made up of part of Mason's (1995) PC2 (13%) and PC4 (7.5%), which he found to have periods of 2.7 and 5.2 years, respectively.

The spatial pattern associated with the 5.6-year period appears almost everywhere in the Indian Ocean. The leading mode is positively correlated to the north and east, and negatively but weakly correlated to the south. The highest variance accounted for by the leading mode explains between 16 and 64% of variance in the northern sections as well as the eastern portion of the Indian Ocean. In the south, local variance of between 16 and 36% is explained by this period. The presence of the 5.6-year period corresponds to the 5-6 year period found by Nicholson and Entekhabi (1987), along the east coast of southern Africa and is associated with the Southern Oscillation.

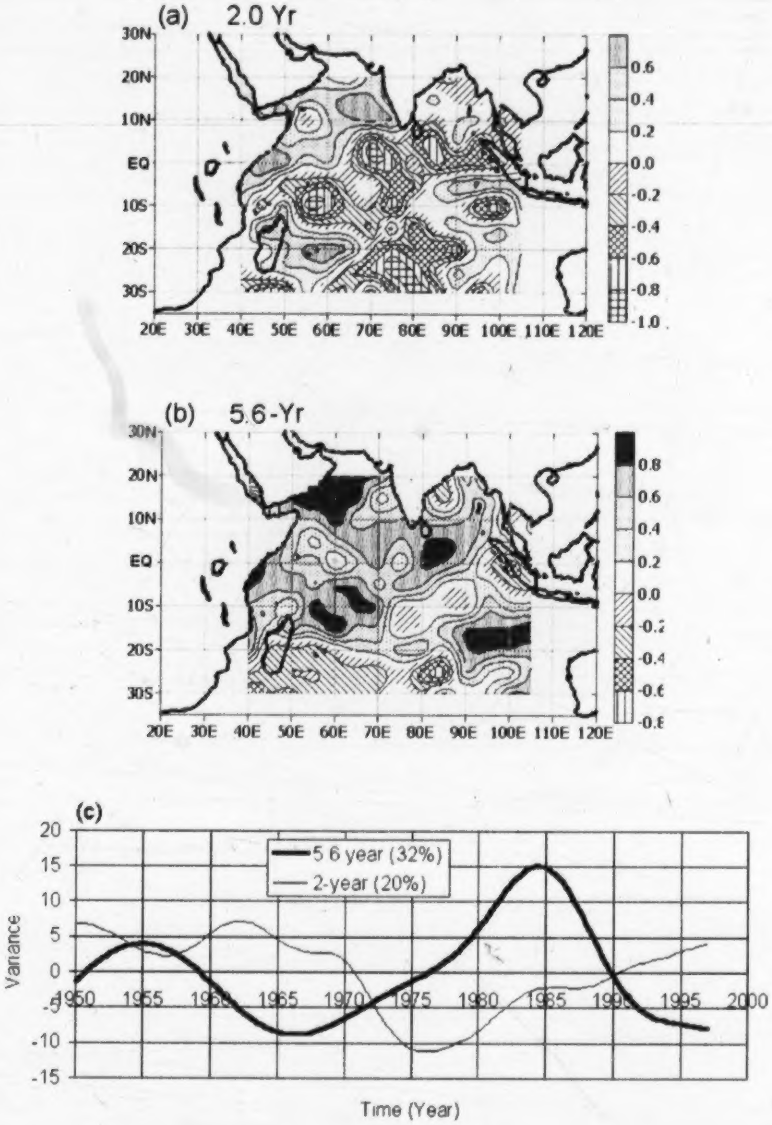

Figure 3.23. The spatial and temporal patterns of energy at the 2 and 5.6-year periods of the Indian Ocean, (a) 2-year period, (b) 5.6-year period, and (c) the temporal models.

3.4 ENSO impacts on Rainfall Variability via Space-Time analysis of Scale Energy.

3.4.1 Introduction

The objective of this section is to examine how the spatial and temporal variability of rainfall of Eastern, Central South and Southern Africa responded to El Nino-Southern Oscillation (ENSO) signals during the 1900-1997 and 1950-1997 periods by examining the interaction of energy variations at various scales within the 2-8-year spectral band. The return period of El Nino ranges from 3 to 7 years. Since this is the same range of periods over which the spatial, temporal and frequency variability of the rainfall and SST has been analyzed, it will be of interest to see how the occurrence of these events affected the temporal and spatial variability of the rainfall in these regions.

El Nino often begins early in the year and peaks between November and January. Hence all the rainfall seasons in Eastern, Central South and Southern Africa should be affected during times of ENSO events. It is widely known that ENSO events cause widespread droughts in eastern and southern Africa (Lindesay 1988; Nicholson and Entekhabi, 1987; Nicholson et al., 2001). This is because the persistent low-pressure belts in the Western Pacific and equally persistent high-pressure belts over the Eastern Pacific, weakens the trade wind belt that is responsible for rainfall over Eastern and Southern Africa. Hence during early summer the low pressure troughs that form diagonally (Northwest-Southeast orientation) over Southern Africa are displaced eastwards towards the Mozambique Channel, moisture advection due to

SE trade winds over the Indian Ocean is curtailed, the ITCZ is displaced further north and the wind and moisture transport is offshore.

Between 1900 and 1997, ENSO episodes occurred 22 times (see Table 3.1). Of these events ten occurred between 1900 and 1950 and twelve occurred between 1950 and 1997. From Table 3.2, it is clear that droughts occurred in East Africa during non-ENSO years (e.g. 1900, 1949, 1979 and 1984) and above average rainfall occurred during ENSO years (e.g., all thirteen ENSO years between 1902 and 1957). For Central South and Southern Africa, all the ENSO events prior to 1970 had little or no effect on rainfall compared to the events in the post 1970 period (Richard et al., 2000). In the next few sections, we examine the interaction of energy among the 2 to 8-year scales of rainfall and see the response of rainfall to ENSO events.

3.4.2 East Africa SON Rainfall.

All the power within the 2 to 8-year periods experienced a general increase in the energy between 1900 and 1960, followed by a decrease of energy between 1962 and 1997 (see Figs 3.5 of Section 3.3.2.3). Since the periods around 2-years were dominant in the SON rainfall SAWP, consistent increase of energy in the 2-year cycle offset all the ENSO events between 1900 and 1950. However, ENSO events of 1965, 1977 1987 and 1997 could not be suppressed because the energy associated with all scales was on the decrease during this time. Hence droughts due to ENSO were severe during 1955-1997.

3.4.3 East Africa MAM rainfall

Figure 3.10 of Section 3.3.3.3 showed that the MAM rainfall of East Africa was dominated by the periods around 5.6 years, which have a spatial variability that is similar to the WPC1 of the MAM rainfall SAWP, followed by periods around 2-year.

Table 3.1 ENSO years between 1900 and 1997.

1902	1905	1911	1914	1918	1923	1925	1930	1932	1939
1951	1953	1957	1963	1965	1969	1972	1977	1982	1987
1991	1994								

Table 3.2 Major drought episodes in East Africa in the 20th century[1].

1899	1900	1949[a]	1965	1967	1971	1977	1979	1984[b]	1987
1988[c]	1990[d]	1991[e]	1992[f]	1996[g]	1997[h]				

[1] Ntale (2001)

[a] 1.5 million cattle died or where hastily slaughtered out of 2.5 million.

[b] 600,000 people where affected.

[c] 600,000 people affected, poor seasonal rainfall.

[d] 1.2 million people affected, worst crop in 10 years.

[e] 2.7 million people affected, worst drought in 50 years.

[f] Continuing drought.

[g,h] Worst drought in Tanzania, cities face major water shortages.

Between 1900 and 1920 and 1960 and 1970, the 2-year period experienced an increase in energy, while decreasing energy was dominant during the periods 1930-50 and 1970-97. On the other hand, the 5.6-year cycle experienced increasing energy between 1920 and 1955 and decreasing energy between 1955 and 1997. Since the 5.6-year cycle is associated with ENSO events, the decrease in energy in the period 1955-97 should theoretically have been associated with droughts. However, energy associated with the 2-year period increased between 1960 and 1970. This increase apparently offset any effects ENSO would have had on the rainfall. The synchronous decrease of energy in the 2 and 5.6-year period, between 1980 and 1997 explains the complete failure of the MAM rainfall in 1984 and the increased severity of the droughts during this period.

Between 1980 and 1997 energy at all periods in the 2-8-year band declined for both the SON and MAM rainfall. This 1984 failure of the MAM rainfall caused the worst drought in Kenya in 40 years (Ntale 2001). The 1990 droughts affected 1.2 million people, while the 1992 drought affected 2.7 million people (Ntale 2001). In 1996 the worst drought in 50 years was recorded in Eastern Africa and major cities begun to face water shortages (Ntale 2001; Ntale and Gan 2004). The above findings show that not all ENSO events have the same effect on the rainfall of East Africa. During periods when rainfall energy at the 2-year cycle is on the increase, ENSO events probably have very little or no effect on the East Africa rainfall, while when there is synchronous decrease of rainfall energy in the periods around 2-years and others around 5.6 years, droughts are more prevalent and pronounced.

3.4.4 Central South and Southern Africa Summer Rainfall

The spatial and temporal variability of summer rainfall at 2 and 5.6 years is shown Fig 3.17. These figures revealed that the dominant periods in rainfall of Central South and Southern Africa summer rainfall were periods between 5.6 and 8-years, followed by the 2-year cycle, similar to the MAM rainfall of East Africa. Figure 3.17 shows a consistent increase in the energy of the 2.0-year period, between 1950 and the early 1970's, followed by a consistent decrease of energy between the early 1970's and the late 1990's. Energy at the 5.6-year and other longer periods also increased between 1950 and 1965 and decreased between 1965 and 1997.

Similar to the MAM season of East Africa, the WPCs appear to show that when the 2-year energy is increasing, while the 5.6-8 year energy is decreasing ENSO has little effect on the Central South and Southern Africa rainfall. However, when the energy at the lower and higher scales is decreasing at the same time, ENSO causes droughts to occur in the region.

Richard et al., (2000) also found that pre-1970 ENSO events had little effect on the Southern Africa climate conditions and atmospheric circulation, while the ENSO events after 1970 were characterized by reduced rainfall. Our results confirm their findings.

3.5 Summary of Findings

Wavelet analysis, EMD-Hilbert transformations, Wavelet empirical orthogonal function (WEOF) and EMD-Hilbert empirical orthogonal function (HEOF), and Wavelet Independent Correlation analysis (WICA) were applied to rainfall and sea surface temperature energy within the 2 to 8 year periods to identify and analyze the dominant spatial, temporal and frequency regimes of rainfall of East Africa, Central South and greater Southern Africa and sea surface temperature variability of the South Atlantic and Indian Oceans.

WEOF of SAWP found that excluding areas of extreme altitude such as the Great Rift Valley and Mt Kilimanjaro, the spatial variability of East Africa SON rainfall was homogenous over the region. WEOF of individual scale power found that the variability of the SON rainfall was dominated by energy associated with periods around 2 years. The variability explained by periods higher than 3 years gradually decreased, as the periods got longer. The WPCs and the Hilbert spectrum for SON rainfall found that strong period modulation of between 8 and 25 years occurred throughout the 1900-1997 period. The intense 2 to 8 year periods and the 8 to 25 year periods are all equally modulated by an even longer period of about 50 to 60 years. The leading mode of variability (WPC1) was found to accurately represent the temporal variability of SON rainfall, identifying years of normal rainfall, floods and droughts. Consistent with a 50 to 60 year cycle, power in the rainfall increased between 1900 and 1960 and consistently decreased between 1962 and 1997, contributing to abundant rainfall in the period prior to 1962 and numerous drought during the post 1962 period.

ENSO was found to affect the SON rainfall when the energy in the SON rainfall at periods around 2 year was decreasing.

For the MAM rainfall of East Africa, WEOF and WICA of SAWP identified the rainfall of eastern Tanzania as being out of phase with the rainfall of the rest of the region. Compared to the SON rainfall, the spatial variability pattern of the MAM rainfall was weaker. WEOF of individual scale power found that the variability of the MAM rainfall was dominated by energy associated with periods of 5.6 years, followed by periods around 2 years. Both leading WPCs showed an 70-80-year cycle modulating interdecadal periods. The power in WPC1 was found to have decreased from 1920 until the end of the data period in 1997, while that of WPC2 was found to have experienced an increase between 1900 and 1980 and decrease between 1980 and 1997. The leading modes of variability were also found to accurately represent the temporal variability of MAM rainfall.

ENSO was found to affect the MAM rainfall when energy at the 2 and 5.6-years in the rainfall synchronously decreased.

WEOF of the Central South and greater Southern Africa rainfall summer rainfall SAWP revealed that the interior of the region was out of phase with the coastal areas and lakes Malawi region. WEOF of individual scale power found that the variability of the summer rainfall was dominated by energy associated with periods around between 5.6 and 8 years, followed by energy of the periods around 2 years. The WPCs and the Hilbert spectrum for the summer rainfall also found strong period modulation of between 8 and 25 years during the 1950-1995 period. The rainfall decrease especially between 1974 and 1997 was found to be consistent with the corresponding decrease in streamflow of rivers and dams in Namibia, Angola, Zimbabwe, Zambia, parts of Mozambique and the Veld belt of northern South Africa.

ENSO was found to be more effective during the post 1970 period. However, ENSO only caused droughts when a synchronized energy decrease of the Southern Africa rainfall energy occurred at all scales between 2 and 8 years.

WEOF of the South Atlantic Ocean sea surface temperature (SST) at the seasonal time scales found spatial variabilities that were nonstationary. The spatial patterns were found to migrate seasonally between Africa's west coast and South America east coast. Throughout the dominant spatial pattern of variability was found to be the Benguela, Brazil and the Guinea Ocean currents. The Brazil and Benguela Ocean current SSTs were found to be out of phase with the Guinea Ocean current SSTs. Each of the leading modes of spatial variability was found to explain about 27% of total seasonal power variability, suggesting that for this ocean basin, each season contributed equally to the annual variation. The time domain WPCs showed that an increase in temperature occurred between 1950 and the mid 1960's to early 1970's and the energy declined after the 1970's.

At the annual scale the Benguela Ocean current was found to form the main mode of variability and the Brazil and Guinea Ocean current SST form the second leading spatial patterns of variability of the Atlantic Ocean. Time domain WPC1 and WPC2 show that Benguela and Brazil Ocean current SST experienced an increase between 1950 and late 1960's and a decrease between 1972 and 1997.

WEOF of the Indian Ocean SST showed that, except for the AMJ season, both the annual and the rest of the seasons, the northern Indian Ocean SST formed the dominant spatial variability pattern. The south Indian Ocean SST was found to form the dominant spatial variability pattern during the AMJ season.

CHAPTER 4

ASSOCIATION BETWEEN RAINFALL WPCs AND THE SST SAWP

4.1 Introduction

Several previous studies have examined and found relationships between rainfall in Eastern Africa (EA) and Southern Africa (SA) and sea surface temperatures (SST) of the Indian, Atlantic and Pacific Oceans (e.g., Mutai et al., 1998; Ntale et al., 2003; Mason, 1995; Jury, 1996). As alluded-to in Chapter 1, for SA, the majority of these studies found rainfall-SST relationships for small geographical areas, while some relationships were found using regionalized rainfall indices, thereby ignoring the spatial variability inherent in the complex spatial patterns of rainfall. Chapter 1 also suggested that one of the biggest problems encountered in climate prediction is that most of the predictor datasets have very small signal to noise (S/N) ratios. The noise found in the predictor data compromises the prediction skill of most of these models. For example, only 40% of the variance in the observed data was accounted for in Ntale et al., (2003). Hence, identification of robust relationships between climate elements is a prerequisite to the maximization of the S/N ratio and improved prediction skill of the models.

The objective of this chapter is to establish relationships between the leading modes of rainfall WPCs of East Africa (EA), Central South Africa (CSA) and Southern Africa and the gridded scale-average wavelet power (SAWP) of sea surface temperature (SST) of the Indian and Atlantic Oceans. The associations between SAWP of SST and rainfall WPCs are considered statistically significant if the co-variability is significant above the 95% level. With most of the noise (measurement errors and energy of climate variability below the 95% level) removed, it is expected that the identified predictor SST fields contain signals that explain the majority of the variance found in the spatial and temporal regimes of rainfall variability. We assume that the SST variability derived from the large inertia of the oceans contributes enough memory to the variability of the seasonal rainfall of SA and EA that it is possible to predict the latter at 2 to 8 months lead-time. In this case, we assume that the inertia of the oceans slows down the high-frequency moisture transport components of the atmospheric circulation, dumping it out in time scales of seasons (Ntale 2001). The Pearson correlation, ρ, is extensively used to establish the associations between rainfall WPCs and the SST SAWP time series.

Of the four seasons, (January-March, (JFM), April-June (AMJ), July-September (JAS) and October-December (OND)), the preceding AMJ season provided lead-times of 2, 3 and 8 months for predicting the SON, the summer (OND-JFM) and the MAM rainfalls, respectively. In addition, the JAS and OND also provided 5 and 2 months of lead-time, for predicting the MAM rainfall. The associations between AMJ SST SAWP and the SON (summer) and the MAM rainfall WPCs were investigated. The association between MAM's WPCs and JAS and OND's SAWP were similarly examined. In Chapter 3, we saw that at regional scales, most of the spatial variability of the rainfall could be described mainly by WPC1 and WPC2. These WPCs were also used in this chapter to establish associations between rainfall and SST SAWP.

Due to strong persistency in the SAWP and WPC time series, the effective length of the SAWP and WPCs, N_{eff}, calculated as,

$$N_{eff} = N\frac{1-\rho_1}{1+\rho_1} \tag{4.1}$$

was used to determined the significant level of the correlation between WPCs and the SAWP (Wilks 1995). In Eq (4.1), ρ_1 is the lag-1 autocorrelation and N is the length of the observed rainfall or SST time series. The effective length, N_{eff} was much shorter than the observed length of the time series, N. All associations were determined using the 1950-1997 period, because data quality for this period is higher than for the period prior to 1950, especially for CSA. Using this period, N_{eff} was found to be only around 3 or 4 years and the correlation above the 95% level was 0.997. In most of the spatial correlation patterns between WPCs and SAWP, correlations rarely exceeded the 0.997 level. Since regional rainfall WPC-SAWP correlations generally ranged between 0.4 and 1.0, regions of the oceans correlated with rainfall at values between 0.4 and 1.0 were taken to be areas of the oceans that influence rainfall variability.

Examination of associations between rainfall in EA, CSA, SA and SST in the Indian and Atlantic Oceans is expounded in Sections 4.2 to 4.4. A summary of all results is presented in Section 4.5

4.2 Association Between SON rainfall WPCs and SAWP of Atlantic and Indian Ocean SSTs

The spatial correlation patterns between WPC1 and WPC2 of the SON rainfall of EA and individual 5°×5° SST SAWP time series of the Indian and Atlantic Oceans are shown in Figure 4.1. Rainfall WPC1 is positively correlated to the SST SAWP of SW Indian Ocean, but negatively correlated to the NW portion of the Indian Ocean, Figure 4.1(a). The relationship between SON WPC1 and the SAWP of the Indian Ocean SST is similar to that of the spatial pattern of WPC1 of the Indian Ocean SST SAWP (Figure 3.20 of Chapter 3). Since SON rainfall WPC1 is out of phase with the northern Indian Ocean SAWP and in-phase with the southern Indian Ocean SAWP, increasing power (or warming of SST) of the northern Indian Ocean SST SAWP in AMJ is associated with decreasing power (decreasing SON rainfall) of the SON rainfall of EA and vice-versa. Warming of the southern Indian Ocean results in increased SON rainfall, and vice-versa. The temporal variability of AMJ WPC1 of the Indian Ocean SST (Figure 3.21(g) of Chapter 3) and the SON WPC1 (Figure 3.3(d)) confirm the above relationship. These two figures show that when the AMJ SST of the southern Indian Ocean warmed up during the periods 1950-1960 and 1975-1985 the SON rainfall increased, while when SST cooled during the periods 1960-1975 and 1985-1994, rainfall decreased.

Figure 4.1(b) shows the correlations between SON rainfall WPC1 and individual 5°×5° SST SAWP of the South Atlantic Ocean. Rainfall WPC1 is positively correlated to the Brazil current and negatively (and weakly) correlated to the Guinea and the South Atlantic Ocean between 30°S and 40°S. The positive relationship between rainfall WPC1 and the Brazil Ocean SST show that variabilities in these ocean currents have important climatological implications for SON rainfall variability. Since the SON rainfall variability is positively correlated to the SST of the Brazil Ocean current SSTs, warming in these ocean basins during AMJ is associated with increased SON rainfall, while the association is out of phase with the Guinea Ocean current SST.

Figure 4.1(c) shows that SON rainfall WPC2 is strongly correlated to the Guinea Ocean current SST SAWP of the Atlantic Ocean, while Figure 4.1(d) shows the weak correlation between SON rainfall WPC2 and the Indian Ocean SST SAWP. In Chapter 3, Section 3.3.2.1, it was pointed out that the spatial pattern of the SON rainfall variability was strongest in the east and decreased rapidly westwards, (especially along the Great Rift Valley, GRV). In the GRV region, the SON rainfall variability was best explained by WPC2. The strength of the WPC2 spatial patterns suggested possible sources of the variability more likely from the west (either influences from Congo basin or the Atlantic Ocean) than the east (Indian Ocean SST). Figure 4.1(c) suggests that the variability of the Guinea Ocean current SST modulates atmospheric circulation that affects the rainfall variability of the western areas of EA, which includes the GRV region.

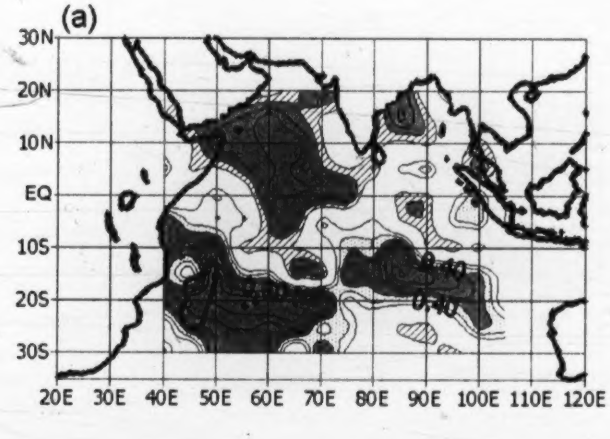

Figure 4.1 The spatial display of the correlation pattern plotted at 0.2 contour intervals between WPCs of the SON rainfall of EA and individual 5°×5° SST SAWP time series of the Indian and Atlantic Oceans, for both annual ((a) and (c)), and AMJ ((b) and (d)) SST data. The darker shadings in (b) and (d) indicate ocean regions where the predictor SST was selected as input data.

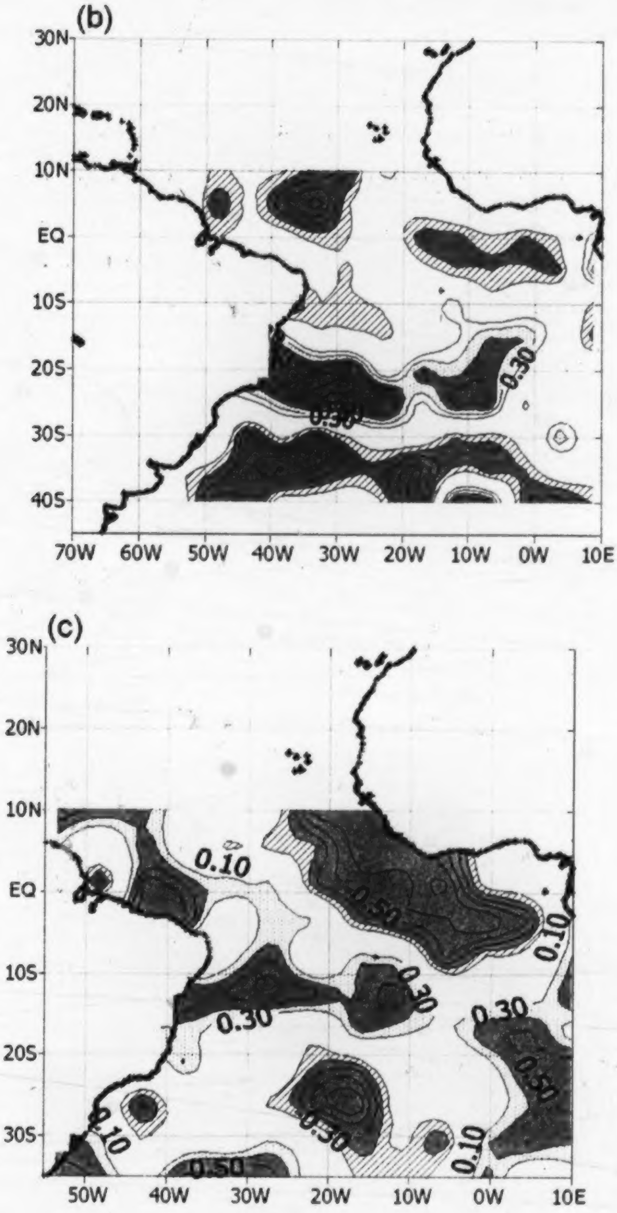
(b)
30N
20N
10N
EQ
10S
20S
30S
40S
0.30
0.30
70W
60W
50W
40W
30W
20W
10W
0W
10E
(c)
30N
20N
10N
EQ
10S
20S
30S
0.10
0.50
0.10
0.30
0.30
0.30
0.50
0.10
0.30
0.10
0.50
0.10
50W
40W
30W
20W
10W
0W
10E

Figure 4.1 continued

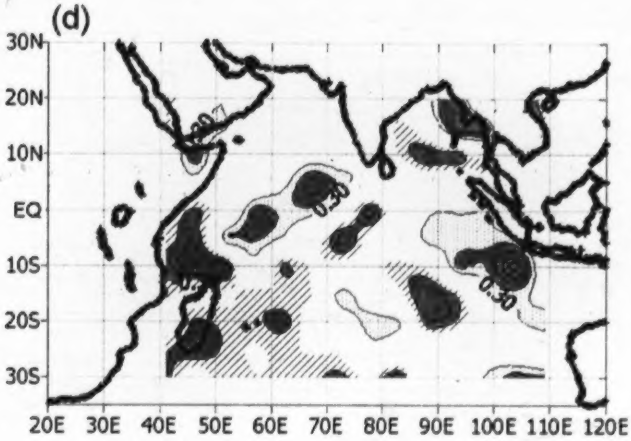

Figure 4.1 continued

4.3 Association Between MAM rainfall WPCs and SAWP of Atlantic and Indian Ocean SSTs

The MAM rainfall WPCs and WICs were correlated with individual 5°×5° SST SAWP of the Indian and Atlantic Oceans. The SST SAWP of the Indian and Atlantic Ocean associated with MAM WPC2 has a much broader and comparatively well-defined spatial distribution pattern (i.e., follows spatial variability pattern of the SST SAWP of the oceans themselves). Figure 4.3 shows correlation patterns between MAM rainfall WPC2 and the SST SAWP of AMJ, JAS and OND seasons. Following Figure 3.19 of Chapter 3, we see that the correlation patterns generally follow the spatial variabilities of the Atlantic Ocean SST SAWP. In AMJ, the SST SAWP variabilities are well developed off the South America coast (shown by strong correlation patterns between rainfall WPCs and Benguela and Brazil SST SAWP).

In JAS, the spatial correlations with the Benguela Ocean SST SAWP begin to move towards the African coast and are well developed by the OND season (see Figs. 4.2(b) and (c)). Conspicuous in Fig 4.2(c) is an area close to the African coast, with correlations above 0.4 that forms a similar spatial pattern similar to WPC1 of the OND season. The MAM WPC2 is in phase with the Brazil and Benguela ocean current SST SAWP and out of phase with Guinea and the areas between 30°S-40°S. Increased SST in the Gulf of Guinea and Brazil currents results in increased (decreased) rainfall in MAM for eastern (western) Tanzania and southern (northern) Uganda and Kenya, and vice versa. Low SSTs in the Gulf of Guinea have been found to affect the strength and moisture content of the Congo air mass that converges in EA by forcing westerly incursions to weaken. The weakened westerly incursions result in particularly dry years for East Africa (Ntale et al., 2003).

Figure 4.3 shows the correlation patterns formed between MAM WPC2 and the Indian ocean SAWP. During the AMJ season, MAM WPC2 is correlated to the southwest Indian Ocean. The extensive spatial correlation pattern between MAM WPC2 and SST SAWP during JAS is positive to the northwest, northeast and southern portions of the Indian Ocean and negatively but weakly correlated to the western Indian Ocean. Although not well organized (not exactly similar to the JAS SST WPC1 spatial pattern), this spatial pattern shows that MAM is associated with the north and southern Indian Ocean. However, the positive association between MAM WPC2 and the south Indian Ocean does not appear similar to the WPC1 of the SST for the JAS season. The same applied to the OND season.

It was shown in Chapter 3 (Figures 3.7 and 3.8 of Section 3.3.3.1) that the MAM rainfall WPC1 was strongest in the western region of EA and decreased eastwards. This showed that the Atlantic Ocean SST accounts for much of the variation of the MAM rainfall.

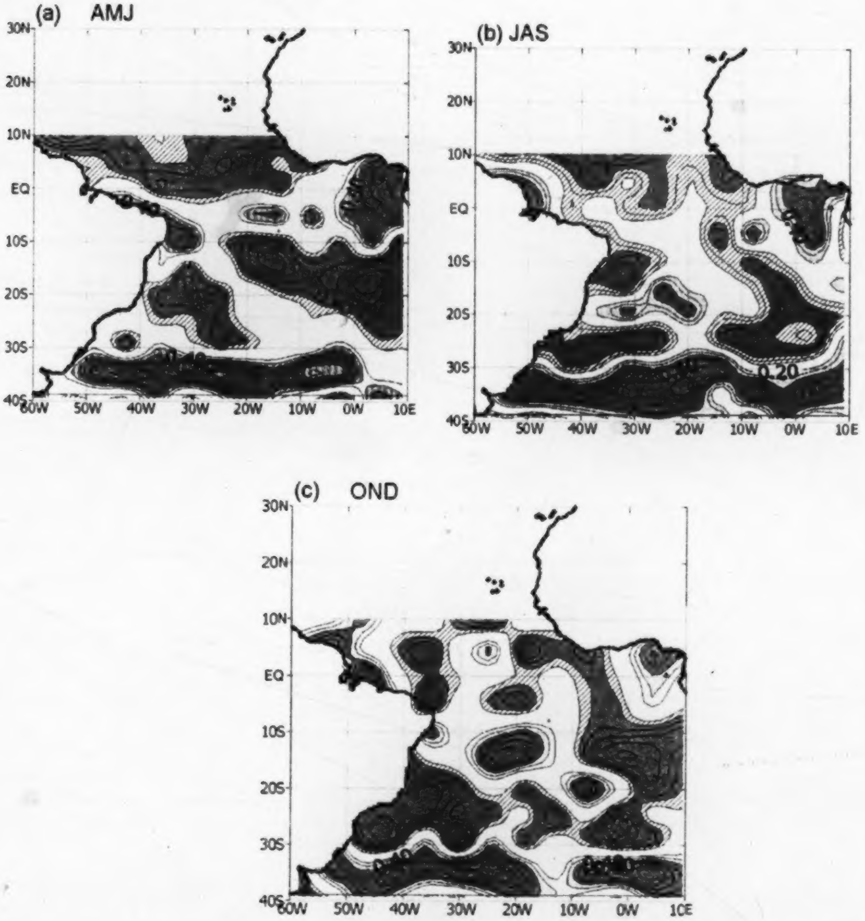
(a) AMJ
(b) JAS
(c) OND
30N
20N
10N
EQ
10S
20S
30S
40S
60W
50W
40W
30W
20W
10W
0W
10E
0.20

Figure 4.2 Associations between MAM rainfall and SST of the Atlantic Ocean for the periods (a) April-June (AMJ), (b) July-September (JAS), and (c) October-December (OND) from the Atlantic Ocean

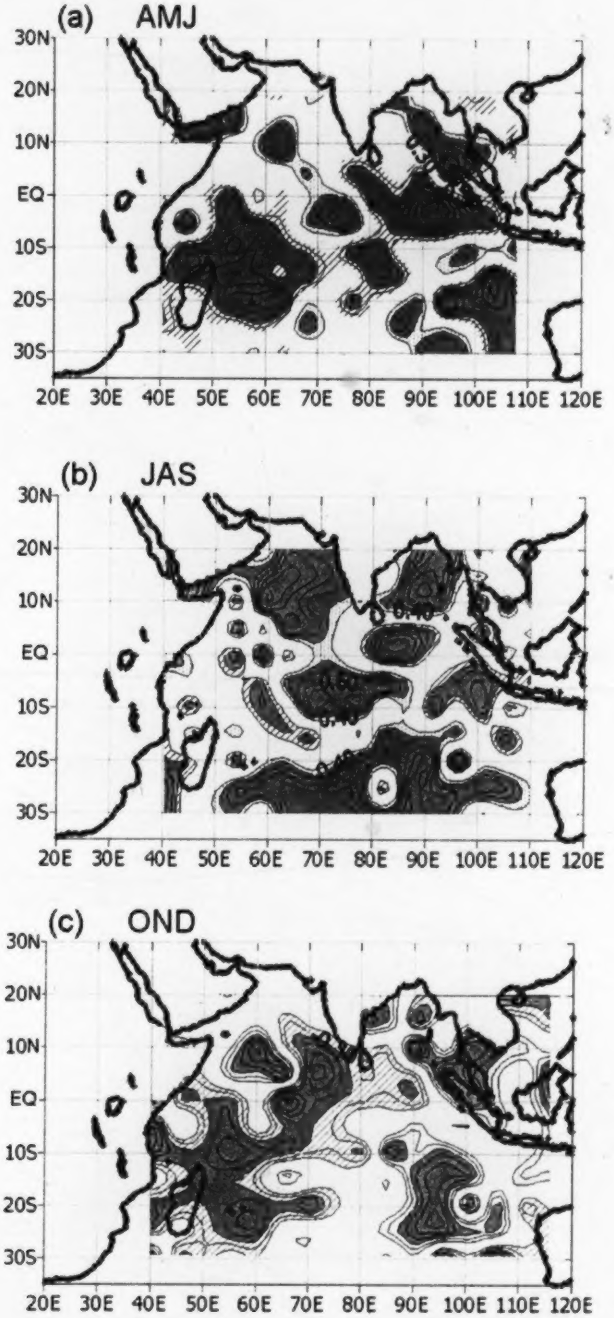
(a) AMJ
(b) JAS
(c) OND
30N
20N
10N
EQ
10S
20S
30S
20E
30E
40E
50E
60E
70E
80E
90E
100E
110E
120E

Figure 4.3 Associations between MAM rainfall and SST of the Indian Ocean for the periods (a) April-June (AMJ), (b) July-September (JAS), and (c) October-December (OND).

4.4. Association Between Central Southern Africa rainfall WPCs and SAWP of Atlantic and Indian Ocean SSTs

Figure 4.4 shows the correlations between CSA rainfall WPC1 and individual 5°×5° SST SAWP of the AMJ season in the south Atlantic and Indian Oceans. Strong positive correlations were found between the rainfall WPC1 and the Benguela and the Brazil Ocean SST SAWP, while negative correlations were found between the rainfall WPC1 and the Guinea Ocean current SST and the South Atlantic Ocean SST SAWP located between 30°S and 40°S. This correlation spatial pattern is similar to WPC1 of the Atlantic Ocean during the AMJ season (Figure 3.19(c) of Chapter 3)

Weak spatial correlation patterns were found between rainfall WPC1 and the AMJ Indian Ocean SST SAWP (see Figure 4.4(b)). Rainfall WPC1 is negatively correlated to the northern Indian Ocean and positively correlated to the southern Indian Ocean, similar to the spatial pattern of WPC1, which shows an out of phase relationship between the northern and southern Indian Ocean. The spatial patterns are, however, not very extensive as compared to those found between the Atlantic Ocean SST SAWP and the rainfall WPC1.

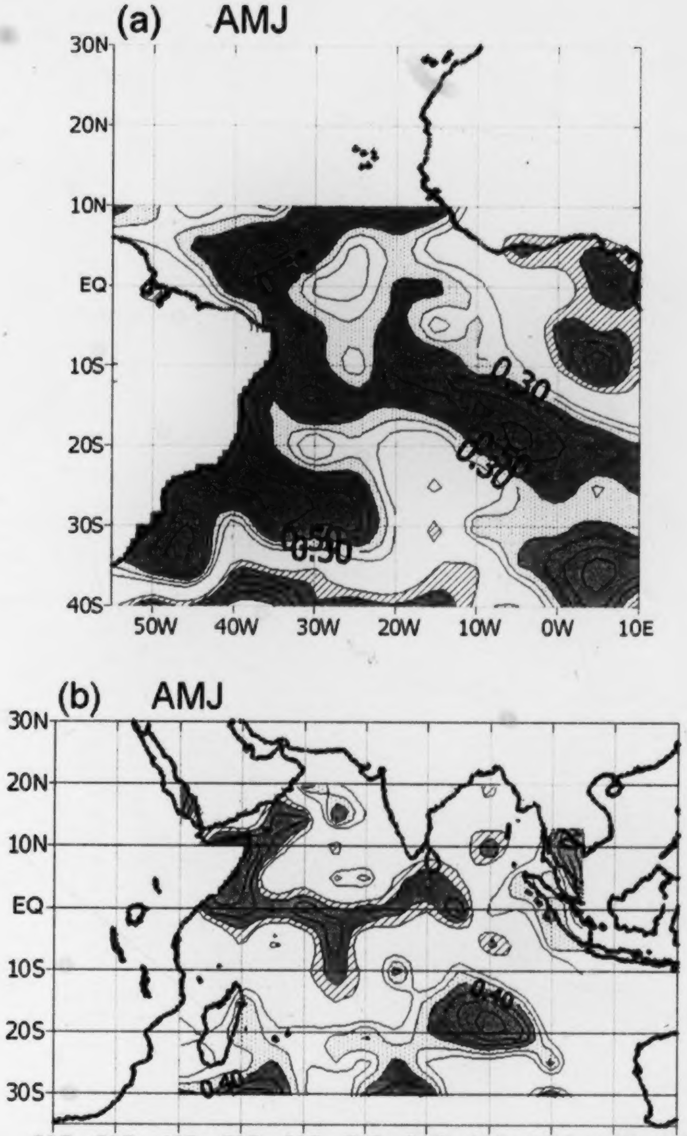
(a) AMJ
30N
20N
10N
EQ
10S
20S
30S
40S
50W
40W
30W
20W
10W
0W
10E
0.30
0.30
0.50
0.50
(b) AMJ
30N
20N
10N
EQ
10S
20S
30S
20E
30E
40E
50E
60E
70E
80E
90E
100E
110E
120E
0.40
0.40

Figure 4.4 Plots showing the spatial correlation patterns between WPC1 of CSA rainfall and individual 5°×5° AMJ SST SAWP time series of the (a) Atlantic, and (b) Indian oceans. The areas inside the dotted line correspond to ocean zones with correlations greater than 0.5. Data from these delineated zones were later used to predict the CSA rainfall.

The associations between rainfall WPC1 and the SST variations in the Brazil, Benguela and Guinea Ocean currents shows that variabilities in these ocean current SSTs also have important climatological implications for CSA rainfall. Since the rainfall variability in central parts of CSA is positively associated with SST in the Brazil and Benguela Ocean currents, warming in these ocean basins results in increased rainfall in this region and vice versa for the coastal areas.

4.4 Association between Southern Africa summer rainfall WPCs and Atlantic and Indian Ocean SSTs SAWP

Figure 4.5 shows the correlations between the SA summer rainfall WPCs and individual 5°×5° SST SAWP time series of the South Atlantic Ocean. Rainfall WPC1 is positively correlated to the Brazil and the Guinea currents and negatively correlated to the South Atlantic Ocean between 30°S and 40°S. The positive relationship between rainfall WPC1, the Brazil and the Guinea current shows that variabilities in these ocean currents also have important climatological implications for SA as well. Rainfall WPC2, which is strongly associated with rainfall along the coastal areas, is positively linked to the Benguela ocean current SST.

The correlation pattern between WPCs of the summer rainfall of SA and individual 5°×5° SST SAWP time series of the Indian Ocean are shown in Figure 4.5(b). Rainfall WPC1 is positively correlated to the SST SAWP of the southern Indian Ocean and negatively correlated to the northern Indian Ocean, similar to the spatial pattern of WPC1 of the Indian Ocean SST SAWP.

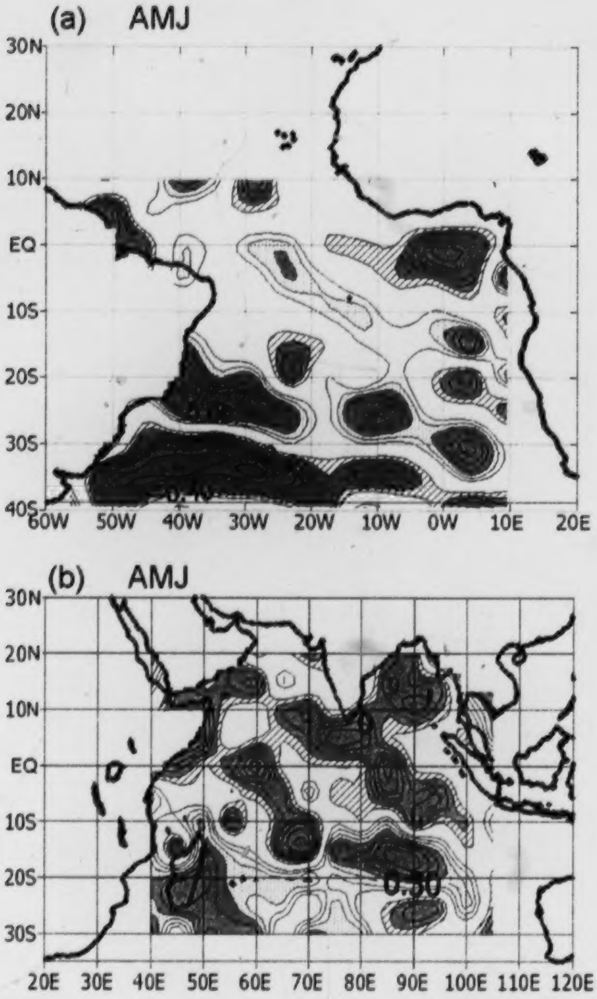
(a) AMJ
30N
20N
10N
EQ
10S
20S
30S
40S
-0.40
60W
50W
40W
30W
20W
10W
0W
10E
20E
(b) AMJ
30N
20N
10N
EQ
10S
20S
30S
0.50
20E
30E
40E
50E
60E
70E
80E
90E
100E
110E
120E

Figure 4.5 Associations between southern Africa summer rainfall and SST SAWP (a) rainfall WPC1 and Indian ocean SST SAWP (b) rainfall WPC1 and Atlantic ocean SST SAWP (c) rainfall WPC2 and Atlantic ocean SST. It is clear that the main mode of variability of summer rainfall is associated with the Brazil ocean current, Sierra Leon basin and the Guinea ocean current SST, while rainfall along the coastal areas is associated with the variations of the Benguela ocean current SST.

Since summer rainfall for the northern parts of SA is out of phase with the northern Indian Ocean and in-phase with the southern Indian Ocean SST SAWP, warming of the northern Indian Ocean resulted in decreased summer rainfall for Zambia, northern Namibia, Zimbabwe, parts of central Mozambique, Botswana, and northern South Africa. Conversely cooling (warming) of the southern Indian Ocean resulted in decreased (increased) rainfall in the northern parts of SA and vice versa for the southern regions. Figure 3.20 of Chapter 3 of the Indian Ocean WPCs shows that the northern Indian ocean began warming in 1960 and the south Indian ocean SST began cooling around 1970. SA summer rainfall WPC1 (Figure 3.15 of Chapter 3) shows that SA responded about the same time to SST changes in the southern Indian Ocean SST variations. The southern Indian Ocean (especially the SW Indian Ocean) has also been found to influence rainfall variability of South Africa (e.g., Mason 1995; Jury 1996; Landman et al., 2001).

When the relationship between the Atlantic Ocean and Indian Ocean SST SAWP, and WPCs from CSA and the whole of SA are compared, it is seen that the relationship between CSA rainfall WPCs and Atlantic Ocean SAWP is stronger and spatially extensive in the Atlantic Ocean than that of CSA and the Indian Ocean SST SAWP, while the relationship between the whole of SA rainfall WPCs is better defined in the Indian Ocean than the Atlantic Ocean. This demonstrates that CSA is influenced more by the variability of the Atlantic Ocean SST than that of the Indian Ocean SST. However, when the region is considered together, the influence from the Indian Ocean SST SAWP becomes important. This shows that most of southern Africa rainfall variability is affected by variations in the Indian Ocean SST. However, variations in the Brazil and Guinea current also have effects on the regions rainfall. This demonstrates that at regional scales, both the Atlantic and Indian Oceans influence rainfall variability in CSA and SA. This finding agrees with Figures 3.1(a) and (b) of Chapter 3, which show convergence of moisture transport winds at the 850-hPa height into the region. Generally, in the southern most part of the continent the Indian Ocean has more influence, while as you move northwards, the SST variations of the Atlantic Ocean explain more of the variance in the rainfall than the Indian Ocean SST.

The spatial patterns of the associations were used to extract the SST data used for prediction of the seasonal rainfall of EA, CSA and SA discussed in Chapter 5.

4.5 Summary of Findings

Associations between rainfall WPCs of EA (SON and MAM seasons), CSA and SA (summer season) and the Atlantic and Indian Ocean SST SAWP for the seasons April-June (AMJ), July-September (JAS) and October-December (OND) seasons were established in this Chapter.

It was found that all the seasonal rainfall WPCs of EA, CSA and SA have links with the South Atlantic Ocean SST SAWP through the Brazil, Guinea and Benguela Ocean current SST. The SON and the summer WPCs were also found to be associated with the Indian Ocean SST SAWP. The MAM rainfall WPC2 was found to be associated with the Atlantic Ocean SST only.

The rainfall WPCs were found to be in phase with the Brazil and Benguela ocean currents but out of phase with the Guinea Ocean SST SAWP and the SST SAWP between 30°S-40°S of the Atlantic Ocean. The SON and summer rainfall WPCs of East and Southern Africa, respectively, were positively correlated to the South Indian Ocean SST SAWP and negatively correlated to the northern Indian Ocean SST SAWP. The decrease in SST of the southern Indian Ocean between 1970 and 1997 is found to be associated with a similar decrease of SON of East Africa and the summer rainfall of some countries within SA.

CHAPTER 5

DEVELOPMENT AND APPLICATION OF THE ANN-GA MODEL FOR SEASONAL CLIMATE PREDICTION

5.1 Introduction

Provision of accurate precipitation forecasts, both in the short and long term has great economic benefits (Shen et al., 2001). For example, in the United States, potential savings over ten years to the agricultural sector from seasonal precipitation forecasts with only 60% accuracy are estimated to be between US$0.5 and US$1.1 billion, (O'Brien, 1992). The predominance of rain-fed agriculture and livestock production across Eastern and Southern Africa serves to ensure that food security is inextricably linked to the accuracy of seasonal precipitation forecast of each precipitation season (Mason, 1997). In other words, an ability to provide accurate seasonal precipitation forecast could contribute substantially to the food security and natural resource management of Eastern, Central South and Southern Africa.

The techniques for predicting the future weather or climate are determined to a large extent by the required lead-time of the forecast, which ranges from a few hours for highly skilled numerical weather prediction, to months or decades in the case of climate prediction (Namias, 1985). On monthly or longer time-scales, a number of models, e.g., linear statistical models, dynamical models, and hybrids of statistical-dynamic models, have been used to make climate prediction by capitalizing on the slow moving boundary conditions, such as sea surface temperature and land surface characteristics (e.g., Mutai et al., 1998, Landman et al., 2001). Although in some parts of the world, dynamical models have performed as well as their linear counterparts (Shen et al., 2001), in Eastern and Southern Africa, these models have performed poorly, in forecasting the climate with lead-times of beyond two weeks, especially in recent years. As such, the continued need for further development and application of statistical models for climate prediction has been suggested (e.g. Mason, 1997).

Since linear statistical models have an obvious limitation of the inability to adequately take into account the non-linear behavior of the ocean-atmosphere system, nonlinear statistical models are advocated. As noted by Landman et al., (2001), many important climate processes demonstrate strong non-linearities and the forecast skill of most linear statistical models is restricted because of the exclusion of these processes. To take into account the nonlinear characteristic of the ocean-atmosphere interaction, this chapter developed a nonlinear statistical climate model for predicting seasonal precipitation. The prediction model uses the nonlinear features of an artificial neural network, (ANNs) and training capability of the genetic algorithm (GA). The inspiration to combine GAs and ANNs comes from the fact that both computation techniques emulate biologically inspired mechanisms (Gallant, 2001).

For example, ANNs are motivated by the way the human brain learns from experiences and the way it processes vast amounts of information in parallel. The brain contains, an estimated 10 billion neurons linked by 60 trillion synapses, which make it possible to efficiently process vast amounts of information related to processes such as motor control (Haykin, 1994). The brain also has memory for pattern recognition. Each time we react to the world around us, or think about something, pulses of signals move through the vast network of neurons mapping routes through cells. Familiarity with the scenes or thoughts is associated with signals following familiar patterns of paths through the brain neurons. This is what is called memory or learning. Memory is thus not stored in any of the physical cells found in the brain. It is a pattern of signals moving through the vast network of neurons. Neural networks try to replicate this massive interconnection of neurons and the memory aspect of the brain by creating massively parallel structures containing weights (neurons) interconnected by links. The weights are modified such that the signals passing through the ANN resemble the pattern of interest at the output. Hence, the memory of the ANNs for a particular pattern is associated with the interconnections and the associated weights. ANNs are obviously limited. Once trained, they must maintain the same number of neurons and associated weights. By looking back over the years and recalling our countless experiences, the incredible power, capability and efficiency of the brain is self-evident.

On the other hand, GAs try to harness the power of natural biological evolution, which nature has demonstrated through millions of years. By repeated processes of recombination (crossover and mutation) and natural selection, original populations of primitive organisms (single atoms) evolved into complex ones that today are adapted to their environments. The power of natural biological evolution can be seen in the tremendous variety and robustness observed in nature.

By combining GAs and ANNs, this chapter hopes to develop an artificial system capable of achieving what nature has achieved for millions of years, albeit in a short period of time (e.g. minutes or hours): i.e., evolving a primitive random population of neural networks to one that is highly adapted to predict the complex, ocean-atmosphere nonlinear interaction. The development of algorithms combining GAs and ANNs to evolve ANN networks structures and to train ANN weights have been promoted since the 1980's (e.g., Whitley 1988; Munro 1993). Since then there has been extensive research and development of ANN-GAs (e.g., Westheider, 1997; Gallant, 2001; Fayad, 2001; Phattanasri, 2002) and applications (e.g., Shin and Han, 2000; Mwale et al., 2004).

Inspite of the advanced development and applications of ANN-GAs in other fields, as far as we know, climate and hydrology are just beginning to benefit from the development and application of such models.

5.2 Origins of Genetic Algorithms

GAs were initially developed by Holland in 1975. Further developments of GAs were made in the late 1980's, and early 1990's (e.g. David Goldberg, 1989; Michalewicz, 1992). However, Holland is regarded as the father of GAs. There are many forms of GAs today, however, whatever forms GAs take, the basic and underlying idea behind their development is to design computer software that models natural biological evolution. From our standpoint, this means creation of primitive populations that evolve through processes similar to natural reproduction and selection. With recent developments in cloning, biological evolution might encompass both natural and artificial reproduction of life and probably both natural and artificial selection. In this thesis natural biological evolution is perused in the development of the algorithm.

Therefore, GAs employ analogies to the mechanisms of adaptation observed in natural evolution to provide solutions to a wide variety of search problems (Brindle

1981). As observed by Goldberg (1994), these algorithms are truly mind boggling in the way they demonstrate power and flexibility in applications to business, engineering, and science. In many practical applications, GAs have found good practical solutions to complex problems in reasonable amounts of time (e.g. Simpson et al., 1994, Savik and Walters, 1997; Wang and Zheng, 1998; Mwale and Mulenga, 1999).

5.2.1 Biological Roots of the Genetic Algorithms

GAs fall under a field of nature inspired computation algorithms broadly classified as evolution programs (i.e., evolution strategies, genetic programming, and classifier systems) (Michalewicz, 1992). The variations among these algorithms are mainly in the genetic operators used, but they are essentially similar in that they all are modeled after evolution. For example, classical genetic algorithms operate on fixed-length binary strings and binary crossover and mutation, while other evolution programs operate on variable length strings and use other genetic operators.

The Darwinian theory of evolution, also called the theory of survival of the fittest is used to expound the biological roots of GAs. By this theory, all complex organisms seen today originated from simple organic atoms. As the complexity of these organisms grew so did the competition for survival (i.e. food, water, air, and the environment). Organisms that outlast the combination of these factors are those that have a high level of fitness. These organisms survive and propagate their genetic characteristics to subsequent generations through sexual reproduction. The ability to outlast the struggle for existence is known as natural selection.

Rare and slight random modifications, commonly called variations or mutations occur in some organisms. These variations introduce new characteristics in the population. Mutations are beneficial to some individuals, but deleterious to others. The reproductive process and natural selection are repeated many times over. After several millions epochs, the pressures of natural selection and reproduction improve the average fitness of the population.

5.2.2 The Genetic Algorithm in Function Optimization

In designing software that models natural biological evolution, the following features of the GA are usually adopted. A large number of possible solutions to a problem called a population are created at random. Each solution (or individual) in a population is represented by a set of parameter values that completely describe each solution to the problem. These solutions are encoded in strings that resemble chromosomes found in our Deoxyribonucleic acid, (DNA). For GAs operating using the binary alphabet, the characters used are either zeros or ones to form the chromosomes. As discussed in section 5.2.2.1, not all genetic algorithms restrict representation of solutions to the binary alphabet, which makes these genetic algorithms more flexible and applicable to a variety of decision-making problems (Michalewicz, 1992)

The initial population is allowed to evolve over several generations or epochs. At each generation a measure of fitness of how good each solution is with respect to an objective function is calculated. For GAs using the binary alphabet, this is achieved by decoding binary strings into parameter values, substituting them into the problem and computing a function fitness value for each of the solutions. For GAs using alphabets other than binary (e.g., decimals), the chromosomes are directly substituted into the problem and the objective function values are computed.

To compute the fitness of the population, the solutions are assessed in terms of some fitness criteria. In all evolution programs, the selection function is designed with a bias towards high fitness solutions, such that high fitness solutions have a higher chance of being selected than weaker ones to be offspring of future generations.

As part of the reproduction process, the newly selected population is subjected to the crossover and mutation operations. Crossover is modeled after the crossover operations observed during Meiosis. Crossover occurs when chromosomes attached to each other break off at the point of attachment. The chromosomes exchange pieces. Mutation, a procedure of randomly altering genes in the population is also applied to a few randomly selected chromosomes. In genetic algorithms based on binary representation, this means randomly altering (or flipping) some of the few bits with a small probability equal to a mutation rate. In other forms of genetic algorithm, mutation is achieved by randomly replacing parameters with new ones from within the range of possible parameters. Other complex processes such as deletion and disjunction occurs during Meiosis, but these cannot be modeled because artificial solutions are of fixed length.

5.2.2.1 Representation of Solutions in the Genetic Algorithm

As observed by Michalewicz, (1992), representation is a key issue in GAs because the representation scheme can severely limit or open the window by which the system observes its world. The most widespread mechanism for representing chromosomes in GA is the bit string, which uses the binary alphabet. Using this scheme, the solutions of the problem being solved are presented in form of ones and zeros and the problem itself is translated into a form that is suitable for binary representation.

Binary representation has been in use since the development of genetic algorithms. Infact, the theoretical basis of genetic algorithms is based on binary coding. In recent years, binary–coded genetic algorithms have failed to handle some real life problems, because many of these problems need other forms of representation such as real coding (or real parameter coding) schemes (e.g., 103.7), lettered alphabets (e.g., A, b, C), or combination coding schemes (e.g., 1fb0C). This has facilitated the direct use of decision variables in evaluating candidate solutions. A good example would be the selection of pipe diameter sizes for the design of water distribution systems. There exist a number of real-parameter GA implementations, (e.g. Mwale et al., 2004). Since real parameters are used directly, without any string coding, solving real-parameter optimization problems is a step easier when compared to binary-coded genetic algorithms, which require separate algorithms for coding and decoding of solutions.

5.2.2.2 Creation and Evaluation of Solutions in the Genetic Algorithm

Most optimization methods start off a search at a single point and gradually move to the optimum point by following a change in the function slope. Single point search can easily be trapped in a local optimum in the presence of billions of possible solutions. To circumvent this problem, GAs create a large number of solutions at the same time, so that the search occurs in parallel. Goldberg (1989) called this implicit parallelism, which is where the power of the GA lies. Since evolution, the basis of the GA, requires diversity in order to work, a large amount of diversity is introduced during this period by randomly creating large initial populations, which enables the search to commence over a vast solution space, minimizing the possibility of the search getting trapped in a local optimum point.

Each chromosome represents a possible solution to the problem being solved. The quality of the solution is assessed in terms of its fitness value, which is concerned with the performance of the solution or parameters against the problem being solved.

5.2.2.3 Selection of Solutions in the Genetic Algorithm

GAs work with the evolvement of a population over many successive generations with the aim of finding better and better offspring as the search moves from one generation to the next. Survival of the fittest means that only the best performing members of the population will survive in the long run. In the short run, the selection process is designed to favor the better solutions, without eliminating all the poor solutions (Bauer 1994). Generally the best solutions of each generation are selected to represent new populations of subsequent generations, with a probability p_i that is dependent on the fitness of each solution (Michalewicz, 1992): i.e.,

$$p_i = \frac{eval(X_i)}{\sum_{i=1}^{X} eval(X_i)} \qquad (5.1)$$

In performing selection, a balance between speed of convergence and the quality of the solutions has to be maintained. If the selection pressure is too high, rapid convergence may result in poor quality of solutions. This is because the population loses diversity as the search emphasizes on the population with the best solutions only. Conversely, low selection pressure slows down the search, and forces too many poor performing solutions to join the search. This causes the search procedure to behave like a random search process. When using real coded GAs, the number of solutions to be selected in each generation is determined empirically, and usually 85% of the best solutions have been retained in the selection process. The selection scheme is also very critical in determining the quality of solutions. Some selection schemes are very efficient at the beginning of the search, but as the distance between solutions narrow down, they become ineffective. Fine-tuning the GA through appropriate selection schemes is an important part of the design of genetic algorithms.

Evolutionary programs use numerous selection schemes to re-create populations for subsequent generations. These schemes can largely be classified into two main groups: fitness proportionate and the rank based selection. The most famous fitness proportionate based selection schemes is the roulette wheel proportionate selection (Goldberg, 1989, Michalewicz, 1992), while that for rank based selection schemes is the linear ranking scheme (Michalewicz, 1992; Bauer, 1994; Savik and Walters, 1997).

In the roulette wheel proportionate selection, the chance of an individual being selected is based on it relative fitness in the population, (see Eq (5.1)). To select an individual, the roulette wheel selection uses a simulated roulette wheel with slots that are sized according to the fitness of each individual. Hence according to Eq (5.1), solutions with higher fitness values have a higher chance of being selected. The roulette wheel proportionate selection is very effective at the beginning of the genetic algorithm run, because the solution objective function fitness values are spread further apart. However, when the solutions begin to converge, the objective function fitness values cluster close together and relative fitness vary only slightly. The clustering together of fitness values is known as the scaling problem.

Scaling problems are easily overcome by rank based selection, which is mainly used in this thesis. Using rank selection, the objective function fitness values are ranked with the best solutions at the top and the worst solutions at the bottom. A proportion of the ranked population, say 85% (Mwale 1998, Mwale et al., 2004), is selected with replacement, to create the new population. Since selection is made from the best portion of the ranked population, the average fitness of the new population is higher than the population from which it is created. Hence, selection shifts the exploration direction of the GA from poor search spaces to near-optimal ones.

Other selection schemes exist, but they are variants of the above selection schemes. For example the genitor selection (variant of rank selection where the best individuals replace the worst individuals) and the ranking selection with roulette wheel (where a rank assignment function is used to build the slots of a roulette wheel) are some of the other selection schemes that may be used (Bauer 1994).

5.2.2.4 Crossover Procedures in the Genetic Algorithm

Crossover is defined as a process in which the newly selected individuals are mated in pairs, either in the same order in which they were selected from the previous population or at random to produce one or more offspring. The offspring produced may inherit the characteristics of the parents or not, depending on the mechanism of crossover used. Each pair of individuals exchanges part of the genetic makeup using a randomly chosen crossover site. There are a number of crossover operators in the genetic algorithm literature. These include one-point, two-point, *n*-point and uniform crossover. However, in almost all crossover operators, two strings are picked from the mating pool in some fashion, and a portion of the strings is exchanged to create two or more new strings. Using more crossover points result in a more exploratory search, as a large variety of information exchange takes place between solutions. However, more crossover points also increase the chance of destroying the good solutions, because good solutions tend to lie together, distinguishable only via small variations.

In a few cases, crossover may also be performed in such a way that it does not follow the biological metaphor. This is achieved by combining material from three or more parents to produce the offspring. Offspring from such combinations usually do not genetically resemble their original parents but attain characteristics that are a combination of more than three parents.

In a single point crossover operation (see Figure 5.1), a crossing site is randomly chosen and portions of the chromosome on either side of the location are exchanged. In a two-point crossover operation, the middle sub-string between the crossover sites is exchanged. In uniform crossover, all the genes in the chromosomes are used. Crossover is a powerful process that extends the search in many directions by cutting through the search space in a highly efficient manner. Not every crossover between any two solutions results in solutions in the new generations better than the original individuals.

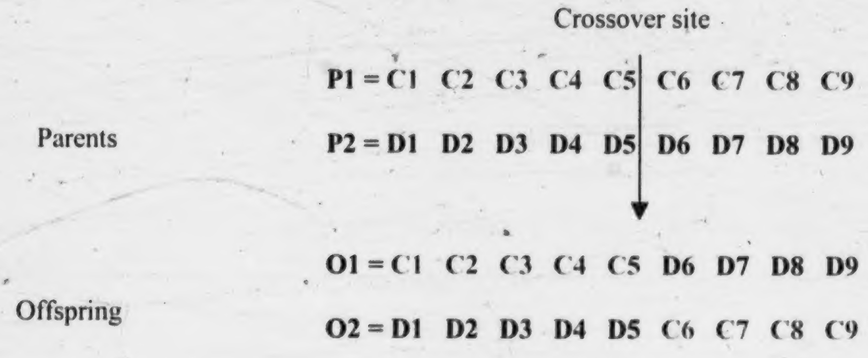
Crossover site
Parents
P1 = C1 C2 C3 C4 C5 C6 C7 C8 C9
P2 = D1 D2 D3 D4 D5 D6 D7 D8 D9
Offspring
O1 = C1 C2 C3 C4 C5 D6 D7 D8 D9
O2 = D1 D2 D3 D4 D5 C6 C7 C8 C9

Figure 5.1 An example of one-point crossover.

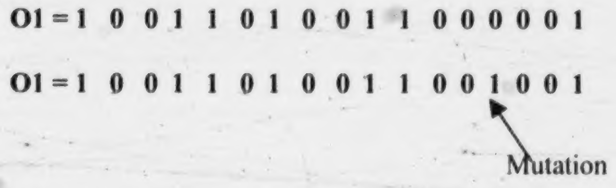
O1 = 1 0 0 1 1 0 1 0 0 1 1 0 0 0 0 0 1
O1 = 1 0 0 1 1 0 1 0 0 1 1 0 0 1 0 0 1
Mutation

Figure 5.2 An example of mutation using binary notation.

However, since the strings being crossed over are high fitness individuals (i.e. they survived selection), they are expected to have good bit combinations in their string representations and they are expected to create offspring that are also likely to be good strings. If poor solutions are created due to crossover, they are eliminated in the next selection and hence have a short life. However, if good performing solutions are created by the crossover operator, these solutions are likely to get more copies in the next selection and improve their chances to crossover with equally good solutions in subsequent generations. In order to preserve good strings in the selected during reproduction operator, only a proportion of the population is allowed to undergo cross over.

The frequency with which the crossover operator is applied to the individuals in a new generation is governed by the crossover rate. A low crossover rate will cause fewer individuals to be introduced into the population and may lead to search stagnation as the reproduction operator tends to dominate. Higher crossover rates explore the search space more quickly. The author of this thesis has experimented with crossover rates ranging from 50 % to 100% and for applications in water distribution network design and climate prediction, a 100% crossover rate works out fine, (e.g. Mwale et al, 2004; Mwale and Mulenga, 1999)

5.2.2.5 Mutation Operators in the Genetic Algorithm

Mutation is another important genetic operation that is usually performed on chromosomes. Again this is a biologically inspired operation. Mutation randomly alters a gene or small number of genes of the chromosome and moves the search in a slightly different direction than crossover.

Mutation is sometimes used to produce diversity in the population (e.g., genetic engineering). However, there is no universal consensus on the role played by mutation in GAs. Some researchers have used mutation simply to replace some of the original diversity lost during the exchange and selection procedures, while others have used mutation to create variety and new solutions for the GA search. In our experience, we have found that after the GA initially converges, mutation, being undirected and deleterious, fails to introduce better new genetic information in the GA population.

The frequency of mutation must also be controlled in order to produce an effective GA. Mutation governs the introduction of new areas in the search. A high mutation rate will introduce excessive randomness in the search, making it too diverse and preventing convergence. Conversely, too low a mutation rate will reduce diversity and may lead to a sub-optimal solution. From experience, optimal mutation rates seem to vary between 0.001 and 1% (Simpson et al., 1994, Savik and Walters, 1997; Wang and Zheng, 1998; Mwale, 1998; Mwale et al, 2004).

5.2.2.6 Convergence of the Genetic Algorithm

The whole processes of fitness evaluation, selection, crossover and mutation are repeated over and over again on a finite population. At each generation, the selection pressure reduces the diversity of the population towards high fitness solutions. The best surviving solution(s) gradually replaces the poor solutions and eventually only the best surviving solution(s) reproduce. Since mutation is always active, convergence is reached when at least 99% of the population is similar in composition. In other words at the end of the genetic algorithm run, there is only one optimal solution represented by at least 99% of the population.

5.3 Overview of Artificial Neural Networks

ANNs are also a form of biologically inspired computing systems configured from a number of parallel operating processors, termed neurons. Hence, as in GAs, parallel processing of information is the main attribute of ANNs. Individually, the neurons perform trivial tasks, but collectively, in the form of a neural network, they are capable of solving complex problems. Neural networks have their roots in psychology and physiology that date back to the 1940's, with the works of McCullough and Pitts in 1943, (ASCE task committee 2000). In the 1970's neural network development stalled because of disappointments stemming from criticisms of some of the earlier research. Significant work in neural networks was revived in the early 1980's when Hopfield mathematically tied together many ideas from the previous investigations (Bauer, 1994). However, the hiatus in neural network development truly ended in the second half of 1980's, after the development of the back propagation algorithm by Rumelhart et al., in 1986 (Hsieh, 1998). Since then, interest in ANNs and algorithms for training them mushroomed in many different fields (ASCE Task committee, 2000).

5.3.1 The Neuron

The fundamental building block of biological neural networks is based on a nerve cell called the neuron. The neuron has input connectors attached to it called dendrites, which carry signals into the neuron and the axons, which carries signals out of the neuron. The neurons 'sum up' each incoming signal, and if a signal's sum exceeds a preset threshold value, then the neuron fires it across the synapse to another neuron; if not, nothing happens (Haykin, 1994).

In all ANNs, the neuron is also called a node (see Figure 5.3), with one or more input signals, which correspond to dendrites, and one output signal, which correspond to an axon. In all neural networks, the signals arriving at the node are assigned weights and summed to produce an output. This output is forced through an activation function, (usually nonlinear). Biases (b_k) or threshold, ($-b_k$) are added to the output, which increases (or decreases) the output of the activation function. The net output coming out of the node is designated as, O_k.

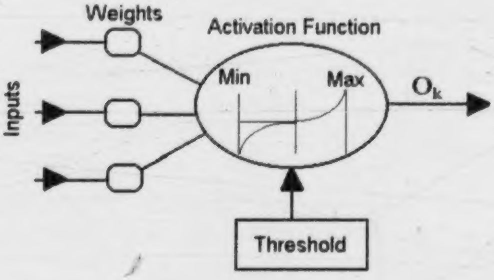

Figure 5.3a The neuron

5.3.2 The Neural Network

In designing neural networks, the important step involves the determination of the neural network architecture and selection of a training algorithm. An optimal architecture may be considered as the one yielding the best performance in terms of objective function optimization, while retaining a simple and compact structure. No unified theory exists for determination of such optimal neural network architectures.

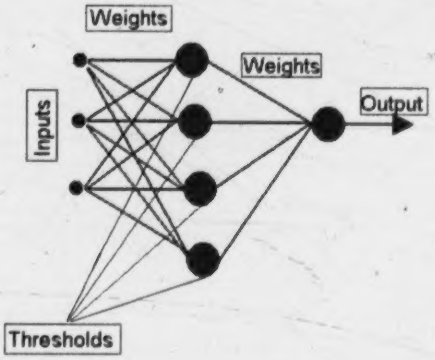

Figure 5.3b Configuration of the artificial neural network

The most commonly used architectures are the multiple layer feedforward networks and the recurrent neural networks. The feedforward network that is used in this thesis, is shown Figure 5.4. Recurrent neural networks have feedback loops and are designed to process recursive functions. This network is not used in this thesis and hence is not discussed further.

In all neural network architectures, the number of neurons in the input and output layers depends on the number of input and output signals to be modeled. The only flexibility lies in selecting the number of hidden layers in the network and the number of nodes of the hidden layers. The number of hidden nodes is selected by trial-and-error, but mainly depends on the complexity of the problem.

5.3.2.2 Training of Neural Networks.

Training the network involves the calibration of weights and neuron thresholds (or biases) so that the difference between the output and the target values is minimized. This difference between the observed and predicted values can be measured by many of the available statistical measures (e.g. correlations, coefficient of determination, root-mean-square-error, bias and others).

The input data is generally divided into three portions for training, cross training, and validation. The data used for training should contain sufficient patterns for the network to adequately learn the patterns. The weights and thresholds are assigned values between ±1.0, which are adjusted during training based on the difference between observed and outputs. The adjustment of the weights and threshold can be continued until a set of weights is found, which results in the smallest difference between outputs and observed. Over-training, which results if the weights and thresholds are fine-tuned so that the network also learns the noise in the data, can be avoided in one of the many ways (e.g., stopped training). Over-training results in poor predictive capability of neural networks, when they are supplied with new input data, other than the training patterns.

In order to train the weights and threshold, various methods are applicable, such as error back propagation, gradient descent, simulated annealing, evolutionary programming (e.g., genetic programming, genetic algorithms, classifier systems and evolution strategies). Since the weight and threshold spaces are spread all throughout the –1.0 to 1.0 range, global optimization algorithms are preferred to local search algorithms.

5.4 The Integrated Genetic Algorithm Neural Network Model (ANN-GA)

From Sections 5.2 and 5.3, it is clear that developing an integrated genetic algorithm neural network (ANN-GA) system has to be formulated as a combination of primitive set of weights and thresholds (or biases) evolving to parameters that can adaptively generalize the performance of the neural networks for predicting seasonal precipitation. The neural network weights (-1.0 to 1.0) and thresholds or biases (–0.05 to 0.05) were encoded using real parameters. The feedforward neural network with three layers: the input, hidden and output layers were trained by the GA. The flow diagram of the combined ANN-GA model is shown in Figure 5.4. Details of the functional operation of the ANN-GA are outlined in the steps below.

Step 1. Initial Population Generation and Evaluation

In random fashion, the ANN-GA creates an initial set of weights, $\mathbf{W}^1$ and $\mathbf{W}^2$ and biases (or thresholds), $\mathbf{B}^1$, for a large number of neural networks, (capital bold letters and the superscripts, respectively indicate a population and the layer numbers). Because of hardware limitations, a maximum of 2300 neural networks were created and maintained at each generation.

To evaluate each neural network, the predictand, O, is obtained as a nonlinear translation of a number of predictors, x, which are usually normalized as,

$$x = \frac{X - \overline{X}}{\sigma_X} \tag{5.2}$$

where $\overline{X}$ and σ_X are the mean and standard deviation of X. The procedure begins by assigning weights to the predictors in the input layer and the weighted inputs are directed to the hidden layer

$$hidunit_{pj} = \sum_{i=1}^{N} W_{ji} x_{pi} + B_{jo} \tag{5.3}$$

where $hidunit_{pj}$ is the weighted input to the jth hidden unit, N the total number of input nodes W_{ji}, are the weights from input unit i to the hidden unit j, B_{jo} are the biases for hidden neuron j and x_{pi} is the i^{th} input of pattern p. The hidden layer undergoes a nonlinear translation,

$$f_1(hidunit_{pj}) = \frac{1}{1+e^{-hidunit_{pj}}} \tag{5.4}$$

where $f_1(hidnunit_{pj})$ is the j^{th} neuron nonlinear activation function. The contents of the hidden layer are further assigned weights and directed to the output layer

$$O_{pk} = \sum_{j=1}^{M} W_{kj} f_1\left(hidunit_{pj}\right) + B_{ko} \tag{5.5}$$

The output, O_{pk} is computed as a weighted average of the hidden units, where M is the number of hidden units, W_{kj} represents the weight connecting the hidden node j to the output k, B_{ko} is the bias for output neuron k.

Each neural network output in the population is evaluated against a known predictand through an objective function (fitness) based on either the Pearson correlation or the root mean square error (RMSE). The ANN-GA model searchers for the weight space (-1 to 1) and bias space (-0.05 to 0.05) to maximize the correlation or minimized the RMSE between the predictor and predictand.

Step 2: Ranking and Selection of Neural Networks.

The linear ranking selection scheme was used in this thesis. The correlation values were ranked, with the best at the top and the worst at the bottom. Next, random selection of solutions was done with replacement. Here a random number was created between 1 and 1955 (i.e. 85% of 2300) and the neural network corresponding to that number was copied from the ranked population and placed in the offspring population. This procedure was repeated 2300 times. Selection from

85% meant that at each step, 354 neural networks were discarded from the population.

Step 3: Crossover of the Neural Networks

The selected neural networks were mated in pairs from the offspring pool at random. To perform mating or crossover, a random number was generated between 1 and 3 to identify the location of the crossover point. The weights of the neural network on either side of the location were swapped between the two networks. The crossed-over networks were then thrown back into the mating pool as part of the new population. The procedure was continued until another 2300 neural networks were created. Only one-point crossover was performed in this thesis.

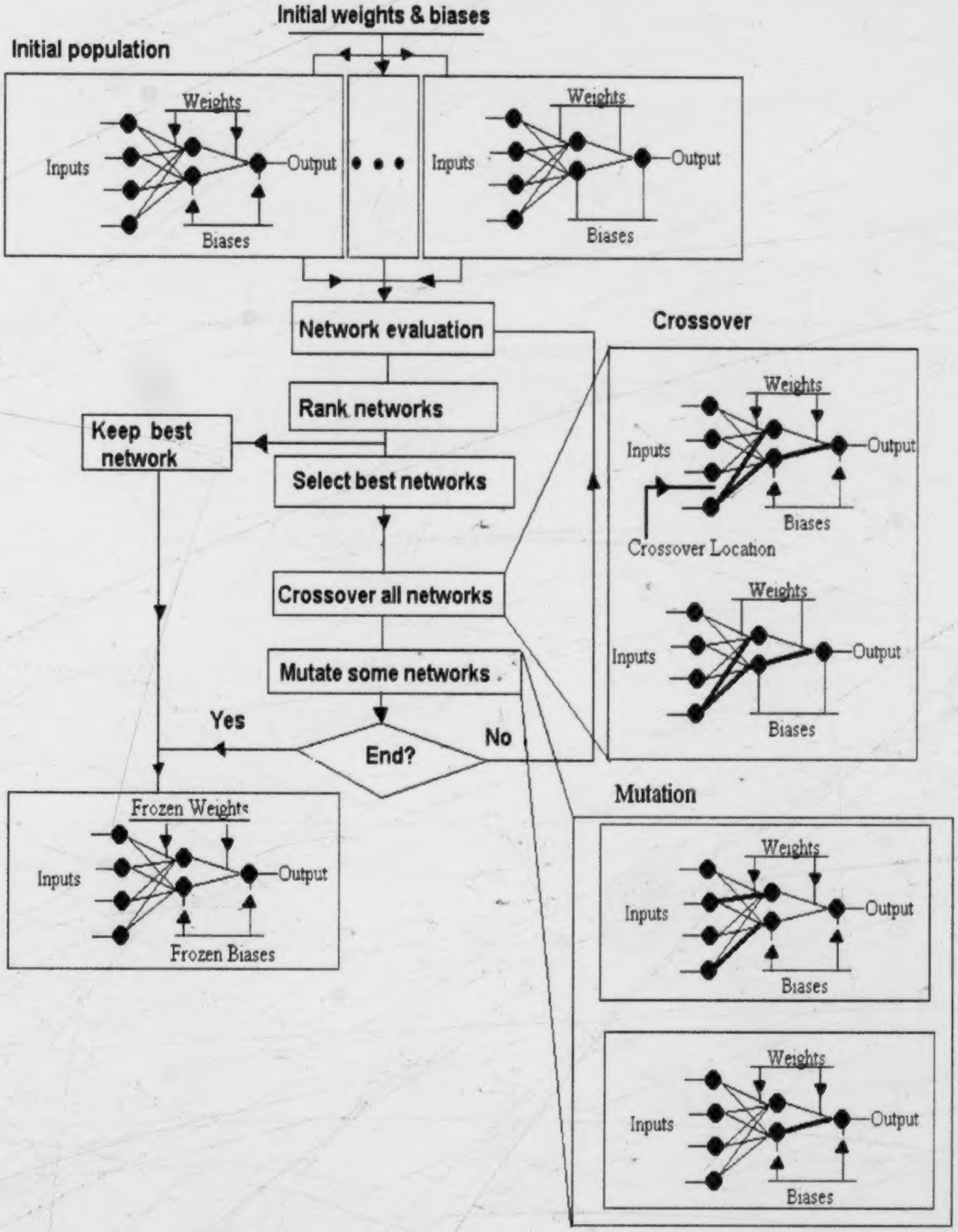
Initial weights & biases
Initial population
Weights
Inputs
Output
Biases
Weights
Inputs
Output
Biases
Network evaluation
Rank networks
Keep best network
Select best networks
Crossover all networks
Mutate some networks
Yes
End?
No
Crossover
Weights
Inputs
Output
Biases
Crossover Location
Weights
Inputs
Output
Biases
Mutation
Weights
Inputs
Output
Biases
Weights
Inputs
Output
Biases
Frozen Weights
Inputs
Output
Frozen Biases

Figure 5.4 The ANN-GA model.

Step 4: Mutation of the Neural Networks

Some (1% of 2300 (i.e., 23 neural networks)) were randomly selected and a handful of their weights and biases (about 10%) were randomly replaced (see dark lines in insert of Figure 5.4).

After crossover and mutation, the neural networks were put back into the mating pool for further reproduction and selection. The above procedures were repeated through several epochs (or generations in genetic algorithm terminology). The genetic algorithm neural network developed in this thesis is an elitist model. That means that at each generation, the ANN-GA model kept the best network in a separate location until a better solution was found in successive generations. At the end of the calibration the weights and biases of the best surviving neural network were kept for use with new input data, (i.e. during the validation stage).

5.4.1 Generalization in Neural Network Training

Due to a large number of parameters and the flexibility of neural networks, training of the neural networks usually results in model outputs that fit the data very well during training but perform poorly during the validation or test period. Two reasons were identified during the applications of the ANN-GA model. These are as follows:

(1) The nature of the objective function used.

(2) The information contained in the predictor field is too closely mapped on to the weights and biases during training, which could result in the neural network

memorizing information from both the signal and the noise, instead of just learning the general relationships found in the training data.

The other reason not directly related to this research might be that the training data and the validation data differ from each other so much that the general relationships found from the training data may not be quite applicable to the validation data, which is not common with climate.

It was observed that when the RMSE was used as the objective function, GA tended to over fit ANN to the training data, resulting in very low errors between the observed and predicted data. However, during validation the errors could turn out to be too large. When correlation was used as the objective function, better generalization was achieved.

5.4.1.1 Bootstrap Split-Sampling Training

Bootstrap split-sampling training is a procedure where the training data is randomly split into two portions. One portion of the data is used to train the model and the other portion of the data is used to test the model. This procedure is repeated for each network at each generation. The idea is that weights and biases should be selected based on training that provides a maximum number of patterns of the training data. The portions of training and testing datasets are created by randomly choosing the sections of data used for training and testing. Bootstrap split-sampling training was experimented on in the ANN-GA, along with training that involves only one sample. Although a theoretically sound approach, no obvious advantage was found in using the split sample training in the ANN-GA prediction model. Hence, the one split-sample training and testing was extensively used in this thesis.

5.5. Application of the ANN-GA model

5.5.1 Introduction

This section describes the application of the ANN-GA model. The aim is to assess the performance of the model and to demonstrate its robustness and viability. The performance of the ANN-GA model is examined by using the statistical measures of Hanssen Kuipers (HK) categorical skill scores, the Pearson correlation coefficients (generally called the correlation coefficient) and the root-mean-square-error (RMSE).

5.5.2 Evaluation of the Prediction Skill

The Hanssen Kuipers (HK) skill score, which is also known as the Kuipers' performance index (KPI) or the true skill score (TSS) is based on categorical forecasts of discrete predictands, where the prediction consists of a flat statement that one and only one of a set of possible events will occur (Wilks, 1995). For rainfall, the categories of "Dry", "Near Normal" and "Wet", with tercile percentages of below 33%, 33% – 66% and above 66%, respectively have been used (e.g., Ntale et al., 2003, Mwale et al., 2004, Mwale and Gan, 2004). In this thesis, the HK score was applied to the rainfall grid boxes, each 2.75° x 3.75° (or 290 km x 394 km). The reference point of the HK skill score is the number of correct observation hits expected by chance. With this reference point, the HK skill score is computed as follows (Ntale et al., 2003):

$$HK = \frac{C - C_c}{P - C_{oc}} \tag{5.6}$$

In Eqn 5.6, C is the total number of correct forecasts, P is the total number of forecasts obtainable with a perfect forecast model, C_c is the number of correct hits expected by chance. and C_{oc} is the reference point. HK skill score can also be expressed using probabilities. For example, for the “Dry”, “Near Normal” and “Wet”, categorical forecasts, the HK score is computed as follows (Wilks, 1995, Ntale et al., 2003):

$$HK = \frac{\sum_{i=1}^{3} p(O_i, P_i) - \sum_{i=1}^{3} p(O_i) \times p(P_i)}{1 - \sum_{j=1}^{3} [p(O_j)]^2} \tag{5.7}$$

where O_i and P_i are the i^th^ observed and i^th^ predicted values in a square contingency table. To take into account the “Dry”, “Near Normal” and “Wet”, categories, a 3 x 3 contingency table is used. The maximum and minimum values of HK score are between -1 and +1. HK scores of +1 represent perfect forecast, while HK scores of zero represents random forecasts and HK of less that zero represent forecasts that are inferior to random forecasts. Hence all forecasts greater than zero represent forecasts better than random.

The Pearson correlation coefficient, ρ, is a single-valued measure of the linear association between two variables. ρ is computed as

$$\rho = \frac{\sum_{k=1}^{n} (O_k - \overline{O})(P_k - \overline{P})}{\left(\sum_{k=1}^{n} (O_k - \overline{O})^2 \right)^{0.5} \left(\sum_{k=1}^{n} (P_k - \overline{P})^2 \right)^{0.5}} \tag{5.9}$$

where O_k and P_k are the observed and predicted values, $\overline{O}$ and $\overline{P}$ their respective means and n the sample size. The correlation coefficient ranges between 1 and –1. The extreme positive and negative values indicate perfect positive and negative linear associations, respectively.

The square of the correlation coefficient, ρ^2 presented as a percentage specifies the proportion of variability of the observed rainfall, locally, accounted for by the predicted rainfall. It it ranges from 0 (for zero explained variance) and 1(for complete explained variance).

The root mean square error (RMSE) is computed as

$$RMSE = \left(\frac{1}{n} \sum_{k=1}^{n} \left(O_k - P_k \right)^2 \right)^{0.5} \qquad (5.10)$$

The RMSE for a perfect prediction is zero and increasing RMSE indicates decreasing accuracy of the prediction.

5.5.3 Predictor Data Selection

The existence of statistically significant oscillations of around 2 years in both the SST of the Indian and Atlantic Oceans, and the SON and MAM rainfall of East Africa and the summer rainfall of Central South and Southern Africa (Chapter 3) and the strong relationships found between the SST SAWP of the south Atlantic and Indian Oceans and the rainfall WPCs (Chapter 4) suggests that:

(1) The seasonal rainfall of SON, MAM and the summer are predictable using some selected Atlantic and Indian Ocean sea surface temperature fields, and

(2) The preceding April-May-June seasonal sea surface temperature variability of the Atlantic and Indian Oceans are suggested predictors of the rainfall.

Since the lag-1 autocorrelation of the SAWP and WPCs was high (around 0.9), from Eqn. 4.1 of Chapter 4, the effective lengths of the SAWP and the WPCs decreased to about 3-4 years and the significant correlation between rainfall WPCs and SST SAWP at 95% level was above 0.997. The ocean areas covered by this level of correlation were small and very few data could be collected. Since the spatial correlation patterns between rainfall WPC1 and rainfall SAWP of Chapter 3, covering most of the region generally varied between some threshold correlation value (e.g., 0.3), it was decided that SST data be collected from areas of the oceans where the correlation between rainfall WPC1 and SST SAWP exceeded the threshold correlation. In Central South Africa correlations exceeding 0.4 were used (Mwale et al., 2004), while for the SON rainfall of East Africa, correlations exceeding 0.5 were used (Mwale and Gan, 2004). For the rainfall of southern Africa and MAM season of East Africa, correlations of between 0.3 and 1 were used. Generally the stronger the signal the higher was the threshold value. During each prediction experiment, the observed raw SST data was standardized and averaged over the three months for each grid station to give one seasonal data set.

SST data from all the seasons (i.e., OND, JFM, AMJ and JAS) could be used for predicting the rainfall. However, the AMJ season was chosen to take advantage of time lag common to all rainfall seasons. The AMJ provides a 2-month lead-time for SON rainfall, 4-month lead for the summer rainfall (which begins in October) and 8-month lead time for the MAM rainfall.

To speed up the computations, EOF was applied to the AMJ SST dataset and 6 PCs accounting for 87% of the SST data for central south, 5 predictor PCs accounting for 77% for SON rainfall and 6 PCS 87% of predictor data for the summer rainfall was used. The 77% variance accounted for by the SST data for predicting the SON rainfall appeared low, probably indicating there was some noise associated with SST data correlated with rainfall at the 0.5 level. Higher values of the correlation threshold such as 0.6 might have resulted in less PC modes explaining more of the variance. Standardized rainfall data from the 21, 31 and 58-grid stations from Eastern, Central and Southern Africa, respectively, were used.

The correlation coefficients, the HK scores and the RMSE of the predicted rainfall were computed using a 11-year validation period, 1987-1997 for eastern and southern Africa and for 10 years for central south Africa (1985-1994). For an 11-year period, statistically significant correlation at the 5% level is 0.602 while that for 10 years is 0.632.

5.5.4 Prediction of the SON Rainfall of East Africa

The spatial display of the correlation coefficients, HK scores and RMSEs between the predicted and observed SON rainfall is shown in Figure 5.5. Correlation coefficients of between 0.7 and 0.9, RMSEs of 0.4 and 0.75 and HK scores of between 0.2 and 0.8 were achieved.

High skill was achieved in central and eastern Tanzania, Kenya and almost all of Uganda with correlations greater than 0.8, RMSE less than 0.65 and HK scores greater than 0.4. These regions were also found to have the largest positive correlation between SON WPC1 and the SAWP (Chapter 3) (i.e. they had the strongest SON rainfall signal). The prediction skill decreased westwards from about 33°E to 30°E following the strength of the SON rainfall signal. In Figure 3.3(a) of

Chapter 3, this area was identified as the Great Rift Valley (GRV), where SON rainfall is probably modulated by the equatorial Congo basin or by the sudden change in altitude when entering into the GRV. The prediction skill of this region was low compared to the rest of the region.

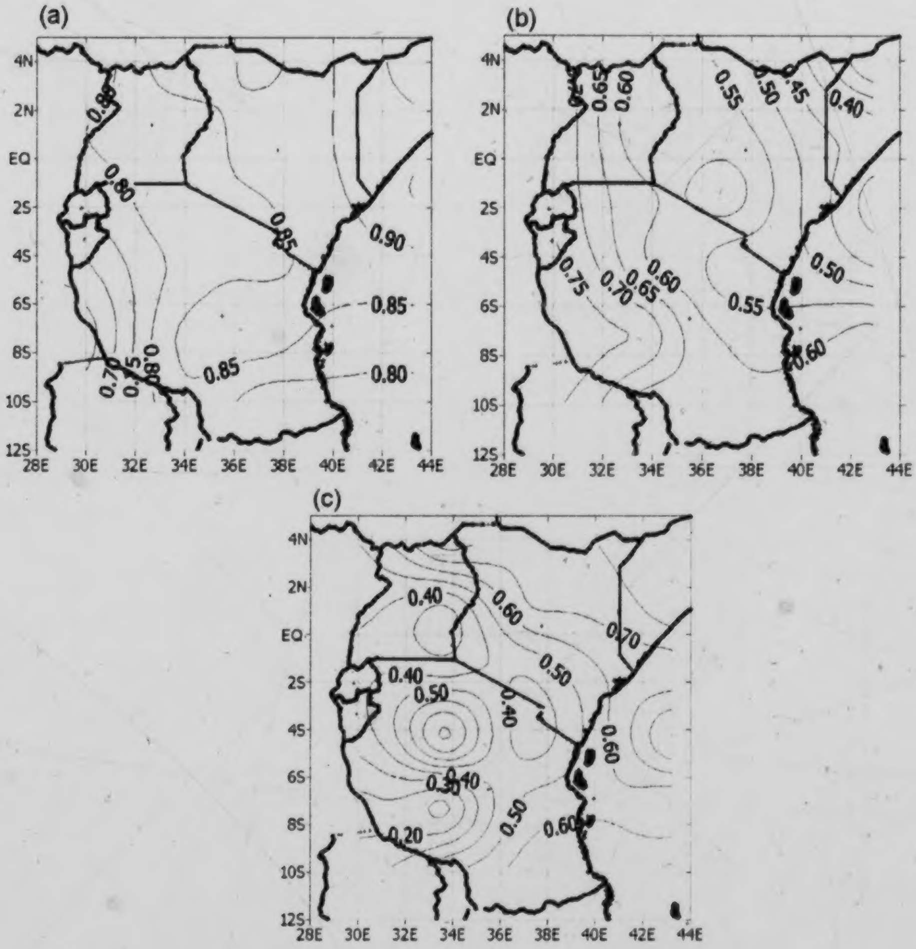
(a)
(b)
(c)
4N
2N
EQ
2S
4S
6S
8S
10S
12S
28E
30E
32E
34E
36E
38E
40E
42E
44E
0.85
0.80
0.85
0.90
0.85
0.85
0.80
0.70
0.75
0.80
0.65
0.60
0.55
0.50
0.45
0.40
0.75
0.70
0.65
0.60
0.55
0.50
0.60
0.40
0.60
0.70
0.50
0.40
0.50
0.40
0.60
0.30
0.40
0.50
0.60
0.20

Figure 5.5 Contour plots at 0.05 or 0.1 intervals (to avoid crowding) showing the (a) correlation coefficient, (b) RMSE, and (c) HK scores between predicted and observed SON standardized rainfall of East Africa using the ANN-GA model, driven by SST predictor fields from the Indian and Atlantic Oceans.

The above results show that the SON rainfall variability is influenced by SST variations in the SW and NW Indian Ocean and the South Atlantic Ocean. Overall, using sectors of predictor fields identified in these ocean basins, the non-linear ANN-GA system could predict between 42% and 80% of the SON rainfall variability at 2-month lead-time.

5.5.5 Prediction of the MAM Rainfall of East Africa

The skill scores between the predicted and observed MAM rainfall is shown in Figure 5.6. As can be seen in these figures, the regions with the best prediction skill are the eastern Tanzania and southern Uganda, SW Tanzania and Kenya. These regions also showed strong MAM signals. Correlations coefficients of between 0.82 and 0.9, RMSEs of 0.5 and 0.6 and HK scores of between 0.5 and 0.8 were achieved.

Camberlin and Philippon (2002) indicated that MAM rains as a whole do not exhibit very strong relationships with any large-scale climate anomalies due to a weak internal coherence. Our results seem to suggest that although the MAM signal is weak, it does have associations with SST variabilities, and these associations are strong enough to be exploited for predicting the MAM rainfall. Overall, the non-linear ANN-GA system could predict between 67% and 81% of the precipitation variability at 8-month lead-time.

5.5.6 Prediction of Central Southern Africa Summer Rainfall

The spatial display of the correlation, HK scores and RMSEs between predicted and observed central southern Africa (CSA) rainfall is shown in Figure 5.7. Correlations of between 0.8 and 0.9, RMSEs of 0.4 and 0.9 and HK scores of between

0.4 and 0.8 were achieved for most of the Central Southern Africa region. The skill slightly decreased towards the coastal areas following the strength of the rainfall WPC1.

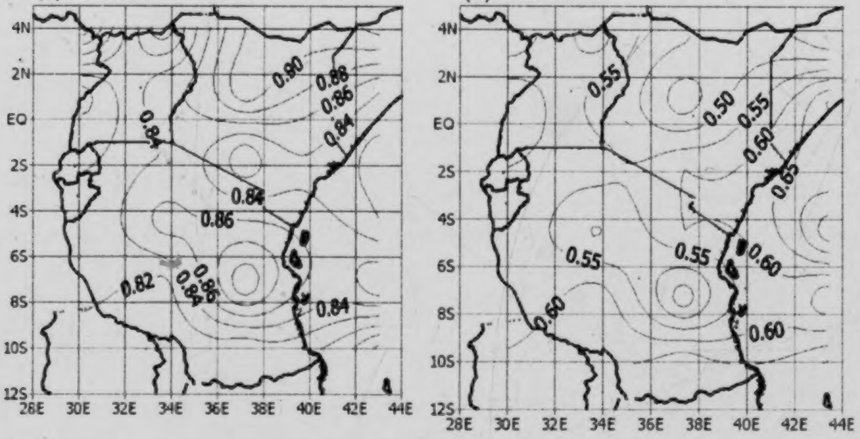
(a) Correlation

(b) RMSE

4N
2N
EQ
2S
4S
6S
8S
10S
12S
28E
30E
32E
34E
36E
38E
40E
42E
44E
0.90
0.88
0.86
0.84
0.84
0.84
0.86
0.82
0.84
0.86
0.84
0.55
0.50
0.55
0.60
0.65
0.55
0.55
0.60
0.60
0.60

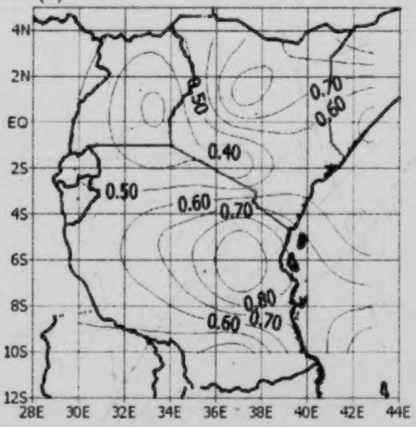
(c) HK

4N
2N
EQ
2S
4S
6S
8S
10S
12S
28E
30E
32E
34E
36E
38E
40E
42E
44E
0.50
0.70
0.60
0.40
0.50
0.60
0.70
0.80
0.60
0.70

Figure 5.6 Contour plots at 0.1 intervals showing the (a) correlation coefficient, (b) RMSE, and (c) HK scores between predicted and observed standardized MAM rainfall of East Africa using the ANN-GA model driven by the SST predictor fields from the Indian and Atlantic Oceans.

The high correlations show that the linear correlation between the predicted and observed rainfall was captured almost everywhere in the region. The higher HK score also showed that most forecasts fell in their correct categories. The results also show that the rainfall variability of the region is influenced by SST variations in the Atlantic and parts of the southern Indian Ocean. Overall, using sectors of predictor fields identified in the oceans, the non-linear ANN-GA system could predict between 64% and 81% of the (CSA) rainfall variability at 3-month lead-time.

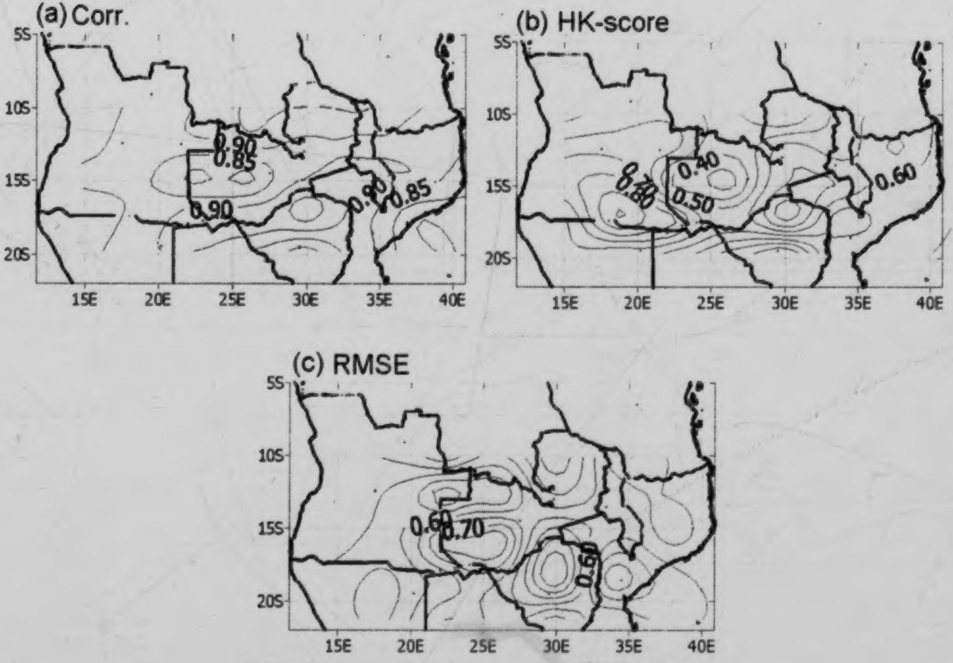

Figure 5.7 Contour plots at 0.1 intervals showing the (a) correlation coefficient, (b) RMSE, and (c) HK scores between predicted and observed standardized summer rainfall of Central Southern Africa using the ANN-GA model driven by the SST predictor fields from the Indian and Atlantic Oceans.

5.5.7 Prediction of Southern African Summer Rainfall

The correlation coefficients, the categorical HK scores and the RMSE of the Southern Africa summer rainfall are shown in Figure 5.8. The ANN-GA performed well in the regions where the summer rainfall signals were strong. In most of southern

Africa, the correlations generally ranged between 0.75 and 0.9 (56-81% of explained variance). The RMSE ranged between 0.4 and 0.8 and these were generally higher in areas where correlation between predicted and observed rainfall was low. Elsewhere, RMSE ranged between 0.4 and 0.8. The HK scores ranged between 0.5 and 0.9.

Given that the prediction skill of ANN-GA was consistently high for rainfalls of eastern and southern Africa, it shows that the nonlinear relationships between rainfall in these areas and SST variations of the Indian and Atlantic Oceans are well captured by the ANN-GA model. These results also demonstrate that selection of relevant predictor data constitutes an important step in seasonal climate prediction.

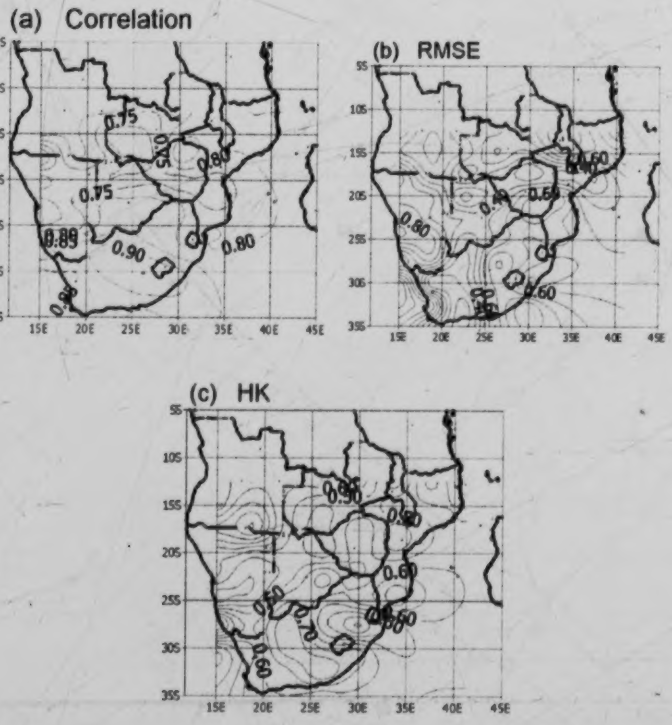
(a) Correlation
(b) RMSE
(c) HK
5S
10S
15S
20S
25S
30S
35S
15E
20E
25E
30E
35E
40E
45E
0.75
0.75
0.80
0.80
0.85
0.90
0.80
0.60
0.60
0.60
0.90
0.60
0.60
0.50

Figure 5.8 Contour plots at 0.1 intervals showing the (a) correlation coefficient, (b) RMSE, and (c) HK scores between predicted and observed standardized summer rainfall of greater southern Africa using the ANN-GA model driven by SST predictor fields from the Indian and Atlantic oceans shown in shaded dark areas of Figs. 4.5(a) and (b).

5.6 Recent developments in Genetic Algorithms

5.6.1 Competent Genetic Algorithms

The GA algorithm presentation in this Chapter is based on what is called a simple GA. As we saw, this algorithm operates on fixed length chromosomes and mix building blocks of chromosomes by crossover and mutation operators. The trouble with using fixed length strings, crossover and mutation operators in the GA is that the GA sometimes gets trapped in local optimum neighborhoods, because it fails to adequately reproduce high fitness populations when the complexity of the problem being solved increases (Goldberg, 2002; Wu and Simpson, 2001). Because of the above problem, other structures of GAs have been sought since the late 1980's (e.g. Goldberg et al., 1989). Improved hybrid GAs (also called Competent GAs), such as messy GAs have been developed and shown to perform better than simple GAs (e.g., Wu and Simpson 2001). These algorithms are called messy because they have variable length representation of chromosomes. The lengths of the chromosomes are different within a single population and the lengths of the chromosomes also change at each generation

In the messy GA, the crossover operator is replaced by "cut" and "splice" operations. The cut operator cuts the chromosome into two and the splice operator joins the head of one chromosome to the tail of the other. The idea behind the use of variable string chromosomes comes from the theory of biological evolution, which assumes that the original individual chromosomes were created from single atoms, which became joined and developed into complex organisms.

Different forms of messy GA exist. In the structured messy GA of Goldberg et al., (1989), the GA start with short strings, but were concatenated over generations. As concatenated stings increase in length, they are "cut" and "spliced" at a rate that depends on the length of the chromosome (i.e.)

$$P_c = P_k(\lambda - 1) \tag{5.11}$$

where P_k is the specified cutting probability, and λ is the length of the chromosome. Cutting is done when P_c exceeds a prescribed threshold, otherwise splicing is performed on the short strings. Hence in the beginning, when the strings are short, the chromosomes have a higher chance of being spliced than cut. In successive generations the splicing will result in strings that that grow longer until P_c is exceeded.

In other forms of messy GA such as the "fast" messy GA (Wu and Simpson, 2001), an original population of fixed length chromosomes is initially created. Then a building block filter is applied to the fixed length chromosomes to extract a number of high fitness short-length strings to comprise the initial set of short-strings. These short-strings are then juxtaposed to produce the initial population of full-length strings, which undergo reproduction as in the simple GA.

The GA developed in this thesis is a simple GA. It will therefore be a benchmark against which the performance of all future competent GAs that will be tested for predicting climatological variables

CHAPTER 6

PREDICTION OF WEEKLY STREAMFLOW FROM SEASONAL OCEANIC VARIABILITY

6.1 Introduction

Chapter 3 demonstrated that the nonstationary variability of the rainfall has been a consistent feature of the climate of Eastern and Southern Africa. The decrease in energy of the SON and summer rainfall SAWP after 1965 for both Eastern and Southern Africa rainfall was found to be consistent with the decrease in the streamflow of most major rivers of the subcontinent, (Fanta et al., 2001; Mwale et al., 2004). Associated with these rainfall variations have been significant economic losses and widespread famine (BBC, 2002a, b and c; Ntale, 2001). Effects of droughts extend beyond agriculture and affect other sectors, such as water supply and hydroelectric power generation. For example between 1992 and 1996, dams in Namibia were less than 20% full, prompting the government to express grave concerns about the ability of the country to provide water to its people (Jury and Engert, 1999). Since many of the rivers and lakes in Eastern and Southern Africa form or cross international boundaries and some rivers within individual countries serve conflicting interests (e.g., agriculture, power generation, industry, game reserves, tourism and urban water supply, and ecosystems), it has become necessary to integrate seasonal climate prediction of rainfall to the prediction of streamflow, at smaller time steps adequate for aiding water resource distribution for the approaching year.

Despite the apparent evidence that rainfall in Eastern and Southern Africa is influenced by nonstationary SST variability, efforts to predict annual streamflow of the rivers from seasonally averaged variability of SST and other oceanic variables have been very limited. To our knowledge only Landman et al., (2001) has made such as an attempt. In their work, Landman et al., (2001) downscaled GCM output to predict seasonal (December-February) streamflow to twelve dams in South Africa. Although the need for forecast guidance at seasonal time scales is becoming necessary, the time steps involved are too coarse to meet most water resource management needs.

In the last two decades, hydrologists have managed to model the dynamics of the interaction between historical rainfall, runoff and evaporation at the land surface-atmosphere interface, using distributed physics-based hydrologic models (e.g. Beven and Kirkby 1979; Gan and Biftu, 2000) and lumped parameter moisture accounting hydrologic models (e.g., Gan and Biftu, 1996; Nijssen and Lettenmaier, 1997). Depending on basin scale, however, the time steps involved have been mostly hours or days. Using these time steps, accurately calibrated hydrological models have been used to simulate or even extend runoff records, necessary for sizing of reservoir yield and storage, from long records of historical rainfall. With climate variability and climate change issues being increasingly blamed to affect basin streamflow (Kahya and Dracup, 1993; Lall and Mann, 1995; Coulibaly et al., 2000, Mwale et al., 2004), there are more and more demands to assess such climatic effects on basin hydrology using physics-based and/or lumped parameter hydrologic models. These demands include (1) assessment of streamflow arising from climate and land use changes, (2) evaluation of the seasonal and geographical patterns of water supply and, (3) determination and maintenance of ecological in-stream flow requirements at smaller time steps. While all of the above issues are equally important, the increasing imbalance between water supply and demand in Eastern and Southern Africa, resulting from decades of declining rainfall and streamflow, (Mwale et al., 2004, Fanta et al., 2001) and a recent shift towards more integrated management of limited water resources requires that efforts in accurate long-term prediction of rainfall and streamflow at smaller time steps be accelerated.

Many approaches are available to forecast streamflow from atmospheric and oceanic variability. A majority of these approaches have focused on employing general circulation model (GCM) or regional climate model outputs to model the rainfall-runoff process (e.g., Bindlish and Barros, 2000; Yu, 2000; Canon and Whitefield, 2002). In Yu (2000) a hydrologic model is forced using outputs from a mesoscale meteorological model, MM5, to forecast the streamflow of the Susquehanna River Basin in Pennsylvania (USA). Bindlish and Barros (2000) used spatial patterns of terrain and wind fields to disaggregate precipitation fields of MM5 to force a hydrological model to predict streamflow of the west branch of the Susquehanna River Basin. Using GCM fields, Canon and Whitefield (2002) downscaled five-day averages of streamflow of British Columbia Rivers of Canada by forcing an ensemble of artificial neural networks (ANNs). The linked meteorological-hydrological systems of Yu (2000) and Bindlish and Barros (1999) were forced with individual storm data, at hourly time steps. While at basin-scale it generally makes sense to use shorter modeling time steps, it is difficult to forecast individual storm events one season ahead of time at hourly or even daily time steps. Hence, these models may not be directly applicable to predicting both the seasonal rainfall and the streamflow at hourly or daily time steps for the approaching year.

Fully coupled meteorological-hydrologic models capable of accounting for feedback mechanisms in the energy and moisture fluxes at the land-atmosphere interface may be used to simulate seasonal precipitation fields at hourly or daily time steps by forcing them with predicted or observed monthly SSTs. However, problems associated with scale incompatibility make it difficult to integrate GCM outputs to hydrological fields. In addition, the failure of these models to properly account for local sub-grid variability is another cause for concern. The length scale of rainfall ranges between a few kilometers to about 60 km (Shen et al., 2001), and it is highly variable spatially, especially for convective storms. Precipitation is a major governing factor in the temporal and spatial distributions of runoff production and soil moisture dynamics. However, sub-grid parameterization schemes proposed to account for local synoptic-scale processes had resulted in erroneous precipitation fields (e.g., Jenkins and Barron, 1997; Xu, 1999). As more and more powerful computers are being built, coupled meteorological-hydrological modeling systems may eventually become promising for predicting streamflow at seasonal lead time, but that may not happen in the foreseeable future. As of now, the growth of numerical round-off errors, and more climate-based parameterizations still need to be improved, prevent these models from being directly applicable for rainfall-runoff prediction at relatively long lead time. We believe the successful development of such models are still many years away (Yarnal et al., 2000).

Although climate processes do not repeat themselves exactly, given a historical record of the rainfall and streamflow data, one would obviously like the prediction model to have the ability to reproduce the statistics of the historical data. More importantly, however, one would also like the model to produce the statistical properties of the future rainfall and streamflow. If the statistical properties of the past and future rainfall and streamflow can somehow be conserved, it may be argued that the model used for the reconstruction of past and prediction of the future is adequate. Such important properties would include the mean, variance, co-variances between different levels of aggregation of the rainfall and streamflow and the probability distributions. The projected climatic fields of GCM usually cannot replicate the historical properties of basin-scale hydrologic data.

The literature seems to suggest that only the disaggregation and the analog approaches are known to conserve historical statistical properties of the data (e.g., Salas et al., 1980; Zorita and von Storch, 1999; Kumar et al., 2000). The analog method has been applied to weather forecasting (e.g., Lorenz, 1969) and short-term climate prediction (e.g., using analogues of GCM output) (e.g. van den Dool, 1994). Since the climate does not repeat itself exactly, paleoclimatic data of several thousands years are required for analogs to be useful. With longer data sets, there is a higher chance of finding close matches of large-scale circulations that are similar to the ones being downscaled. Since data recording in Eastern and Southern Africa, like most parts of Africa did not begin until after World War II in 1945, the analog method is not applicable, unless paleoclimate data is available. Therefore the disaggregation method, which can model seasonally varying historical hydrologic processes, was used in this thesis.

Disaggregation modeling is a process by which one or several time series at a coarse time scale are broken down to a finer time scale. If more than one level is involved the disaggregation is usually performed in stages, such as from annual time scales to monthly time scales and from monthly to weekly time scales and so on. The basic idea of disaggregation began in the 1940s (Hsieh et al., 1986). However, Valencia and Schaake (1973) were the first to present a well-accepted disaggregation model and the latter laid the groundwork for the majority of subsequent disaggregation approaches. Temporal or spatial disaggregation is usually based on the co-variance structures of the streamflow at different levels of aggregation. However other approaches, such as the nonparametric approach of Lall et al., (1996) based on the kernel density estimation, the random cascade process of Schertzer and Lovejoy (1987) and the nonparametric approach using the *k* nearest neighbors of Kumar et al., (2000) have also been proposed. The Valencia and Schaake (1973) model is used in this thesis.

To predict streamflow at weekly time steps from predicted seasonal rainfall, this thesis proposed the integration of ANN-GA, disaggregation, evapotranspiration and the Sacramento moisture accounting (SAC-SMA) models. In this approach, we applied the disaggregation model to downscale seasonal rainfall of CSA temporally to weekly time steps. We then forced the SAC-SMA model to predict streamflow at weekly time steps. This combined approach is referred to as ANN-GA-DIS-SMA. The other approach we tried was to integrate the ANN-GA, a disaggregation model and an evapotranspiration model, so that we directly downscale predicted seasonal precipitation, less evapotranspiration into weekly streamflow. The combined approach is referred to as ANN-GA-DIS. The above approaches are shown in Figures 6.1 and 6.2, respectively. The components making up Figures 6.1 and 6.2 are described in detail in sections 6.2 to 6.4 and the summary and conclusions are presented in section 6.5.

6.2 Valencia and Schaake Model

The derivation of the model after Valencia and Schaake (1973) and Tao and Delleur (1976) is given below. The general disaggregation model takes the form:

$$Y(t) = AX(t) + BV(t) \qquad (6.1)$$

In Eq (6.1), *Y(t)* maybe an *n* x *1* vector of seasonal values of the tth year, *n*, the number of seasons in a year (for examples, 12 if monthly values are generated), *X(t)* being the value of the annual series for the tth year, *V(t)* is an *n* x 1 vector of independently distributed standard normal deviates (with a mean zero and variance of one), A is an *n x 1* vector of coefficients, and B is an *n* x *n* matrix of coefficients. The vector A and matrix B are obtained by analysis of N years of the historic data that may relate, say, seasonal to annual values. The second moments needed to estimate A and B are the covariance matrices

$$S_{XX} = E[X][X]^T \ , \ S_{XY} = E[X][Y]^T, \ S_{YX} = E[Y][X]^T, \ S_{YY} = E[Y][Y]^T \qquad (6.2)$$

where S_{YY} and S_{XX} are the variance matrices over N years of *n* seasonal values Y, and that of observed annual values X respectively, S_{YX} is the *n* x 1 covariance matrix between the *n* seasonal observations, Y, and the annual values X, over N years. Valencia and Schaake (1973) showed that:

$$E[Y][X]^T = AE[X][X]^T \tag{6.3}$$

so that

$$A = S_{YX} S_{XX}^{-1} \tag{6.4}$$

and that

$$E[Y][Y]^T = AE[X][X]^T A^T + E[W][W]^T \tag{6.5}$$

or

$$S_{WW} = BS_{VV} B^T = BB^T \tag{6.6}$$

so that

$$BB^T = S_{YY} - S_{YX} S_{XX}^{-1} S_{XY} \tag{6.7}$$

If A and B are chosen according to Eqs (6.4) and (6.7) the first and the second-moments resemblance criterion is satisfied regardless of the underlying multivariate distribution of Y, X and V (Valencia and Schaake, 1973). Eq (6.7) shows that only the matrix BB^T and not B is given. Matrices of the form $BB^T = C$ are called Gramian matrices, C being the Gramian of B. Given C there is no unique solution to the matrix B, since any matrix of the form B.E, where E is orthogonal will satisfy the above relation. The necessary and sufficient condition for the estimation of matrix B is that the covariance structure of BB^T (or C) be positive semi-definite. Grammian matrices are known to be positive semi-definite (Valencia and Schaake, 1973) since they contain the co-variances of the observed variables. There are two ways to estimate the matrix B.

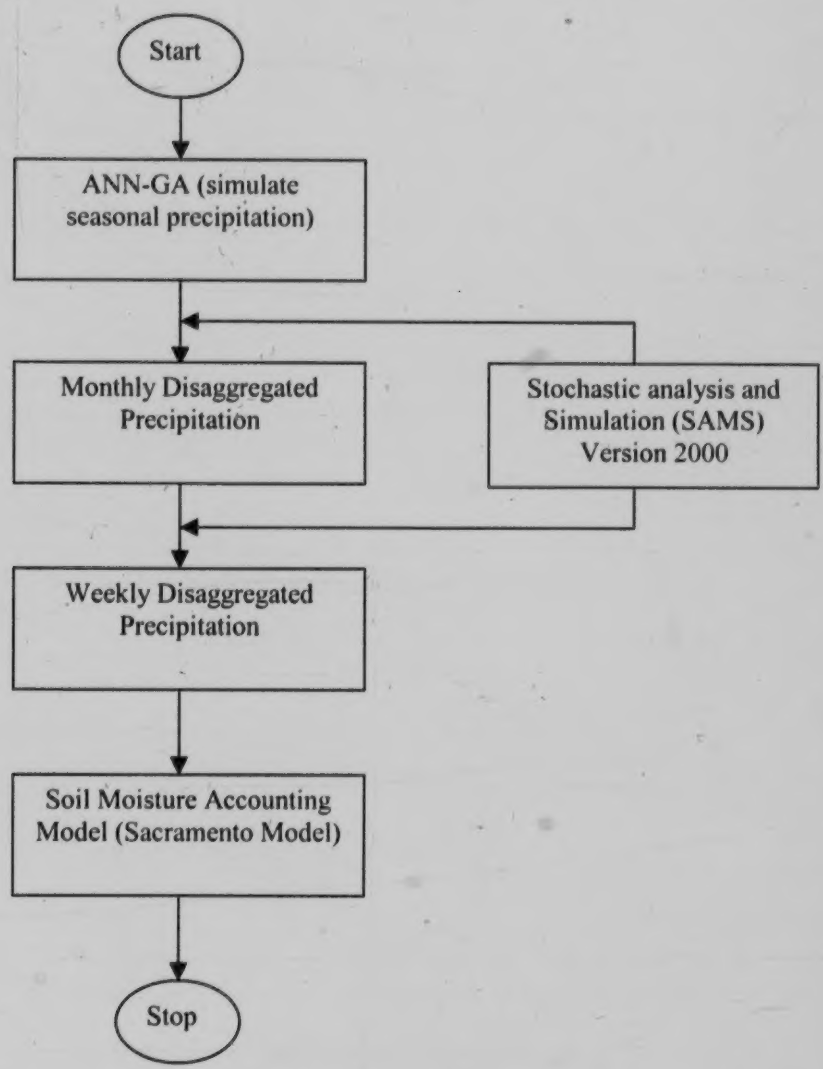
Start
ANN-GA (simulate seasonal precipitation)
Monthly Disaggregated Precipitation
Stochastic analysis and Simulation (SAMS) Version 2000
Weekly Disaggregated Precipitation
Soil Moisture Accounting Model (Sacramento Model)
Stop

Figure 6.1: Flowchart of the ANN-GA-DIS-SMA approach

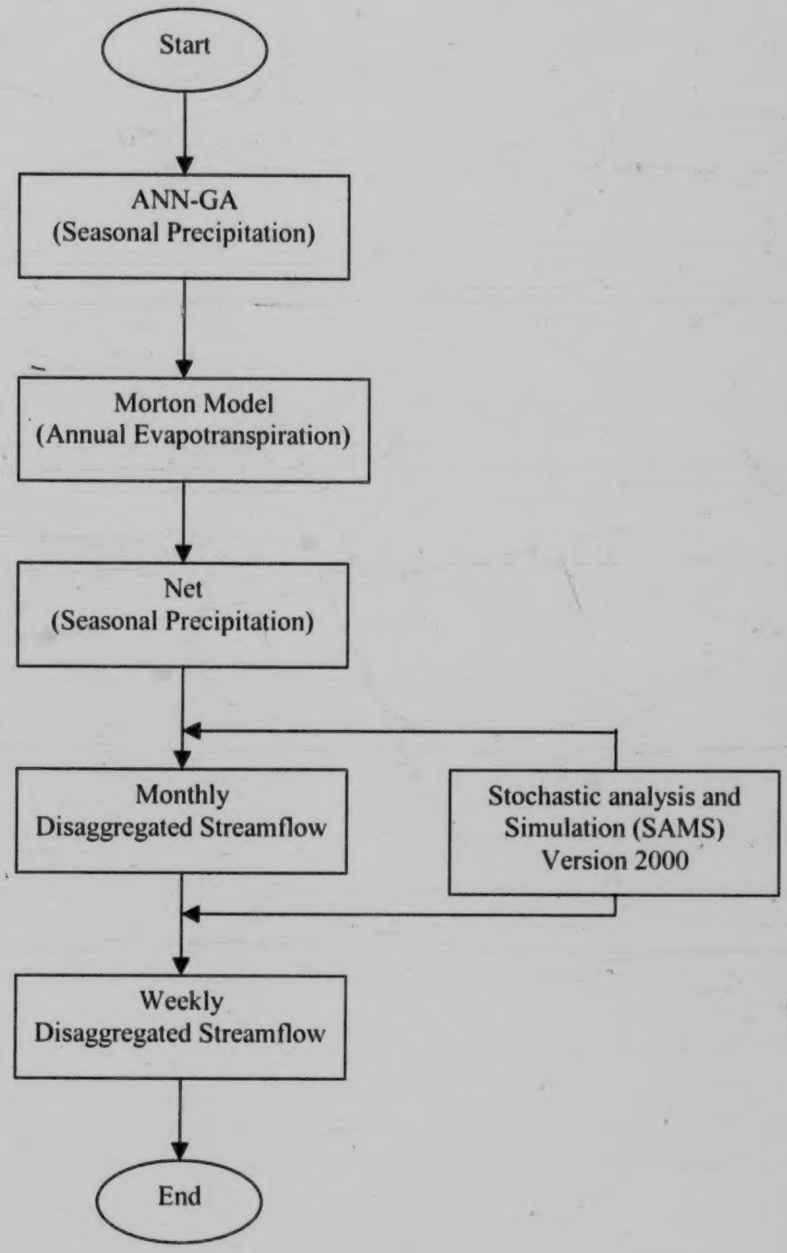
Start
ANN-GA
(Seasonal Precipitation)
Morton Model
(Annual Evapotranspiration)
Net
(Seasonal Precipitation)
Monthly
Disaggregated Streamflow
Stochastic analysis and
Simulation (SAMS)
Version 2000
Weekly
Disaggregated Streamflow
End

Figure 6.2. Flowchart of the ANN-GA-DIS approach

The first method is through the empirical orthogonal function (EOF) analysis approach. The second method uses sequential algebraic equations to solve for B, from the matrix C. In this thesis the EOF method was used as described below.

By letting

$$BB^T = S_{YY} - S_{YX} S_{XX}^{-1} S_{XY} = C_{nxn} \tag{6.8}$$

we can solve the eigenvector problem

$$CE = E\lambda , \tag{6.9}$$

to obtain the eigen values, λ_i, and the corresponding matrix of eigenvectors, E_i, (i=1,….,n). The eigenvectors have the property of orthogonality, i.e.,

$$E^T E = I$$

Multiplying either side of En (6.9) by the inverse of E, i.e., E^{-1}, we obtain

$$C = E\lambda E^{-1} = BB^T \tag{6.10}$$

which reduces to

$$B = E\lambda^{\frac{1}{2}} \tag{6.11}$$

Where $$\lambda^{\frac{1}{2}} = \begin{bmatrix} \sqrt{\lambda_1} & \cdot & \cdot \\ \cdot & \cdot & \cdot \\ \cdot & \cdot & \sqrt{\lambda_n} \end{bmatrix}$$

The matrix B and vector A are used in Eq (6.1) to generate Y, the disaggregated time series from X, which is the aggregate of Y.

According to Tao and Delleur (1976), regardless of the underlying distribution of Vectors X and Y and the one resulting from matrix B and vector V, the mean and variance properties of historical events will be preserved in vector A and matrix B. Hence, when annual and monthly data are used, vector A will retain the disaggregation proportions of monthly data related to the annual data and the vector resulting from the product of matrix B and vector V will have the disaggregation proportions of variances relating annual and monthly data. Thus the mean and variances resemblance criteria for the monthly scale series generated by Eq (6.1) will be satisfied. Valencia and Schaake (1973) have shown that the parameters A and B preserve continuity between seasonal (or monthly) and annual values, i.e.,

$$X_i = \sum_{i=1}^{n} Y_{ij} \tag{6.12}$$

The vector A and matrix B are used in Eq (6.1) along with a random number generator to create random numbers for vector V. In this thesis the A and B were computed by the SAMS version 2000 or SAMS 2000 (in short) computer package of Salas et al., (2000), available on-line at http://www.engr.colostate.edu/Sams-CSU-USBR. This package has been developed for the stochastic analysis, modeling, and simulation of streamflows. SAMS 2000 has the capability to generate many years of synthetic single site and multi-site streamflows based on the model parameters described by the vectors A and matrices B and some random number generator defined by vector V.

Instead of computing A and B directly from the observed data, SAMS 2000 initially fits the observed data to one of the several available stochastic models. In this thesis, the univariate autoregressive moving average [ARMA (K, M)], model, where K and M are the autoregressive (Φ_k) and moving average (θ_m) terms of the model was extensively used. This model maybe expressed as follows:

$$x_{t+1} - \mu = \sum_{k=1}^{K} \Phi_k \left(x_{t-k+1} - \mu \right) + \varepsilon_{t+1} - \sum_{m=1}^{M} \theta_m \varepsilon_{t-m+1} \tag{6.13}$$

where the anomaly for the next time process $x_{t+1}-\mu$ is a weighted average of the previous K terms, a random component ε_{t+1} and the M moving average terms that constitute the weighted average of the M previous ε values. The ARMA (2, 1) model was adequate to fit the weekly and monthly streamflow and rainfall data. In the above equation, the weights are the autoregressive coefficients Φ_k and θ_m. These weights were found by the least squares approach, in which the weights are estimated by minimizing the sum of squares between the observed (*Obs*) and modeled (*Mod*) values,

$$e = \sum_{t=1}^{N} \Phi_k \left(Obs_t - Mod_t\right)^2 \qquad (6.14)$$

where N is the length of the data.

6.3 The Sacramento Soil Moisture Accounting (SAC-SMA) Model

The SAC-SMA model (Burnish et al., 1973), illustrated in Figure 6.4, is a lumped-parameter conceptual model, which consists of a series of sub-models each representing a particular hydrologic process such as Horton overland flow, infiltration, subsurface flow and moisture storage. Most of the hydrological process and storages are represented in the model as millimeter depths of moisture.

The soil moisture storages of the SAC-SMA model are conceptually made up of the upper and lower zones (Figure 6.4). The upper zone represents the topsoils and the basin interception layers, while the lower zone represents the groundwater storage or the hydrogeology of the basin. The upper zone is represented by two conceptual storages, called "tension moisture, UZTWM" and "free moisture, UZFMW"

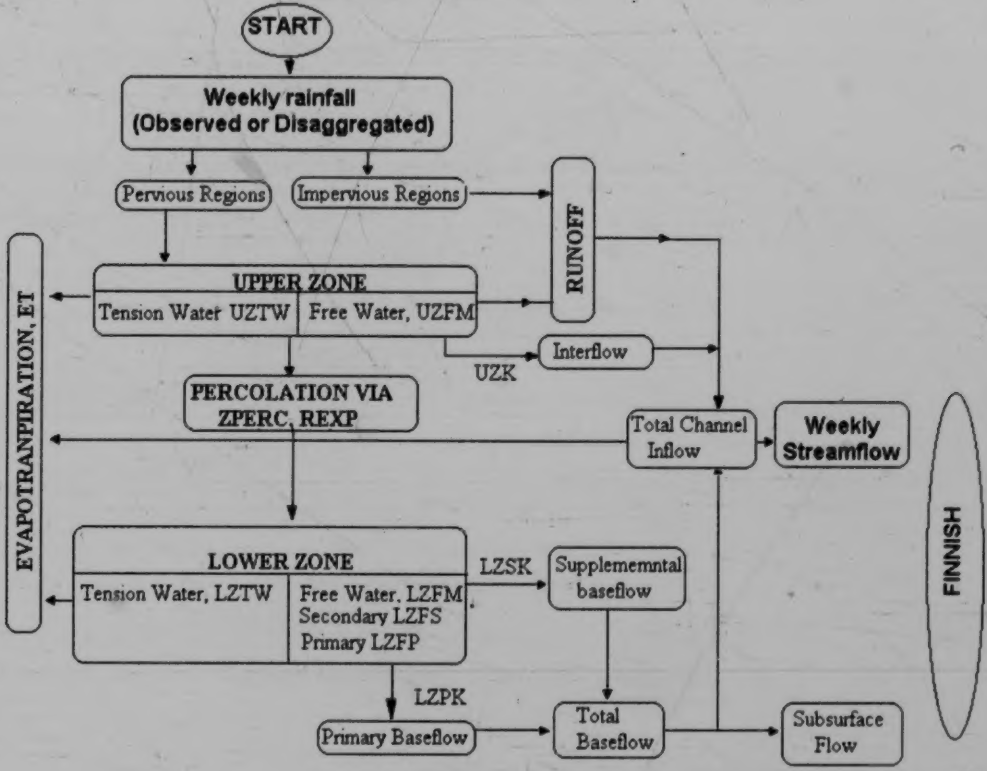
START
Weekly rainfall
(Observed or Disaggregated)
Pervious Regions
Impervious Regions
RUNOFF
EVAPOTRANPIRATION, ET
UPPER ZONE
Tension Water UZTW
Free Water, UZFM
Interflow
UZK
PERCOLATION VIA
ZPERC, REXP
Total Channel
Inflow
Weekly
Streamflow
FINNISH
LOWER ZONE
Tension Water, LZTW
Free Water, LZFM
Secondary LZFS
Primary LZFP
LZSK
Supplememntal
baseflow
LZPK
Primary Baseflow
Total
Baseflow
Subsurface
Flow

Fig 6.34 Flow diagram of the Sacramento Model as implemented in this thesis.

storages, while the lower zone is represented by three conceptual storage zones (tension, primary and secondary storage zones, respectively LZTWM, LZPW, LZSM). The upper storages are used to model the rising limp of the runoff hydrograph, while the lower zone is used to model the falling limb of the hydrograph. More than two storage zones are required for the lower zone in order to describe the various recession rates of the lower limb of the runoff hydrograph.

Figure 6.4 describes the following process. Following precipitation (P_x), initial moisture either contributes to direct runoff from the impervious areas of catchment (PCTIM, % and ADIMP,%) or goes to fill up the tension water requirements of the soil (UZTW). After satisfying the tension water requirements, the rest of the moisture fills up the free spaces between the soil particles (UZFW). Evapotranspiration (ET) is allowed from the impervious, tension and free water storages. The rest of the moisture is allowed to percolate to the lower zone, at maximum rates of ZPERC, where some of it becomes lateral flow, while the rest either evaporates, or becomes part of the lower zone storage. Contribution to the lateral flow occurs through a daily upper zone free water withdrawal rate, UZK. Some of the moisture from the lower zone is also allowed to evaporate, while some moisture becomes part of permanent lower zone tension and free water storages, LZTW and LZFW respectively, which can also be divided into primary (P) and secondary (S) zones. The lower zone storage contributes to the base flow through the primary and secondary supplementary base flow withdrawal rates, LZPK and LZSK respectively.

The SAC-SMA model, like any other conceptual model requires the parameters representing the storage and flow processes to be carefully calibrated for it to reproduce good fit between observed and modeled runoff for that catchment. Calibration is therefore an important part of conceptual modeling. For the SAC-SMA model, a successful and meaningful calibration means that the model results should as closely as possible match the observations, both during the calibration and validation periods. Successful calibration also means that the model parameters successfully represent the catchment characteristics. This requirement is, however, practically not plausible due to the lumped nature of the parameters.

To calibrate the parameters, manual as well as automatic calibration procedures are available in the SAC-SMA model. In automatic calibration, the parameter values are initialized, and optimized by an optimization algorithm, such as Newton-Raphson, genetic algorithm or the Nelder-Mead Simplex algorithm. The Nelder-Mead Simplex algorithm is available as the optimization algorithm in the SAC-SMA model and was used in this thesis. Depending upon the nature of the rainfall-runoff process, initial parameter values such as those suggested by Gan (1988) may be used. Most parameter values vary over a wide range, e.g., the tension storages, (0 - 250 mm), and the lower zone free water storages (0 - 900 mm), suggesting the difficulties associated with finding an optimal set of parameter values for a catchment

Once the initial parameters have been set, they are adjusted based on the difference between the observed and simulated runoff. Since the streamflow has various recession rates, this part of the streamflow hydrograph, represented by the lower zone parameters is calibrated first. This is followed by the percolation parameters and the upper free and tension moisture parameter values.

6.3.1 Evapotranspiration in SAC-SMA

Estimates of upper constraints on actual ET are required as input in the SAC-SMA model. There are numerous methods for estimating the upper limits of ET. These include physics-based methods such as energy balance and aerodynamics, and the empirical methods such as pan ET. For large areas that are free of discontinuity, the Fred Morton complementary relationship areal ET (CRAE) model has been recommended (e.g. Chiew and McMahon, 1991; Hobbins et al., 2003) to compute the upper limit of ET. Fred Morton (1978) developed the CRAE model. The model has been calibrated on a monthly basis and applied to diverse environments in Africa, Australia, the United States, Canada, Ireland, and New Zealand. Figure 6.3 illustrates the complementary relationship between ET_p and ET_a. It shows that under dry conditions, ET_p is maximum, while ET_a is zero. As moisture becomes available, the actual ET increases, while the ET_p decreases because of the cooling effect of ET. As the supply of moisture is increased, ET_a increases while ET_p decreases until a time when ET_p and ET_a become equal to each other. Under such conditions, the ET is called wet environment ET, ET_w and is computed as follows:

$$ET_a + ET_p = 2ET_w \tag{6.15}$$

Morton's (1983) model is derived from Penman's combination equations. According to Penman (1948), ET_p occurs due to a combination of the energy and aerodynamic forces,

$$ET_p = \frac{\Delta}{\Delta + \gamma_p} R_n + \frac{\gamma_p}{\Delta + \gamma_p} f(u)(e_a - e_d) \tag{6.16}$$

where Δ (mbar °C^{-1}) is the slope of the saturation vapor pressure/temperature curve at air temperature, T, and is equal to

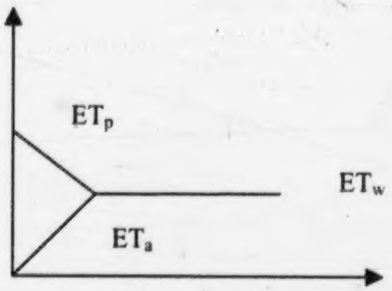

Figure 6.4 An illustration of the complementary relationship between potential and actual ET.

$$\Delta = \frac{4098 e_a}{(237.3 + T)^2} \qquad (6.16a)$$

γ_p (mbar °C^{-1}) is the psychometric constant equal to 66.8 Pa/°C, R$_n$(Wm^{-2}) is the net radiation at air temperature, *f(u)* (Wm-^{2} mbar^{-1}) is wind function, e$_a$(mbar or Pa) is the saturation vapor pressure at T,

$$e_a = 611 \exp\left(\frac{17.27T}{237.3 + T}\right) \qquad (6.16b)$$

and e$_d$(mbar) is the saturation vapor pressure at dew point temperature or actual vapor pressure of air. In Eq (6.16), ET$_p$ has the units of Wm^{-2} and can be converted to depth of water by dividing ET$_p$ by latent heat of vaporization of water (J kg^{-1}) and the density of water (Kg m^{-3}) over the appropriate time period. The quantities $\frac{\Delta}{\Delta + \gamma_p}$ and $\frac{\gamma_p}{\Delta + \gamma_p}$ of Eqn. 6.16 are weighting factors that sum to one. The wind function varies from place to place and also with the prevailing climatic conditions. For Penman's equation, *f(u)* is given as

$$f(u) = \frac{0.622k^2 \rho_a u_a}{p\rho_w \left[\ln\left(\frac{Z_a}{Z_0} \right) \right]^2}$$

where ρ is the density of air , u_a is the wind velocity at Z_a, the height where the measurements are taken and Z_0 is the roughness height of vegetation. Since the wind varies with location data and are difficult to obtain, Morton (1983) replaced the wind function with a vapor transfer coefficient, which is constant for a given atmospheric pressure and independent of wind.

$$f(u) = \left(\frac{p_o}{p} \right)^{0.5} f_z \zeta^{-1} \qquad (6.17)$$

where p_o is atmospheric pressure at sea level(mbar), and p is the atmospheric pressure (mbar), f_z is a coefficient whose value is 28.0 $Wm^{-2}mbar^{-1}$ for above freezing temperature. For below freezing temperatures this value is increased by a factor of 1.15, the ratio of latent heat of sublimation to the latent heat of vaporization. The exponent 0.5 represents the effects of atmospheric pressure on ET process and vapor transfer coefficient, and ζ represents a dimensionless stability factor with values greater than or equal to 1.0. Hence, the advantage of this model is that it does not require wind data.

To calculate ET_p, Morton (1983) applied Penman's equation written in terms of the energy balance and the vapor transfer process. ET_p is then derived by solving for an equilibrium temperature, T_p iteratively such that at T_p Morton's (1983) energy budget and mass transfer methods for a moist surface yield the same result for ET_p (Chiew and McMahon, 1991) i.e.,

$$ET_p = R_n - \left(\gamma_p f_a + 4\varepsilon\sigma\left(T_p + 273\right)^3\right)\left(T_p - T\right) = ET_p = f_a\left(e_p - e_d\right) \qquad (6.18)$$

where f_a ($Wm^{-2}mbar^{-1}$) is the vapor transfer coefficient (given by an empirical equation), ε is the surface emissivity, σ (5.87×10^{-8} Wm^{-2} $°K^{-4}$) is Stephan Boltzmann constant, T(°C) is air temperature, and e_p(mbar) is the saturation vapor pressure at T_p, which is the equilibrium temperature T_p computed iteratively. Having obtained T_p, ET_w maybe obtained as follows.

$$ET_w = b_1 + b_2 \frac{\Delta_p}{\Delta_p + \gamma_p}\left[R_n - 4\varepsilon\sigma T_p^3\left(T_p - T_a\right)\right]$$

or (6.19)

$$ET_w = b_1 + b_2 \frac{\Delta_p}{\Delta_p + \gamma_p} R_n^*$$

where R_n^* is the net radiation adjusted to T_p, $b_1=14Wm^{-2}$ (to account for large scale advection during seasons of low or negative radiation and represents the minimum energy available for ET_w) and b_2 = 1.2 is an empirical constant that Morton (1983) obtained through calibration. ET_a may be obtained by substituting results from Equations 6.18 and 6.19 into Equation 6.15.

6.4 Hydrologic Modeling of the Kafue and Lunga River Catchments

6.4.1 Introduction

The Kafue River basin is located on the central African plateau, approximately between 11-17°S and 25-29°E. The basin lies completely within central Zambia (see Figure 6.5) and covers an area of 157,000 km^2, (i.e., 21% of the total land area of Zambia, 753,313 km^2) (UNDP/FAO, 1968). The Kafue basin can be divided into three zones: the upper basin, which extends from the head waters to the Iteshi-Teshi dam, the middle basin, which extends from Iteshi-Teshi dam to the Kafue gorge dam and the lower basin, which extends from the Kafue Gorge to the Zambezi River confluence. Two large rivers with naturalized streamflow (i.e., the Kafue and Lunga) and their tributaries drain the upper basin. The eastern part of the upper Kafue river basin contains the Lukanga swamps. Most rivers to the east of the basin drain into these swamps. When the Kafue River breaks its banks, part of its streamflow drains into the swamps. Daily streamflow and rainfall records of 27 and 21 years respectively are available for the Kafue (34, 162 km^2) and Lunga River catchments (24, 268 km^2).

The land surface data for the basin, (i.e., soils, vegetation types, topography, and elevation), were obtained from the ECOCLIMAP land use classification, developed at Meteofrance. This data is gridded at 0.5° x 0.5° resolution. The mean monthly air temperature data, 1950-1998 and gridded at 0.5° x 0.5° was obtained from New et al., (2002) (SAFARI 2000 project), available on-line at http://www.daac.ornl.gov. Data on the number of sunshine hours was obtained from the UNDP/FAO (1968) climatology and hydrology, Volume I report. The rainfall station data for the catchment was obtained from the Southern African FRIEND Project data achieve.

6.4.2 Land Surface Characteristics

The antecedent moisture condition (AMC) and the surface conditions of a catchment play an important role in determining what part of the rainfall appears as surface runoff. Streamflow may result from rainfall intensity exceeding infiltration rate into soil layers (Hortonian overland flow), precipitation over saturated ground (saturation overland flow), or from base flow. Factors that influence the proportions of runoff mechanisms include vegetation cover, geology, topography, soil properties, AMC, and the climate.

Figure 6.6 shows the soil and the vegetation distribution, in percentage of area covered in each 0.5° x 0.5° grid. This figure shows that clays, sands and mixture of clays and sands (or sandveldt) form the dominant features of soil types of the Kafue basin. The sandy soils are predominant in the southwestern corner of the basin, where they account for between 80 and 100% of the soil types. In the middle and eastern sections of the basin, sandy soils account for 40-80% of the soil types, while in the northern sections of the basin, sandy soils account for 30-40% of the soils types.

Clay is predominant in the northern reaches of the basin, where it accounts for between 30-40% of soil types (Figure 6.6b). In the middle and eastern sections, clay soils account for 20-30% of the soil types. The mixture of sands and clays (or "sandveldt"), which are the dominant soil type covering the middle and entire eastern section of the basin have more sandy soil than clay soils.

In addition to the clay soils, there are innumerable "dambos" in the upper reaches of the basin (UNDP/FAO 1968). These saucepan-shaped, low laying areas are seasonally water logged by seepage from surrounding high ground and in times of wet years, most dambos do not drain off quickly after the rains. As a result considerable runoff results from rainfall from these areas, contribution to the Horton overland flow created by the clay soils. During dry years or droughts, the detention storage of the dambos increase considerably and little rainfall becomes runoff.

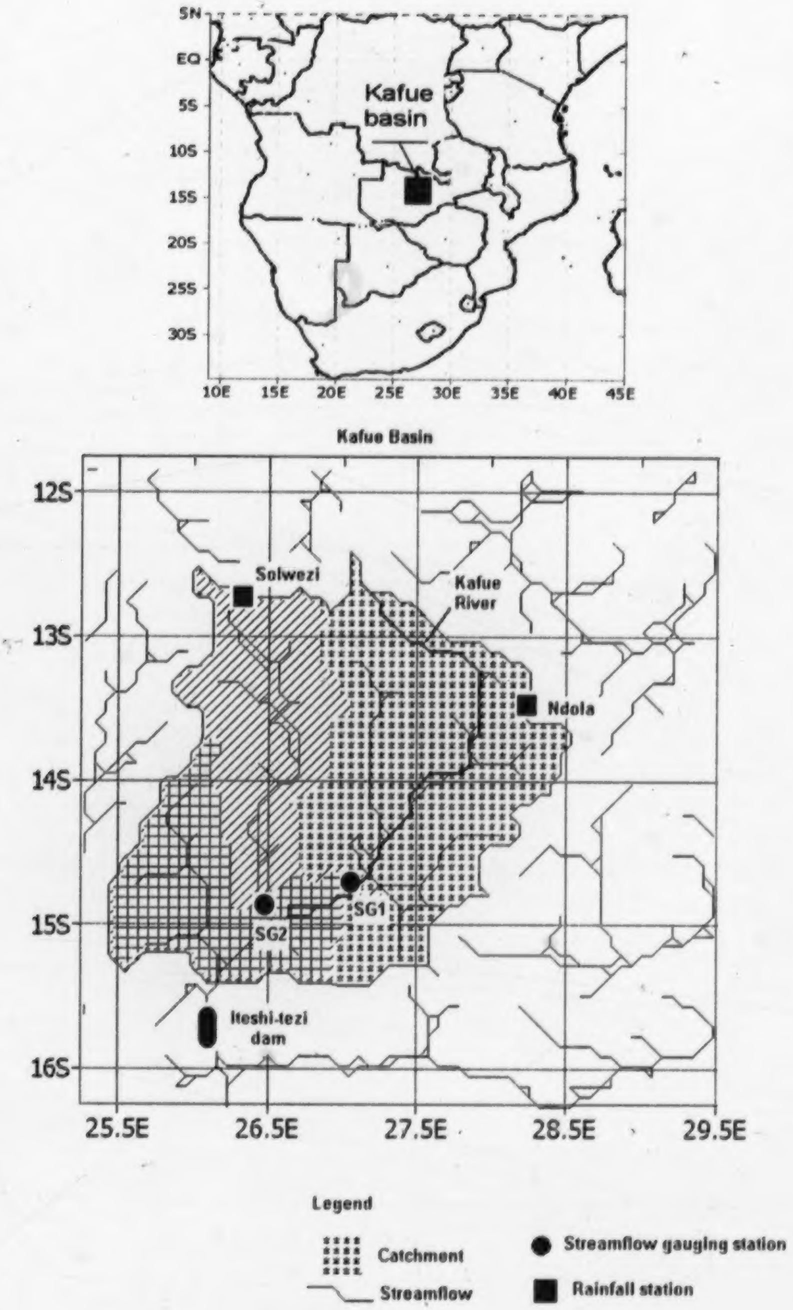
5N
EQ
5S
10S
15S
20S
25S
30S
10E
15E
20E
25E
30E
35E
40E
45E
Kafue basin
Kafue Basin
12S
13S
14S
15S
16S
25.5E
26.5E
27.5E
28.5E
29.5E
Solwezi
Kafue River
Ndola
SG1
SG2
Iteshi-tezi dam
Legend
Catchment
Streamflow
Streamflow gauging station
Rainfall station

Figure 6.5 The location of the Kafue and Lunga river basins, and the stream gauging (SG) and rainfall stations.

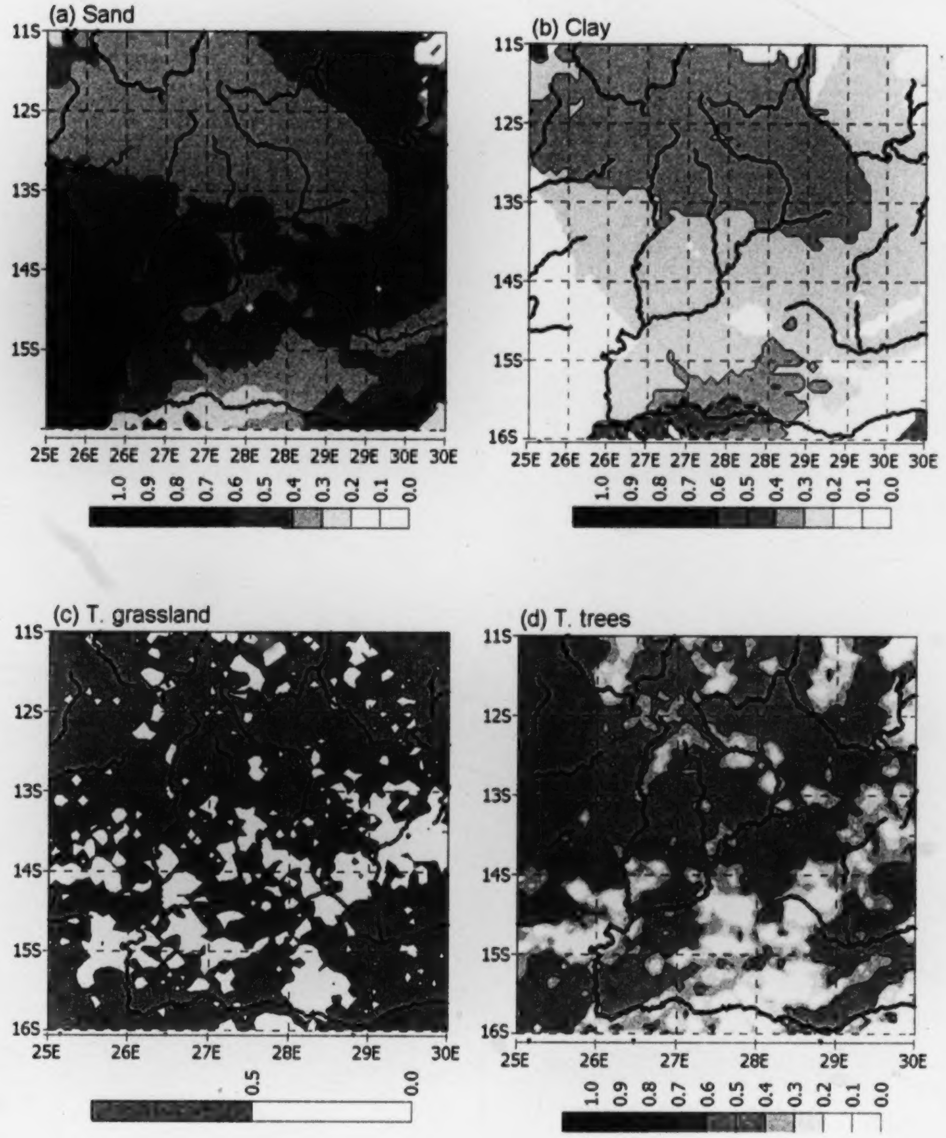
(a) Sand
11S
12S
13S
14S
15S
25E 26E 26E 27E 27E 28E 28E 29E 29E 30E 30E
1.0 0.9 0.8 0.7 0.6 0.5 0.4 0.3 0.2 0.1 0.0
(b) Clay
11S
12S
13S
14S
15S
16S
25E 26E 26E 27E 27E 28E 28E 29E 29E 30E 30E
1.0 0.9 0.8 0.7 0.6 0.5 0.4 0.3 0.2 0.1 0.0
(c) T. grassland
11S
12S
13S
14S
15S
16S
25E 26E 27E 28E 29E 30E
0.5 0.0
(d) T. trees
11S
12S
13S
14S
15S
16S
25E 26E 27E 28E 29E 30E
1.0 0.9 0.8 0.7 0.6 0.5 0.4 0.3 0.2 0.1 0.0

Figure 6.6. The spatial distributions of basin soils and vegetation

Tropical grasslands and broadleaved trees (Figures 6.6(c) and (d)) are dominant features of the basin. In the northern section of the basin grasslands account for between 50 and 100% of each grid cell, while in the middle and eastern swampy and flood plains, grasslands account for 0-50% of the grids. Tropical trees are also dominant in the northern sections but are sparse in the eastern and southern flood sections of the basin, where they account for between 40 and 50% of each 0.5° x 0.5° grid.

Much of the basin ranges in altitude between 1300 m above mean sea level (amsl) in the upper reaches of the basin and 1100 m amsl in the southern limits of the upper basin (Figure 6.7). The slopes in large portions of the upper reaches are about 1% while in the middle and lower reaches; they drop to about 0.1%. Since the gradients are not uniform, the velocity of the rivers changes throughout the course of the basin. Because of low slopes in the middle portion of the basin, swamps and flood plains form main features of the middle and the lower reaches of the upper basin.

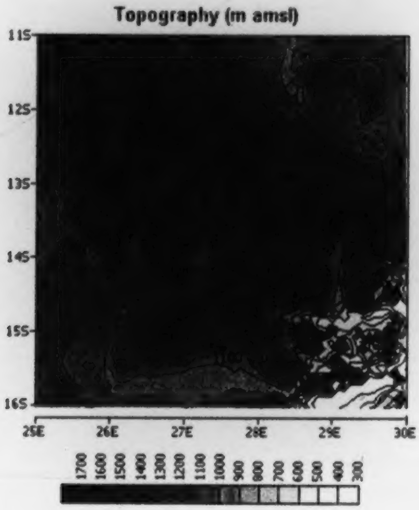
Topography (m amsl)
11S
12S
13S
14S
15S
16S
25E
26E
27E
28E
29E
30E
1700
1600
1500
1400
1300
1200
1100
1000
900
800
700
600
500
400
300

Figure 6.7 Topographic features of the Kafue basin.

6.4.3 Climate of the Basin

The rainfall regime in the entire basin is characterized by the annual migration pattern of the sun between the northern and southern Hemisphere (Section 3.2.1 of Chapter 3). The rainfall lasts for about six months, beginning at the end of October and ending in April. Following the southward movement of the sun between March and September 22, the interior of the CSA and the Kafue basin in particular warms up and atmospheric pressure decreases. The decreased pressure draws into the basin the moist Congo air mass. After December 22nd the sun begins its journey to the northern Hemisphere. By this time, the Congo air mass has reached the southward-most portion of the basin. Cool air from the south following the northward movement of the sun reaches the Kafue basin in March and displaces the moist Congo air from the southern border of the basin. However, rainfall continues in the northern sections of the basin until about April. The length of the rainy season is determined by the period the Congo air mass is present in any part of the basin. Between 1000 and 1500 mm of rainfall falls in the northern sections of the basin, while between 750-1300 mm falls in the southernmost portions of the Kafue river basin.

According to the UNDP/FAO 1968 report, each year rainfall begins between October 20 and November 15 and ends between March 31 and April 25 in the northern part of the basin. Because the revolution of the earth around the sun and its apparent upward and downward movement are deterministic, we believe the rainfall bearing system of northern CSA and the Kafue basin in particular is caused by a fairly deterministic atmospheric system. That system is the intrusion of the Congo air mass into the Kafue basin when atmospheric pressures drop in the interior of CSA, following the migration of the sun to the southern Hemisphere and the extrusion of the Congo air system when the sun makes its northward migration. Although earth's orbital parameters change with time, they can be considered almost stable for about 100 years (e.g., see http://aom.giss.nasa.gov/srorbpar.html). Although the rainfall quantities differ from day to day in space and time, we believe that the average weekly rainfall over the middle and upper basins is generally quantifiable (i.e., the weekly mean and variance for the rainy season). This observation motivated us to exploit the statistical relationships that exist between the weekly, monthly and annual rainfalls in order to model the rainfall and runoff processes over the basin.

The basin experiences a dry winter between June and July. This is the coldest part of the year with average temperatures of about 15°C. August to October is the hottest part of the year with maximum temperatures about 30°C.

6.4.4 Application of ANN-GA-DIS-SMA and ANN-GA-DIS

This section describes the application of the ANN-GA-DIS-SMA and ANN-GA-DIS models. The aim is to assess and compare the performance of the models with respect to observed runoff data to determine their robustness and viability. Ideally we wish to minimize the differences between the simulated runoff of a model and the observed runoff. The performance of a model is assessed through statistics such as the correlation coefficient, bias and the RMSE, and visual comparisons of hydrograph plots.

6.4.4.1 Travel Time

For the Kafue river catchment, the total length of river from the source to the gauging station is about 410 km and has a slope between the source (1494 m) and the gauging station (1112 m) of about 0.09% (UNDP/FAO, 1968). For natural channels of slopes ranging between 0 and 3%, the approximate average velocity of streamflow is between 0 and 0.61 m/s (Chow et al., 1988). Assuming the streamflow occurs at an velocity of 0.61 m/s (upper bound), the travel time of streamflow from the source to the gauge is about 7.8 or 8 days. Therefore the travel time (time of concentration) at which the entire watershed begins to contribute to streamflow at the gauging station was taken to be 8 days. For months ending with 31 days, the streamflows for the first three weeks were averaged over 8 days, while the streamflows over the last week were averaged over 7 days. For months ending with 30 days, the first two weeks were averaged over 8 days and the last two weeks over 7 days. For months ending with 28 days, the streamflow was averaged over 7 days. Hence instead of 52 weeks in a year, only 48 weeks were considered. This approach also simplified the disaggregation scheme between monthly and weekly time steps. For the Lunga Catchment, the entire catchment begins to contribute to the measured discharge after about 7 days.

The SAC-SMA model was initially designed to operate at hourly or daily time steps. To accommodate the 7 or 8 days of moisture using hourly time steps, the moisture accounting process was performed by updating the sum of the runoff and infiltrated flows over a period 168 or 192 hours, respectively.

6.4.4.2 Water Balance and Dynamics of Rainfall-Runoff

Water balance components and streamflow generation of the two basins are largely influenced by rainfall, ET and Changes in storage, (see Figure 6.8). ET accounts for between 70 and 100% of the total rainfall that falls in the basin each year. Rainfall was less than potential ET in 1967, 1972, 1981 and 1986. These years also recorded reduced streamflow. The years of high rainfall, such between 1973 and 1976 and 1981 and 1984, which were preceded by periods of decreasing rainfall such as 1970-1972 and 1978-1980, generally did not result in dramatic increases in the streamflow, especially for the first two years (Figure 6.8). This shows that the catchments need at least a year to be fully recharged following a few dry years.

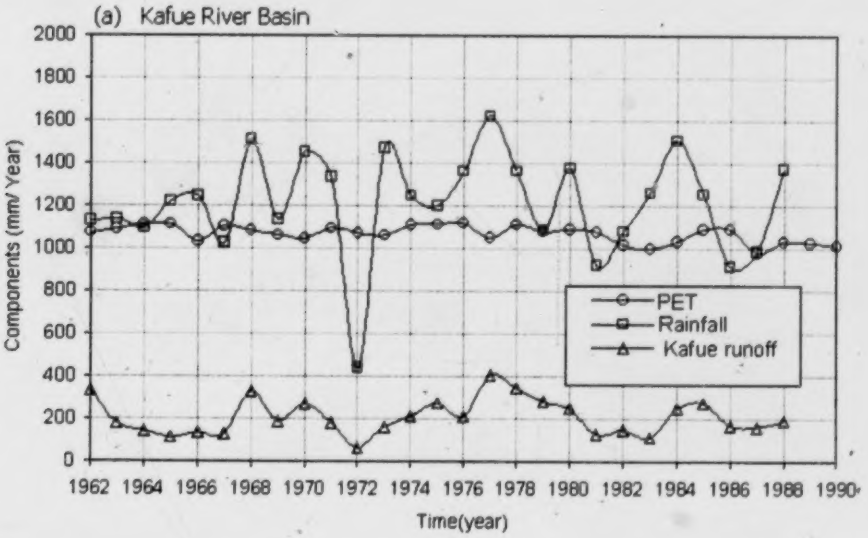

Figure 6.8 The water balance of the (a) Kafue, and (b) Lunga River catchments.

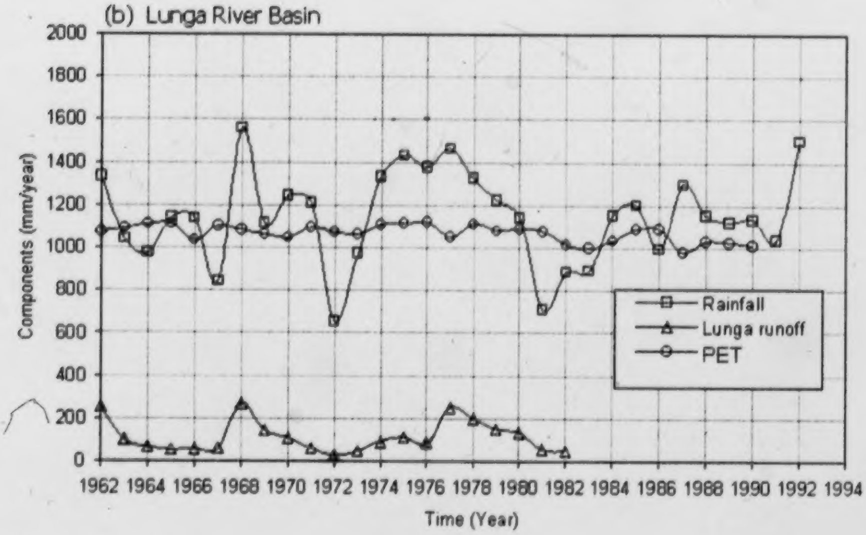

Figure 6.8 Continued.

As was noted in Section 6.4.2.1, the upper reaches of the Kafue basin are dominated by clay soils and dambos. During periods of low rainfall, the detention capacity of the upper reaches increases dramatically causing low streamflow to dominate the years following consistently less than average rainfall. This shows that the hydrologic response of Kafue basin is heavily dependent on its AMC. The SAC-SMA model is designed to simulate each year's rainfall-runoff process with specified initial moisture content of UZTW, UZFW, LTZW, LZPW, and LZSW. At the end of each year, the state variables of the above conceptual storages determine its AMC for the next year's run for the catchment. Hence the non-linear response of the catchment to the rainfall did not present challenges to the SAM-SMA in modeling the rainfall-runoff process of the basins.

6.4.4.3 Disaggregation of Seasonal to Weekly Rainfall

The weekly rainfall and discharge data for the two catchments are shown in Figure 6.9. The disaggregation vectors A and matrices B were computed from aggregated weekly and monthly series using the SAMS computer package (Salas et al., 2000). Since rainfall is a nonstationary process (Chapter 3), long enough datasets that contained as much information as possible were utilized to compute realistic A and B matrices.

The ANN-GA model (Chapter 4) was used to predict the seasonal rainfalls of both basins from SSTs of the Indian and Atlantic Ocean identified in the previous April-May-June (AMJ) season (see Figure 6.10). This seasonal rainfall was disaggregated, first into monthly rainfall and then into weekly rainfall (Figure 6.10). To generate monthly or weekly rainfall from the predicted seasonal rainfall, 2000 statistically generated samples were created through Eq (6.1).

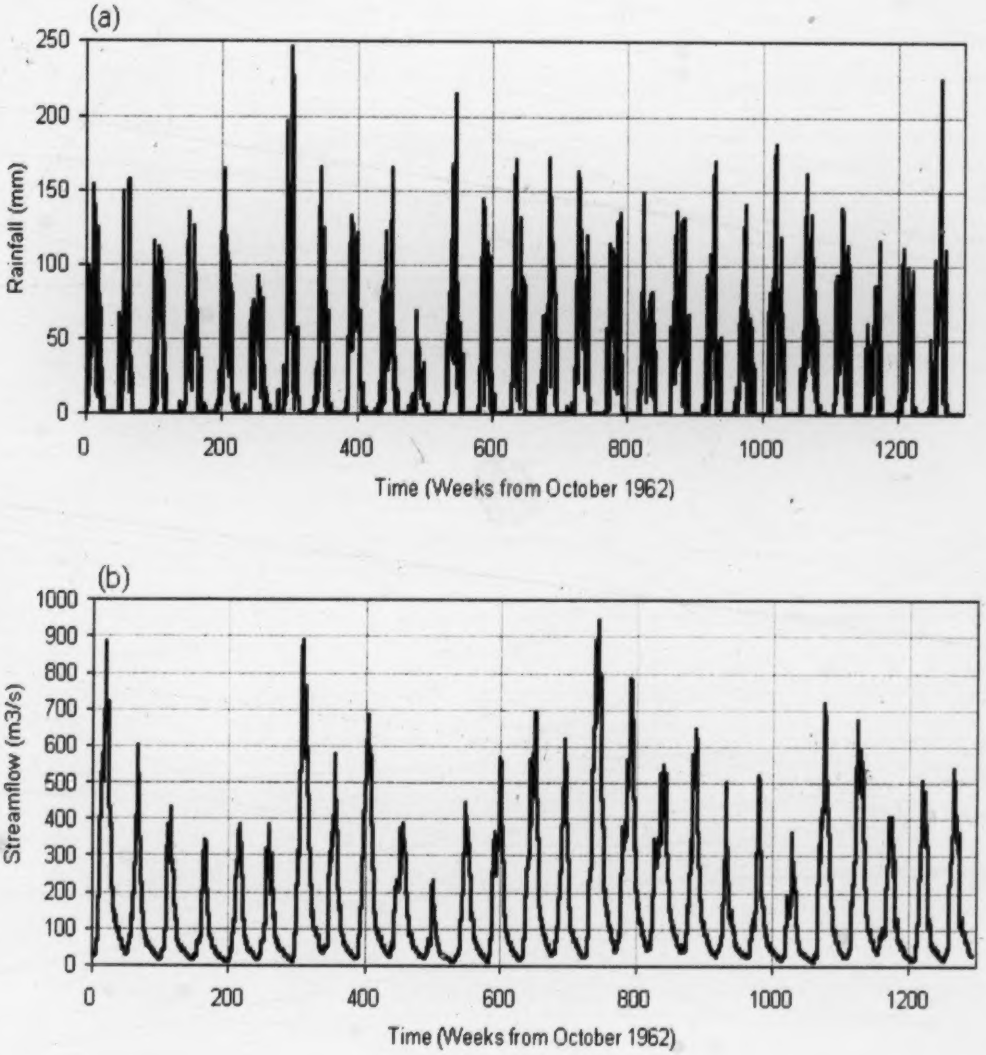

Figure 6.9 The data used in the study, (a) Kafue basin rainfall, (b) Kafue basin runoff, (c) Lunga river basin rainfall and (d) Lunga river rainfall.

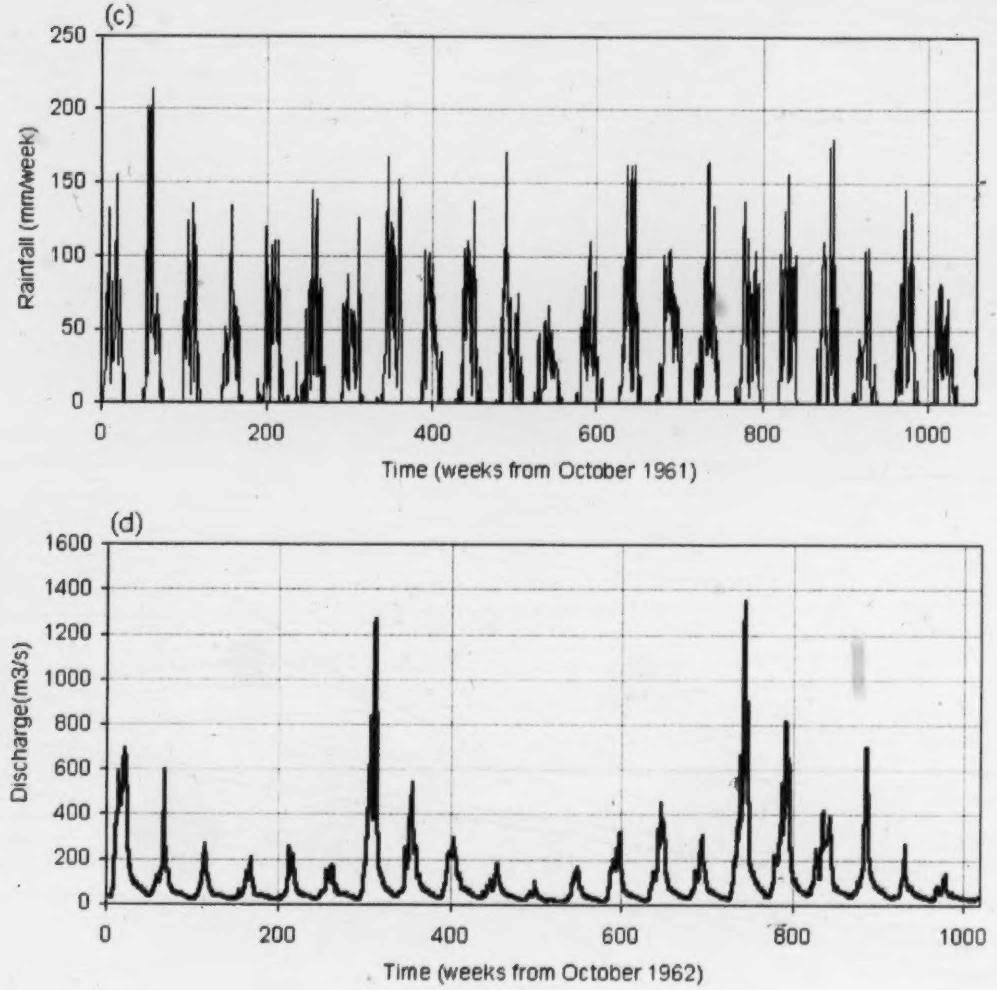

Figure 6.9 continued

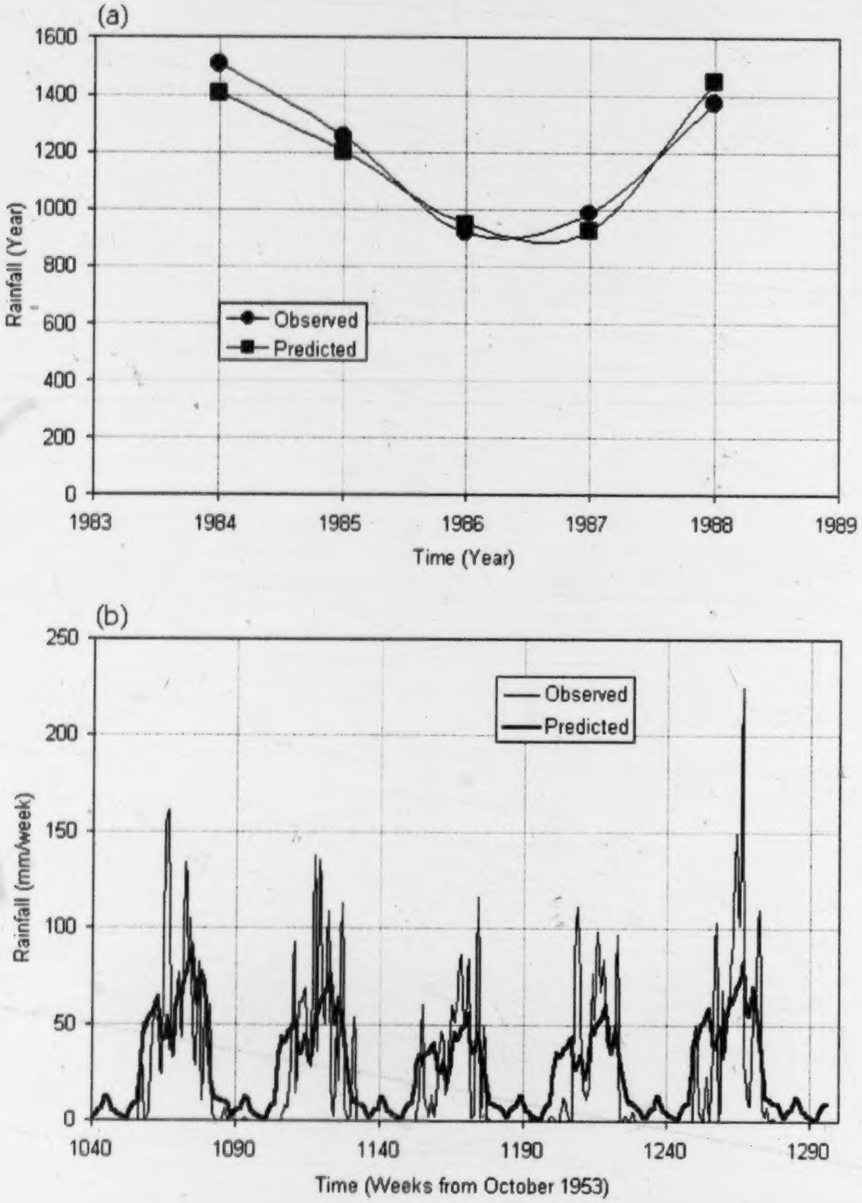

Figure 6.10. Plots of: (a) the predicted and observed seasonal rainfall of the Kafue basin, (b) the observed and statistically predicted weekly rainfall of the Kafue basin, (c) the predicted and observed seasonal rainfall of the Lunga river basin, and (d) the observed and statistically predicted weekly rainfall for the Lunga River basin.

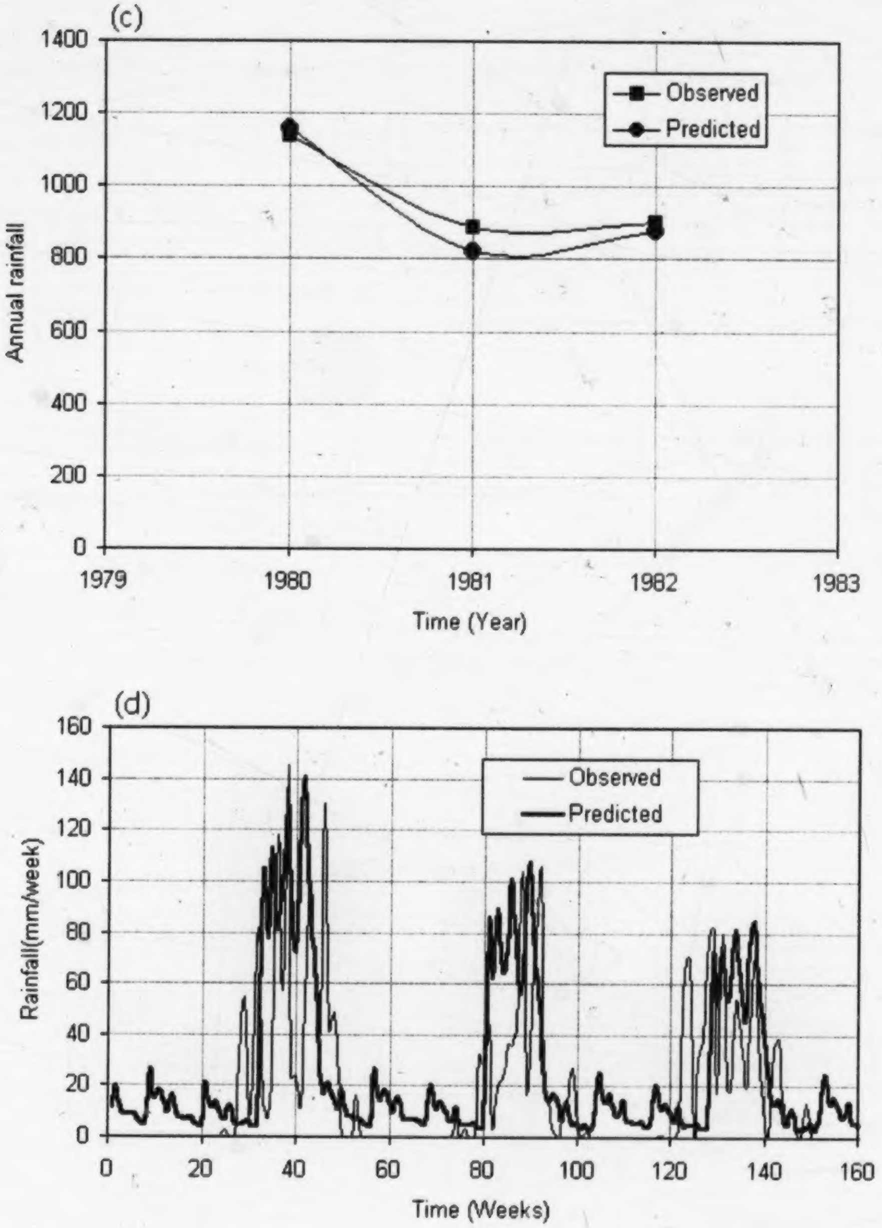

Figure 6.10 Continued

These rainfall samples were then averaged to form one monthly or weekly dataset. The weekly rainfall realizations (see Figure 6.10) were used as input to SAC-SMA model calibrated to the hydrologic condition of say, Kafue and Lunga basins.

Figures 6.11 show the time series plots for the validation periods of the weekly streamflow for the Kafue basin. Figure 6.12 shows the corresponding scatter plots for the validation periods. The statistics summary corresponding to Figures 6.11 and 6.12 are presented in Tables 6.1 and 6.2. From Table 6.1, it is clear that 81-96% of the variance in the observed streamflow was accounted for by the predicted weekly streamflow using both the observed as well as the statistically predicted rainfall. With biases of between –4.8 and 9.3% for 1984, 1986, 1987, and 1988 meant that four of the five years of predicted streamflow values were very close to the observed values. The model performed poorly for the year 1985, with a bias of -28.1% using the observed rainfall and –18.4%, using statistically predicted rainfall. We suspect that SAC-SMA grossly under-simulated the streamflow simply because observed runoff data for 1985 may be erroneous. Using the observed rainfall data, the RMSE averaged 37%, while using statistically generated rainfall the RMSEs average 38%. The modeling efficiency of the streamflow using the observed and statistically predicted rainfall was thus within small percentage errors (Table 6.1).

Figure 6.9 shows the scatter plots of observed and predicted streamflow using both the observed and statically predicted rainfall. Except for 1985, Figure 6.9 and the statistics of Tables 6.1 and 6.2 clearly shows that statistically generated rainfall performed as well as observed rainfall. Hence statistically generated rainfall can be used in the SAC-SMA model for the prediction of weekly streamflow for the next water year.

(a) Machiya (using observed rainfall)

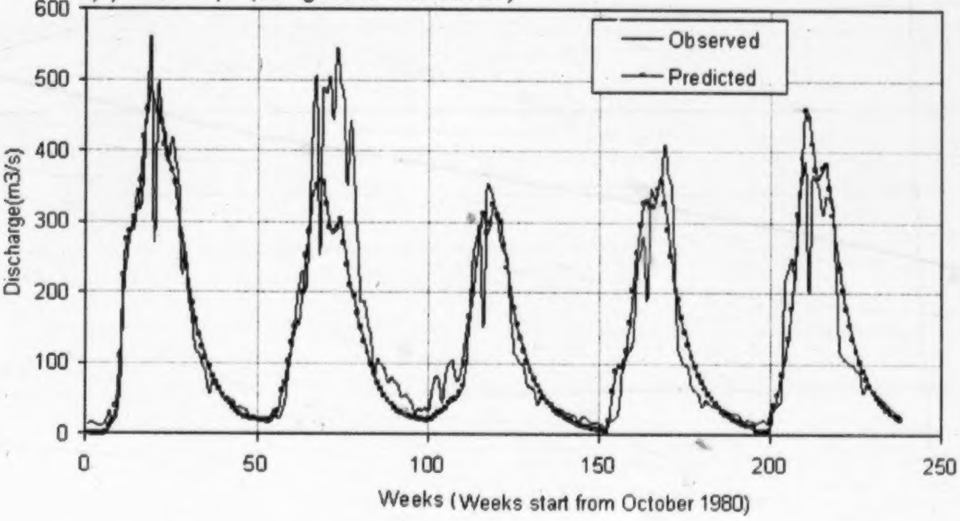

(b) Machiya (using disaggregated rainfall)

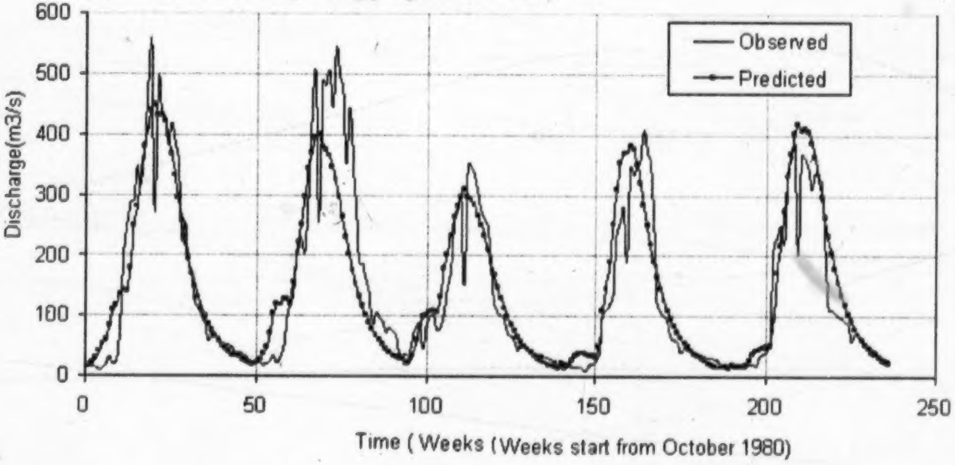

Figure 6.11 Plots showing observed and predicted weekly streamflow (m^3/s) from the SAC-SMA model using (a) Observed rainfall and, (b) from the ANN-GA-DIS-SMA model using statistically predicted rainfall.

Table 6.1 Summary statistics of SAC-SMA's predicted versus observed streamflow under the observed rainfall of the Kafue River basin.

Year	1984	1985	1986	1987	1988
R^2 (%)	96.0	81.1	88.4	90.2	88.4
RMSE (%)	21.8	50.7	33.1	37.4	41.2
BIAS (%)	2.1	-28.1	-4.8	6.3	9.3

Table 6.2 Summary statistics of ANN-GA-DIS-SMA's predicted versus observed streamflow for the Kafue River basin.

Year	1984	1985	1986	1987	1988
R^2 (%)	90.8	78.1	88.4	88.5	89.1
RMSE (%)	30.1	48.2	31.5	40.5	37.2
BIAS (%)	-1.7	-18.4	-7.4	11.4	13.1

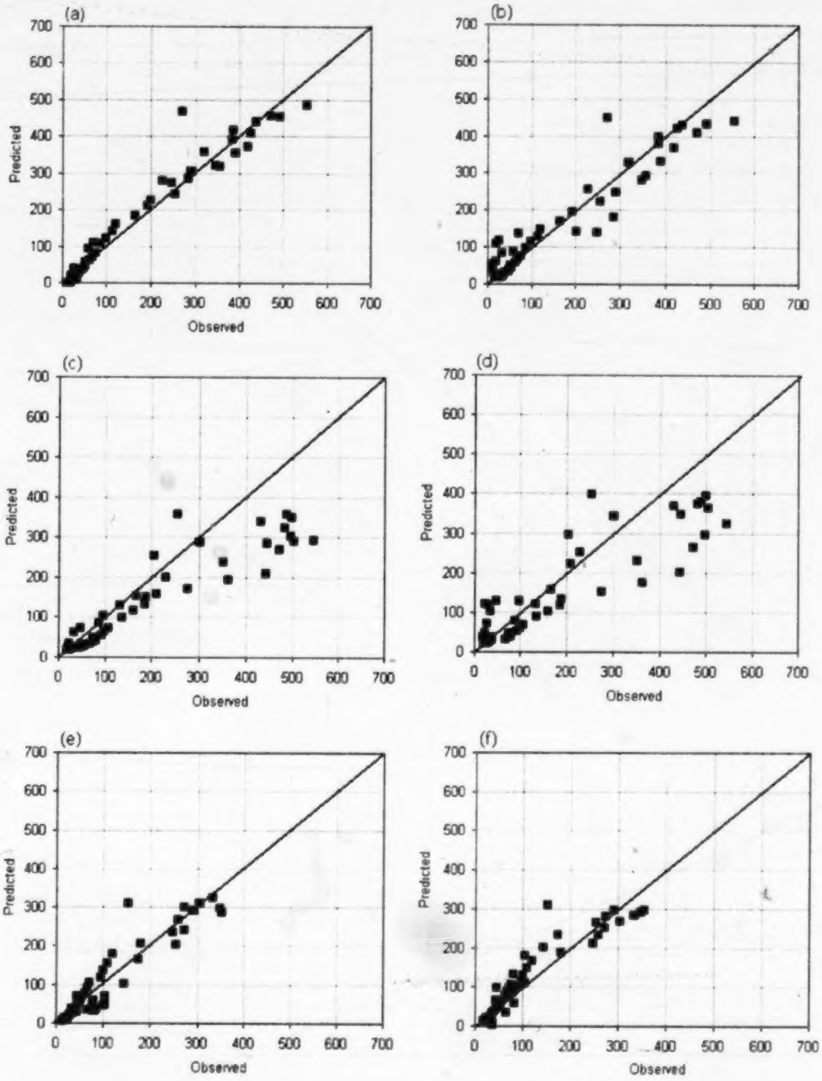

Figure 6.12. Scatter plots of observed versus predicted Kafue river weekly streamflow (m3/s) based on observed input rainfall, (a),(c) (e), (g) and (i); and that based on statistically predicted rainfall, (b), (d), (f), (h) and (j) for the period 1984 to1988.

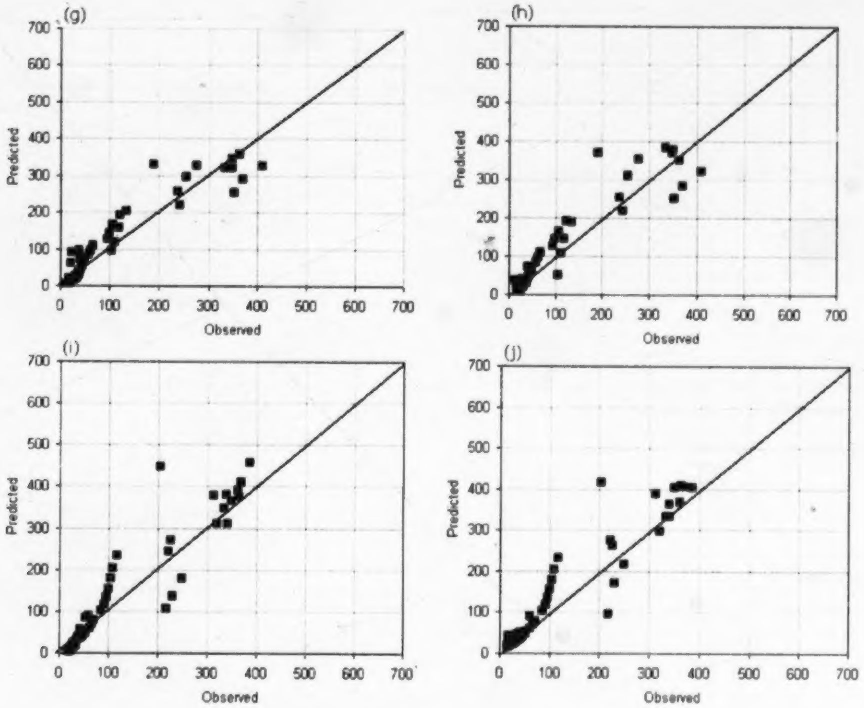

Figure 6.12 Continued.

Figures 6.13 show the time series plots for the validation periods of the weekly streamflow for the Lunga River basin. Figure 6.14 shows the corresponding scatter plots for the validation periods. The statistics summary corresponding to Figures 6.13 and 6.14 are presented in Tables 6.3 and 6.4. The correlations between the predicted and observed weekly streamflow show that between 69 and 90% of the variance of observed streamflow was accounted for by the predicted streamflow of SAC-SMA forced by observed rainfall, and 61 to 84% of the variance of the observed streamflow was accounted for when SAC-SMA was forced by the statistically predicted rainfall. Generally both the low and high streamflows were difficult to predict as shown by the Figure 6.13 and the statistics in Tables 6.3 and 6.4. Using both the observed and statistically generated rainfall, the streamflow in 1980 and 1981 was under-predicted. From Figure 6.8 between 1977 and 1981, rainfall consistently decreased, which directly affected the streamflow. The increased rainfall in 1982 was largely small to offset the effects of five years of decreasing rainfall. During the 1977-1981 period, the detention capacity of the upper reaches increased, causing the 1982 rainfall to start recharging the catchment. Hence the response of the catchment to the 1982 rainfall was suppressed, even though slightly high rainfall was recorded in 1982. Results indicate that ANN-GA model was able to capture the SST-rainfall dynamics.

It is clear from the two examples that AMC plays an important role in modeling the Kafue and Lunga basins. Although the performance of the SAC-SMA model was not as encouraging for the Lunga River than the Kafue, the SAC-SMA could still predict the weekly streamflow of the Lunga River reasonably well.

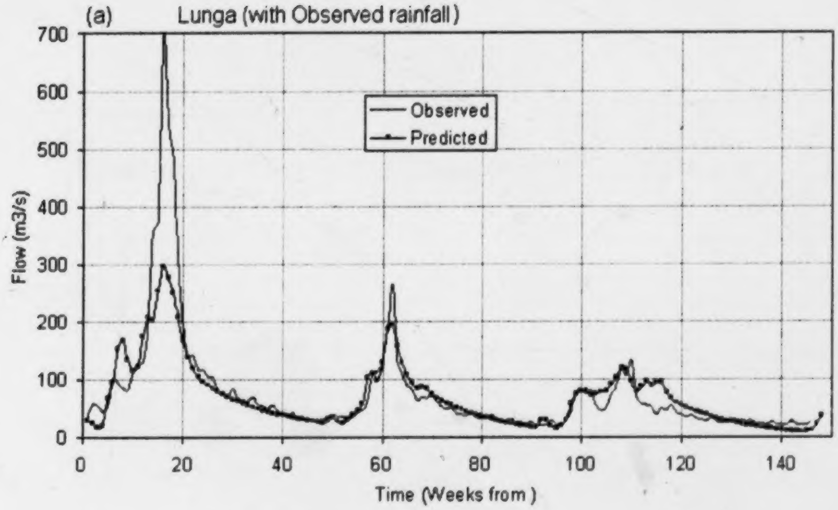

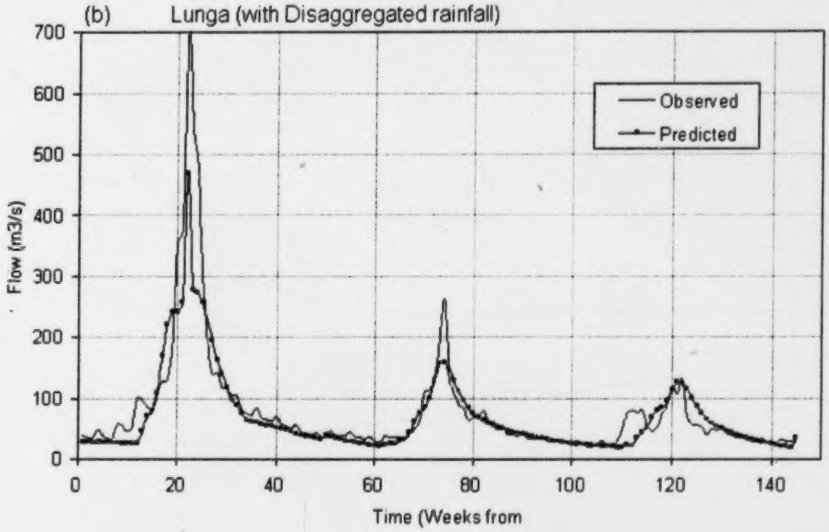

Figure 6.13 Plots showing observed and predicted weekly streamflow (m3/s) by SAC-SMA forced by (a) Observed rainfall and, (b) statistically predicted rainfall.

Table 6.3 Summary statistics of SAC-SMA's predicted versus observed streamflow using the observed rainfall in the Lunga River basin.

	1980	1981	1982
R^2 (%)	81.0	95.0	83.3
RMSE (%)	57.3	25.6	67.0
BIAS (%)	-14.1	3.2	43.6

Table 6.4 Summary statistics of ANN-GA-DIS-SMA predicted versus observed streamflow for the Lunga River basin.

Year	1980	1981	1982
R^2 (%)	90.7	84.1	61.5
RMSE (%)	48.8	30.4	41.2
BIAS (%)	0.1	-6.1	-0.3

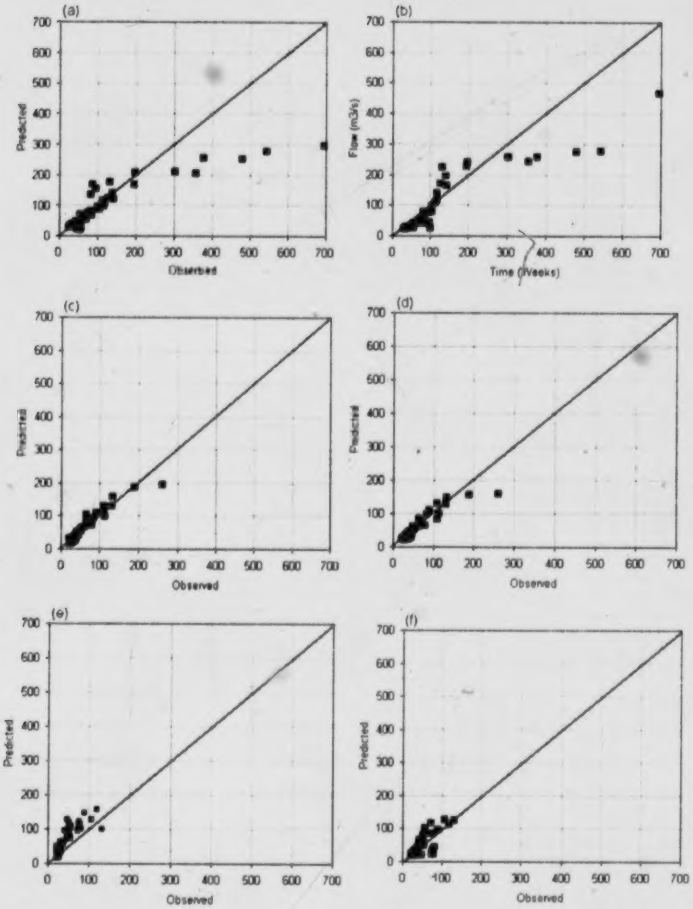

Figure 6.14. Scatter plots between the Lunga River's observed and predicted weekly streamflow of SAC-SMA forced by observed data (a),(c),(e), and that of ANN-GA-DIS-SMA forced by statistically generated rainfall data (b), (d), and (f).

6.4.4.4 Model Parameters

Tables 6.5 shows the optimized parameters calibrated through a combination of manual effort and the global optimization algorithm called SCE-UA of Duan et al., (1992) for the Kafue and Lunga River basins. The upper zone tension moisture capacity and the free water storages of these two basins were found to be 382 and 299 mm respectively, which were above the upper limits suggested by Gan (1988) (i.e.5-250 and 3-30 mm respectively). These values were found by automatic calibration, by starting off with parameter values of 29 and 15 mm, respectively. Considering the types of soil prevailing in this region, these relatively high conceptual upper storage parameters are possible. Besides, the bounds recommended by Gan (1988) were mainly based on North American experience. These figures probably reflect the high storage capacity associated with the dominance of the innumerable dambos found in the upper reaches of the basin, and the sandy and veldt soils in the middle and lower basins. To effectively simulate decreasing runoff (Fanta et al., 2001) under years of decreasing rainfall, it will be necessary for SAC-SMA to be represented with high upper conceptual tension and free water storages. This might partly reflect that under the presence of tropical grasslands and trees, the soil is well penetrated with roots, leading to the presence of many bore holes and hence more storage capacity. The lower zone parameters are within the parameter bounds suggested by Gan (1988) but equally high suggesting that the basin might have a big lower zone reservoir. The lower zone parameters of the Lunga basin are however slightly lower than those of the Kafue river.

The parameters presented in Tables 6.5 represent the optimal solutions derived from the multi-dimension, parameter search space with infinite number of solutions. In order that SAC-SMA can accurately predict the streamflow of Kafue and Lunga river basins, these parameters must be realistic and representative of the hydrologic characteristics of these basins.

Table 6.5 Optimal parameters for the Kafue and Lunga River basins.

1	2	3	4
Parameter	Kafue Optimized Parameters	Lunga Optimized Parameters	Parameter Definition
UZTWM	382	388	Upper zone tension water
UZFWM	299	299	Upper zone free water capacity
UZK	0.06	0.06	Upper zone withdrawal rate
ZPERC	28	24	Maximum percolation rate
REXP	1.001	1.026	Exponent for the percolation Equation
LZTWM	300	253	Lower zone tension water
LZFSM	345	328	Lower zone free water capacity
LZFPM	893	869	Lower zone primary free water capacity
LZSK	0.21	0.28	Lower zone secondary withdrawal rate
LZPK	0.18	0.021	Lower zone primary withdrawal rate
PEADJ	0.604	0.401	ET-demand adjustment factor

Even though model parameters were optimized through good calibration effort, SAC-SMA is still a lumped-parameter, conceptual hydrologic model that ignores the spatial variabilities of basin characteristics (e.g., soil properties, terrain, vegetation) and climate data, that conceptualizes the essential basin-scale hydrologic processes with a model structure that is a simplified version of nature that is highly heterogeneous and complex.

6.4.5 Direct Disaggregation of Seasonal Rainfall to Weekly Streamflow

Instead of using a hydrologic model to predict weekly streamflow, we also experimented with the disaggregation of predicted seasonal rainfall directly to weekly streamflow. This experiment was based on the assumption that in the absence of significant storage changes in the basin, streamflow runoff is the difference between evapotranspiration and rainfall falling on the basin. By removing the annual evapotranspiration from the predicted seasonal rainfall, the net should be approximately equal to the seasonal streamflow, which can then be directly disaggregated into the weekly streamflow. In this case the vector A and matrix B of Eqn 6.1 are determined directly from the observed historical weekly and monthly streamflow data.

Figures 6.15 (a) and (b) show the weekly streamflow time series plots of the Kafue and Lunga river basins for the validation period. Figure 6.16 shows the corresponding scatter plots for the validation periods. The statistics summary corresponding to Figures 6.15 and 6.16 are presented in Table 6.6 and 6.7. Table 6.6 and 6.7 show that between 68.1 and 84.6% and between 31.1 and 63.2% of the variance in the observed streamflow were accounted for by the predicted weekly streamflow for the Kafue and Lunga rivers, respectively. Although the bias was small, the RMSE errors were large, 46.8-56.2%, which also indicates that the performance of direct disaggregation of net seasonal rainfall to annual weekly streamflow was poor.

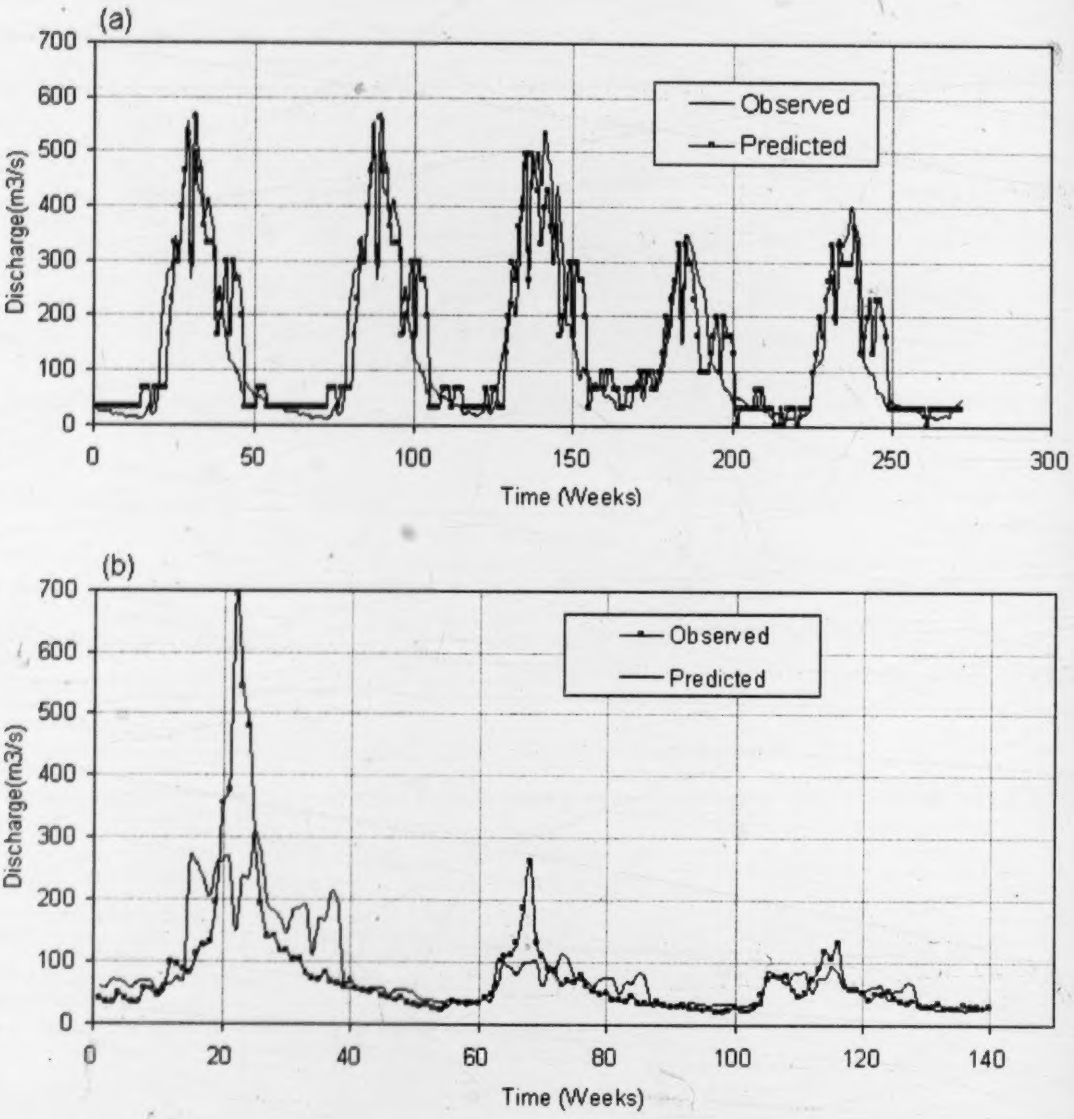

Figure 6.15 Plots showing observed and predicted weekly streamflow (m3/s) from the direct disaggregation of statistically predicted net rainfall for (a), Kafue River basin and (b) Lunga River basin.

Table 6.6 Summary statistics between observed and simulated weekly Kafue River streamflow, where the latter was directly disaggregated from the difference between seasonally predicted rainfall and evapotranspiration.

Year	1984	1985	1986	1987	1988
R^2 (%)	84.6	81.5	81.5	68.1	78.5
RMSE (%)	46.8	42.6	38.1	48.1	56.2
BIAS (%)	8.3	8.0	1.7	2.7	14.4

Table 6.7 Summary statistics between observed and simulated weekly Lunga River streamflow, where the latter was directly disaggregated from the difference between seasonally predicted rainfall and evapotranspiration

Year	1978	1979	1980
R^2 (%)	31.1	46.4	63.2
RMSE (%)	92.4	58.5	34.4
BIAS (%)	8.1	2.7	4.4

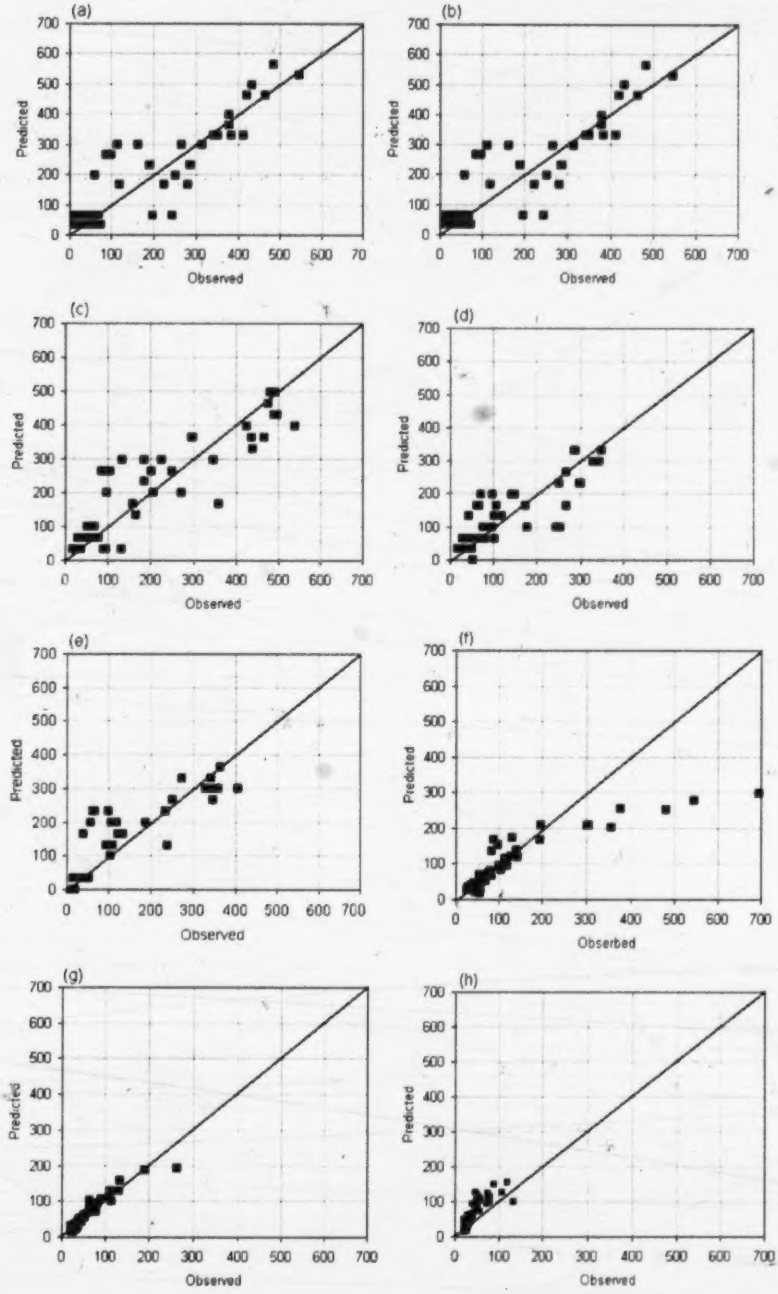

Figure 6.16 Scatter plots between the observed and predicted weekly streamflow of the Kafue river, (a),(b),(c) (d), and that of Lunga River, (e), (f) (g).

Figure 6.15(a) shows that only the upper limb was correctly generated. The modeling performance was generally low compared to the ANN-GA-DIS-SMA that used SAC-SMA to model transform rainfall to streamflow, which is a more plausible and realistic approach than a direct disaggregation of net rainfall (rainfall minus evapotranspiration) into streamflow. This is not a surprise because a purely statistical approach is not expected to effectively mimic the complex nature of basin scale hydrologic processes governed by a number of interconnected storages (e.g., thresholds) and soil layers, and several runoff mechanisms. We would expect a hydrologic model such as SAC-SMA specifically designed to simulate such hydrologic processes to do a better job than a disaggregation model governed by matrices A and B derived from the co-variances of observed runoff only. Besides, SAC-SMA must also be carefully calibrated for the observed hydrologic conditions of any watershed before it can be applied to simulate its rainfall-runoff transformation process.

6.5 Summary of Findings

To predict streamflow at weekly time steps from predicted seasonal rainfall, this thesis proposed the integration of ANN-GA, disaggregation, evapotranspiration and the Sacramento moisture accounting (SAC-SMA) models. We also tried to integrate the ANN-GA, a disaggregation model and an evapotranspiration model, so that we could directly downscale predicted seasonal precipitation, less evapotranspiration into weekly streamflow. The combined approaches were referred to as ANN-GA-DIS-SMA and ANN-GA-DIS, respectively.

The modeling performance was generally higher for the ANN-GA-DIS-SMA model than the ANN-GA-DIS model. This is not a surprise because a purely statistical approach is not expected to effectively mimic the complex nature of basin scale hydrologic processes governed by a number of interconnected storages and soil layers, and several runoff mechanisms.

Overall this Chapter demonstrated that an integration of ANN-GA, disaggregation, ET and SAC-SMA models results in a more robust model than direct disaggregation of net rainfall to streamflow without consideration of the complex rainfall-runoff generation process.

CHAPTER 7

CONCLUSIONS AND SUGGESTED FUTURE WORK

7.1 Summary and Conclusions

Fascinated by the desire to understand the nonstationary variability of climate processes on regional and global scales and the desire to develop capability to predict non-linear interactions between hydroclimatic variables, this thesis conceptualized the novel and integrated approaches of wavelet empirical orthogonal function analysis (WEOF), Hilbert transformation empirical orthogonal function analysis (HEOF), wavelet independent component analysis (WICA) and Hilbert transformation independent component analysis (HICA) and artificial neural network genetic algorithm (ANN-GA) model. This thesis also integrated ANN-GA, disaggregation techniques and the Sacramento soil moisture accounting model to predict annual streamflow at weekly time steps from seasonal oceanic variability through two approaches referred to as the ANN-GA-DIS-SMA and ANN-GA-DIS.

The various nonstationary methods of analysis are detailed in Chapter two. Chapter three identified and analyzed the space-time and frequency variation of the rainfall over Eastern Africa, Central South and greater Southern Africa and the sea surface temperature (SST) of the Indian and South Atlantic Oceans. The new findings of Chapter three are summarized below:

(1) Changes in the frequency regimes of the Indian Ocean SST, the SON rainfall and Southern Africa rainfall that have implications for long term planning had been identified. For example, the oscillation period of the September-November (SON)

rainfall of Eastern Africa shifted from about 20-years to about 10-years between 1900 and 1950 and about 10 to 14 years between 1950 and 1997. Since the data was short we could not precisely determine the background periodicity of these frequency variations. Between 1900 and 1960 rainfall increased consistently and between 1960 and 1997 rainfall decreased consistently resulting in numerous droughts between 1965 and 1997. Due to a short data length, it is not clear whether or not the SON droughts continued after 1997. Similar changes were noted in Southern Africa that helped explain the declining levels in the streamflows and dam levels especially after 1970. The current dataset seems to suggest that longer background periods exist in the rainfall and incorporating them in the development of long term plans in water resources and agriculture will help countries within Eastern and Southern Africa.

(2) The nonstationary spatial variability of the South Atlantic Ocean seasonal SSTs that have important implications for the weather and climate in Eastern, Central South and greater Southern Africa and probably most of sub-Saharan Africa and parts of South America. However, we have to be selective in choosing the SST predictor field from the South Atlantic or Indian Ocean because some sectors of SST fields are not significantly correlated to the predictands. Including "redundant" predictor fields basically adds data noise to the predictor data that compromises the prediction skill of most prediction models.

(3) Within the 2 to 8 year band, the dominant periods of the SON rainfall of East Africa were around 2-years, while for the MAM rainfall of east Africa and the summer rainfall of Central South and Southern Africa, dominant periods were

around 5.6 years, followed by the periods around 2 years. Therefore, besides identifying the sectors of relevant SST fields, identifying the dominant scale-bands also help to exploit the interannual oceanic variability to predict rainfall.

(4) ENSO affects the rainfall of Eastern, Central South and Southern Africa when the energy within the 2-year period was decreasing. When there was a synchronous decrease of energy at all periods within the 2-8 year band, droughts result. Hence by following the energy levels within 2-8 year band, it is possible to predict when ENSO will cause drought or below normal rainfall and when it will not. Knowledge of this effect of ENSO on Eastern, Central South and Southern Africa will be useful to these countries in preparing themselves for the impending threat of droughts to mitigate the potential impact of ENSO.

Chapter 4 outlined how Eastern, Central South and Southern Africa responded to changes in SSTs in the Indian and Atlantic Oceans. It was discovered that seasonal variabilities of SST in both oceans affect rainfall in this African sub-continent. The northern Indian Ocean and the Guinea Ocean current SST were found to have negative associations, while the Brazil, Benguela and the southern Indian Ocean current SST were found to be positively associated with the rainfall of these African regions.

Chapter 5 developed the non-linear, artificial neural network, prediction model calibrated by the genetic algorithm (ANN-GA). The model was shown to be robust and a more powerful alternative to linear models such as canonical correlation analysis (CCA). The performance of the model was evaluated against the SON and MAM rainfall of East Africa and summer rainfall of Central South and Southern

Africa. The skill was as follows: For the SON rainfall, correlation coefficient (ρ) was between 0.70 and 0.9, HK score between 0.2 and 0.8, and RMSE between 0.4 and 0.75; while for the MAM rainfall, ρ ranged from 0.82 to 0.9, RMSEs from 0.5 to 0.6 and HK scores ranged from 0.5 to 0.8. In Central South Africa, ρ was between 0.8 and 0.9, RMSEs of 0.4 and 0.9, and HK scores of between 0.4 and 0.8; while in most Southern Africa, the ρ generally ranged between 0.70 and 0.9, RMSE ranged between 0.4 and 0.8, and HK scores ranged between 0.5 and 0.9.

The ANN-GA-DIS-SMA developed in Chapter Six showed considerable skill in predicting weekly streamflow from seasonal rainfall predicted from seasonal SST variability. Predicted streamflow using the ANN-GA-DIS-SMA model explained between 81 and 96% of the variance in the observed streamflow. Except for one year, the biases ranged between –4.8 and 9.3% and the errors averaged 37%. However, a direct disaggregation of net rainfall to streamflow (the ANN-GA-DIS model) did not perform well. The variance accounted for by this model ranged between 61 and 84%. The errors were large, ranging from 30 to 67%. The ANN-GA-SMA approach appeared as the only approach for predicting the annual streamflow at weekly time steps. Given the complex nature of basin-scale, hydrologic processes which involve threshold controls and highly nonlinear behavior, we can only expect a hydrologic model carefully designed for modeling such hydrologic processes, and specifically calibrated for the specific basin characteristics and climatic features of each particular basin, instead of a simple linear disaggregation model, to handle such complex rainfall-runoff transformations effectively. As a cautionary note, ANN-GA-DIS-SMA could accurately predict weekly streamflow out of predicted seasonal rainfall for this part of Africa partly because its intra-annual climate regime is relatively stable. We cannot expect a system such as ANN-GA-DIS-SMA to work well in climate systems that does not exhibit stable intra-annual climate structure similar to that of Southern Africa.

Although the above applications were confined to Africa and the surrounding oceans, the techniques developed in this thesis, after some degree of modifications, should be applicable to other continents.

7.2 Suggested Future Work

As with all techniques, there is always room for improvement. The following are some of the suggestions for future work

7.2.1 The End Point Problem

The biggest problem for both wavelet and Hilbert transformations is what is called the end point problem. Since time series are finite, lots of zeros are added to the end and beginning of the time series to bring the length of the time series to the next high power or two (e.g. 512 or 1024) to facilitate the use of the Fourier analysis. The addition of zeros suppresses power computed at the ends of the time series as one goes towards longer scales. This makes it difficult to interpret the energy variability at the ends and beginning of the time series. This difficulty might be solved by including six or more cosine or sine waves at the ends of the time series. This suggestion was made by Norden Huang, the inventor of the EMD-Hilbert transformation method during the May 16-May 25 2004 visit to NASA's Goddard Space Flight Center in Greenbelt, Maryland, USA. Although he suggested that this method has worked well in his applications, this method has not being tried out in this thesis.

7.2.2 Experimentation with Wavelet or Hilbert Spectral Images

The multivariate WEOF, HEOF, WICA, HICA techniques use scale averaged power (e.g., such SAWP) to analyze the nonstationarity of the climate processes. We suggest using Wavelet and Hilbert spectral images to minimize the amount of information lost through scale averaging.

7.2.3 Application of WEOF, HEOF, WICA and HICA to Global Scales and Other Atmospheric Variables

Since rainfall variability is affected by local and remote SST variability, it will be interesting to analyze the global SST variability via the above approaches and see linkages with local climate, especially across scales. Since large datasets overwhelm prediction models, EOF could be used to compress the global-scale datasets to increase the effectiveness of the ANN-GA or other prediction models. Besides, SST was the only data used in this thesis. Other atmospheric variables, such as Sea Level Pressure (SLP) are suggested. Important influences such El Nino (by using gridded SST data from the ENSO region) would be interesting. Since this region is adjacent to the Atlantic Ocean, it will also be interesting to see linkages if any between the ENSO region and the Atlantic Ocean.

7. 2.4 Improvements in the ANN-GA prediction Model

As noted in Chapter five, new and improved GAs such as the messy GAs have been developed in recent years. It will be interesting to incorporate the improved messy GA as the weight search algorithm. Other emerging optimization algorithms such as Particle Swam optimization (PSO) algorithms (e.g., Eberhart and Shi 1998) may also be used.

REFERENCES

Abbort, M. A., and T. G. J. Dyer, 1976: The temporal variation of rainfall over the summer rainfall region of South Africa. *South African Journal of Science,* **72**: 276-278.

Alexander, W. J. R., 1995: Floods, droughts and climate change. *South African Journal of Science,* **91**: 403-408.

ASCE Task committee on application of Artificial Neural Networks in hydrology, 2000: Artificial neural networks in hydrology I: Preliminary concepts. *ASCE Journal of hydrologic engineering,* **5:** 115-123.

Bakshi, B., 1998: Multiscale PCA with applications to multivariate statistical process monitoring. *AIChE,* **44:** 1596-1610.

Barnston, A, G., H. M., van den Dool, S. E. Zebiak, T. P. Barnet, M. Ji, D. R. Rodenhuis, M. A. Cane, A., Leetma, N. E., Graham, C. R. Ropelewski, V. E. Kousky, E. A., O'Lenic, and R. E. Livezey, 1994: Long-lead seasonal forecasts- where do we stand? *Bulletin of American Meteorological Society,* **66**: 2097-2114.

BBC: 2002a, Africa's famine: country-by-country http://news.bbc.co.uk/2/hi/africa/2027079.stm

BBC: 2002b, Hunger spectre over Angola http://news.bbc.co.uk/2/hi/africa/2504661.stm

BBC: 2002c, Why famine stalks Africa, http://news.bbc.co.uk/2/hi/africa/2449527.stm

Bauer, R. J., 1994: Genetic algorithms and investment strategies, John Wiley and sons, 308 pp.

Beven, K. J. and M. J. Kirkby, 1979: A physically based variable contributing area model of basin hydrology. *Hydrologic Science Bulletin,* **24:** 43-69.

Bindlish, R. and A. Barros, 2000: Disaggregation of rainfall for one-way coupling of atmospheric and hydrological models in regions of complex terrain. *Global and Planetary Change,* **25**: 111-132.

Brindle, A. 1981: Genetic algorithms for function optimization. PhD dissertation, Technical report TR81-2, University of Alberta. Edmonton, Canada, 193 p.

Burnash, R. J., R. L. Ferral, and R. A. Maguire, 1973: A generalized streamflow simulation system, in Conceptual modeling for digital computers, National Weather Service. Sacramento, California.

Cahalan, F. R., L. E. Wharton and M-L. Wu, 1996: Empirical orthogonal functions of monthly precipitation and temperature over the United States and homogenous stochastic models. *Journal of Geophysical Research.* **101**, D21, 26,309-26,318

Canon, A., J. and P. H. Whitfield, 2002: Downscaling recent streamflow using ensemble neural network models. *Journal of Hydrology,* **259:** 136-151.

Cardoso, J. F., and A. Souloumiac, 1993: Blind beam forming for non-Gaussian signals. *IEEE proceedings.* **140:** 362-370.

Castleman, K. R., 1996: *Digital Image Processing.* Prentice hall: Englewood cliffs, New Jersey, 667 p.

Chiew, F. H. S., and T. A. McMahon, 1991: The applicability of Morton and Penman's evaporation estimates in rainfall-runoff modeling. *Water Resources Research,* **27:** 611- 620.

Chow, V. T., D. R. Maidment and L. M. Mays, 1988: *Applied Hydrology.* McGraw Hill series in water engineering, 572 p.

Crane, R. G. and B. C., Hewitson, 1998: Doubled CO2 precipitation changes for the Susquehanna basin: down-scaling from the genesis general circulation model. *International Journal of Climatology,* **18:** 65-76.

Coulibaly, P. F., Anctil, P. Rasmussen and B., Bobée, 2000: A recurrent neural networks approach using indices of lo-frequency climatic variability to forecast regional annual runoff. Hydrological processes, **14**: 2755-2777.

Crick, F., 1989: The recent excitement about neural networks. *Nature,* **337:** 129-132

Currie, R. G., 1993: Lunar-solar 18.6 and 10-11-year solar cycle signals in South African rainfall. *International Journal of Climatology,* **13**: 237-256.

Ding, P. and L. Zhang, 2003: ICA feature extraction-framework and application. *Chinese Journal of Electronics,* **12:** 106-110.

Dlamini, E. M., 1995: Modeling of an Africa basin using 4 rainfall-runoff models, *MSc Thesis*, University of Alberta, 129 p.

Dracup, J. A and E. Kahya, 1994: The relationship between US streamflow and La Nina events. *Water Resources Research,* **30**: 2133-2141.

Duan, Q., S. Sorooshian, and V. Gupta, 1992. Effective and efficient global optimization for conceptual rainfall-runoff models. *Water Resources Research,* **28**: 1015-1031.

Dyer, T. G. J., and P. D. Tyson, 1977: Estimating above and below normal rainfall periods over South Africa 1972-2000. *Journal of Applied Meteorology,* **16**: 145-147.

Eberhart, R. and Y. Shi, 1998: Comparison between Genetic Algorithms and Particle Swarm Optimization. The 7th Annual Conference on Evolutionary Programming.

Fanta, B., B. T., Zaake and R. K. Kachroo, 2001: A study of the variability of the river flow of the southern Africa region. *Hydrological Sciences* **4**: 513-524.

Gallant, P. J. 2001: A hybrid evolutionary algorithm to train neural networks as time series predictors. PhD Thesis. Queens University, Canada, 144 p.

Gan, T. Y., 1988: Applications of scientific modeling of hydrologic responses from hypothetical small catchments to assess a complex conceptual rainfall-runoff model. Technical report no. 111, University of Washington, Seattle, 258 p.

Gan, T. Y., and S. J. Burges, 1990: An assessment of a conceptual rainfall-runoff models ability to represent the dynamics of small hypothetical catchments, 1, Models, Model properties and experimental design, *Water resources research*, **26:** 1595-1604.

Gan, T. Y., and G. F. Biftu, 1996: Automatic calibration of conceptual rainfall-runoff models: Optimization algorithms, catchment conditions and model structure. *Water Resources Research,* **32:** 3513-3524.

Gan, T. Y., and G. F, Biftu, 2000: Assessment of evapotranspiration models applied to a watershed of Canadian Prairies with mixed land uses. *Hydrological Processes*, **14:** 1305-1325.

Goddard, L. and N. E. Graham 1999: Importance of the Indian Ocean for simulating rainfall anomalies over eastern and southern Africa. *Journal of Geophysical Research*, **104:** 19099-19116.

Goldberg, D. E. 1989: Genetic algorithms in search, optimization, and machine learning. Reading Mass: Addison-Wesley.

Goldberg, D. E. 1994: Genetic algorithms and evolutionary algorithms come of age. *Communications of the ACM.* **37:**113-119.

Goldberg, D. E., 2002: The design of innovation, lessons from and for Competent Genetic Algorithms. Kluwer Academic Publishers, 247 p.

Goldberg, D. E., B. Korb and K. Deb, 1989: Messy genetic algorithms. Motivation, analysis and first results. *Complex systems*, 3: 493-530.

Hastenrath, S., 1995: Recent advances in tropical climate prediction. *Journal of climate*, **8**: 1519-1532.

Hastenrath, S. 2000: Zonal circulation over the equatorial Indian Ocean. *Journal of Climate*, **13**: 2746-2756.

Haykin, S. 1994: *Neural Networks: A Comprehensive Foundation*, 696 p.

Hendrickson, J., S. Sorooshian and L. E. Brazil, 1988: Comparison of Newton-type and direct search algorithms for calibration of conceptual rainfall-runoff models. *Water resources research*, **24:** 691-700.

Hobbins, M. T., J. A. Ramirez, T. C. Brown and L. H. M. Claessens, 2001: The complementary relationship in estimation of regional evapotranspiration: The complementary relationship areal evaporation and advection-aridity models. *Water Resources Research*, **37:** 1367-1387.

Holland, J. 1975: Adaptation in natural and artificial systems. Ann Arbor, MI: The university of Michigan.

Houghton, R., and Y. Tourre, 1992: Characteristics of low frequency sea surface temperature fluctuations in the tropical Atlantic. *Journal of Climate,* **7:** 141-157. 2256.

Hsieh, W. W., and B. Tang. 1998: Applying Neural Network models to prediction and data analysis in meteorology and oceanography. *Bulletin of the American Meteorological Society,* **79:** 1855-1868.

Hsieh, W. S., J. T. B. Obeysekera, V. Yevjevich and D. G. Decoursey (eds), 1986: Multivariate analysis of hydrologic processes. *Proceedings of the fourth international hydrology symposium*, July 15-17, 1985, 1077 p.

Huang, N. E., Z. Shen, Q. Zheng, N. Yen, C. C. Tung and H. H. Liu, 1998: The empirical mode decomposition and the Hilbert spectrum for nonlinear and non-stationary time series analysis. *Proceedings of the Royal Society of London*, **454**: 903-995.

Hulme, M., 1994: *Validation of large-scale precipitation fields in general circulation models. p 387-406 in Global precipitations and climate change* (eds.) Desbois, M and Desalmand F., NATO ASI Series, Springer-Verlag, Berlin, 466 p.

Hutchinson, M. F. and T. I. Dowling 1992: A continental hydrological assessment of a new grid-based digital elevation model of Australia. In Terrain analysis and distributed modeling in hydrology, Beven, K. J. and I. D. Moore (eds). John Wiley and Sons. Pages 49-62.

Hyvärinen, A., 1998: New approximations of differential entropy for independent component analysis and projection pursuit. *Advances in neural information processing systems*, **10**: 273-279.

Hyvärinen, A., and E. Oja, 2000: Independent component analysis: algorithms and applications. *Neural Networks,* **13**: 411-430.

IPPC, 1998: The regional impacts of climate Change, An assessment of vulnerability. Special report of the IPPC working group II, Cambridge University press, 514 p.

Jenkins, G., and E. J. Barron, 1997: General circulation model and coupled regional climate model simulations over the eastern United States: GENESIS and RegCM2 simulations. *Global and Planetary Change,* **15**: 3-32.

Jung, T. P., C. Humphries, T. Lee, S. Makeig, M. McKeown, V. Iragui and T. Sejnowski, 1998: Extended ICA removes artifacts from electroencephalographic recordings. *In advances in neural information processing systems*, **10**: 894-900.

Jury, M. R, 1996: Regional teleconnection pattern associated with summer rainfall over

South Africa, Namibia and Zimbabwe, *International Journal of Climatology*, **16:** 135-153.

Jury, M. R., and S. Engert, 1999: Teleconnections modulating inter-annual climate variability over northern Namibia. *International Journal of Climatology*, **19**: 1459-1475.

Kahya, E., and J. A. Dracup, 1993: US streamflow patterns in relation to El Nino southern oscillation. *Water resources research*, **29**, 2491-2503.

Kang, Boo-Sik 2003: Precipitation downscaling and its use in the assessment of hydrologic effects of climate variability and change. PhD thesis. Colorado State University at Fort Collins, 220 p

Klein, W. H., 1993: Objective specification of monthly mean temperature from mean 700 mb heights in winter. *Monthly Weather Review*, **113:** 277-290.

Kumar, D. N., U. Lall and M. R. Petersen, 2000: Multi-site disaggregation of monthly to daily streamflow. *Water Resources Research*, **36:** 1823-1833.

Landman, W. E., and S. J. Mason, 1999: Change in the association between Indian Ocean sea surface temperatures and summer rainfall over South Africa and Namibia. *International Journal of Climatology*, **19**: 1477-1492.

Landman, W. E., S. J. Mason, P. D. Tyson and W. J. Tennant, 2001: Retroactive skill of multi-tiered forecasts of summer rainfall over southern Africa. *International Journal of Climatology*, **21:** 1-19.

Lall, U., and M. E. Mann, 1995: The Great Salt Lake: A barometer for interannual climate variability. *Water Resources Research*, **31:** 2503-2515.

Leupod, L. B. and W. B. Langbein, 1960. A primer on water, US Geological survey, p 50.

Lindesay, J. A., 1988: South African rainfall, the southern oscillation and a southern hemisphere semi-annual cycle. *Journal of climatology*, **8**: 17-30.

Lorenz, E. N., 1969: Atmospheric predictability as revealed by naturally occurring analogs. *Journal of Atmospheric Sciences*, **26:** 639-646.

Mason, S. J., 1995: Seas-surface temperature-south African rainfall associations, 1910-1989. *International Journal of Climatology*, **15**: 119-135.

Mason, S. J., 1997. Review of recent developments in seasonal forecasting of rainfall. *Water SA*, **23**: 57-61.

Mason, S. J., and P. D. Tyson, 2001: *The Occurrence and Predictability of Droughts Over Southern Africa.* In drought volume 1: A global assessment Wilhite DA(ed). Routledge: New York.

Michaelwicz, Z., 1992: *Genetic Algorithms + Data Structures = Evolution Programs*, Spring-Verlag, New York Inc New York N.Y.

Mistry, V. V and D. Conway, 2003: Remote forcing of east African rainfall and relationships with fluctuations in levels of Lake Victoria. *International Journal of Climatology*, **23**: 67-89.

Morton, F. I., 1978: Estimating evapotranspiration from the potential evaporation: Practicality of an iconoclastic approach. *Journal of Hydrology*, **38:** 1-32.

Morton, F. I., 1983: Operational estimates of Actual Evapotranspiration and their significance to the science and practice of hydrology, *Journal of hydrology*, **66:** 1-76.

Mutai, C. C., M. N. Ward and A. Colman, 1998: Towards the prediction of the East Africa short rains based on sea surface temperature-atmosphere coupling. *International Journal of Climatology*, **18**: 975-997.

Mwale, D. 1998: Genetic algorithms for water distribution network design and rehabilitation. MSc Thesis. Hohai University, Nanjing.

Mwale, D., and J. Munalula, 1999: The experience of using genetic algorithms in water supplies systems-the case at Lusaka Water and Sewerage Company. *Hotel Inter-continental, Lusaka,* Zambia on the theme "Recent advances in engineering research and development.

Mwale, D., and M. N. Mulenga, 1999: Optimization in water distribution network design: Saving investment capital and operational costs of water distribution networks through the use of genetic algorithms. Conference, Pamodzi Hotel, Lusaka, Zambia. On the theme: Engineering- a sub-regional perspective.

Mwale, D., T. Y. Gan, and S. P. Shen, 2004: A new analysis of variability, teleconnectivity and predictability of rainfall of central southern Africa, 1950-1994, in press, *International Journal of Climatology*, **24**: 1509-1530.

Mwale, D., and T. Y. Gan, 2004: Wavelet Analysis of Variability, Teleconnectivity and Predictability of the September-November East African Rainfall, in press, *Journal of Applied Meteorology (in press).*

Namias, J. 1985: Remarks on the potential for long-range forecasting. *Bulletin of the American Meteorological Society,* **66:** 165-173.

New et al., (2002) (SAFARI 2000 project), http://www.daac.ornl.gov

Nicholson, S. E 1996: A review of climate dynamics and climate variability in eastern Africa. Pp. 25-26 in *The limnonology, climatology and pale-climatology of the EAST Africa lakes*, Eds, T.C Johnson and E.O Odada, Gordon and Breach Publications, Amsterdam, the Netherlands.

Nicholson, S. E and D. Entekhabi, 1987: Rainfall variability in equatorial and southern Africa: Relationships with sea surface temperature along the southwestern coast of Africa. *Journal of applied meteorology*, **26**: 561-578.

Nicholson, S. E., D. Leposo and J. Grist, 2001: The relationship of the EL Nino and drought over Botswana. *Journal of Climate*, **14**: 323-335.

Nicholson, S. E., and J. Kim, 1997: The relationship of the EL Nino-southern oscillation to African rainfall. *International Journal of Climatology*, **17**: 117-135.

Nijssen, B. and D. P., Lettenmaier, 1997: streamflow simulation for continental-scale river basins. *Water Resources Research*, **33:** 711-724.

Ntale, H. K., 2001: *The Analysis and Prediction of Droughts in East Africa*, PhD dissertation, University of Alberta, Edmonton, 178 p.

Ntale, H. K., and T.Y., Gan, 2004: East African Rainfall Anomaly Patterns in Association with El Niño/Southern Oscillation, *Journal of Hydrologic Engineering,* ASCE, **9:** 257-268.

Ntale, H. K., T. Y., Gan and D. Mwale, 2003: Prediction of East African Seasonal Rainfall Using Simplex Canonical Correlation Analysis, *Journal of Climate,* **16:** 2105–2112.

O'Brien, J. J., 1992: Report of the workshop on socio-economic impact of ENSO. Florida State University.

Ogallo, L. J., 1989: The spatial and temporal patterns of East Africa seasonal rainfall derived from principal component analysis. *International Journal of Climatology,* **9**: 145-167.

Overland, J. E., and R. W., Preisendorfer, 1982: A significance test for principal components applied to a cyclone climatology. *Monthly Weather Review*, **110**: 1-4.

Phattanasri, P., 2002: *Associative learning in evolving dynamical neural networks*. PhD dissertation, Case Western Reserve University. 220 p.

Philippon, N., P. Camberlin, and N. Fauchereau 2002: Empirical predictability study of October-December East African rainfall. *Quarterly Journal of the Royal Meteorological* Society, **128**: 2239-2256.

Potts, A., 1971: Application of harmonic analysis to the study of east African rainfall data. *Journal of Tropical Geography,* **34**: 31-42.

Reason, C. J. C. and H. Mulenga, 1999: Relationships between South African rainfall and SST anomalies in the southwest Indian Ocean. *International Journal of Climatology*, **19**: 1651-1673.

Risbey, J., and P. Stone, 1996: A case study of the adequacy of GCM simulations for input to regional climate change. *Journal of Climate*, **9:** 1441-1467.

Rodhe, H., and H. Virji 1976: Trends and periodicities in East African rainfall data. *Monthly Weather Review*, **104**: 307-315.

Ropelewski, C. F., and M. S. Halpert, 1987: Global and regional scale precipitation patterns associated with EL Nino/southern oscillation. *Monthly Weather Review*, **115**: 1601-1626.

Rumelhart, D. E, G. E. Hinton and R. J. Williams, 1986: Learning internal representations by error propagation. *Parallel Distributed Processing*, Vol. 1, Rumelhart DE, McClelland JL, Group, PR (eds). MIT press: 318-362.

Salas, J. D., N. Saada, C. H. Chung, W. L. Lane and D. K. Frevert, 2000: Stochastic analysis, modeling and simulation (SAMS) Version 2000. Users manual- Technical report no. 10, Colorado State University.

Savik, D. A., and G. A. Walters, 1997: Genetic algorithms for least cost design of water distribution networks *Journal of Water Resources Planning and Management*, **123:** 67-77.

Saxton K. E., 1982: Evapotranspiration: Hydrological modeling of small watersheds. *American Society of Agriculture Engineers*. Haan, C. T., Johnson H. P, and Brakensiek, D. L (eds).

Schertzer, J. C., and S. Lovejoy, 1987: Physical modeling and analysis of clouds and rain by anisotropic scaling multiplicative processes. *Journal of Geophysical Research*, **92**, 9692-9714.

Singh, D., C. V. V. Bhadram and G. S. Mandal, 1995: New regression model for Indian summer monsoon rainfall, *Meteorology of Atmospheric Physics*, **55**: 77-86.

Shen, S. P. S., W. K. M., Lau, K.Y. Kim and G. Li 2001: *A canonical ensemble correlation prediction model for seasonal precipitation anomaly*, Technical memorandum NASA/TM-2001-209989. Greenbelt, Maryland 20771.

Shen S. S. P., P. Dzikowski, G., Li and D. Griffith, 2001: Interpolation of the 1961-1997 daily temperature and precipitation data onto Alberta Polygons of Ecodistrict and soil landscapes of Canada. *Journal of Applied Meteorology*, 40: 2162-2177.

Shin, T. and I., Han, 2000: Optimal signal multi-resolution by genetic algorithms to support artificial neural networks for exchange rate forecasting. *Expert Systems with Applications*, **18:** 257-269.

Simpson, A. R., G. C., Dandy, and L., J., Murphy, 1994: Genetic algorithm compared to other techniques for pipe optimization. *Journal of Water Resources Planning and Management*, **120**: 423-443.

Sorooshian, S., Q. Duan and V. K. Gupta, 1993: Calibration of rainfall-runoff models: Application of global optimization to the Sacramento soil moisture accounting models. *Water Resources Research*, **29**(4)**:** 1185-1194.

Tao, P. C., and J. W. Delleur, 1976: Multi-station, multiyear synthesis of hydrologic time series by disaggregation. *Water Resources Research*, **12:** 1303-1312.

Torrence, C., and G. P. Compo, 1998: A practical guide to wavelets analysis. *Bulletin of the American Meteorological Society*, **79**: 61-78.

Tyson, P. D, 1971: Spatial variation of rainfall spectra in South Africa. *Annals of the Association of the American Geographers*, **61**:711-720.

Tyson, P. D., 1986: Climate change and variability over southern Africa, Cape Town, Oxford University press, 220 p.

UNDP/FAO/GRZ, 1968: Multipurpose survey of the Kafue River basin, Zambia, Vol. III, Climatology and hydrology. Report No. FAO/SF; 35/ZAM.

Valencia, D. R., and J. C. Schaake, 1973: Disaggregation process in stochastic hydrology. *Water Resources Research*, **9:** 580-585.

Van den Dool, H. 1994: Searching for analogs, how long must we wait? *Tellus*, **46A**, 314-324.

Venegas, S. A., L. A. Mysak and D. N. Straub, 1997: Atmosphere-ocean coupled variability in the South Atlantic. *Journal of Climate,* **10**: 2904-2920.

Walker, N. D., 1987: Interannual sea surface temperature variability and associated atmospheric and associated forcing within the Benguela system. *South African Journal of Marine Science*, **5**: 121-132.

Wang, M., and C. Zheng, 1998: Ground water management optimization using genetic algorithms and simulated annealing: Formulation and comparison. *Journal of the American water resources association*, **3**(34): 519-530.

Webster, P. J., C. Clark, G. Cherikova, J. Fasullo, W. Han, Loschnigg and K. Sahami, 2002: The monsoon as a self-regulating coupled ocean-atmosphere system. In Meteorology at the Millennium (Edited by Pearce). *The Royal Meteorological Society*, **83**: 198-219.

Westheider, O., 1997: *Predicting stock index returns by means of genetically engineered networks*. PhD dissertation, University of California, Los Angles. 152 p.

Whitley, D., 1988: Applying genetic algorithms to neural net problems. *Neural Networks*, **1**: 230-230.

Wilks, D. S., 1995: *Statistical Methods in the Atmospheric Sciences*. Academic press: San Diego, 467 p.

Wu, Z. Y., and R. Simpson, 2001: Competent genetic-evolutionary optimization of water distribution systems. *Journal of Computing in Civil Engineering*, **15**(2): 89-101.

Xu, C., 1999: From GCMs to river flow: a review of downscaling methods and hydrologic modeling approaches. *Progress in Physical Geography*, **23:** 229-249.

Yarnal, B., M. N. Lakhtakia, Z. Yu, R. A. White, D. Pollard, D.A. Miller and W.M. Lapenta, 2000: A linked meteorological model system: the Susquehanna River Basin Experiment (SRBEX). *Global and Planetary Change*, **25:** 149-161.

Yu, Z. 2000: Assessing the response of sub-grid hydrologic processes to atmospheric forcing with a hydrologic model system. *Global and Planetary Change*, **25:** 1-17.

Yu, Z., M. N. Lakthakia, B. Yarnal, R. A. White, D. A. Miller, B. Frakes, E. J. Barron, C. Duffy and F. W. Schwartz, 1999: Simulating the river-basin response to atmospheric forcing by linking a meso-scale meteorological model and hydrologic model system. *Journal of Hydrology*, **218:** 72-91.

Zorita, E and H. von Storch, 1999: The analog method as a simple statistical downscaling technique: Comparison with more complicated methods. *Journal of Climate*, **12:** 2474-2489.

APPENDIX

APPENDIX A

VERIFICATION OF WEOF METHODOLOGY USING DIFFERENT DATA FROM DIFFERENT SOURCES

1. Introduction

All the analysis in this thesis was presented using data obtained from the UK meteorological office. During the candidacy exam Dr Samuel Shen proposed that some of the results be repeated with data from different sources to see the consistency of the WEOF methodology.

Since rainfall is the most variable of all climatic elements analyzed in this thesis, an effort was made to collect new rainfall data for the re-analysis. The new rainfall data was obtained on-line from the SAFARI 2000 project (http://www.daac.ornl.gov). The data set is gridded at 0.5° x 0.5 latitude/longitude resolution. According to the documentation available on this website, New et al., (2000) used an anomaly approach which attempts to maximize station data in space and time. Station measurement data for the years 1961-1990, extracted from the monthly data holdings of the Climatic Research Unit and the Global Historic Climatology Network (GHCN), served as the normal period (New et al., 1999). The anomaly grids were then combined with high-resolution mean monthly climatology to arrive at fields of estimated historical monthly surface climate.

We found that data for the 1916-1926 period had gross outlier errors and hence only data from 1927 to 1998 was used for the analysis. In this appendix we present results of WEOF analysis for the SON rainfall of East Africa, which as was alluded to in Chapter three was the most variable of the two East African rainfall seasons.

2. Results (1927-1998)

2.1 Spatial Patterns of SON rainfall (East Africa)

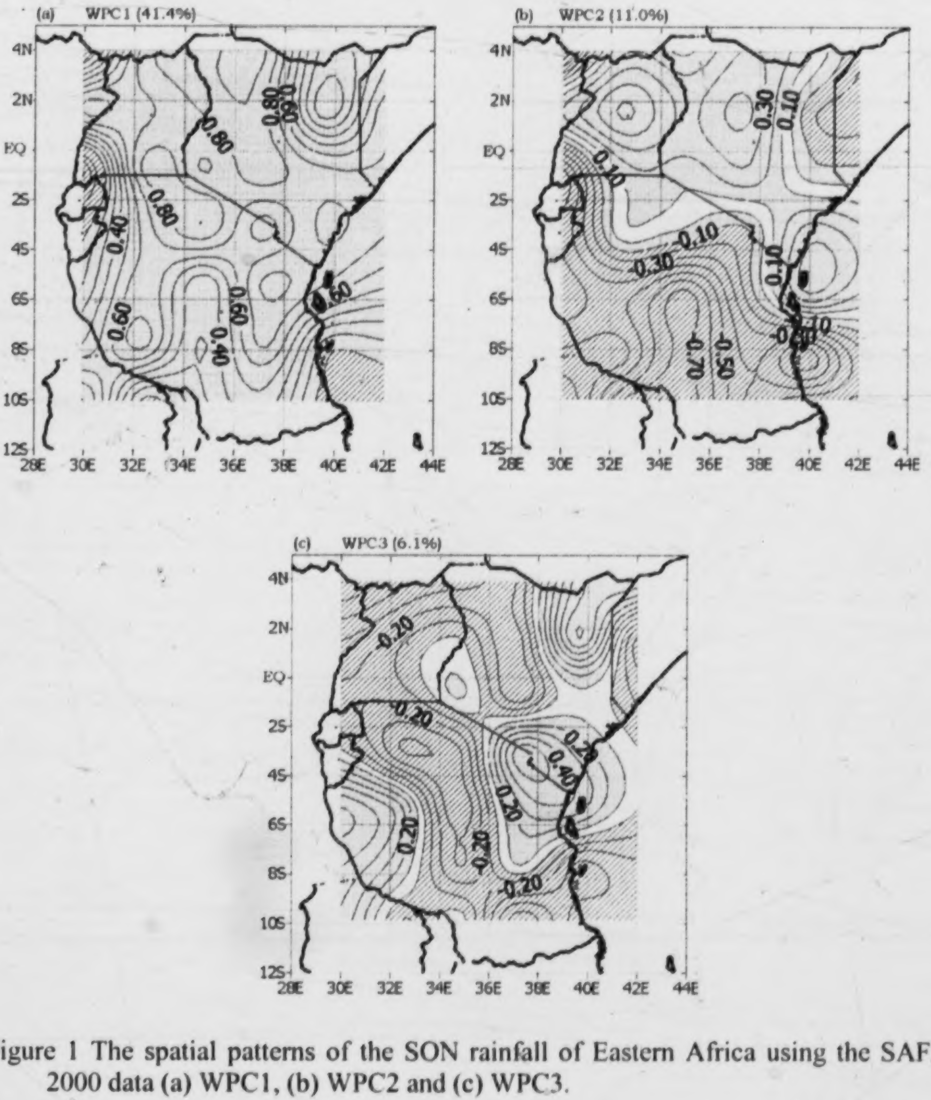
(a) WPC1 (41.4%)
(b) WPC2 (11.0%)
(c) WPC3 (6.1%)
4N
2N
EQ
2S
4S
6S
8S
10S
12S
28E
30E
32E
34E
36E
38E
40E
42E
44E
0.80
0.60
0.40
0.30
0.10
-0.10
-0.30
-0.50
-0.70
-0.20
0.20
0.40

Figure 1 The spatial patterns of the SON rainfall of Eastern Africa using the SAFARI 2000 data (a) WPC1, (b) WPC2 and (c) WPC3.

Since the length scale of rainfall storms is 60 km (see Chapter six), the 0.5° x 0.5 (~50km x 50 km) resolution provides us a chance to examine the spatial resolution using greater detail. It is seen in Figure 1 and 2

2.2 Temporal Patterns of SON rainfall (East Africa)

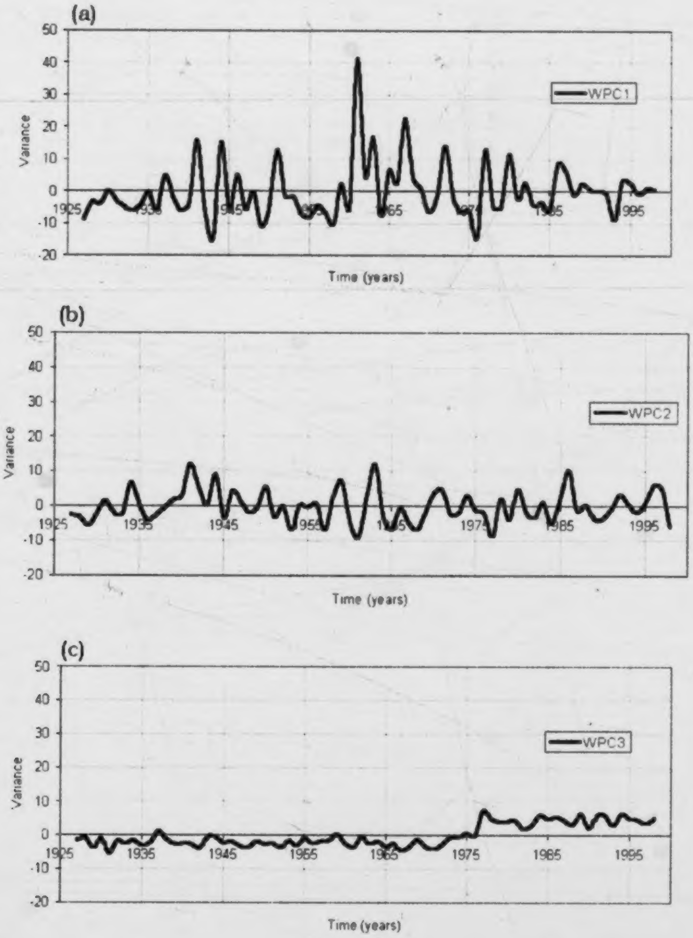

Figure 2 The temporal patterns of the SON rainfall of Eastern Africa using the SAFARI 2000 data at 0.5° x 0.5° resolution (a) WPC1, (b) WPC2 and (c) WPC3.

Figures 1 and 2 shows the spatial and temporal patterns found by using the SAFARI 2000 project data. It is seen that the patterns are consistent with the ones found in Chapter three, using the UK met data.